UNIVERSITY OF SOUTHAMPTON

FACULTY OF NATURAL AND ENVIRONMENTAL SCIENCES

Chemistry

Surface Enhanced Raman Spectroscopy of the Ionic Liquid - Metal Interface

by

Danai Emily Panagoulia

Thesis for the degree of Doctor of Philosophy

January 2018

UNIVERSITY OF SOUTHAMPTON

ABSTRACT

FACULTY OF NATURAL AND ENVIRONMENTAL SCIENCES

Chemistry

Thesis for the degree of Doctor of Philosophy

Surface Enhanced Raman Spectroscopy of the Ionic Liquid – Metal Interface

Danai Emily Panagoulia

When a charge is applied to an electrode in the metal – Ionic Liquid (IL) interface, an electrochemical double layer is expected to form due to the arrangement of ions to counter the charge on the electrode surface. However, this arrangement of ions in ILs can be complicated by effects such as specific adsorption, ion re-orientation and superoxide ion and Au oxide formation. Traditional techniques used in the study of metal-IL interfaces, have provided a good indication of underlying processes. However, additional proof from new methods is required, as interpretations of the results sometimes vary.

In this work, surface enhanced Raman (SERS) spectra have been acquired from the electrochemically controlled interface between Au and 1-butyl-1-methylpyrrolidinium bis(trifluoromethylsulfonyl)imide (BMP TFSI). By analysing the intensity and positions of peaks in the spectra corresponding to specific vibrations in the different ions of the IL, useful information has been obtained about the processes occurring at the interface at a molecular level.

By using impedance spectroscopy, the potential of zero charge (PZC) was tentatively assigned to -0.85 V vs. PQRE. Cathodic features in cyclic voltammograms and in current-potential data of the SERS experiment, at potentials negative to the PZC, have been assigned to the re-orienting of the BMP cations, increase in axial BMP conformers and superoxide ion formation, tying together varying interpretations from the literature. Au oxide formation from trace water was detected in the SERS spectra and corresponded to a small increase in current at positive potentials.

Due to the high concentration of ions in ILs, the effect of the bulk signal on Raman and SERS spectra of ILs has also been examined. The depth resolution of the spectrometer, the SERS signal decay with distance from the substrate and the concentration of molecules in the analyte, have all been taken into account.

Table of Contents

Academic Thesis: Declaration Of Authorship

I, DANAI EMILY PANAGOULIA

declare that this thesis and the work presented in it are my own and has been generated by me as the result of my own original research.

SURFACE ENHANCED RAMAN SPECTROSCOPY OF THE IONIC LIQUID – METAL INTERFACE

I confirm that:

1. This work was done wholly or mainly while in candidature for a research degree at this University;
2. Where any part of this thesis has previously been submitted for a degree or any other qualification at this University or any other institution, this has been clearly stated;
3. Where I have consulted the published work of others, this is always clearly attributed;
4. Where I have quoted from the work of others, the source is always given. With the exception of such quotations, this thesis is entirely my own work;
5. I have acknowledged all main sources of help;
6. Where the thesis is based on work done by myself jointly with others, I have made clear exactly what was done by others and what I have contributed myself;
7. None of this work has been published before submission.

Signed: .....

Date: 8th of January 2018

Acknowledgements

I would like to start by thanking my supervisor Professor Andrea Russell, for all her help and support, both professional and emotional, throughout my years as a PhD candidate. Your enthusiasm and passion has consistently been a great source of motivation for me and your consideration and support has been extremely valuable, especially over the course of the last year which has been especially hard for me.

I would also like to acknowledge my advisor Professor Phil Bartlett for constructive discussions and for offering his expertise and knowledge of SERS and electrochemistry and current and past members of his research group who have helped with experimental work; in particular Victor Costa Bassetto and Dr. Evanthia Papadopoulou, for teaching me the method of making SSV substrates and SERS spectroscopy, Dr. Robert Johnson for useful discussions on SERS of ionic liquids and Dr. Jack Branch for teaching me how to make sealed electrodes for the spectroelectrochemical cell. I would further like to thank Professor David Smith and Liam McDonnell from the department of Physics and Astronomy for all their help with reflectance spectroscopy.

I owe a debt of gratitude to the staff of the mechanical workshop and in particular Alan Glass, for the construction of the spectroelectrochemical cell and Alistair Clarke, for the preparation of the gold-coated microscope slides and training on SEM, all of which were critical for the success of this project.

Next, I would like to thank my colleagues from the electrochemistry group, with whom I have worked alongside for the past four years. In particular I would like to express my gratitude to members of my research group Alex Keeler, David Inwood, Dr. Turgut Sonmez, Andrew Leech, Howard Huang, Dr. Stephen Thompson and Dr. Scott Gorman. Our coffee breaks kept me going!

Outside of the University, I would like to thank staff at Renishaw plc and especially Richard Wrighton, Shaun Buckley and Ian Hayward, for all their advice and support with the use and maintenance of the Raman spectrometers.

I would like to thank my friends who travelled to Southampton to support me when I needed them the most and Alex, for being brave and staying positive at the toughest of times. I would also like to thank my whole family, but especially my parents and my sister who are always the greatest source of inspiration and strength to me. Finally, I would like to dedicate this report to my grandmother Kalliopi Dimaki.

Definitions and Abbreviations

4’-MBPCN	4’-Mercaptobiphenylcarbonitrile
4-MBN	4-Mercaptobenzonitrile
a	antisymmetric
AFM	Atomic Force Microscopy
Ax	Axial
BMI	1-Butyl-3-Methylimidazolium
BMP	1-Butyl-1-Methylpyrrolidinium
CE	Counter Electrode
CPE	Constant Phase Element
CV	Cyclic Voltammetry/Voltammogram
DFT	Density Functional Theory
DMF	Dimethyl Formamide
DMSO	Dimethyl sulfoxide
EC	Electrochemical(ly)
EDL	Electrochemical Double Layer
EMI	1-Ethyl-3-Methylimidazolium
Eq	Equatorial
FR	Fermi Resonance
FWHM	Full Width at Half Maximum
IL	Ionic Liquid
ip	in plane
KF	Karl Fischer

Definitions and Abbreviations

(N)IR	(Near-)Infrared
NIST	National Institute of Standards and Technology
OCP	Open Circuit Potential
oop	out of plane
PPB	Potassium Phosphate Buffer
PQRE	Pt Quasi-Reference Electrode
PS	Polystyrene
Py	Pyridine
PZC	Potential of Zero Charge
RE	Reference Electrode
RHE	Reversible Hydrogen Electrode
s	symmetric
SAM	Self-Assembled Monolayer
SCE	Saturated Calomel Electrode
SEM	Scanning Electron Microscope
SERS	Surface Enhanced Raman Spectroscopy
SMSE	Saturated Mercury Sulphate Electrode
(SP)EIS	(Staircase Potential) Electrochemical Impedance Spectroscopy
SSV	Sphere Segment Void
STM	Scanning Tunnelling Microscopy
t	torsion
TFSI	bis(trifluoromethylsulfonyl)imide
TLC	Thin Layer Cell
WE	Working Electrode

δ	bending
ν	stretching
ρ	rocking
τ	twisting
ω	wagging

Chapter 1: Introduction

1.1 Ionic Liquids and Electrochemistry

Ionic Liquids (ILs) are a class of solvents composed solely of ions and are liquid below 100°C. They consist of asymmetric organic cations and low coordinating organic or inorganic anions, which provide them their relatively low melting points. Examples of some popular ions used in ILs, which will be investigated in this thesis, may be seen in figure 1-1.

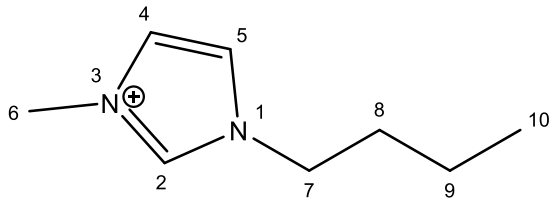

1-Butyl-3-Methylimidazolium
BMI

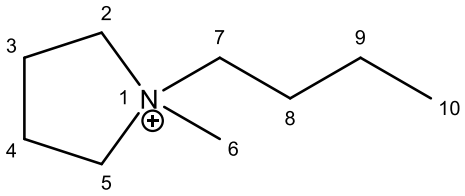

1-Butyl-1-Methylpyrrolidinium
BMP

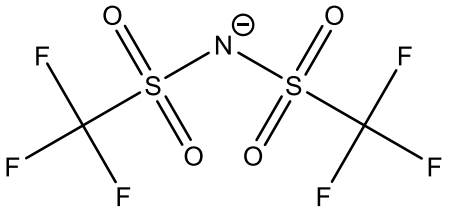

bis(trifluoromethylsulfonyl)imide
TFSI

Figure 1-1 Structures, full and abbreviated names of ions of ILs studied in this report.

There are a large number of combinations of constituent ions which can be used to form ILs. For example, Iolitec, the manufacturer of the ILs used in this study, has approximately 250 ILs in their standard product portfolio.[1] Each ion combination can yield different beneficial properties, which makes ILs very versatile for a wide range of applications. Some of the properties which can be tuned by changing the constituent ions of ILs are melting point, volatility, thermal stability and conductivity. There are published tables of measured properties for large numbers of ILs studied, which can be used to find the ideal IL for a specific application.[2, 3] There is also a very useful online database by the United States National Institute of Standards and Technology (NIST) which

includes up to date information from publications of experimental thermophysical properties for ILs.[4, 5]

The most prominent reason for the high degree of interest in ILs for electrochemical (EC) applications is the wide potential stability windows they can possess, compared to conventional aqueous or organic electrolytes.[2] This allows the investigation or use of EC properties which would otherwise be impossible due to the EC decomposition of the electrolyte, hydrogen or oxygen evolution. For example, the energy density of an electrochemical double layer (EDL) capacitor is proportional to the square of the operating potential window of the system, so the wider the potential stability window of the IL, the higher the energy density of the capacitor.[6] ILs have also been used in EC biosensor applications, in order to improve their stability which has been limited in the past due to the narrow stability windows of conventional aqueous electrolytes.[7]

1.1.1 The Significance of the Metal – Ionic Liquid Interface

In EC applications the electrolyte-metal interface and more specifically the EDL, plays a major role. The EDL is formed when the presence of a charge at the electrode surface causes the attraction or repulsion of certain ions towards or away from the electrode surface.[8] This effect results in an arrangement of ions close to the electrode which creates a charge equal and opposite to that of the electrode. This potential-dependent arrangement of ions, along with processes such as adsorption, charge transfer and mass transfer, define the potential distribution at the electrolyte-electrode interface.[9]

The distribution of ions in dilute aqueous electrolyte solutions is usually described by Gouy-Chapman-Stern theory.[9] This theory suggests the presence of a compact layer of ions in contact with the electrode surface and a diffuse layer of ions extending to a certain distance into the bulk solution. The theory also assumes that ions act as point charges in solution that interact via Coulombic forces. However, these assumptions are not valid in ILs, because of high ionic concentrations and because the ions are more complex, often asymmetric and contain charge delocalisation. The complex structures of various IL ions lead them to have different responses to potential changes at EC interfaces. IL-metal electrode interfaces are much more complex than conventional electrolyte interfaces, resulting in an on-going debate about the potential-dependent structure at these interfaces.[10]

Knowledge of the processes taking place at the IL-metal interface is crucial for the optimised use of these interfaces in EC applications.[10] For example, Borishenko et al. have studied the metal-IL interface in order to understand the details of Ta, Ga and Si electrodeposition. [9] They achieved

this by using vibrational spectroscopy, atomic force microscopy (AFM) and scanning tunnelling microscopy (STM) to study how the addition of various precursors affected the structures of the bulk IL and the metal-IL interface.

Another example was the study by Wippermann et al. which involved examining the effect of water content at the interface between proton-conducting ILs and Pt electrodes for use in polymer electrolyte fuel cells at high temperatures.[11] Through the use of cyclic voltammetry (CV) and electrochemical impedance spectroscopy (EIS), the authors found that water competed with the cations in all reactions involving protons, which resulted in alternate reaction paths and adsorbates that complicated the interface.

These examples demonstrate how further understanding of the metal – IL interface structure could assist in the improvement of the design of IL electrolyte applications.

1.1.2 Common Techniques in the Study of Metal – Ionic Liquid Interfaces

As also seen in the two examples described above, the most commonly used methods in the study of the IL – metal interface are CV, EIS, AFM and STM, often complimented by computational modelling techniques to accompany these experimental techniques.[12] The numerous studies which have used these techniques on this type of EC interfaces provide researchers with a decent understanding on the response of various ILs to the EC potential.

CV and EIS are the most commonly used EC techniques for the study of interfaces and they are often used in conjunction with one another.[13, 14] CV is often the first step in most EC studies, including those of metal-IL interfaces, as it allows the user to determine the potential stability window of a system. This window is defined by the potential region of the CV where the current does not change significantly, often between large current increases due to degradation of the electrode material or degradation of the IL ions. The technique has also been used to detect current arising from more subtle processes occurring at the interface, such as ion re-arrangements and superoxide ion formation from the presence of O_2 in the system.[15, 16]

CV is thus a great technique for indicating the potential regions in which Faradaic or even non-Faradaic processes may be occurring. Furthermore, if the processes are known and the electroactive surface area of the electrode can be measured, the amount of reagents or products taking part may be calculated. However, additional techniques are required if the processes producing the current are unknown, as CV cannot provide structural information about the interface.

The analysis of EIS data is much more complex than CV data. It often requires modelling of the data by predicting the impedance response of an electrical circuit containing components corresponding to characteristics of the interface, such as uncompensated solution resistances.[14, 17] One of the most commonly calculated variables is the interfacial capacitance, which is a measure of the charge stored at the interface and is the result of the arrangement of the ions to counteract the charge applied to the electrode surface.[17, 18] The potential-dependent behaviour of the interfacial capacitance is complex and varies between ILs and between metal surfaces.[14] However, the potential of zero charge (PZC), i.e. the potential at which the overall charge at the interface is 0, is often estimated to be at the potential where the capacitance is at a minimum.[17, 19, 20] The PZC is useful to know as it can be a point of reference in the interpretation of data obtained from other experimental techniques. It is expected that preferential arrangement of the ions will begin when the potential is scanned away from the PZC, with the positive or negative charging at the electrode.

EIS is thus an invaluable technique for predicting the PZC of well-known and simple systems. However, it is limited by complex data analysis and just like CV, cannot provide much information for unknown processes taking place at the metal-IL interface.

AFM and STM are extremely useful microscopy techniques which can be run in situ with controlling the EC potential of the interface.[13, 21-23] AFM can detect the thickness of individual ion layers at various distances from the electrode surface, providing useful information about the potential-dependent arrangement and layering of ions and the thickness of the EDL.[24] Other publications have also used AFM to understand the relationship between the EDL structure and properties such as temperature, ion size and mechanical properties.[25-28] STM can provide information about structured patterns of ions covering an electrode surface and can detect re-construction of metal surfaces due to strong specific adsorption which sometimes occurs at the metal – IL interface.[22, 29]

Lastly, Georgi, Fedorov and Kornyshev have demonstrated the importance and power of computational chemistry in studying the metal-IL interface with their numerous publications on the subject.[12, 18, 30-33] They compare their results, obtained from Monte Carlo simulations of a model system, to experimental results, both on a qualitative and a quantitative level. This allows them to model capacitance responses, density distributions of ions and even the orientation of ions with respect to the electrode surface. However, Georgi, Fedorov and Kornyshev have generally acknowledged that the double layer structure will be affected by the fact that ions have different sizes, are non-spherical and asymmetric and that there are forces acting between them, which may not always be successfully predicted by computational models.[12, 31, 33] Furthermore,

the number of ion layers will vary with ion size, symmetry and electrode charge. Therefore, a generalisation of the EDL structure for IL-based interfaces based on one model is difficult, as every IL is unique.

While these techniques are all valuable in the ongoing study of individual metal-IL interfaces, it is crucial to find new ways to extract information from them. Spectroscopic methods, including surface enhanced Raman spectroscopy (SERS), are being used more and more in the study of the metal-IL interface as they can provide detailed chemical and structural details of molecules present close to the electrode surface.[17, 34-38] More details about SERS and this literature is included in the following section.

1.2 Surface Enhanced Raman Spectroscopy for the Study of ILs

1.2.1 Raman Spectroscopy

The main spectroscopies used to detect vibrations in molecules and thus obtain chemical and structural information are infrared (IR) absorption and Raman scattering. Unlike IR spectroscopy, Raman spectroscopy can be used to examine aqueous samples and no preparation of the sample is needed, such as mixing with Nujol.

Raman spectroscopy uses a single frequency of radiation to illuminate the sample, usually generated from a laser. Photons interact with the electron cloud of the sample and excite molecules to a short-lived 'virtual' energy state, as can be seen in figure 1-2. As this state is unstable, the molecules rapidly relax and photons are re-emitted. These photons are collected and their respective energies are determined:

$$h\nu_{\mathrm{vib}} = h\nu_{\mathrm{in}} \pm h\nu_{\mathrm{out}}$$

where $h\nu_{\mathrm{in}}$ is the energy of the incident photons, $h\nu_{\mathrm{out}}$ is the energy of the scattered photons and $h\nu_{\mathrm{vib}}$ is the energy of the molecular vibration.[39]

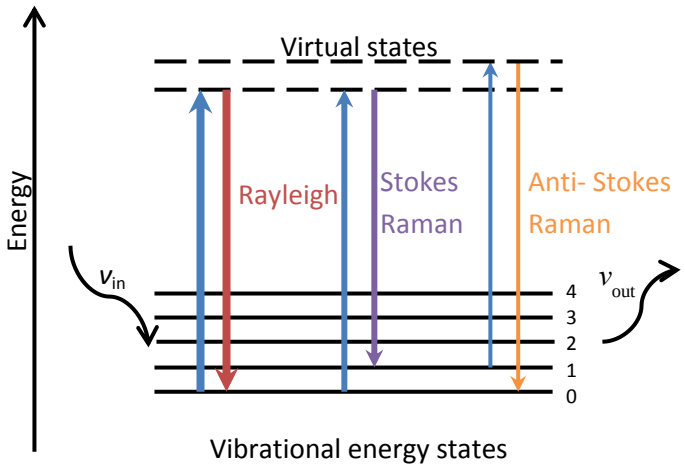

Figure 1-2 Energy diagram and schematic of Raman and Rayleigh processes.

Upon relaxation the molecule can return to states of different energies, as shown in figure 1-2. It can return to its initial energy state, resulting in elastic scattering called Rayleigh scattering. This is the process in which the majority of incident photons take part. If the molecule returns to an energy state of higher energy, the photon will be inelastically scattered. This is termed the Stokes Raman scattering. Similarly, if the molecule returns to a lower energy state there is inelastic scattering called anti-Stokes Raman scattering. The last two processes are the ones that contribute to Raman spectroscopy. Unfortunately, they are very weak as approximately only one in 10^7 photons takes part.[40] As a result, distinguishing Rayleigh from Raman scattering becomes a difficult process and Raman intensity can be very weak.

1.2.2 Surface Enhanced Raman Spectroscopy

SERS results in enhanced Raman signals of molecules attached to SERS-active surfaces, by an average of 10^6-10^8.[41] There are two different enhancement mechanisms used to explain the SERS effect, electromagnetic enhancement and chemical enhancement.[42] Electromagnetic enhancement occurs due to excitation of surface plasmons by coupling with incident photons on rough metal surfaces. Surface plasmons are collective excitations of free electrons in the near surface region of solids, as demonstrated in figure 1-3. Surface roughness or curvature affects the surface plasmon wave vectors and frequencies, by increasing the parallel wave vector by an amount related to the surface structure of the metal. When the frequency of the plasmon matches the frequency of the incident photon there is an increase of the local electric field intensity which induces a dipole moment in nearby or adsorbed molecules.[43] This process constitutes the electromagnetic SER mechanism.[42, 44]

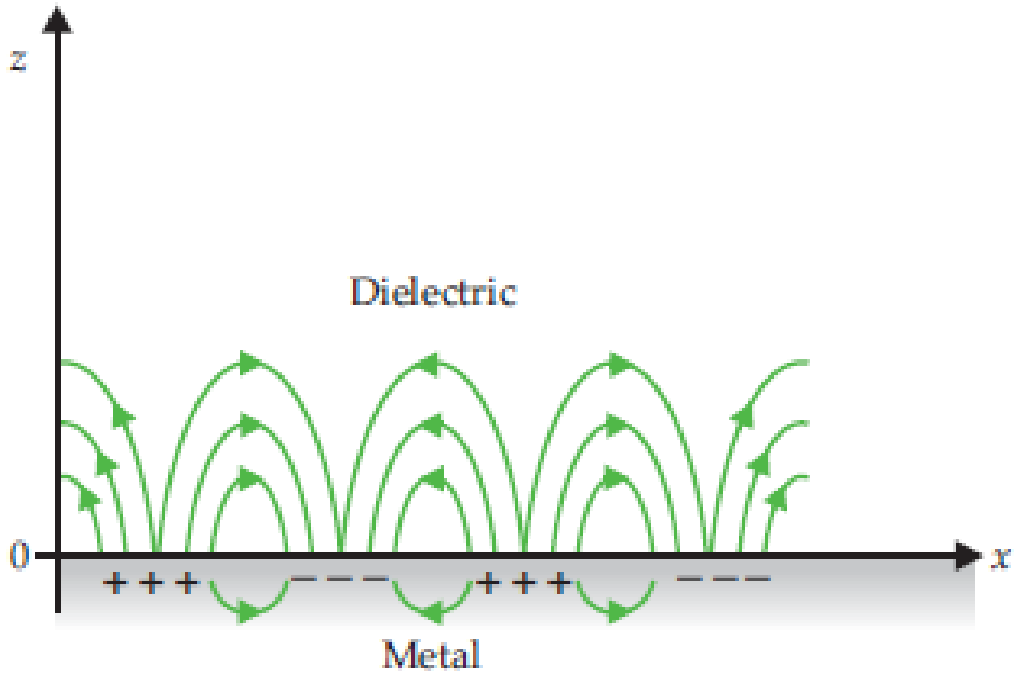

Figure 1-3 Diagram obtained from the literature demonstrating electric field lines (green) and charge distributions associated with a surface plasmon travelling along a metal-dielectric interface.[45]

However, there are cases in which SER enhancements cannot be explained solely by electromagnetic enhancement mechanisms. Chemical enhancements are related to electronic coupling between the adsorbed molecule and the metal substrate resulting in an "electronic" enhancement.[44] Upon absorption of a laser photon, an electron from the Fermi level of the metal can reach the energy of the delocalised electrons in the adsorbate. As a result, an electron from the metal is transferred to an unoccupied molecular orbital on the adsorbate, changing the polarisability of certain vibrations and creating a vacancy on the surface. When the metal surface is flat, the time this electron spends at the adsorbate is similar to the time it takes for the vacancy to recombine with another electron, resulting in a continuum of electron-vacancy excitation, instead of a Raman peak. On the other hand, if the metal surface is nanostructured, the vacancies can be trapped for long enough in order for the charge transfer vibration to occur.[46]

Today, it is widely accepted that the principal contribution to SERS enhancement is due to strong electric fields associated with surface plasmons.[41] Chemical enhancement only contributes a factor of 10-100, while the remaining 10^4-10^7 enhancement comes from electromagnetic field enhancement.

Using SERS a number of peaks at specific wavenumbers are obtained and these can be correlated with specific bonds in molecules that are very close to the metal surface. This can help distinguish between adsorbed molecules or ions from molecules in solution. Small changes in the orientation of the adsorbate relative to the substrate will result in changes in the intensities of Raman bands associated with certain vibrations. As SERS is based on surface-specific processes, single molecules can be detected on appropriate substrates at low concentrations, creating the opportunity to use SERS in a variety of fields, such as polymer and materials science, biochemistry and bio-sensing, catalysis and electrochemistry.[47]

The vibrational Stark effect is a useful tool in the direct measurement of interfacial electric fields.[48] It is the perturbation of the vibrational energy of a molecular bond by the presence of a local electric field. The Stark tuning rate dν/dE is the shift in vibrational frequency with changing electric field and is a measure of the sensitivity of a vibrational frequency to an electric field. For Raman spectroscopy the Stark effect is anticipated for dipolar molecules. Therefore, by performing EC-SERS at metal-IL interfaces with an added probe molecule which has a high molecular dipole moment, the Stark tuning rate can be measured for various potentials. This can provide information about the PZC and structural changes at the interface, affected by the local electric field.

1.2.3 Sphere Segment Void Substrates

As described in the previous section, SERS results in strongly increased Raman signals from molecules on SERS-active substrates. The oldest and simplest way of preparing these is by electrochemically roughening metal surfaces.[49, 50] However, the degree of surface enhancement for these substrates is not reproducible, varies from one area of the surface to another and is unstable. Many alternative substrates have been employed that range in structure from nano-rods to three-dimensional colloidal solutions and they can have tuneable plasmon resonances and a range of enhancement factors.[47] Despite this, not all substrates are suitable for electrochemical SERS measurements and a substrate which is also robust and easy to fabricate and reproduce is required.[51]

Sphere segment void (SSV) substrates have been developed within the last 15 years at the University of Southampton and their plasmonic properties have been actively studied.[41, 51-58] They have a well-known and reproducible nanostructure and give Raman enhancements of the order of approximately 10^6. They are created by controlled electrodeposition of the desired metal through a close-packed hexagonal array of self-assembled polystyrene (PS) nanospheres, as displayed in

figure 1-4. When the PS is dissolved, an ordered metallic structure is left behind, which is ideal for SERS. [41, 58]

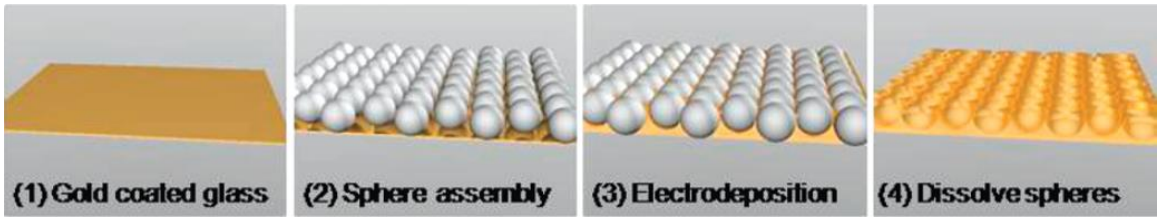

Figure 1-4 Schematic obtained from the literature, demonstrating the steps of SSV substrate fabrication.[41]

The morphology of the voids determines the spatial and spectral positions of surface plasmons. The spherical voids support the existence of localised plasmons which are trapped within the void, while the 'bridges' between the voids support the existence of de-localised plasmons which can move along the 2-dimentional grating, as displayed in figure 1-5. By tuning the thickness and diameter of the voids in the SSV structure, its plasmonic properties can be optimised to significantly enhance optical fields at precise locations, in order to give maximum enhancement for the laser wavelength used.

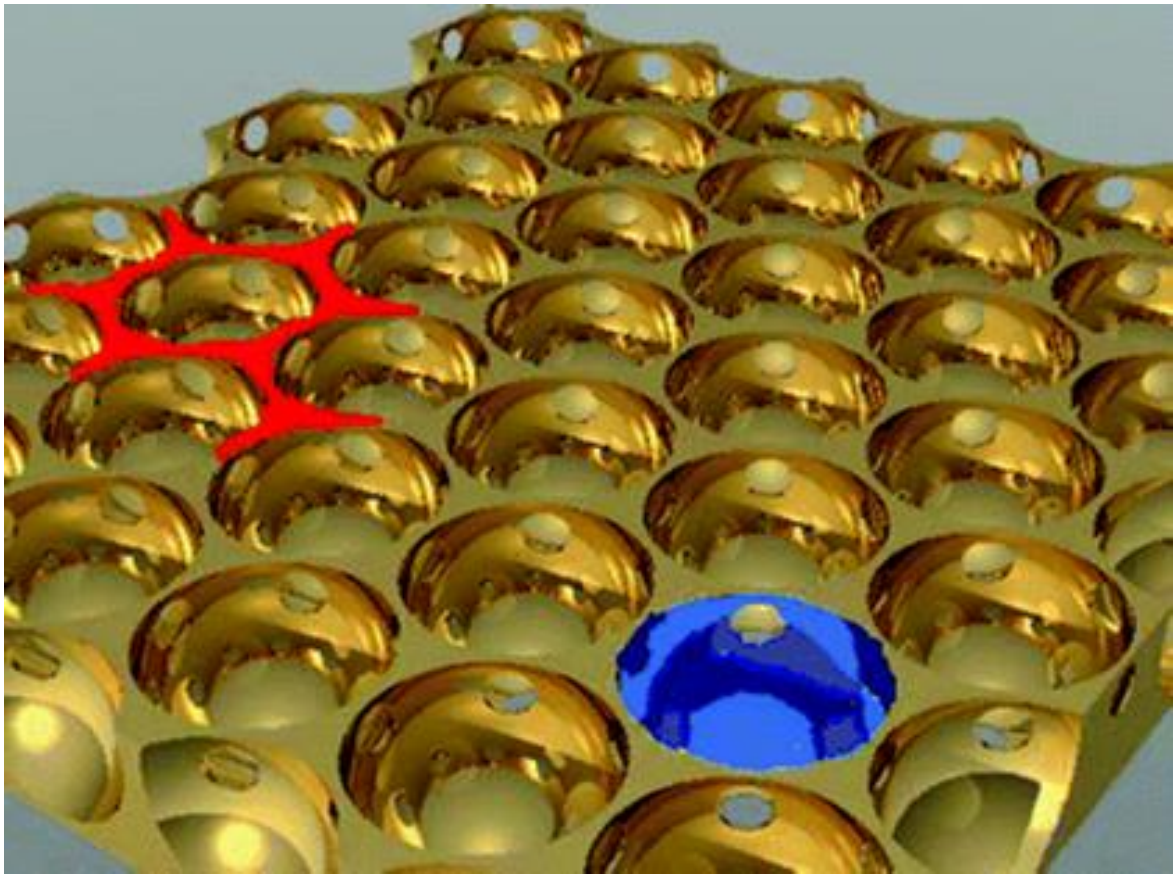

Figure 1-5 Illustration of the localised plasmons (blue) and the delocalised plasmons (red) on a SSV substrate.[59]

1.2.4 SERS in the Study of Molecular Orientation and Conformation

Surface selection rules of vibrational spectroscopy describe the level of enhancement of vibrational intensities of molecules near metal surfaces, depending on the orientation of vibrational modes with respect to the metal surface.[60] For SERS, vibrations whose polarisability tensors are normal to the metal surface have their intensities enhanced, while vibrations whose polarisability tensors are parallel to the metal surface have their intensities quenched. This is due to the electric field normal to the metal surface being most intense, thus enhancing the SERS intensity of vibrations with tensors in the same direction.[61]

The direction of polarisability tensors is difficult to define for complex molecules and this can complicate the application of surface selection rules in the determination of molecule orientations using SERS.[62, 63] However, evidence from existing studies has demonstrated with molecules such as pyridine, pyrazine and substituted benzene molecules, that generally, peaks corresponding to vibrations along the surface normal are more enhanced than those parallel to the substrate surface.[61, 64]

This surface selection rule has also been applied to SSV substrates, in a study by Johnson et al., who utilised the surface selection rule to determine the binding mechanism and orientation of acridine orange to a DNA strand.[65] Even though this type of analysis was purely qualitative, it can be a very useful tool in determining the orientation of any molecule close to a SSV substrate. Therefore, the SERS surface selection rule will be used later on in this report to examine the orientation of both IL ions and self-assembled monolayer (SAM) molecules adsorbed onto the Au SSV substrate.

1.3 SERS of the Ionic Liquid-Metal Interface

EC-SERS of the metal-IL interface is a relatively new field of research, which has only really existed for just over a decade. To the best of our knowledge, Santos et. al. were the first to report a study of the EC IL-metal interface by SERS in 2006.[35] They studied the BMI PF_6 IL at an electrochemically roughened Ag electrode surface at various potentials. More specifically, they monitored the potential dependence of peaks corresponding to BMI cations. At potentials positive to the PZC, the peaks were very weak and so they suggested that the BMI cation adsorbs on the Ag surface with the imidazolium ring perpendicular to the metal surface, allowing the approach of the PF_6 anions. At potentials negative to the PZC the peaks increased in intensity and so they proposed that the cation orientates itself so that the imidazolium ring is parallel to the Ag. At very negative potentials they explained the appearance of new peaks in the SERS spectra as the result of the BMI cation reduction to a carbene.

This first publication on the study of pure ILs on roughened metal surfaces by SERS was followed up by similar publications. Examples include publications by Brandao et. al and Yuan et al., who studied interfaces between Cu and BMI-based ILs and Liu et al., who studied the interface between Ag and a series of imidazolium-based BF_4 ILs with different cation alkyl chain lengths.[66-68] All of these studies have used roughened metal surfaces as their electrodes and SERS-active substrates. However, as explained earlier, these types of substrates are unreliable as the degree of surface enhancement is not reproducible, and vary from one area of the surface to another.

The need for more reliable SERS substrates let to the publication by Harroun et al. on the study of a series of novel, pyridinium-based, biodegradable ILs on electrodes modified with Ag NPs, using EC-SERS.[69] They found, by using the SERS surface selection rule described earlier, that the structure of the alkyl chain on the cation strongly affected its orientation at the electrode surface. While more structured substrates that are not roughened metals have been used extensively in SERS, there aren't that many studies that have used these in EC interfaces between pure ILs and metal surfaces.

ILs are ideal as non-aqueous solvents for electrochemistry. However, they can be very hydrophilic and can quickly absorb atmospheric water, which can severely affect their electrochemical stability window and so the effect of water at the metal-IL interface needs to be examined.[70] In 2011 Niu et. al. used EC-SERS to study the effect of different concentrations of water on the interface between BMI Br and a rough Ag surface, by monitoring the potential-dependence of the weak peak corresponding to the O-H stretch of water.[71] In the system with lowest water contents (< 0.5 M), the water molecules form hydrogen bonds with the BMI cations of the IL. In the system with higher water content (> 0.5 M), hydrogen bonding between water molecules causes them to aggregate, forming a 'network' of water adhered to the electrode surface.

Many studies involve more applied versions of the metal-IL interface and the study of third party molecules in these interfaces. For example, by monitoring the intensity of distinct new peaks in the SERS spectra of a metal-IL interface, researchers are able to monitor the adsorption or desorption of molecules, such as additives or contaminants, on the electrode surface. Yuan et al. have studied the adsorption of the methylimidazole contaminant at the interface between Cu and BMI-based ILs.[68] Costa et al. monitored the formation of a polymeric film from benzotriazole on Cu at the interface with BMI BF_4, which inhibits the Cu corrosion process.[72] Another example of an application of EC-SERS at the metal-IL interface is the study of metal electrodeposition in ILs. Bozzini et al. monitored the nitrile stretching peaks from Au(I) cyanocomplexes, used in Au electrodeposition at the interface between Au and an imidazolium-based TFSI IL.[73] Lastly, the formation of the superoxide ion has been studied at a rough Au – IL interface, which is the main cause of electrolyte instability in Li-O_2 batteries.[38]

Even though there have been various studies of ILs on metal surfaces using SERS, they have been mostly qualitative, as they have used ill-defined substrates which do not give reproducible enhancement from experiment to experiment. It is crucial to study ILs on metal substrates such as SSV substrates, which give reproducible and reliable spectra, leading to more accurate quantitative interpretations of the results. Furthermore, bulk IL effects have not been discussed in the literature, which, as will be discussed later on in this report, can heavily influence the EC-SERS spectra of metal-IL interfaces. Lastly, the SERS surface selection rule has sparsely been used throughout the literature. It is important to carry out a fundamental, comprehensive study using EC-SERS on a simple metal-IL interface, in order to establish what information can reliably be extracted.

1.4 Objectives and Thesis Overview

The research described in this thesis builds on the small amount of existing literature on the use of EC-SERS on the metal-IL interface and also on the vast body of research that has been carried out on these interfaces using alternate techniques. The aim of this project has been to establish what information can be extracted from a simple Au-IL interface using EC-SERS and to use this information to investigate the structure of the IL-metal interface.

The literature review presented in the current chapter has been kept brief, as more descriptions of the relevant literature have been included in the introduction and main body of each chapter.

In chapter 2, the chemicals, equipment and experimental and computational methods used are described. An equation has also been derived to accurately predict the electrodeposition height of SSV substrate films.

In chapter 3, a comprehensive vibrational assignment of the Raman peaks of the BMP TFSI IL has been made. This was achieved with the help of DFT calculations and the presence of multiple ion conformers in the IL has been taken into account. These assignments and the visualisation of certain vibrational modes using the Gaussian software package have been fundamental in the accurate and reliable analysis of peaks corresponding to specific BMP TFSI IL vibrations.

In chapter 4, the SERS response of SSV substrates in concentrated liquids, such as ILs, has been characterised. Spectra have been compared of ILs on flat Au and on SSV Au, alongside spectra of a thiol-based SAM. Pyridine (Py) has then been utilised to study the SERS response on a SSV substrate compared to the Raman response on flat Au, as function of concentration. The experimental results have been discussed with respect to depth resolution and the theoretical SERS signal decay with distance from the substrate. The work of this chapter has provided a fundamental understanding of the counter-intuitively low SERS intensity of ILs, which has never been discussed in the literature.

In chapter 5, the potential-dependent Au-BMP TFSI interface has been studied with a combination of CV, EIS and EC-SERS. The PZC, cation/anion ratios, BMP cation orientations and conformations and superoxide ion and Au oxide formations have all been examined and discussed. This chapter has added valuable information about the potential-dependent behaviour of the Au-BMP TFSI interface, for which there have been varying interpretations in the literature.

Chapter 6 contains a brief EC-SERS study of the 4-mercaptobenzonitrile (4-MN) SAM on a Au SSV substrate in two ILs and in an aqueous potassium phosphate buffer (PPB). The Stark effect of the SAM has been examined and the orientation of the molecule has also been taken into account.

The Stark effect of the 4-MBN SAM in BMP TFSI has also been compared to that of a 4'-MBPCN SAM and the SERS signal decay with distance has been revisited. The work of this chapter constitutes a brief introduction into the types of measurement which can be achieved with SAMs in ILs and confirms the agreement of the experimental results on SSV substrates with the theoretical prediction of the SERS signal decay with distance from the substrate.

In chapter 7 the conclusions of this thesis are summarised and proposals for future work are presented. The results of the previous chapters are discussed with regards to the insight gained into the metal-IL interface and with regards to the benefits and challenges with using EC-SERS as method in the study of these interfaces. Finally, some future experiments are proposed for improving the technique and our understanding of potential-dependent processes.

1.5 References

1. Introduction, https://iolitec.de/index.php/en/products/ionic_liquids/introduction, (accessed 4th January, 2018).

2. S. J. Zhang, N. Sun, X. Z. He, X. M. Lu and X. P. Zhang, *J. Phys. Chem. Ref. Data*, 2006, **35**, 1475-1517.

3. H. Tokuda, S. Tsuzuki, M. Susan, K. Hayamizu and M. Watanabe, *J. Phys. Chem. B*, 2006, **110**, 19593-19600.

4. A. Kazakov, J. W. Magee, R. D. Chirico, E. Paulechka, V. Diky, C. D. Muzny, K. Kroenlein and M. Frenkel, NIST Standard Reference Database 147: NIST Ionic Liquids Database - (ILThermo), http://ilthermo.boulder.nist.gov/, (accessed 5th January, 2018).

5. Q. Dong, C. D. Muzny, A. Kazakov, V. Diky, J. W. Magee, J. A. Widegren, R. D. Chirico, K. N. Marsh and M. Frenkel, *J. Chem. Eng. Data*, 2007, **52**, 1151-1159.

6. Q. Y. Dou, L. Y. Liu, B. J. Yang, J. W. Lang and X. B. Yan, *Nature Communications*, 2017, **8**.

7. Z. Q. Shi, W. J. Hou, Y. C. Jiao, Y. M. Guo, X. Sun, J. Zhao and X. Y. Wang, *Int. J. Electrochem. Sc.*, 2017, **12**, 7426-7434.

8. D. Pletcher, *A First Course in Electrode Processes*, Royal Society of Chemistry, Cambridge, 2nd edn., 2009.

9. N. Borisenko, A. Lahiri, G. Pulletikurthi, T. Cui, T. Carstens, J. Zahlbach, R. Atkin and F. Endres, *Faraday Discuss.*, 2018, **206**, 459-473.

10. P. Reichert, K. S. Kjaer, T. B. van Driel, J. Mars, J. W. Ochsmann, D. Pontoni, M. Deutsch, M. M. Nielsen and M. Mezger, *Faraday Discussions*, 2018, **206**, 141-157.

11. K. Wippermann, J. Giffin, S. Kuhri, W. Lehnert and C. Korte, *Phys. Chem. Chem. Phys.*, 2017, **19**, 24706-24723.

12. M. V. Fedorov and A. A. Kornyshev, *Chem. Rev.*, 2014, **114**, 2978-3036.

13. R. Atkin, N. Borisenko, M. Druschler, S. Z. El Abedin, F. Endres, R. Hayes, B. Huber and B. Roling, *Phys. Chem. Chem. Phys.*, 2011, **13**, 6849-6857.

14. V. Lockett, M. Horne, R. Sedev, T. Rodopoulos and J. Ralston, *Phys. Chem. Chem. Phys.*, 2010, **12**, 12499-12512.

15. M. Gnahm, C. Muller, R. Repanszki, T. Pajkossy and D. M. Kolb, *Phys. Chem. Chem. Phys.*, 2011, **13**, 11627-11633.

16. L. Grande, E. Paillard, G. T. Kim, S. Monaco and S. Passerini, *Int. J. Mol. Sci.*, 2014, **15**, 8122-8137.

17. S. Baldelli, *Acc. Chem. Res.*, 2008, **41**, 421-431.

18. A. A. Kornyshev, *J. Phys. Chem. B*, 2007, **111**, 5545-5557.

19. S. Baldelli, *J. Phys. Chem. B*, 2005, **109**, 13049-13051.

20. V. Lockett, R. Sedev, J. Ralston, M. Horne and T. Rodopoulos, *J. Phys. Chem. C*, 2008, **112**, 7486-7495.

21. R. Atkin, S. Z. El Abedin, R. Hayes, L. H. S. Gasparotto, N. Borisenko and F. Endres, *J. Phys. Chem. C*, 2009, **113**, 13266-13272.

22. M. Druschler, N. Borisenko, J. Wallauer, C. Winter, B. Huber, F. Endres and B. Roling, *Phys. Chem. Chem. Phys.*, 2012, **14**, 5090-5099.

23. F. Endres, N. Borisenko, S. Z. El Abedin, R. Hayes and R. Atkin, *Faraday Discuss.*, 2012, **154**, 221-233.

24. R. Hayes, N. Borisenko, M. K. Tam, P. C. Howlett, F. Endres and R. Atkin, *J. Phys. Chem. C*, 2011, **115**, 6855-6863.

25. X. Zhang, Y. X. Zhong, J. W. Yan, Y. Z. Su, M. Zhang and B. W. Mao, *Chem. Commun.*, 2012, **48**, 582-584.

26. R. Atkin, N. Borisenko, M. Druschler, F. Endres, R. Hayes, B. Huber and B. Roling, *J. Mol. Liq.*, 2014, **192**, 44-54.

27. H. Li, R. J. Wood, F. Endres and R. Atkin, *J. Phys.-Condens. Matter*, 2014, **26**.

28. J. Hoth, F. Hausen, M. H. Muser and R. Bennewitz, *J. Phys.-Condens. Matter*, 2014, **26**.

29. M. Gnahm, T. Pajkossy and D. M. Kolb, *Electrochim. Acta*, 2010, **55**, 6212-6217.

30. M. V. Fedorov and A. A. Kornyshev, *J. Phys. Chem. B*, 2008, **112**, 11868-11872.

31. N. Georgi, A. A. Kornyshev and M. V. Fedorov, *J. Electroanal. Chem.*, 2010, **649**, 261-267.

32. M. V. Fedorov and A. A. Kornyshev, *Electrochim. Acta*, 2008, **53**, 6835-6840.

33. M. V. Fedorov, N. Georgi and A. A. Kornyshev, *Electrochem. Commun.*, 2010, **12**, 296-299.

34. N. Nanbu, Y. Sasaki and F. Kitamura, *Electrochem. Commun.*, 2003, **5**, 383-387.

35. V. O. Santos, M. B. Alves, M. S. Carvalho, P. A. Z. Suarez and J. C. Rubim, *J. Phys. Chem. B*, 2006, **110**, 20379-20385.

36. J. C. Rubim, F. A. Trindade, M. A. Gelesky, R. F. Aroca and J. Dupont, *J. Phys. Chem. C*, 2008, **112**, 19670-19675.

37. C. Aliaga, C. S. Santos and S. Baldelli, *Phys. Chem. Chem. Phys.*, 2007, **9**, 3683-3700.

38. P. M. Radjenovic and L. J. Hardwick, *Faraday Discuss.*, 2018, **206**, 379-392.

39. P. W. Atkins, *Physical chemistry*, Oxford University Press, Oxford, 4th edn., 1940.

40. Z. D. Zhu, Q. Q. Li, B. F. Bai and S. S. Fan, *Nanoscale Res. Lett.*, 2014, **9**, 1-8.

41. S. Mahajan, R. M. Cole, B. F. Soares, S. H. Pelfrey, A. E. Russell, J. J. Baumberg and P. N. Bartlett, *J. Phys. Chem. C*, 2009, **113**, 9284-9289.

42. A. Campion and P. Kambhampati, *Chem. Soc. Rev.*, 1998, **27**, 241-250.

43. K. Fukami, M. L. Chourou, R. Miyagawa, A. M. Noval, T. Sakka, M. Manso-Silvan, R. J. Martin-Palma and Y. H. Ogata, *Materials*, 2011, **4**, 791-800.

44. K. Kneipp, H. Kneipp, I. Itzkan, R. R. Dasari and M. S. Feld, *Chem. Rev.*, 1999, **99**, 2957-+.

45. T. W. Ebbesen, C. Genet and S. I. Bozhevolnyi, *Phys. Today*, 2008, **61**, 44-50.

46. Y. X. Chen and A. Otto, *J. Raman Spectrosc.*, 2005, **36**, 736-747.

47. B. Sharma, R. R. Frontiera, A. I. Henry, E. Ringe and R. P. Van Duyne, *Mater. Today*, 2012, **15**, 16-25.

48. V. Oklejas, C. Sjostrom and J. M. Harris, *J. Phys. Chem. B*, 2003, **107**, 7788-7794.

49. Z. Q. Tian, B. Ren and D. Y. Wu, *J. Phys. Chem. B*, 2002, **106**, 9463-9483.

50. M. A. Bryant and J. E. Pemberton, *J. Am. Chem. Soc.*, 1991, **113**, 3629-3637.

51. M. E. Abdelsalam, P. N. Bartlett, J. J. Baumberg, S. Cintra, T. A. Kelf and A. E. Russell, *Electrochem. Commun.*, 2005, **7**, 740-744.

52. P. N. Bartlett, J. J. Baumberg, S. Coyle and M. E. Abdelsalam, *Faraday Discuss.*, 2004, **125**, 117-132.

53. J. J. Baumberg, T. A. Kelf, Y. Sugawara, S. Cintra, M. E. Abdelsalam, P. N. Bartlett and A. E. Russell, *Nano Letters*, 2005, **5**, 2262-2267.

54. S. Cintra, M. E. Abdelsalam, P. N. Bartlett, J. J. Baumberg, T. A. Kelf, Y. Sugawara and A. E. Russell, *Faraday Discuss.*, 2006, **132**, 191-199.

55. S. Mahajan, J. J. Baumberg, A. E. Russell and P. N. Bartlett, *Phys. Chem. Chem. Phys.*, 2007, **9**, 6016-6020.

56. S. Mahajan, M. Abdelsalam, Y. Suguwara, S. Cintra, A. Russell, J. Baumberg and P. Bartlett, *Phys. Chem. Chem. Phys.*, 2007, **9**, 104-109.

57. M. E. Abdelsalam, S. Mahajan, P. N. Bartlett, J. J. Baumberg and A. E. Russell, *J. Am. Chem. Soc.*, 2007, **129**, 7399-7406.

58. S. Mahajan, R. M. Cole, J. D. Speed, S. H. Pelfrey, A. E. Russell, P. N. Bartlett, S. M. Barnett and J. J. Baumberg, *J. Phys. Chem. C*, 2010, **114**, 7242-7250.

59. Barnes, Tian, Aggaral, Goodacre, Donaldson, M. Muniz, Baumberg, Vlckova, Creighton, Natan, Kosower, Alexander, Khan, Russell, Murakoshi, Kneipp, Domke, R. Le, Green, Poponin, Stone, Ren, Pettinger, Milton, Jarvis, Tantra, Kall, Sugawara, Roy, Whitby and Richards, *Faraday Discuss.*, 2006, **132**, 227-247.

60. M. Moskovits, *J. Chem. Phys.*, 1982, **77**, 4408-4416.

61. J. R. Lombardi and R. L. Birke, *J. Phys. Chem. C*, 2008, **112**, 5605-5617.

62. X. P. Gao, J. P. Davies and M. J. Weaver, *J. Phys. Chem.*, 1990, **94**, 6858-6864.

63. S. H. Cho, H. S. Han, D. J. Jang, K. Kim and M. S. Kim, *J. Phys. Chem.*, 1995, **99**, 10594-10599.

64. A. G. Brolo, D. E. Irish and B. D. Smith, *J. Mol. Struct.*, 1997, **405**, 29-44.

65. R. P. Johnson, J. A. Richardson, T. Brown and P. N. Bartlett, *J. Am. Chem. Soc.*, 2012, **134**, 14099-14107.

66. Y. Liu, Y. X. Yuan, X. R. Wang, N. Zhang, M. M. Xu, J. L. Yao and R. A. Gu, *J. Electroanal. Chem.*, 2014, **728**, 10-17.

67. C. R. R. Brandao, L. A. F. Costa, H. S. Breyer and J. C. Rubim, *Electrochem. Commun.*, 2009, **11**, 1846-1848.

68. Y. X. Yuan, T. C. Niu, M. M. Xu, J. L. Yao and R. A. Gu, *J. Raman Spectrosc.*, 2010, **41**, 516-523.

69. S. G. Harroun, T. J. Abraham, C. Prudhoe, Y. Zhang, P. J. Scammells, C. L. Brosseau, C. C. Pye and R. D. Singer, *Phy. Chem. Chem. Phys.*, 2013.

70. A. W. Taylor, F. L. Qiu, J. P. Hu, P. Licence and D. A. Walsh, *J. Phys. Chem. B*, 2008, **112**, 13292-13299.

71. T. C. Niu, Y. X. Yuan, J. L. Yao, F. Lu and R. A. Gu, *Sci. China Ser. B*, 2011, **54**, 200-204.

72. L. A. F. Costa, H. S. Breyer and J. C. Rubim, *Vib. Spectrosc.*, 2010, **54**, 103-106.

73. B. Bozzini, E. Tondo, A. Bund, A. Ispas and C. Mele, *J. Electroanal. Chem.*, 2011, **651**, 1-11.

Chapter 2: Experimental Methods

The experimental methods described in this chapter are the general methods employed throughout this work.

2.1 Chemicals and Materials

The materials and reagents used, along with their suppliers are detailed in table 2-1. All water used for cleaning and preparing solutions was deionised from a Purite Select system and with a resistivity of 18.2 MΩ cm. All glassware and other equipment used throughout this study, such as needles and spatulas, were cleaned using acetone and were dried at 105°C in a Thermo Scientific Heratherm oven. Any further purification or drying has been described later on in this chapter.

Table 2-1 List of reagents and materials used and their suppliers.

Reagent/ Material	**Supplier**
1-Butyl-1-methylpyrrolidinium bis(trifluoromethylsulfonyl)imide (BMP TFSI), 99.5 %	Iolitec
1-Butyl-3-methylimidazolium bis(trifluoromethylsulfonyl)imide (BMI TFSI), 99.5%	Iolitec
4'-Mercaptobiphenylcarbonitrile (4'-MBPCN)	Sigma-Aldrich
4-Mercaptobenzonitrile (a.k.a. 4-Sulfanylbenzonitrile, 4-MBN)	Enamine
Acetone, general purpose grade	Fisher Chemical
Brightener additive (E3)	Metalor
Ethanol (a.k.a ethyl alcohol), Pure, 200 proof, anhydrous, ≥99.5 %	Sigma-Aldrich
Gold plating solution, cyanide-free (MetGold ECF 60)	Metalor
Gold surface cleaning solution, $H_2O \geq 90$ % & $H_2SO_4 \leq 10$ %	Sigma-Aldrich
Gold wire, 0.2 mm diameter, evaporation	Agar Scientific

Reagent/ Material	Supplier
Gold wire, 1 mm diameter, 99.9%	Alfa Aesar
Hydranal Coulomat-A (anolyte solution for Karl Fischer titration)	Fluka
Hydranal Coulomat-GC (catholyte solution for Karl Fischer titration)	Fluka
Isopropyl alcohol (a.k.a. Propan-2-ol, IPA), laboratory reagent grade	Fisher Chemical
Mercury (I) chloride, 99.999 %	Sigma-Aldrich
Mercury (I) sulfate, 98 %	Sigma-Aldrich
Mercury quicksilver	Fluka
Molecular sieves, 4 Å, beads, 8-12 mesh	Sigma-Aldrich
N,N-Dimethylformamide (DMF), anhydrous, 99.8 %	Sigma-Aldrich
Nail polish, clear, 60 s	Rimmel
Nitrogen	BOC
Polystyrene (PS) spheres, 600 nm diameter, 1 wt % aqueous suspension	Fisher Scientific
Potassium dihydrogen orthophosphate, AnalaR, ≥99.5 %	BDH Chemicals
Potassium phosphate dibasic, ACS reagent, ≥98 %	Sigma-Aldrich
Pyridine (Py), ACS reagent, >99.8%	Fluka
Silver plating solution, cyanide-free (MetSil 200)	Metalor
Silver wire, 1 mm diameter, 99.9%	Alfa Aesar
Toluene – low in sulfur	Fisher Scientific

2.2 Preparation of Sphere Segment Void Substrates

Sphere Segment Void (SSV) substrates were developed at the University of Southampton to create stable, reusable and tuneable surface enhanced Raman spectroscopy (SERS)-active substrates, with reproducible surface enhancement across the sample, which could be used as

electrodes for electrochemical (EC)-SERS.[1-8] The substrates were prepared using the well-established procedure, first described by Abdelsalam et al. and is described in detail below.[1]

2.2.1 Template Preparation

Gold slides were prepared by evaporating 10 nm of chromium followed by 200 nm of gold onto standard 76 mm x 26 mm x 1 mm glass microscope slides. These gold slides were cut into 8 equal rectangular pieces using a glass cutter and each piece was cleaned in a commercial sulfuric acid-based gold surface cleaning solution, before they were rinsed with water and dried using N_2.

Thin layer cells (TLCs) were created by using a clean gold slide as a base, Parafilm as the spacer and a glass cover slide on the top, as can be seen in figure 2-1. A hot plate at 50-60 °C was used to soften the Parafilm and to stick all the components together. This created a trapezoid-shaped cavity in which to create a PS nanosphere template. A 1.8 wt% aqueous suspension of 600 nm diameter PS spheres was made from a commercial 1 wt% aqueous suspension. Each TLC was filled with 10 µl of the resulting suspension and they were placed in an incubator at 14 °C for ~48 hours.

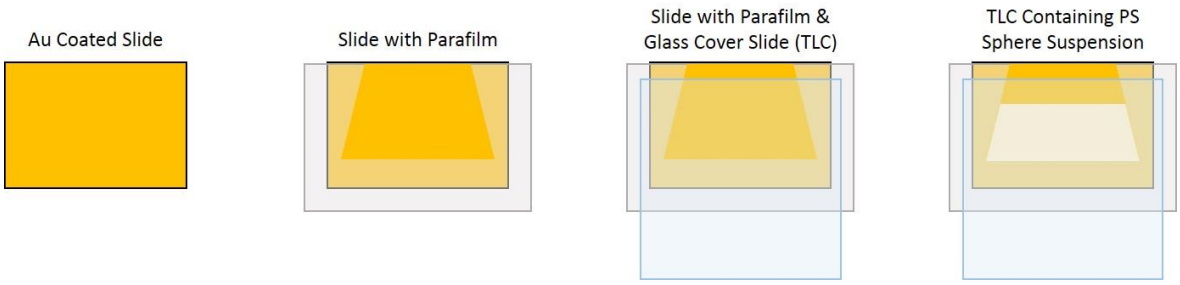

Figure 2-1 Preparation of a TLC and a hexagonal PS nanosphere template.

During incubation, the water evaporated at a slow and steady rate and the spheres arranged in a hexagonal array, under the influence of hydrodynamic forces and attractive lateral capillary immersion forces between the nanospheres, as displayed in figure 2-2.[9] These attractive forces occurred due to the overlap of the water menisci around each nanosphere and caused their two dimensional aggregation and ordering. The result was a self-assembled, hexagonal template of the 600 nm TLC spheres.

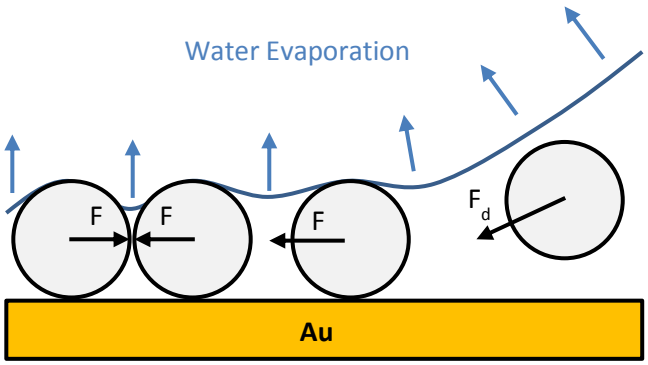

Figure 2-2 Diagram showing the ordering of PS nanospheres from a water suspension on a Au substrate, as the water evaporates. The attractive lateral capillary forces F result from the overlap of the water menisci around each sphere. F_d is a hydrodynamic force which drags the spheres from the deeper water levels to the shallower levels.

2.2.2 Electrodeposition

Before electrodeposition, the TLCs were taken apart by gently heating them to ~60°C on a hot plate to soften and remove the Parafilm along with the cover slide. The flat Au surface and non-ordered areas of the PS template were covered using clear nail polish for insulation, so that only the area of the template to be electrodeposited was left exposed.

EC deposition was performed using a three-electrode configuration as can be seen in figure 2-3. The electrolyte was a commercial Au or Ag plating solution, the Au one containing ~0.15 % of an additive to give a smooth finish. The working electrode (WE) was the template, the counter electrode (CE) was a Pt mesh and the reference electrode (RE) was a homemade saturated calomel electrode (SCE) for Au deposition, or a homemade saturated mercury sulphate electrode (SMSE) for Ag deposition.

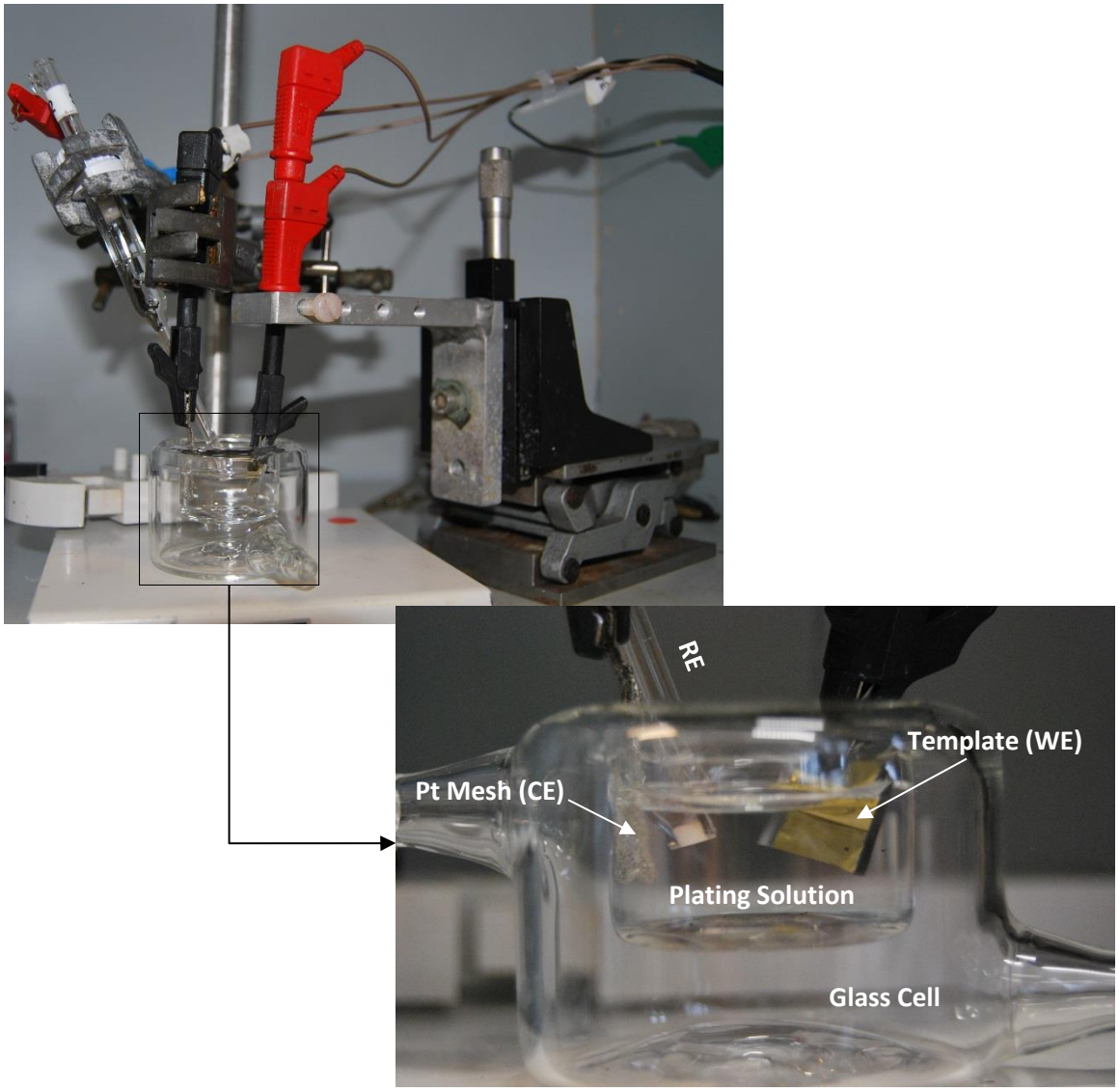

Figure 2-3 Photographs of the three-electrode set up used for Au or Ag electrodeposition through a hexagonal PS nanosphere template to make a SSV substrate.

A homemade SCE is displayed in figure 2-4. Firstly, a few drops of Hg quicksilver were used to cover a Pt wire sealed in a glass tube. Then, Hg quicksilver was ground into Hg_2Cl_2 powder until it was saturated and this Hg_2Cl_2/Hg mixture was placed and tightly pressed onto the Hg quicksilver. These two layers were then secured using glass wool which had been previously soaked in a saturated aqueous KCl solution. The inner and outer glass tubes of the electrodes were finally filled with and stored in saturated KCl in H_2O solution. The SMSE electrode looked similar to the SCE electrode shown in figure 2-4 and was made using the same method. However, Hg_2Cl_2 powder was replaced by Hg_2SO_4 powder and KCl was replaced by K_2SO_4. The potentials of the SCE and SMSE electrodes were measured to be +0.24 V and +0.68 V vs. the standard hydrogen electrode (SHE), respectively, which were within 0.04 V of values found in the literature.[10]

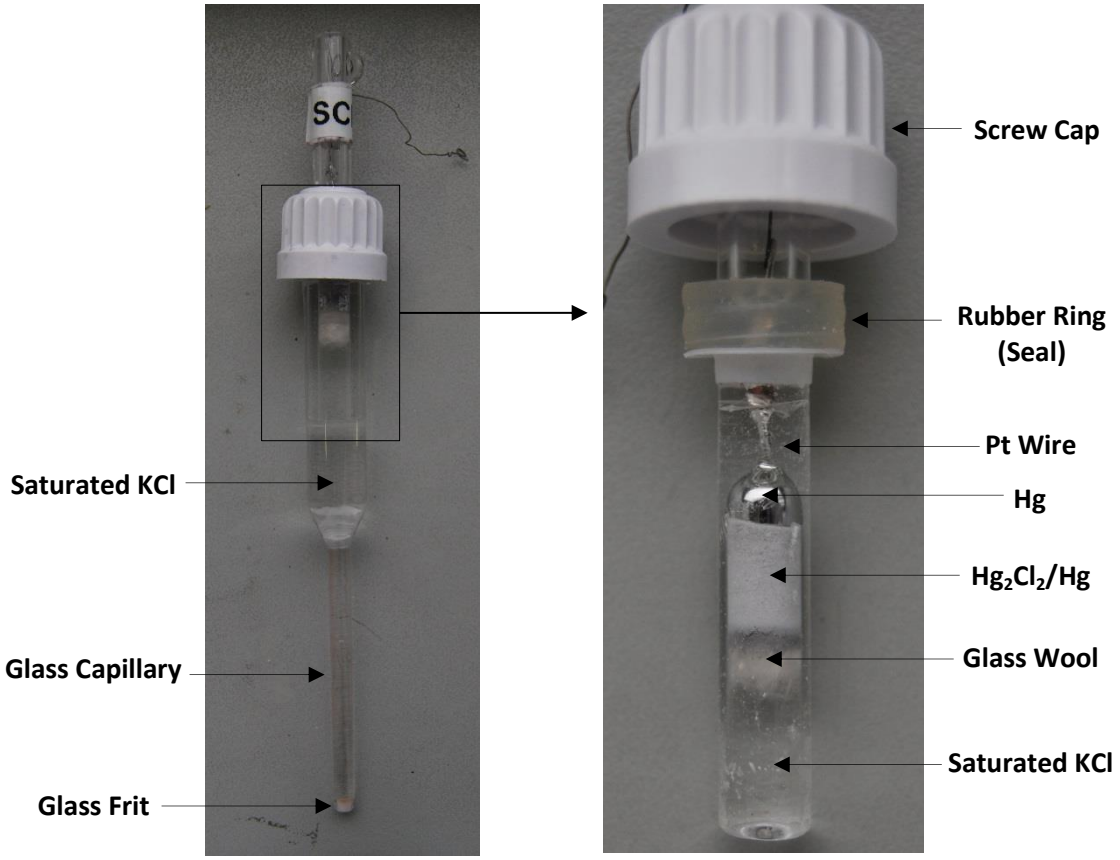

Figure 2-4 Photographs of the homemade SCE.

The depositions were controlled by chronoamperometry, using NOVA 1.10.3 software and a Metrohm Autolab PGSTAT101 potentiostat. The potential passed was -0.72 V vs. SCE for Au electrodeposition and -0.95 V vs. SMSE for Ag electrodeposition.[11] The desired height of electrodeposited Au or Ag film was 468 nm, as the highest intensity of SERS peaks has been found for normalised thicknesses of ~0.78 D, where D = 600 nm was the diameter of the nanosphere template.[12] The height of the deposited layer can be carefully controlled by monitoring the charge applied during the chronoamperometry measurement.

A typical chronoamperometry curve for Au deposition through a hexagonal PS nanosphere template can be seen in figure 2-5. The point at which the metal had deposited half way up the nanospheres was denoted by a 'peak' at which the current reached a minimum, due to the minimum amount of conductive area available to deposit onto. At this point the height was $h_{1/2}$ = 300 nm and the charge $Q_{1/2}$ was noted. The process can be stopped when the metal has deposited to the desired height h_f, by noting the charge $Q_{1/2}$ and calculating the charge Q_f expected when

the film reaches h_f. To calculate this charge, a relationship must be derived between the two charges as a function of the deposited film heights, which has been derived below.

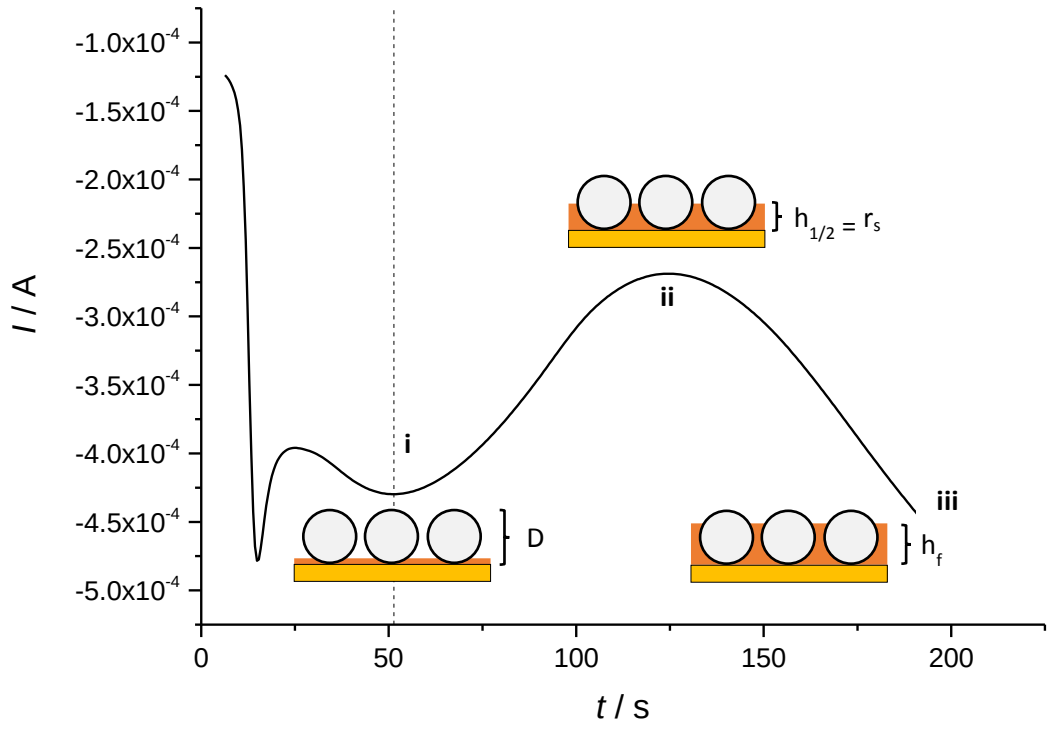

Figure 2-5 Chronoamperometry curve produced during Au electrodeposition through a hexagonal 600 nm diameter PS nanosphere template on a flat Au slide, by applying -0.72 V vs SCE. The electrolyte was a commercial Au plating solution and the CE was a Pt mesh. The dashed line and denotes the point at which the shape of the spheres starts to affect the current. (i) Start of current decrease as the conducting area available to deposit onto decreased; (ii) current minimum as the deposited film height reached r_s = 0.5 *D* (charge reached $Q_{1/2}$); (iii) stop point when deposited film height reached ~0.78 *D* (charge reached Q_f = 1.27 $Q_{1/2}$).

According to Faraday's law:

$$Q = nzF$$

$$Q = \frac{\rho zF}{M}V$$

where Q is the amount of charge needed to deposit n moles of Au or Ag, F is the Faraday constant, z is the number of electrons involved in the electrode reaction, M is the molecular/atomic weight of Au or Ag, ρ is the density of Au or Ag, V is the volume of Au or Ag deposited.[10]

At the point at which the deposited Au or Ag film reaches $h_{1/2}$ = 0.5 D = 300 nm, the above equation becomes:

$$Q_{1/2} = \frac{\rho n F}{M} V_{1/2}$$

Equation 2-1

At the point at which the deposited Au or Ag film reaches h_f = 0.78 D = 468 nm, the same equation becomes:

$$Q_f = \frac{\rho n F}{M} V_f$$

Equation 2-2

By dividing equation 2-2 by equation 2-1:

$$\frac{Q_f}{Q_{1/2}} = \frac{V_f}{V_{1/2}}$$

Equation 2-3

The volume of Au or Ag deposited at film height h is equal to the volume of the total template area to a height h, minus the volume occupied by all the spherical caps of the PS spheres to a height h, as demonstrated in figure 2-6:

$$V = V_t - N_s V_s$$

$$V = A_t \times h - N_s V_s$$

Equation 2-4

where V_t was the total volume of the template area to a height h, A_t was the total area of the template, N_s was the number of spheres and V_s was the volume of each spherical cap.

Assuming that the spheres are all touching each other and that their packing was a perfect hexagonal arrangement, as demonstrated in figure 2-6, the packing density of the spheres is:

$$\eta = \frac{N_s A_s}{A_t} = \frac{\pi\sqrt{3}}{6}$$

$$A_t = \frac{6N_s A_s}{\pi\sqrt{3}}$$

$$A_t = \frac{6N_s {r_s}^2}{\sqrt{3}}$$

Equation 2-5

where A_s is the area of a circle with a radius r_s = 300 nm, equal to that of the PS sphere.[13]

The volume of a spherical cap of a sphere with radius r_s, to a height h, as demonstrated in figure 2-6, is:

$$V_s = \frac{\pi h^2 (3r_s - h)}{3}$$

Equation 2-6[14]

(a) View of template from above

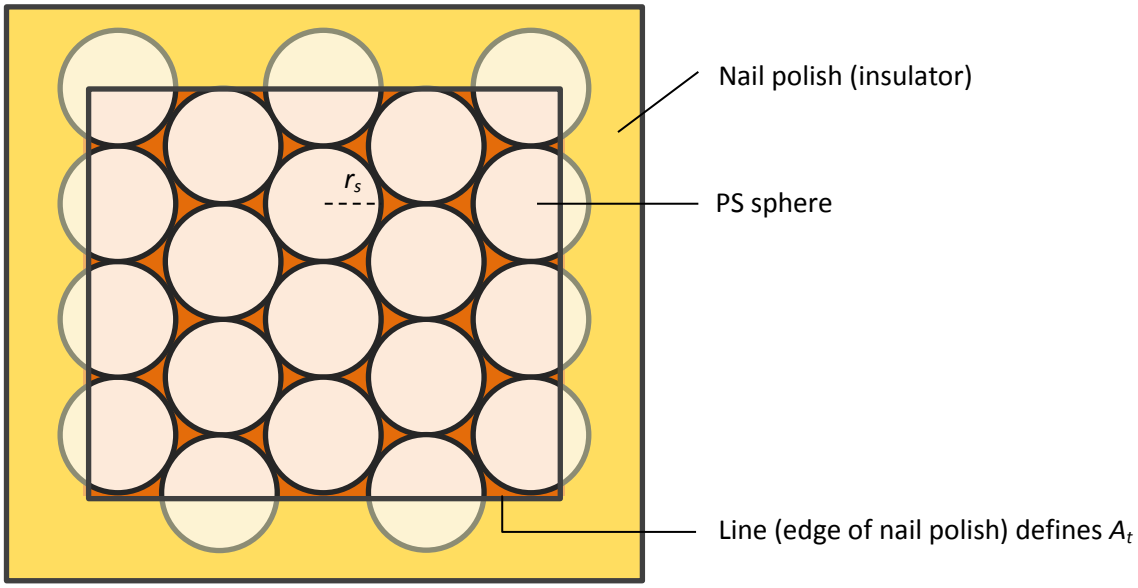

(b) Deposited metal around a PS sphere

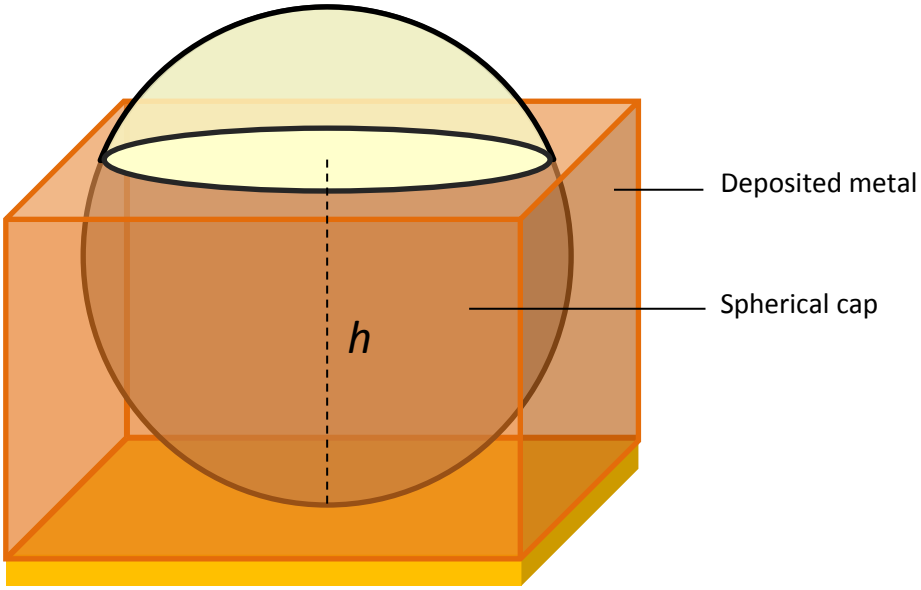

Figure 2-6 (a) Diagram of a SSV substrate with the tightly packed hexagonal PS sphere template, as viewed from above. Nail polish covers the area of the template not to be electrodeposited. The remaining area corresponds to A_t and r_s = 300 nm was the radius of the PS spheres. (b) Diagram of electrodeposited metal surrounding a PS sphere. *h* was the height of deposited metal and the height of the spherical cap.

By substituting equations 2-5 and 2-6 into equation 2-4, the volume of Au or Ag deposited becomes:

$$V = N_s \left[\frac{6h{r_s}^2}{\sqrt{3}} - \frac{\pi h^2 (3r_s - h)}{3} \right]$$

Equation 2-7

For deposited Au or Ag films with heights of $h_{1/2}$ = r_s and h_f, equation 2-7 becomes:

$$V_{1/2} = N_s r_s^3 \left[\frac{6\sqrt{3} - 2\pi}{3} \right]$$

$$V_f = N_s \left[\frac{6\sqrt{3} h_f {r_s}^2 - \pi {h_f}^2 (3r_s - h_f)}{3} \right]$$

Substituting these into equation 2-3 and considering r_s = 300 nm and h_f = 468 nm:

$$\frac{Q_f}{Q_{1/2}} = \frac{6\sqrt{3} h_f {r_s}^2 - \pi {h_f}^2 (3r_s - h_f)}{2r_s^3 (3\sqrt{3} - \pi)}$$

$$\frac{Q_f}{Q_{1/2}} \approx 1.27$$

Therefore, by monitoring the charge, the deposition could be stopped when the charge became equal to 1.27 x $Q_{1/2}$.

The PS spheres were then dissolved by placing the Au substrates in DMF and the Ag substrates in toluene purged with N_2, at room temperature for approximately one hour. The substrates were then dried and cut into smaller pieces for easy handling.

A scanning electron microscope (SEM) image of a Au SSV substrate can be seen in figure 2-7. SEM images were taken in order to study the morphology of the SSV substrate. A Philips XL30 environmental SEM was used, which uses a tungsten filament source to accelerate electrons to energies of 10 kV. The hexagonal array of the voids was evident in the SEM image of the SSV substrate. A few localised defects existed in the film where some over-deposition had occurred,

most likely due to the PS spheres not being arranged perfectly. However, given the area probed during EC-SERS is very large (~5000 μm^2, concluded from the dimensions of the laser line focus specified in section 2.4.2) compared to the dimensions of these defects, they should have very little effect on the overall SERS enhancement and the spectra obtained.

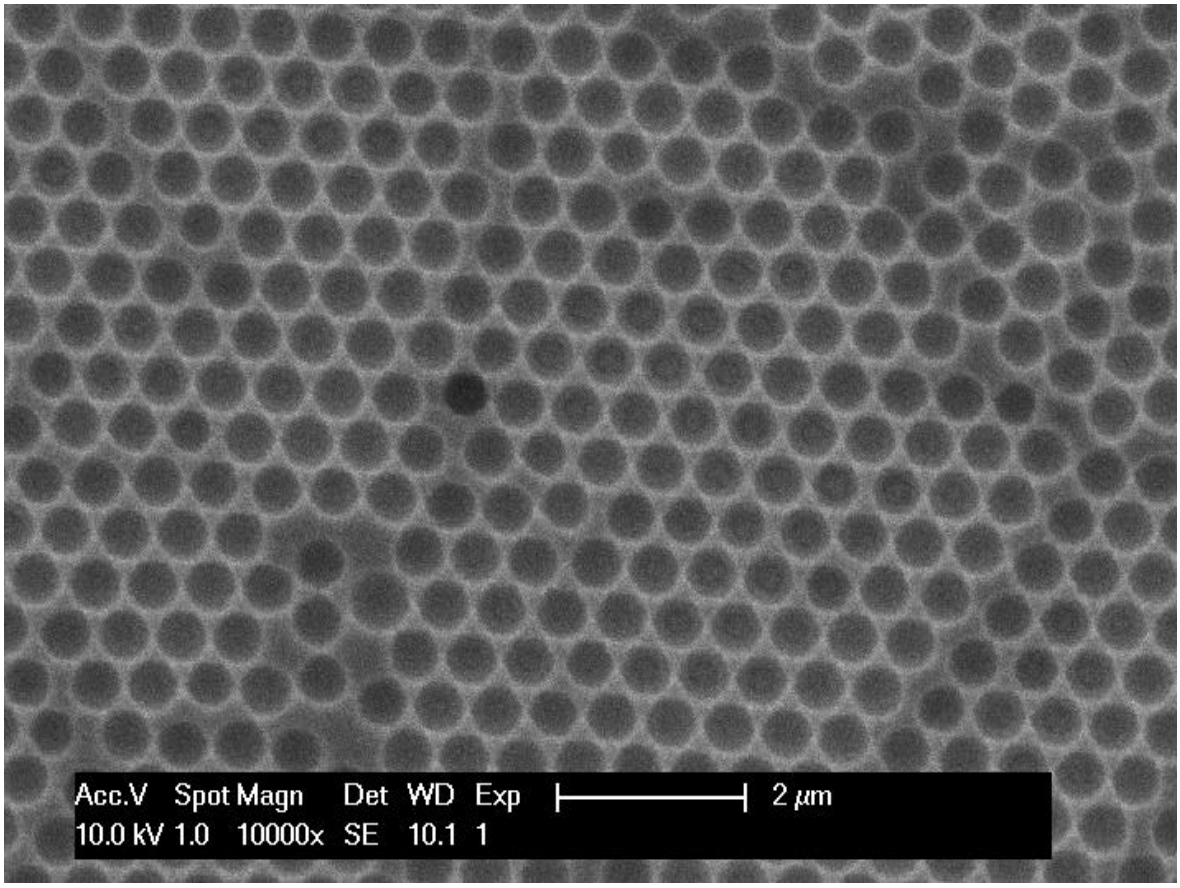

Figure 2-7 SEM image of a Au SSV substrate.

Most substrates were dried under a vacuum and used straight away. If any substrates were not used straight away, they were kept under a N_2 atmosphere to avoid oxidation. Finally, Raman spectra were always obtained of substrates before use, in order to ensure they were clean and no impurities were present.

2.2.3 Self-Assembled Monolayers

According to Sigma-Aldrich, in order to prepare a self-assembled monolayer (SAM) of a thiol on a clean gold substrate, a solution of 1-5 mM of that thiol in solvent is required.[15] In their review on SAMs, Love et al. summarised that immersion of a substrate in a ~1-10 mM ethanolic solution of

thiols for ~12-18 hours was the most common, effective and convenient technique for achieving reproducible SAMs.

The structures of molecules used to create SAMs on Au SSV substrates can be seen in figure 2-8. Ethanol was used as the solvent to make a ~5 mM solution of the thiols used. In order to maintain the driest conditions possible, the ethanol had previously been dried over molecular sieves. The substrate to be used was then soaked in the appropriate solution for at least 12 hours.

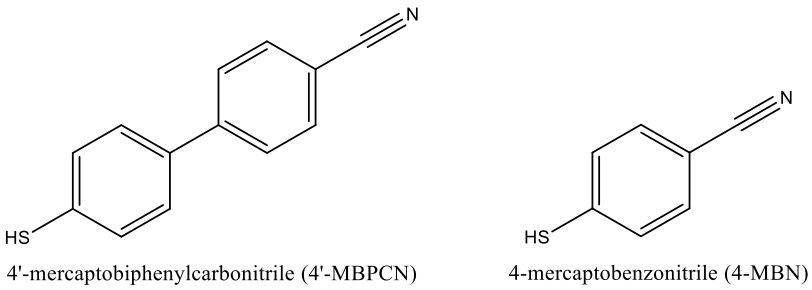

Figure 2-8 Structures and names of the molecules used to create SAMs on Au SSV substrates.

In order to ensure a good SAM coverage had been achieved, Raman spectra were obtained of the substrates in air after they had been dried under N_2. All substrates were dried with N_2 and usually used straight away. If not, then they were stored under N_2.

2.3 Electrolyte Preparation

2.3.1 Ionic Liquids

The structures of the ionic liquids used in this project are displayed in figure 2-9. BMP TFSI and BMI TFSI ionic liquids (ILs) were heat-dried under vacuum to remove water, by stirring and heating to 100°C under vacuum for at least 72 hours. This was achieved by placing the ILs in a sealed RBF connected to an Edwards RV12 vacuum pump and immersed in a silicone oil bath, which was kept at 100°C using an IKA C-MAG HS 7 magnetic stirrer and heating plate and an IKA ETS-D5 electronic contact thermometer. The ILs were then transferred to a N_2-filled Belle Technology glovebox equipped with a Belle O2M-3 O_2 meter (<10 ppm O_2), where they were stored in sample vials.

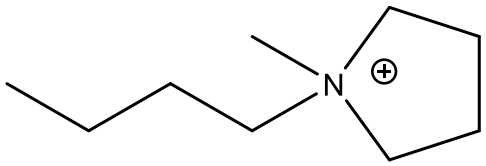

1-Butyl-1-methylpyrrolidinium
(BMP)

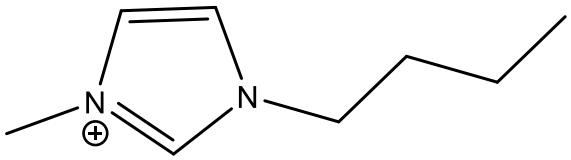

1-Butyl-3-methylimidazolium
(BMI)

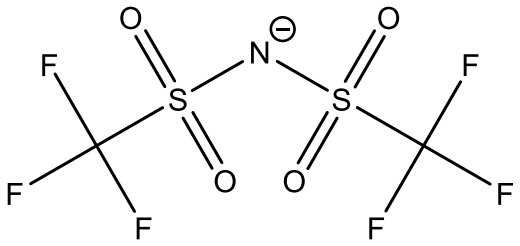

Bis(trifluoromethylsulfonyl)imide
(TFSI)

Figure 2-9 Structures, names and abbreviations of the ILs used.

Karl Fischer (KF) coulometric titration was carried out to determine the water content of the BMP TFSI and BMI TFSI ILs, using a Metrohm 831 KF Coulometer and Hydranal Coulomat-A as the anolyte and Hydranal Coulomat-GC as the catholyte. Each IL was transferred from the sealed sample vial to the KF cell using a syringe and needle. The mass of the IL in the sample vial was weighed before and after transfer to calculate the mass of IL used in each measurement. This mass was typed into the coulometer which outputted the water content in ppm. This was repeated for each IL to ensure reproducibility. Average water content values for each IL are displayed in table 2-2.

Table 2-2 Average water content per IL with associated error.

IL	Average water content and error / ppm
BMI TFSI	75 ± 2
BMP TFSI	109.3 ± 0.4

2.3.2 Potassium Phosphate Solution

In order to make a 10 mM, pH 7 potassium phosphate buffer (PPB) solution the Henderson-Hasselbach equation was used to calculate the amounts of K_2HPO_4 and KH_2PO_4 required:

$$pH = pK_a + log\frac{[K_2HPO_4]}{[KH_2PO_4]}$$

$$\frac{[K_2HPO_4]}{[KH_2PO_4]} = 10^{pH-pK_a} = 10^{7-7.21} \approx 0.62$$

where K_a = 6.2 x 10^{-8} (pK_a = 7.21) is the acid dissociation constant.[16]

$$1.62 \times [K_2HPO_4] = 1 \times [KH_2PO_4]$$

$$\frac{[K_2HPO_4]}{[PPB]} = \frac{1.62}{1 + 1.62} \approx 0.62$$

$$[K_2HPO_4] = 0.62 \times 10\ mM = 6.19\ mM$$

Similarly, for $[KH_2PO_4]$:

$$\frac{[KH_2PO_4]}{[PPB]} = \frac{1}{1 + 1.62} \approx 0.38$$

$$[KH_2PO_4] = 0.38 \times 10\ mM = 3.81\ mM$$

From these concentration values the masses of K_2HPO_4 and KH_2PO_4 required to make 100 ml of PPB were calculated to be 0.11 g and 0.05 g, respectively.

0.109 g of K_2HPO_4 and 0.053 g of KH_2PO_4 were weighed out and placed in a 100 ml volumetric flask which was filled with deionised H_2O. The pH was checked using 4 different types of pH paper and was confirmed to be ~7.

PPB was purged with N_2 for at least 15 minutes before use, to remove dissolved O_2.

2.4 Analytical techniques

The home-made spectroelectrochemical cell used for all measurements is displayed in figure 2-10. It consisted of a quartz window maintaining a thin layer of electrolyte on top of the substrate, with two Pt wires as the counter and the Pt quasi-reference electrode (PQRE) and a Au wire/leaf to make electrical contact with the substrate. After placing the substrate in the cell, assembling and sealing it, it was either filled with PPB or it was transferred into the glove box to be filled with IL. The electrolyte was injected through a luer fitting attached to an Omnifit valve connector using a glass syringe. The valves were then closed in order to seal the cell after it had been filled.

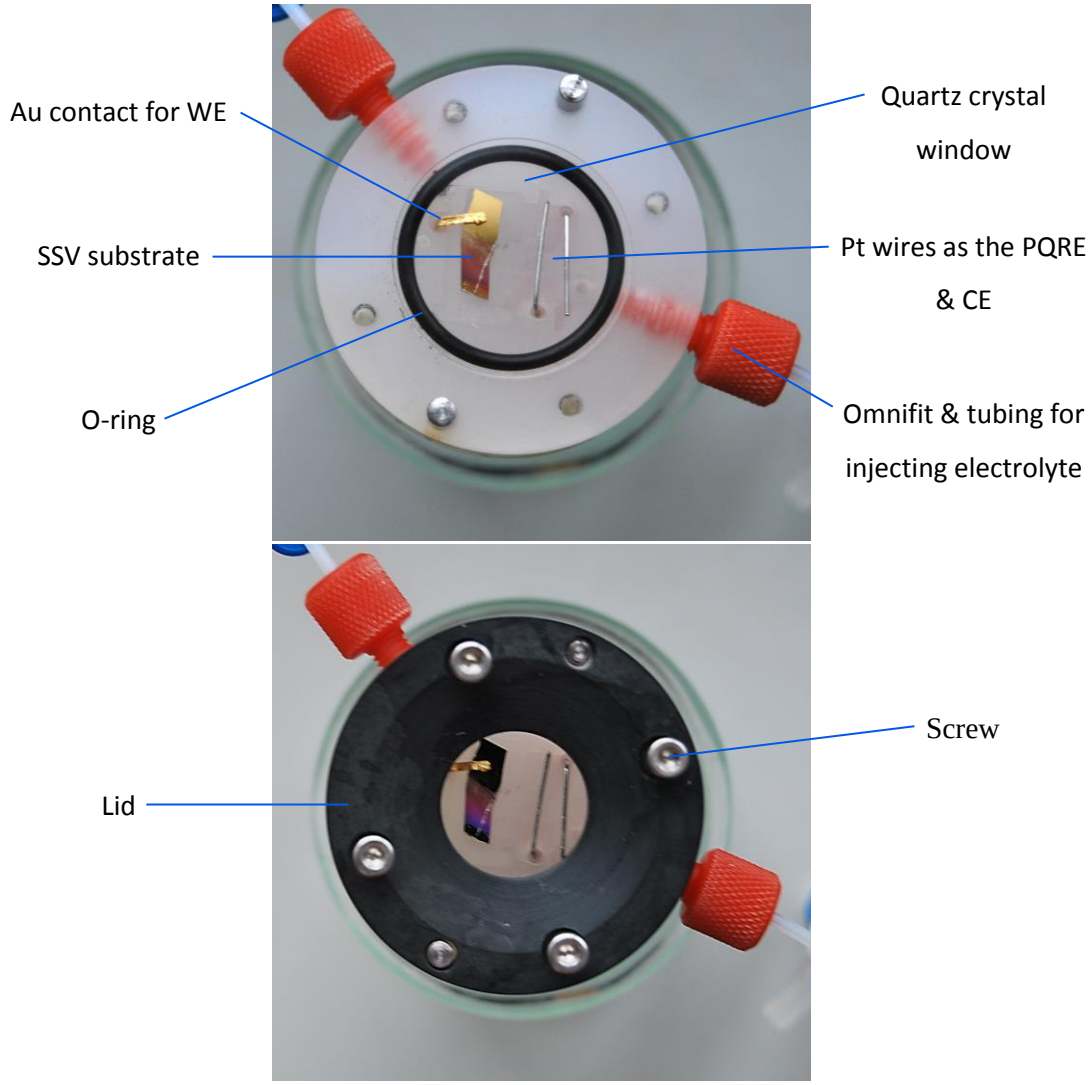

Figure 2-10 Photographs of spectroelectrochemical cell with and without its lid.

The materials used to manufacture the cell were chosen for their chemical and thermal inertness. The main body of the cell was made of Kel-F and the lid was made of glass-filled polyphenylene sulfide. A Viton O-ring was used to make a seal between the cell and the quartz crystal window. The Omnifit fittings were also made of Kel-F and the tubing was made of PTFE.

After use, the cell was emptied by pushing air through it using a syringe. At least 6 x 1 ml H_2O or IPA were then pushed through, when the cell had been used with PPB or IL respectively. The cell was then taken apart and all components were soaked in a beaker of H_2O or IPA for at least 30 minutes. The components were then left to drain and N_2 gas was used to remove any remaining liquid. The components were then placed in the oven at 105°C to dry.

2.4.1 Cyclic Voltammetry

Cyclic voltammetry (CV) was performed using NOVA 1.10.3 or 1.10.1.9 software and a Metrohm Autolab PGSTAT101 or PGSTAT204 potentiostat. The scan rate used was 10 mV s^{-1} and the starting potential was 0 V *vs.* PQRE. The lower and upper potential limits varied depending on the system studied.

2.4.2 Electrochemical Surface Enhanced Raman Spectroscopy

EC-SERS was achieved by changing the potential in steps whilst simultaneously obtaining Raman spectra. The set up used can be seen in figure 2-11. The electrochemistry was controlled using NOVA 1.10.1.9 and a Metrohm Autolab PGSTAT204. Each potential was held for 5 minutes using chronoamperometry before a spectrum was obtained. The same potential was still held during the spectrum acquisition. When the spectrum acquisition was complete the potential was changed and held again for 5 minutes before another spectrum was obtained and so on. Raman spectra were acquired through a Leica DM2500 M microscope and a 50× Olympus LMPlanFL N objective with a 0.5 numerical aperture, on a Renishaw in-Via instrument equipped with a 785 nm, 100 mW near-infrared (NIR) laser. The software used was WiRE 4.1. The dimensions of the line-focus laser on the substrate were ~(20 x 250) µm. The spectral resolution was measured to be 3 cm^{-1} using an atomic emission lamp on the Renishaw Raman calibration source. Before each use the spectrometer was calibrated using a Si wafer, so that the Si peak was at 520.0 ± 0.5 cm^{-1}. The laser power was also measured using a Coherent LaserCheck meter.

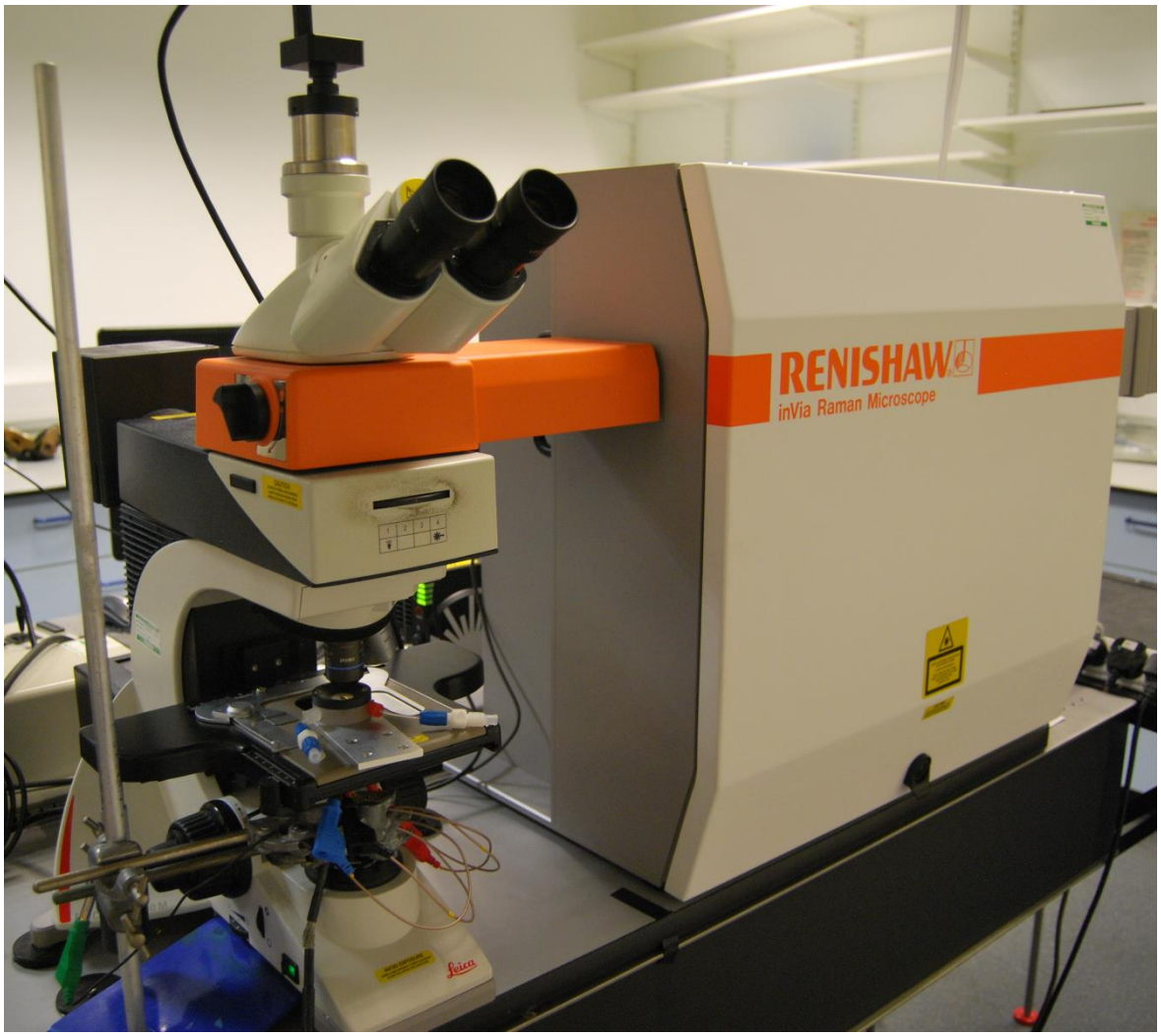

Figure 2-11 Photograph of the EC-SERS set-up, including the Renishaw inVia spectrometer, Leica microscope and the spectroelectrochemical cell connected to the potentiostat via the crocodile clips seen in this photograph under the microscope stage.

Extended scans were used to obtain the whole range of the spectrum, 100-3200 cm^{-1}, whilst static scans were used in order to improve the signal to noise ratio of some of the less intense, but equally important, peaks. The exposure times and number of accumulations for each set of measurements were independently tuned for the different systems studied in order to achieve maximum peak intensities, without saturating the detector. The laser power was chosen in order to achieve maximum peak intensities without damaging the SAMs and/or electrolytes. All spectra presented in this report have been normalised to the laser powers and total exposure times used.

The Curve fit analysis tool on WiRE 4.1 was used to fit peaks and to obtain their position and intensity. An example of this is shown in figure 2-12. Spectra presented in this report have been visualised using Origin 9.1.

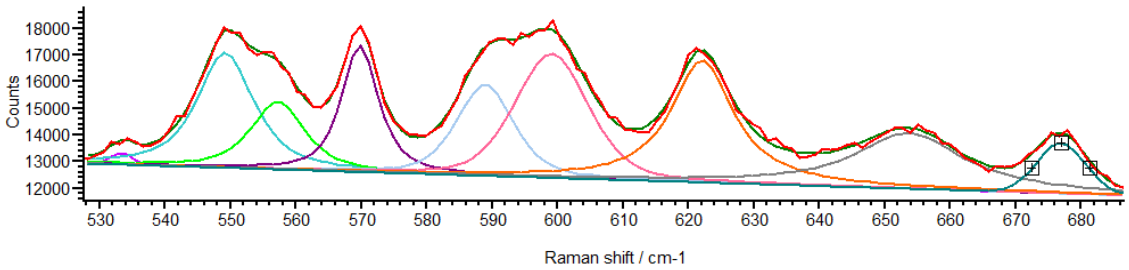

Curve Name	Centre	Width	Height	% Gaussian	Type	Area	ChiSq
Curve 1	533.532	3.97637	478.024	100	Mixed	2023.34	0.713821
Curve 2	549.349	10.3034	4439.76	23.298	Mixed	66459.1	
Curve 3	557.361	9.76488	2634.83	25.4161	Mixed	37103.6	
Curve 4	569.987	6.7514	4873.55	27.8291	Mixed	47048	
Curve 5	589.088	10.4436	3495.06	51.8302	Mixed	47756.8	
Curve 6	599.277	13.2332	4779.58	65.7791	Mixed	78286	
Curve 7	622.307	11.4113	4710.33	0	Mixed	84431.8	
Curve 8	653.955	20.1303	2150.08	0	Mixed	67987	
Curve 9	677.262	8.83127	1938.41	100	Mixed	18222.2	

Figure 2-12 Example of peak fittings using the WiRE 4.1 Curve fit analysis tool on a spectrum of BMI TFSI on a Au SSV substrate (static scan with a centre of 860 cm^{-1} taken at OCP ≈ -397 mV vs. PQRE, 10% laser power, 1 accumulation of 120 s). The red line was the spectrum obtained, the dark green line shows the simulated spectrum resulting from the peak fittings and the coloured lines show the individual fittings for each peak. The straight blue line under all peak fittings represents the baseline taken by the software. The table includes the detailed information for each fitted peak, including their centres and heights.

2.4.2.1 Choice of Gold as the Ideal Material for SSV Substrates

The most commonly used metals for SERS-active substrates are Au and Ag. Ag is a better material for substrates as it offers better SERS enhancement.[1, 2] However, Ag tarnishes easily in ambient air and is less electrochemically stable than Au. In this section Au and Ag SSV substrates have been compared. Spectra have been compared for Au and Ag SSV substrates in air and in BMI TFSI IL and with and without a 4-MBN SAM in figures 2-13 and 2-14, respectively. Spectra were obtained in air in order to establish the cleanliness of the SSV substrates. For a full assignment of the peaks in the Raman spectrum of BMP TFSI, see chapter 3.

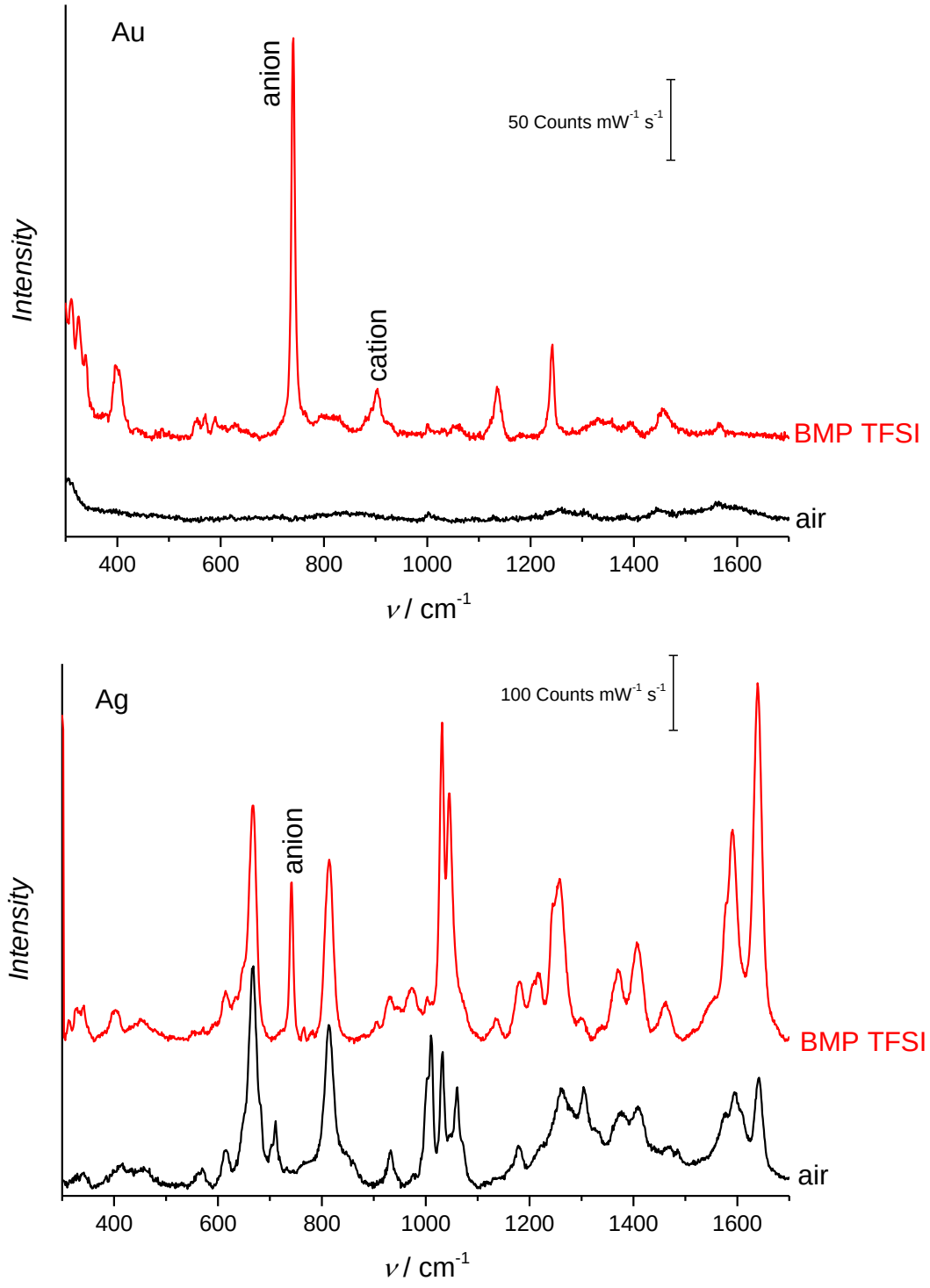

Figure 2-13 Raman spectra of Au and Ag SSV substrates (made with 600 nm diameter spheres and a thickness of 468 nm) in air and in BMP TFSI IL. Characteristic anion and cation peaks of BMP TFSI at 742 and 905 cm^{-1}, respectively, have been labelled. The Au spectra have been offset by 50 Counts mW^{-1} s^{-1} and the Ag spectra have been offset by 200 Counts mW^{-1} s^{-1} for clarity. All spectra have been normalised by the laser power and exposure time used.

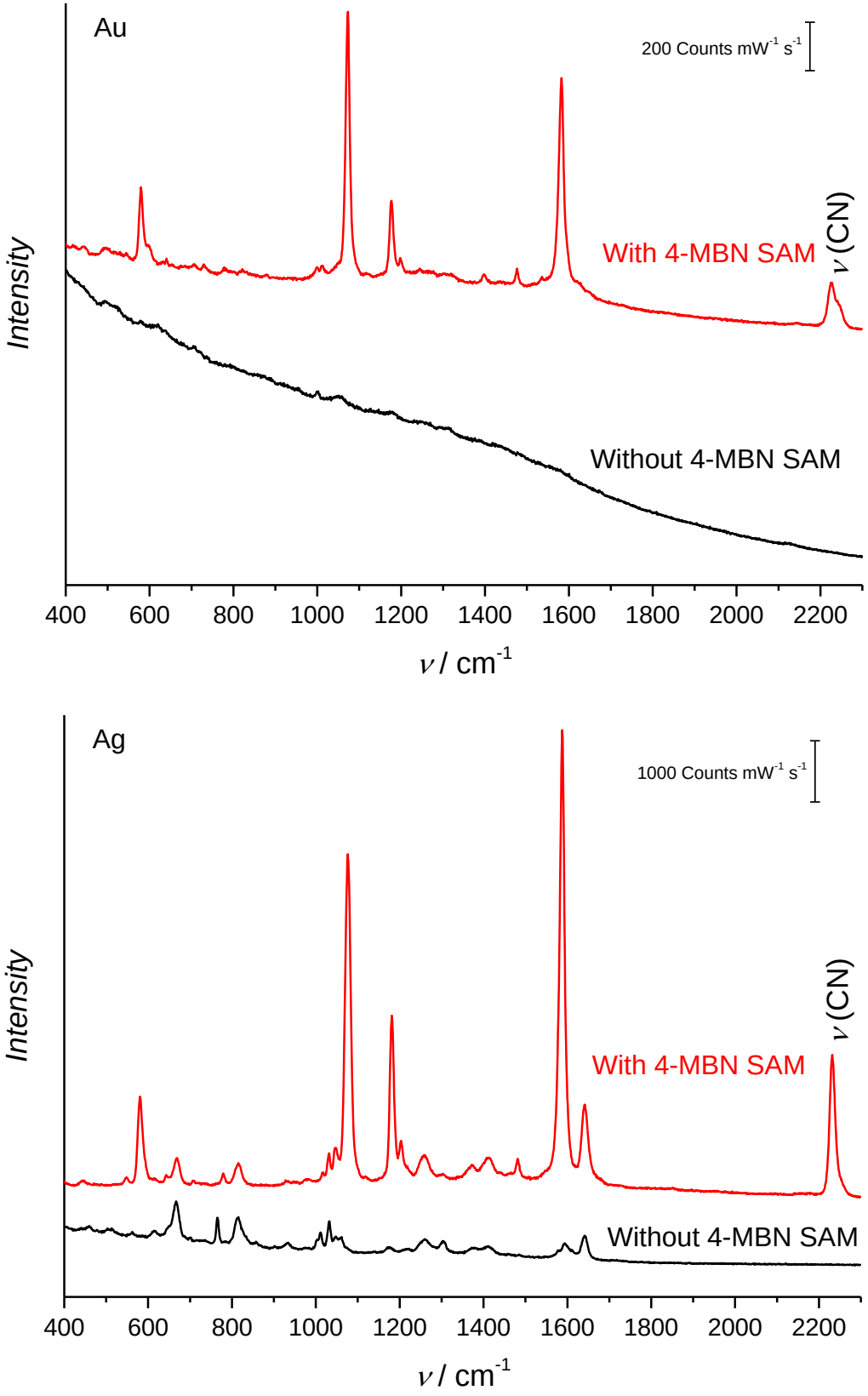

Figure 2-14 Raman spectra of Au and Ag SSV substrates (made with 600 nm diameter spheres and a thickness of 468 nm), with and without a 4-MBN SAM monolayer. The *ν*(CN) peak of 4-MBN at 2230 cm^{-1} has been labelled. The spectra have been offset by 1000 Counts mW^{-1} s^{-1} for clarity. All spectra have been normalised by the laser power and exposure time used.

The method of cleaning the SSV substrates after electrodepositing Ag or Au was to immerse them in toluene or DMF, respectively. However, as can be seen in the spectra above in figures 2-13 and 2-14, the solvent is unable to effectively remove all impurities from the Ag surface. As a result, many peaks which appear on the Ag substrate in air also appear in the spectra of the IL and the 4-MBN SAM. These impurities can alter the metal-IL interface and can also interfere with the analysis of the IL and SAM peaks. On the other hand, significant impurity peaks were not visible on the Au substrate as shown figures 2-13 and 2-14.

In figure 2-13 the impurity peaks on Ag were more intense than the peaks from the BMP TFSI IL. This is likely due to the adsorbed impurities keeping the IL ions from approaching the metal surface. This was not seen for the 4-MBN monolayer on the Ag substrate in figure 2-14, where even though the impurity peaks were still visible, they were less intense than the peaks corresponding to the 4-MBN SAM. As the 4-MBN molecules form a strong Ag-S bond to the substrate, the signal from the SAM was higher than that from impurity molecules.

In figure 2-14, the better enhancement expected from the Ag substrate compared to the Au substrate was evident. The 4-MBN peaks were at least 4 times more intense on Ag then on Au. For example the characteristic *ν*(CN) peak, which will be extensively studied in following chapters for its Stark effect, was approximately 12 times more intense on Ag than on Au. However, this was not the case in figure 2-13, where the anion peak of BMP TFSI was slightly smaller on Ag than it was on Au and the cation peak was not even visible on the Ag SSV substrate. This was due to the presence of the adsorbed impurity peaks as mentioned earlier and re-enforces the justification for using Au SSV substrates instead of Ag for the study of ILs.

EC cycling of metal surfaces has been used as an effective method to remove impurities and adsorbates.[15] However, Ag is very electrochemically active and will corrode at a relatively low potential. For example, a Ag wire dissolved at potentials higher than +0.2 V vs. PQRE in BMP TFSI, as can be seen in figure 2-15. This makes Ag substrates difficult to further clean electrochemically, as there is a high risk of damaging the SSV nanostructure. On the other hand, a Au wire dissolved at potentials higher than +2 V vs. PQRE, providing a much wider EC stability window. The wide EC window of Au also makes Au SSV substrates more beneficial for carrying out EC-SERS experiments, especially for the study of ILs, which generally have wider EC windows than conventional electrolytes.

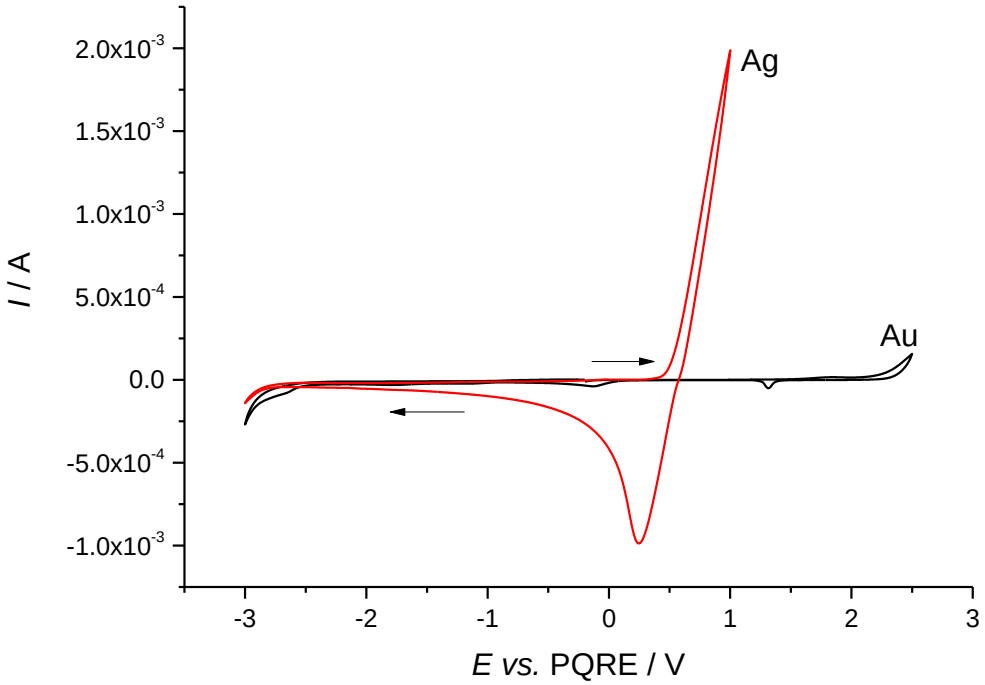

Figure 2-15 CVs of a Ag and a Au wire in BMP TFSI. The counter electrode was a Pt mesh and the reference electrode was a PQRE. The scan rate for both CVs was 50 mV s^{-1} and the start potential was 0 V vs. PQRE.

As a result of the superior cleanliness and EC stability found for Au over Ag SSV substrates and despite the generally higher peak intensities seen for Ag in figure 2-14, all measurements in this project have been carried out using Au SSV substrates.

2.4.3 Potential Dependent Reflectance Spectroscopy

Potential dependent reflectance spectroscopy measurements were obtained of the BMP TFSI ionic liquid on a Au SSV substrate. Measurements were carried out in the clean room of the Department of Physics, University of Southampton. The procedure used was similar to the one described by Bartlett et al. and the set up used is displayed in figure 2-16.[17] An incoherent white light source, emitting wavelengths of 400-900 nm, was used to illuminate the substrate with a spot diameter of ~30 µm, through an Olympus BX51 optical microscope and a 50× Olympus LMPlan IR objective, with a 0.55 numerical aperture. The spectral response was recorded using a fibre-coupled Ocean Optics HR4000 spectrometer with a resolution of 0.75 nm, controlled using OceanView 1.5.2 software.

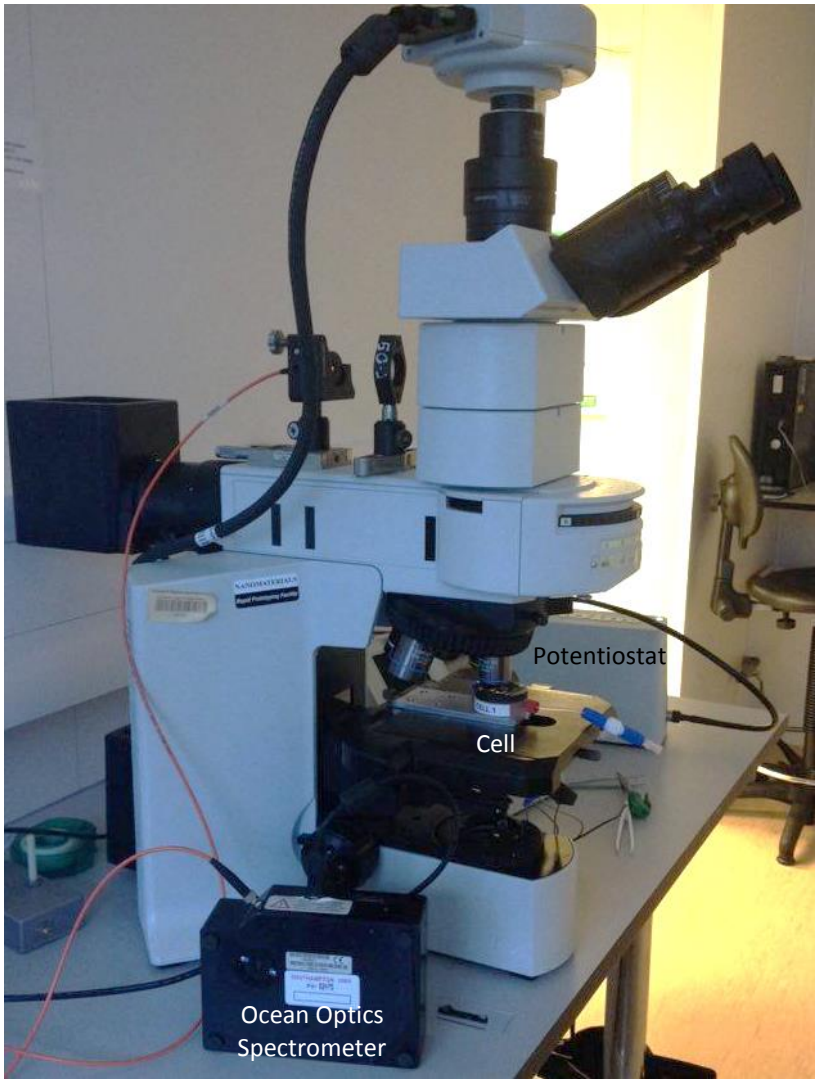

Figure 2-16 Photograph of the set-up used for potential dependent reflectance spectroscopy, including the Olympus microscope, spectroelectrochemical cell, Ocean Optics Spectrometer in the foreground and Autolab potentiostat in the background.

Each measurement was obtained using 100 accumulations of 100 ms. The spectra were normalised against a Thor labs silver mirror reference with constant reflectivity over the wavelength range studied. The electrochemistry was controlled using NOVA 1.11 software and a Metrohm Autolab PGSTAT101 potentiostat. As with EC-SERS, the *E* was held using chronoamperometry for 5 minutes before a spectrum was obtained, whilst still holding the potential. Spectra were obtained every 0.1 V vs. PQRE between 0 V and -1.85 V vs. PQRE, -1.85 V and +0.5 vs. PQRE and +0.5 V and -1.85 V vs. PQRE.

2.4.4 Density Functional Theory Calculations

Density functional theory (DFT) calculations were carried out using the Gaussian 09W software package with the functional B3LYP functional. Following on from the literature, the 6-311G+(d,p) basis set was used in the calculations for all molecules, except for the TFSI ion calculations, for which the larger 6-311G+(3df) basis set was used, as this molecule was negatively charged.[18-20] The geometry of each molecule was firstly optimised before the vibrational frequencies and Raman spectrum were calculated.

2.4.5 Electrochemical Impedance Spectroscopy

Staircase potential electrochemical impedance spectroscopy (SPEIS) was performed on BMP TFSI on a Au SSV substrate using a Biologic SP-150 potentiostat and EC-Lab V11.10 software. The frequency sweep used was 200 kHz to 100 mHz with 10 points per decade and a peak to peak amplitude of 25 mV. Measurements were obtained every 0.05 V vs. PQRE over the same potential ranges used for potential dependent reflectance spectroscopy described above.

2.5 References

1. M. E. Abdelsalam, P. N. Bartlett, J. J. Baumberg, S. Cintra, T. A. Kelf and A. E. Russell, *Electrochem. Commun.*, 2005, **7**, 740-744.

2. J. J. Baumberg, T. A. Kelf, Y. Sugawara, S. Cintra, M. E. Abdelsalam, P. N. Bartlett and A. E. Russell, *Nano Letters*, 2005, **5**, 2262-2267.

3. Barnes, Tian, Aggaral, Goodacre, Donaldson, M. Muniz, Baumberg, Vlckova, Creighton, Natan, Kosower, Alexander, Khan, Russell, Murakoshi, Kneipp, Domke, R. Le, Green, Poponin, Stone, Ren, Pettinger, Milton, Jarvis, Tantra, Kall, Sugawara, Roy, Whitby and Richards, *Faraday Discuss.*, 2006, **132**, 227-247.

4. S. Cintra, M. E. Abdelsalam, P. N. Bartlett, J. J. Baumberg, T. A. Kelf, Y. Sugawara and A. E. Russell, *Faraday Discuss.*, 2006, **132**, 191-199.

5. M. E. Abdelsalam, S. Mahajan, P. N. Bartlett, J. J. Baumberg and A. E. Russell, *J. Am. Chem. Soc.*, 2007, **129**, 7399-7406.

6. S. Mahajan, M. Abdelsalam, Y. Suguwara, S. Cintra, A. Russell, J. Baumberg and P. Bartlett, *Phys. Chem. Chem. Phys.*, 2007, **9**, 104-109.

7. M. Abdelsalam, P. N. Bartlett, A. E. Russell, J. J. Baumberg, E. J. Calvo, N. G. Tognalli and A. Fainstein, *Langmuir*, 2008, **24**, 7018-7023.

8. S. Mahajan, J. Richardson, T. Brown and P. N. Bartlett, *J. Am. Chem. Soc.*, 2008, **130**, 15589-15601.

9. P. A. Kralchevsky and N. D. Denkov, *Curr. Opin. Colloid In.*, 2001, **6**, 383-401.

10. D. Pletcher, *A First Course in Electrode Processes*, Royal Society of Chemistry, Cambridge, 2nd edn., 2009.

11. A. Celiktas, M. A. Ghanem and P. N. Bartlett, *J. Electroanal. Chem.*, 2012, **670**, 42-49.

12. S. Mahajan, R. M. Cole, B. F. Soares, S. H. Pelfrey, A. E. Russell, J. J. Baumberg and P. N. Bartlett, *J. Phys. Chem. C*, 2009, **113**, 9284-9289.

13. E. W. Weisstein, Circle Packing, http://mathworld.wolfram.com/CirclePacking.html, (accessed 4th October, 2017).

14. E. W. Weisstein, Spherical Cap http://mathworld.wolfram.com/SphericalCap.html, (accessed 4th October, 2017).

15. Sigma-Aldrich, Preparing Self-Assembled Monolayers (SAMs) A Step-by-Step Guide for Solution-Based Self-Assembly, https://www.sigmaaldrich.com/content/dam/sigma-aldrich/docs/Aldrich/Instructions/1/al-266.pdf).

16. P. W. Atkins, *Physical chemistry* Oxford University Press, Oxford, 4th edn., 1940-.

17. P. N. Bartlett, J. J. Baumberg, S. Coyle and M. E. Abdelsalam, *Faraday Discuss.*, 2004, **125**, 117-132.

18. T. Fujimori, K. Fujii, R. Kanzaki, K. Chiba, H. Yamamoto, Y. Umebayashi and S.-i. Ishiguro, *J. Mol. Liq.*, 2007, **131–132**, 216-224.

19. K. Fujii, T. Fujimori, T. Takamuku, R. Kanzaki, Y. Umebayashi and S. I. Ishiguro, *J. Phys. Chem. B*, 2006, **110**, 8179-8183.

20. R. Li, H. M. Lv, X. L. Zhang, P. P. Liu, L. Chen, J. B. Cheng and B. Zhao, *Spectrochim. Acta A*, 2015, **148**, 369-374.

Chapter 3: Vibrational Assignment of BMP TFSI

This chapter contains details of the vibrational assignment of the Raman spectrum of 1-butyl-1-methylpyrrolidinium bis(trifluoromethylsulfonyl)imide (BMP TFSI), with the help of density functional theory (DFT) calculations. The carbon atoms in the BMP cation have been numbered as shown in figure 3-1. All vibrational assignments in this report have been presented using the following symbols for clarity: *t*, torsion; *ρ*, rocking; *τ*, twisting; *ω* wagging; *δ*, bending; *ν*, stretching; s, symmetric; a, antisymmetric; ip, in plane; oop, out of plane; FR, Fermi Resonance.

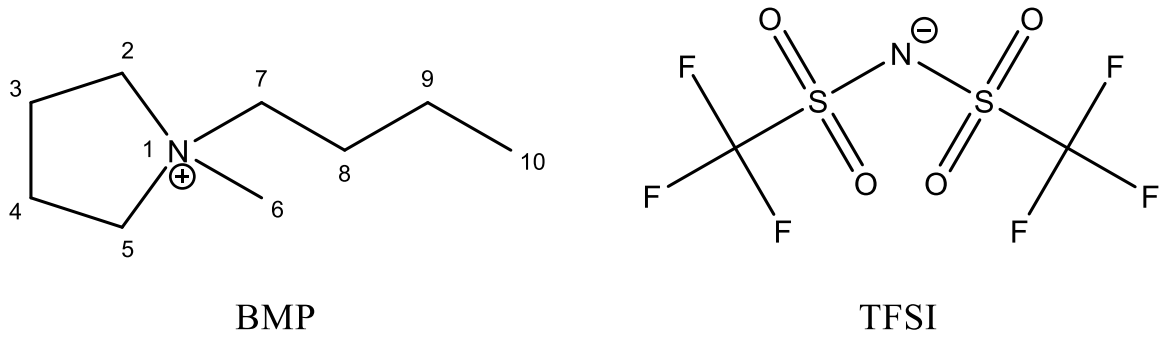

Figure 3-1 Structures and abbreviated names of the BMP TFSI ions.

3.1 Raman Spectrum of BMP TFSI

The Raman spectrum of the BMP TFSI IL can be seen in figure 3-2. This spectrum represents the signal from the bulk BMP TFSI and is not surface-specific, as it was obtained from the ionic liquid (IL) inside a Quartz crystal cuvette. There are a large number of peaks visible in the Raman spectrum, some overlapping, which made their vibrational assignment less straightforward. For the full list of peaks, refer to table 3-3 in section 3.3, which also contains their vibrational assignments.

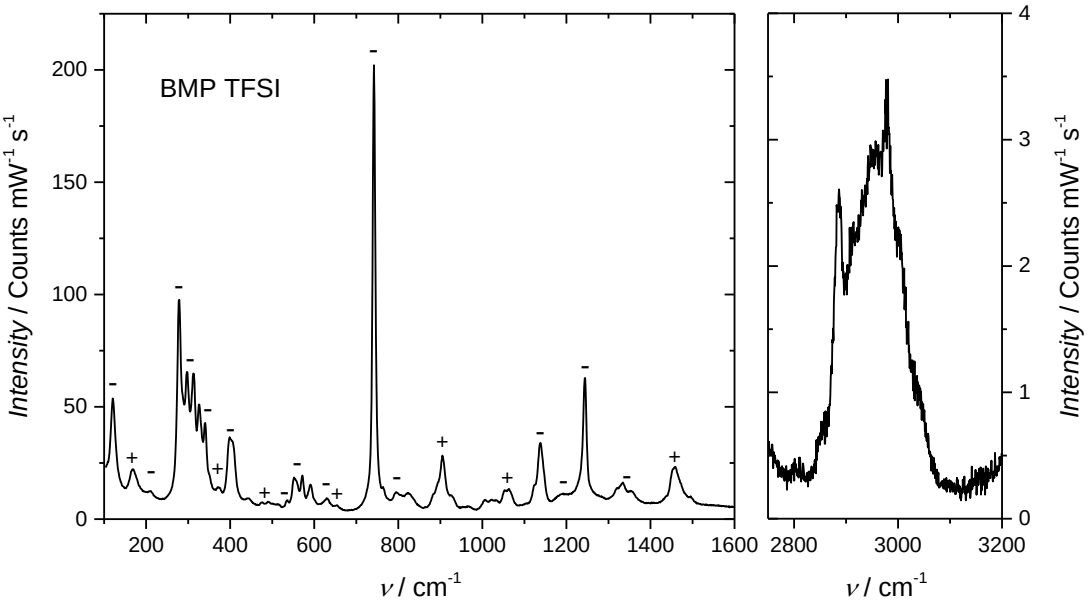

Figure 3-2 Raman spectrum of BMP TFSI in a Quartz crystal cuvette. The spectrum was obtained using a 785 nm near-infrared (NIR) laser and has been normalised by the laser power and exposure time used. A 50 x objective was used. (-) and (+) signs indicate peaks corresponding to the anion and cation, respectively.

Most intense peaks present in Raman spectra were associated with the TFSI anion, because of large polarizability fluctuation resulting from its vibrations.[1] The observed Raman spectrum was weak in the high frequency region 2800-3200 cm^{-1}, making peak identification difficult, which was further complicated by the likely presence of Fermi resonance.[2] As a result, this region will not be used in the electrochemical surface enhanced Raman spectroscopy (EC-SERS) study of BMP TFSI in this report.

The spectrum was in close accordance to Raman spectra previously reported in the literature.[1-4] However, despite the number of publications which contain BMP TFSI Raman spectra, most of them do not contain extensive peak assignments. Publications with full assignment of BMP peaks were especially difficult to find. Furthermore, there are discrepancies between some of the assignments in different publications. For example, Mao et al. assigned the vibration at 1239 cm^{-1} to the $\nu_a(SO_2)$ vibration of the TFSI anion, while Paschoal et al. assigned the peak at 1243 cm^{-1} to the $\nu_s(CF_3)$ vibration of the TFSI anion.[1, 5] As a result, the full assignment of the BMP TFSI spectrum purely based on the literature, was not possible. DFT calculated spectra will be used in the following section, to provide full details for the origin of each peak, both from a molecular and vibrational point of view.

3.2 Density Functional Theory Calculations

As was mentioned earlier, there are limited detailed Raman peak assignments for BMP TFSI in the literature, especially for the BMP ion. For this reason, DFT calculations have been carried out on different conformations of the BMP and TFSI ions. Other than assisting in Raman peak assignments, DFT calculations also assist in the visualisation of the molecular vibrations and of the dipole derivative unit vectors. They also allow the visualisation of small differences in calculated Raman spectra due to different ion conformations, which can then be associated to similar differences in the experimental spectra.

3.2.1 1-Butyl-1-Methylpyrrolidinium Cation

There are more than 50 possible conformations that the BMP cation can theoretically adopt, resulting from the combination of three different ring conformations and many more butyl chain conformations.[6] However, taking all these conformations into account would be computationally costly. Furthermore, there have been many studies on the conformational equilibrium of pyrrolidinium-based ILs in both the crystal and liquid phase, examining which conformations are energetically favourable.[3, 5, 7, 8] The consensus is that the equatorial (eq-) envelope conformer of BMP is the most favourable and is in equilibrium with the axial (ax-) envelope conformer in the BMP TFSI IL.[2] It has also been established that the butyl group of the BMP cation is likely to be restricted to the trans-TT conformation, in which all carbon atoms of the butyl chain are located trans to each other and also against the butyl ring. These two most common conformers have been displayed in figure 3-3.

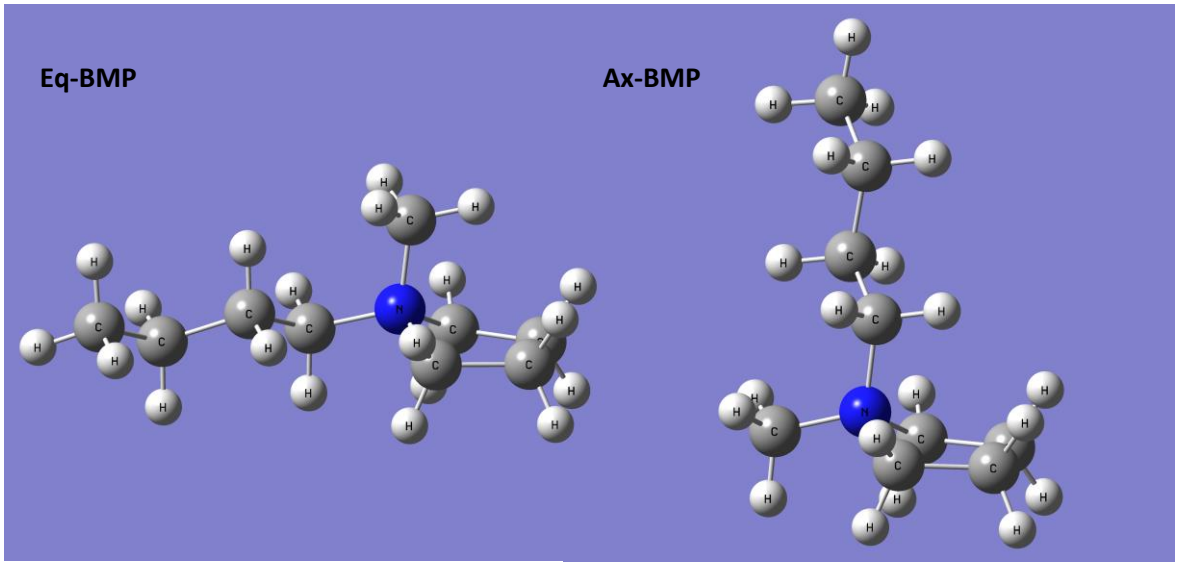

Figure 3-3 DFT-optimised geometries of the eq- BMP and ax-BMP conformers, on the basis of the B3LYP/6-311+G(d,p) levels of theory.

The DFT-calculated Raman spectra of eq-BMP and ax-BMP are compared to the experimentally obtained Raman spectrum of BMP TFSI in figure 3-4. The calculated spectra closely match those found using the same method, by Fujimori et al. and subtle differences can be seen between the calculated spectra of the two conformers.[3] All peaks which appear in these calculated spectra have been tabulated in table A-1, which can be found in appendix A. Table A-1 also contains a full vibrational assignment of the peaks, which will be used in section 3.3 to fully assign the BMP TFSI spectrum.

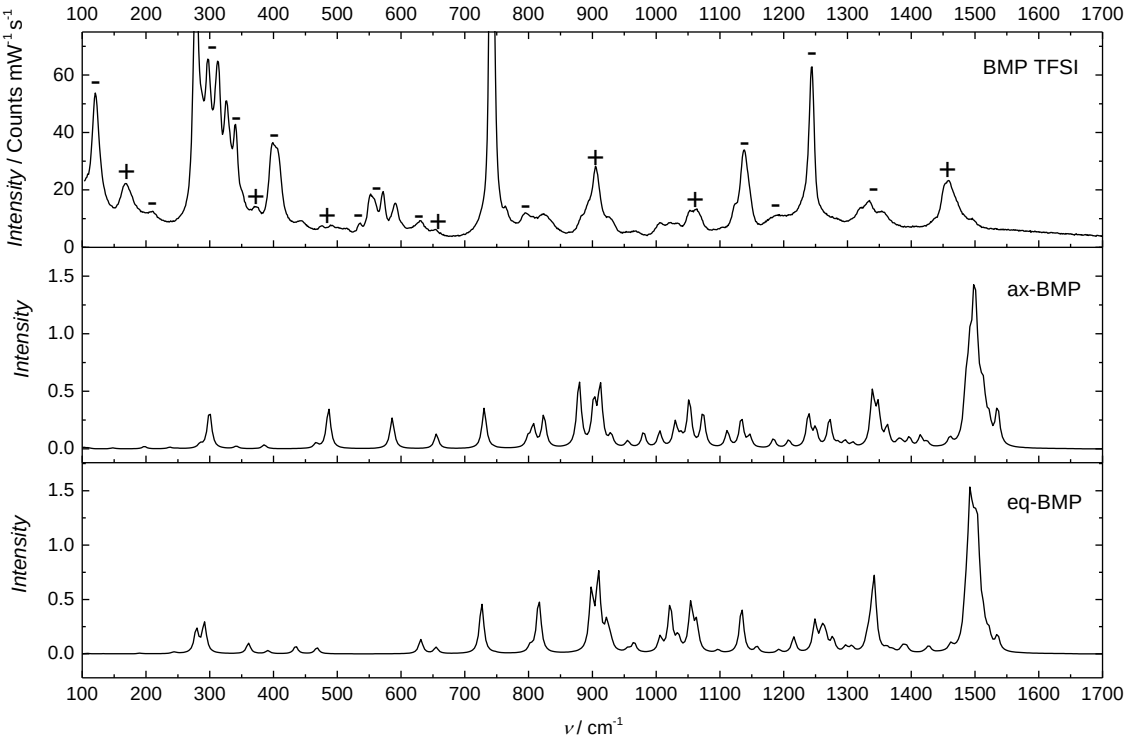

Figure 3-4 Experimentally obtained Raman spectrum of BMP TFSI and DFT-calculated Raman spectra of the optimised ax-BMP and eq-BMP conformers. The Raman spectrum was obtained using a 785 nm NIR laser and a 50x objective and has been normalised by the laser power and exposure time used. DFT calculations were carried out on the basis of the B3LYP/6-311+G(d,p) levels of theory.

The most intense and distinct BMP peak in the BMP TFSI Raman spectrum was the somewhat broad peak at 905 cm^{-1}. The reason it was broad is due to it consisting of four separate peaks. This peak has been compared to those present in the calculated spectra in figure 3-5 and assigned in table 3-1. It was evident that the BMP TFSI spectrum mostly resembled the spectrum of the eq-BMP conformer. This was in accordance to the consensus in the literature that eq-BMP was the most favourable conformer, as mentioned earlier. However, there was an additional shoulder at 884 cm^{-1} in the BMP TFSI spectrum, which was not matched by the calculated spectrum of eq-BMP. This most likely originated from the ax-BMP conformer, further confirming that in the bulk BMP TFSI IL there was equilibrium between the two conformers.

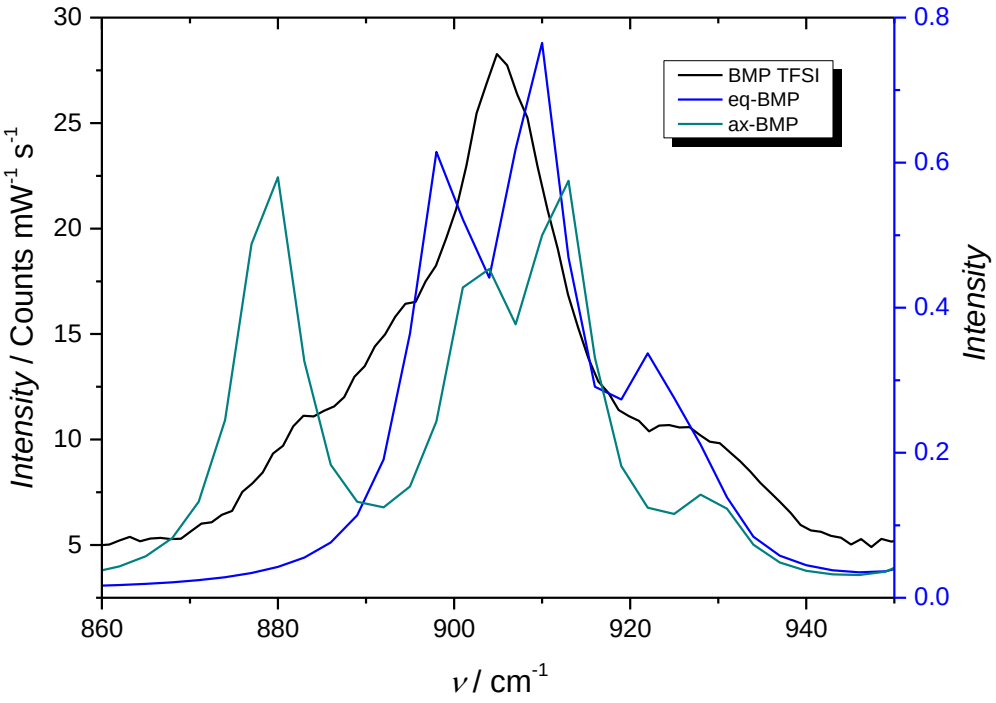

Figure 3-5 905 cm^{-1} peak comparison between the experimentally obtained Raman spectrum of BMP TFSI and the DFT-calculated Raman spectra of the optimised ax-BMP and eq-BMP conformers. Peak assignments for the DFT-calculated spectra have been presented in table 3-1. The Raman spectrum was obtained using a 785 nm NIR laser and a 50x objective and has been normalised by the laser power and exposure time used. DFT calculations were carried out on the basis of the B3LYP/6-311+G(d,p) levels of theory.

Table 3-1 Vibrational assignment of peaks in the DFT-calculated Raman spectra of optimised eq-BMP and ax-BMP structures, in the frequency range 860-950 cm^{-1} and the corresponding peaks in the BMP TFSI Raman spectrum, as displayed in figure 3-5. DFT calculations were carried out on the basis of the B3LYP/6-311+G(d,p) levels of theory. For a full table of assignments for the calculated spectra, refer to table A-1 in appendix A.

DFT peak centre / cm^{-1}	**Raman peak centre / cm^{-1}**	**Conformer**	**Assignment**
879	883	Ax-BMP	$\nu(NC_{(7)})$ + ip ring breathing
899	893	Eq-BMP	$\nu_{ip}(NC_{(7)})$ + ip ring breathing
902	905	Ax-BMP	
909		Eq-BMP	$\delta(C_{(9)}C_{(10)}H_3)$
912		Ax-BMP	
923	928	Eq-BMP	$\omega(C_{(6)}H_3)$
929		Ax-BMP	Whole molecule vibration

These types of conformational differences in Raman peaks have previously been used in the literature to establish conformational changes in ILs with changing temperature and IL phase changes.[1-4, 7, 9] Wen et al. discussed the possibility of a conformational change occurring from eq-BMP to ax-BMP, when the potential was scanned from -1.4 V to -1.6 V vs. Pt quasi-reference electrode (PQRE), in order to increase the packing density of BMP cations on the Au electrode surface.[10] It is hoped that if such a clear and precise conformational change would occur, this would be able to be detected in the conformation-dependent peaks of the EC-SERS spectra of BMP TFSI.

Lastly, due to the excellent visualisation of molecular vibrations that the DFT calculations in the Gaussian software provide, it is possible to accurately assign Raman peaks to different planes in a molecule. SERS selection rules state that when a vibration is normal to the surface it will be enhanced, while a vibration parallel to the surface will not be enhanced.[11] By monitoring the relative intensities of ip and oop vibrations of a molecule with potential, changes in orientation may be detected.[12] However, this may not be straightforward if there is a range of vibrations at a single frequency, or if there is not a clearly defined plane, as is the case of the BMP cation. As can be seen in figure 3-3, the pyrrolidinium ring is not 'flat' like in the case of an imidazolium ring. These issues will be discussed in further detail later on, in chapter 5.

3.2.2 Bis(Trifluoromethylsulfonyl)Imide Anion

According to the literature, there is a conformational equilibrium between the transoid (trans-) TFSI and cisoid (cis-) TFSI conformers.[1, 2, 4, 5, 13-17] The structures of both of these conformers are shown in figure 3-6.The trans-TFSI form has the CF_3 groups on opposite sides of the S-N-S plane and the cis- form has the CF_3 groups on the same side of the S-N-S plane.

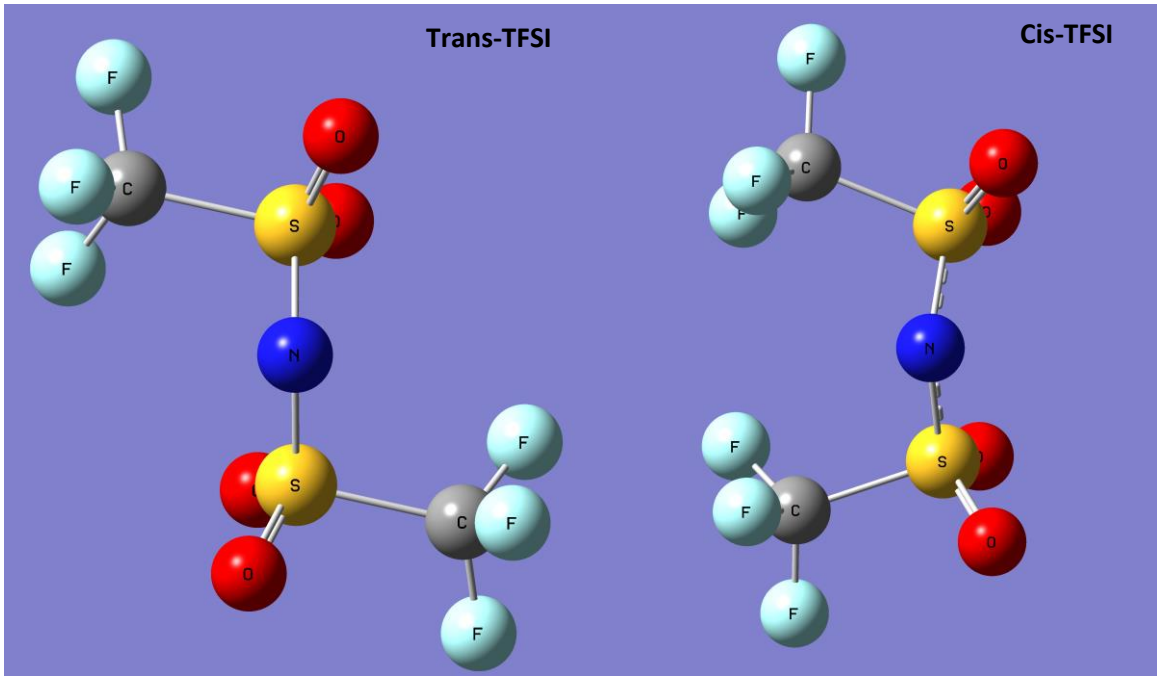

Figure 3-6 DFT-optimised geometries of the trans-TFSI and cis-TFSI conformers, on the basis of the B3LYP/6-311+G(3df) levels of theory.

The DFT-calculated Raman spectra of trans-TFSI and cis-TFSI are compared to the experimentally obtained Raman spectrum of BMP TFSI in figure 3-7. All peaks in these calculated spectra have been tabulated in table A-2, which can be found in appendix A. Table A-2 also contains a full vibrational assignment of the peaks, which will be used in section 3.3 to fully assign the experimental BMP TFSI Raman spectrum. A sub-section of table A-2 is shown here in table 3-2, containing key peaks which will briefly be discussed in this section and comparing them to peaks in the Raman spectra.

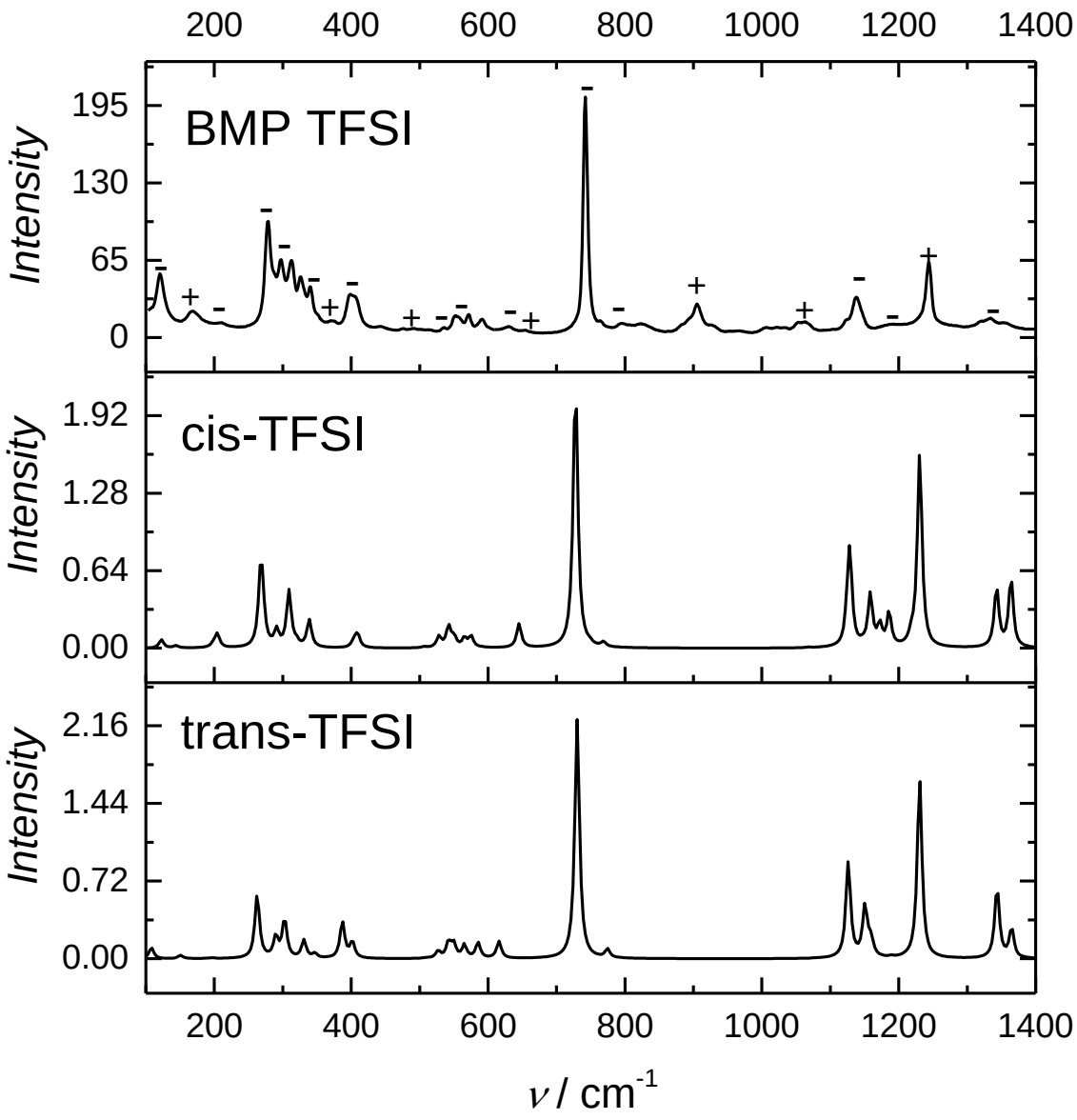

Figure 3-7 Experimentally obtained Raman spectrum of BMP TFSI and DFT-calculated Raman spectra of the optimised cis-TFSI and trans-TFSI conformers. The Raman spectrum was obtained using a 785 nm NIR laser and a 50x objective and has been normalised by the laser power and exposure time used. DFT calculations were carried out on the basis of the B3LYP/6-311+G(3df) levels of theory.

Table 3-2 Vibrational assignment of peaks in the DFT-calculated Raman spectra of optimised cis-TFSI and trans-TFSI structures, discussed in this section, presented in figure 3-7. DFT calculations were carried out on the basis of the B3LYP/6-311+G(d,p) levels of theory. For a full table of assignments for the calculated spectra, refer to table A-2 in appendix A.

DFT peak centre / cm^{-1}	**Raman peak centre / cm^{-1}**	**Conformer**	**Assignment**
387	397	Trans-TFSI	δ(NSO)
396	407	Cis-TFSI	δ(NSO) + $\rho(SO_2)$ + $\omega(SO_2)$ + $\omega(CF_3)$
402	415	Trans-TFSI	$\rho_{ip}(SO_2)$
730	742	Trans-TFSI & Cis-TFSI	Whole anion breathing

The calculated cis-TFSI and trans-TFSI spectra in figure 3-7 closely match those found using the same method in the literature and subtle differences can be seen between the spectra of the two conformers.[14] Furthermore, there are many peaks in the calculated spectra of the TFSI conformers which match similar peaks in the BMP TFSI Raman spectrum. However, as will be discussed later on in this section, the calculated TFSI peaks appear red-shifted by approximately 11 cm^{-1} compared to the experimental BMP TFSI Raman peaks. Some shift in the peaks of DFT-calculated spectra compared to experimental spectra was to be expected. This was especially due to the fact that DFT calculations were performed on isolated TFSI conformers, whereas the experimental Raman spectrum was obtained of the BMP TFSI ion pair. Ion pairing has been found to affect DFT results in the past, due to changes in charge distributions.[5, 18]

The most common peaks used in the literature to distinguish between TFSI conformers are those found at 397 and 407 cm^{-1} in the BMP TFSI spectrum, which have been reported by Fujii et al. to correspond to the trans-TFSI and cis-TFSI conformers, respectively.[14] The BMP TFSI spectrum in this frequency region has been compared to the DFT-calculated spectra of trans-TFSI and cis-TFSI in figure 3-8. The calculated peaks appear at 387 and 396 cm^{-1} for trans-TFSI and cis-TFSI, respectively, which are in good agreement with the spectra calculated by Fujii et al.. However, it is important to note that in this report these peaks have mainly been assigned to δ(NSO), which differs from the assignment to $\omega(SO_2)$ made by Fujii et al.. Even so, the presence of both peaks in the BMP TFSI spectrum confirms the presence of both conformers in the IL in equilibrium.

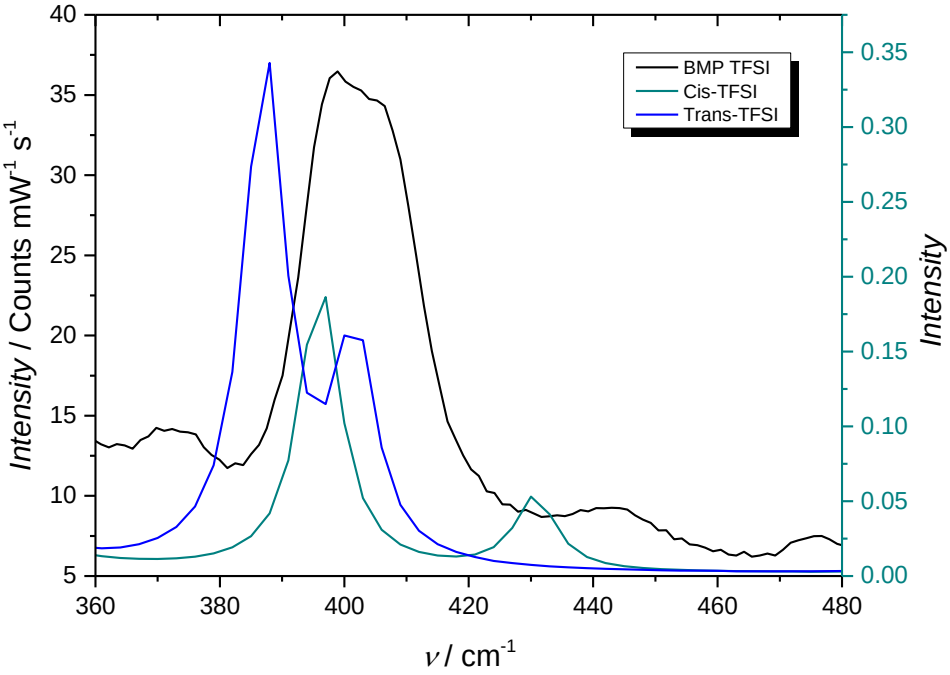

Figure 3-8 360-420 cm^{-1} peaks comparison between the experimentally obtained Raman spectrum of BMP TFSI and the DFT-calculated Raman spectra of the optimised cis-TFSI and trans-TFSI conformers. The Raman spectrum was obtained using a 785 nm NIR laser and a 50x objective and has been normalised by the laser power and exposure time used. DFT calculations were carried out on the basis of the B3LYP/6-311+G(3df) levels of theory.

Differences in the TFSI anion conformation have been found to result from temperature changes, phase transition and pairing with different cations.[1, 13-17, 19] Unlike with BMP cations, no evidence of the TFSI conformation being potential-dependent has been found in the literature. As a result, the TFSI conformation has not been studied in this report. However, it is important to calculate the spectra for both conformations as they exist in equilibrium in the liquid state of BMP TFSI and so they help accurately assign the Raman spectra.

The most intense peak of the BMP TFSI Raman spectrum is the 742 cm^{-1} peak which corresponds to the breathing of the whole TFSI anion. In the DFT-calculated TFSI spectra, this peak appeared at 730 cm^{-1} for both conformers. As a result, the 742 cm^{-1} peak did not originate from a specific TFSI orientation or conformation. This, along with its high intensity, made it ideal to compare to cation peaks, in order to study the relative potential-dependent relationship between cations and anions at the electrode surface. This relationship will be studied later on, in chapter 5.

It is also important to note the lack of peaks in the frequency region 800 - 1100 cm^{-1}, in both the trans-TFSI and cis-TFSI calculated spectra. As a result, it is safe to assume that peaks which appear in this region of the Raman spectra of BMP TFSI correspond to the BMP cation, with no interference from peaks from other molecules.

3.3 Vibrational Assignment of BMP TFSI Raman Spectrum

Based on the DFT-calculated spectra demonstrated in section 3.2 and by visualising the molecular vibrations of the BMP and TFSI ions using the Gaussian software package, the peaks of the BMP TFSI Raman spectrum of figure 3-2 have been assigned to the BMP and TFSI ions and their vibrational modes. Any remaining unassigned peaks have then been assigned with the help of the literature.[1, 3, 5, 15, 20, 21] These assignments are tabulated in table 3-3.

Table 3-3 Centres of peaks visible in BMP TFSI Raman spectra, along with assignments, mainly based on DFT calculated Raman peaks of BMP and TFSI conformers and the review by Paschoal et al..[1] Any additional literature references used have been labelled within the table.

Peak Centre / cm^{-1}		**Ion Conformer**	**Vibration(s)**
Raman	**DFT**		
104	102	Ax-BMP	$\rho(C_{(3)}H_2)$ + $\rho(C_{(4)}H_2)$ + oop ring deformation
	108	Eq-BMP	$\omega(C_{(10)}H_3)$ + $\rho(CH_2)_{ring}$
121	108	Trans-TFSI	δ(NSC)
169	151	Trans-TFSI	δ_{ip}(SNS)
	153	Cis-TFSI	δ_{ip}(SNS) + $\rho_{ip}(SO_2)$
189	190	Eq-BMP	$\rho(CH_2)_{ring}$ + $\rho(C_{(7)}H_2)$ + $\rho(C_{(6)}H_3)$ + $\rho(C_{(10)}H_3)$
210	197	Cis-TFSI	$\tau_{oop}(SO_2)$ + $\tau_{oop}(CF_3)$
278	267	Cis-TFSI	δ_{oop}(FCS) + δ(OSC)
287	285	Ax-BMP	$t(C_{(6)}H_3)$ + $\rho(C_{(5)}H_2)$ + $\rho(C_{(2)}H_2)$ + oop ring deformation + $\rho(C_{(10)}H_3)$
	291	Eq-BMP	$t(C_{(6)}H_3)$ + $\delta(C_{(7)}C_{(8)}C_{(9)})$
297		TFSI[15]	$\rho(CF_3)$[15]
300	300	Ax-BMP	$\rho(C_{(5)}H_2)$ + $\rho(C_{(2)}H_2)$ + $\rho(C_{(6)}H_3)$ + $\delta(C_{(7)}C_{(8)}C_{(9)})$
	290	Trans-TFSI	$\tau_{ip}(SO_2)$
313	301	Cis-TFSI	δ_{oop}(FCSO)
	303	Trans-TFSI	ν_{oop}(CS) + δ(NSO)
325	313	Cis-TFSI	δ_{oop}(FCSO)
331	321		

Peak Centre / cm^{-1}		Ion Conformer	Vibration(s)
Raman	**DFT**		
340	331	Trans-TFSI	$\delta_{oop}(FCS) + \tau_{oop}(SO_2)$
350	341	Cis-TFSI	$\omega_{oop}(NSO) + \tau_{oop}(SO_2) + \tau_{oop}(CF_3)$
371	361	Eq-BMP	$\delta(C_{(6)}NC_{(7)})$
397	387	Trans-TFSI	$\delta(NSO)$
407	396	Cis-TFSI	$\delta(NSO) + \rho(SO_2) + \omega(SO_2) + \omega(CF_3)$
415	402	Trans-TFSI	$\rho_{ip}(SO_2)$
422			
444	431	Cis-TFSI	$\delta_{oop}(NSO) + \rho(SO_2) + \omega(CF_3)$
476	468	Eq-BMP	$\delta(C_{(8)}C_{(9)}C_{(10)}) + \delta(C_{(2)}NC_{(6)})$
490	486	Ax-BMP	$\delta(NC_{(2)}C_{(5)}C_{(6)})$
503	486	Ax-BMP	$\delta(NC_{(2)}C_{(5)}C_{(6)})$
514	506	Cis-TFSI	$\delta_{ip}(SO_2) + \delta_{ip}(CF_3)$
535	524	Cis-TFSI	$\delta(CF_3) + \delta(NSO)$
	527	Trans-TFSI	$\delta(CF_3)$
551	541	Cis-TFSI	
	542	Trans-TFSI	$\delta_{ip}(CF_3)$
558	551	Trans-TFSI	$\delta(CF_3)$
		Cis-TFSI	
571	565	Trans-TFSI	$\delta(CF_3) + \delta(SO_2)$
591	586	Ax-BMP	Ip ring deformation
604		BMP[3]	
630	616	Trans-TFSI	$\delta_{ip}(SNS) + \omega_{oop}(SNS)$
654	655	Eq-BMP	Ip ring deformation
		Ax-BMP	
735	730	Ax-BMP	$\rho(C_{(3)}H_2) + \rho(C_{(4)}H_2)$
742	730	Trans-TFSI	Whole anion breathing
		Cis-TFSI	
747	747	Eq-BMP	$\rho(C_{(8)}H_2) + \rho(C_{(9)}H_2)$
765	750	Cis-TFSI	$\delta(CF_3)$
795	775	Trans-TFSI	$\nu_{ip,s}(SNS)$
807	807	Ax-BMP	$\rho(C_{(3)}H_2) + \rho(C_{(2)}H_2) + \rho(C_{(7)}H_2) + \rho(C_{(9)}H_2)$
825	824	Ax-BMP	$\rho(C_{(4)}H_2) + \rho(C_{(3)}H_2) + \rho(C_{(5)}H_2)$
883	879	Ax-BMP	$\nu(NC_{(7)})$ + ip ring breathing
893	899	Eq-BMP	$\nu_{ip}(NC_{(7)})$ + ip ring breathing
905	902	Ax-BMP	
	909	Eq-BMP	$\delta(C_{(9)}C_{(10)}H_3)$

Peak Centre / cm^{-1}		Ion Conformer	Vibration(s)
Raman	**DFT**		
	912	Ax-BMP	
928	923	Eq-BMP	$\omega(C_{(6)}H_3)$
	929	Ax-BMP	Whole molecule vibration
1007	1006	Eq-BMP	Ip ring deformation + $\rho(C_{(6)}H_3)$
		Ax-BMP	
1021	1022	Eq-BMP	$\nu_a(C_{(7)}NC_{(6)})$
1032	1030	Ax-BMP	$\nu_a(C_{(7)}C_{(8)}C_{(9)}C_{(10)})$
	1034	Eq-BMP	
	1039	Ax-BMP	$\nu(C_{(3)}C_{(4)})$
1051	1052	Ax-BMP	$\nu_a(C_{(7)}C_{(8)}C_{(9)}C_{(10)})$
	1054	Eq-BMP	
1063	1063	Eq-BMP	Ip ring deformation
1113	1112	Ax-BMP	oop ring deformation+ $\omega(C_{(10)}H_3)$+ $\rho(CH_2)_{ring}$
1122		BMP[3] & TFSI[5]	$\nu_s(CF_3)$[5]
1139	1126	Trans-TFSI	ν_a(FCS)
	1127	Cis-TFSI	
1192	1185	Cis-TFSI	ν_a(FCS) + $\nu_{ip,a}$(SNS) + $\nu_s(SO_2)$
1244	1230	Trans-TFSI	$\nu_{oop,a}$(CSO) + $\nu_s(SO_2)$
	1231	Cis-TFSI	
1272	1272	Ax-BMP	$\tau(C_{(3)}H_2)$ + $\tau(C_{(4)}H_2)$
	1277	Eq-BMP	$\tau(C_{(2)}H_2)$ + $\tau(C_{(4)}H_2)$
1320		BMP[3] & TFSI[20]	
1334		TFSI[3, 20]	$\nu_{a,oop}(SO_2)$[20]
1354	1343	Cis-TFSI	$\nu_a(SO_2)$
	1344	Trans-TFSI	
1393	1387	Eq-BMP	$\omega(C_{(9)}H_2)$ + $\omega(C_{(8)}H_2)$
	1393	Eq-BMP	$\omega(C_{(2)}H_2)$
	1397	Ax-BMP	$\omega(C_{(5)}H_2)$ + $\omega(C_{(2)}H_2)$
1434	1427	Eq-BMP	$\omega(C_{(7)}H_2)$ + $\delta(C_{(10)}H_3)$
1454	1461	Ax-BMP	$\delta(C_{(6)}H_3)$
1465	1462	Eq-BMP	
1496	1490	Ax-BMP	$\delta(C_{(10)}H_3)$ + $\delta(C_{(6)}H_3)$ + $\delta(C_{(7)}H_2)$ + $\delta(C_{(8)}H_2)$
	1493	Eq-BMP	$\delta(C_{(9)}H_2)$ + $\delta(C_{(8)}H_2)$ + $\delta(C_{(10)}H_3)$ + $\delta(CH_2)_{ring}$ + $\delta(C_{(6)}H_3)$
	1500	Ax-BMP	$\delta(C_{(10)}H_3)$ + $\delta(C_{(6)}H_3)$ + $\delta(C_{(5)}H_2)$
	1503	Eq-BMP	$\delta(C_{(10)}H_3)$

3.4 Summary

What is immediately evident from table 3-3, is that the assignment of IL Raman spectra can be very complex. There are 70 peaks of varying intensities to assign, many of which overlap. Furthermore, the peaks originate from a combination of vibrational modes, which couple to each other differently in various ion conformers and cation-anion pairings compared to the isolated ions, creating peak shifts. This chapter has highlighted the importance of utilising DFT calculations in the successful assignment of IL spectra and the visualisation of their vibrational modes in 3-D.

Future work would also benefit from the use of ILs with simpler structures, for example ILs with a smaller anion or cation, such as BF_4. This would allow the study of just the cation peaks, unimpeded by the presence of a large number of intense anion peaks.

3.5 References

1. V. H. Paschoal, L. F. O. Faria and C. C. Ribeiro, *Chem. Rev.*, 2017, **117**, 7053-7112.

2. R. W. Berg, *Monatsh. Chem.*, 2007, **138**, 1045-1075.

3. T. Fujimori, K. Fujii, R. Kanzaki, K. Chiba, H. Yamamoto, Y. Umebayashi and S.-i. Ishiguro, *J. Mol. Liq.*, 2007, **131–132**, 216-224.

4. Y. Umebayashi, T. Mitsugi, K. Fujii, S. Seki, K. Chiba, H. Yamamoto, J. N. C. Lopes, A. A. H. Padua, M. Takeuchi, R. Kanzaki and S. Ishiguro, *J. Phys. Chem. B*, 2009, **113**, 4338-4346.

5. J. X. Mao, H. B. Nulwala, D. R. Luebke and K. Damodaran, *J. Mol. Liq.*, 2012, **175**, 141-147.

6. T. Endo, S. Hoshino, Y. Shimizu, K. Fujii and K. Nishikawa, *J. Phys. Chem. B*, 2016, **120**, 10336-10349.

7. K. Fujii, S. Seki, S. Fukuda, T. Takamuku, S. Kohara, Y. Kameda, Y. Umebayashi and S. Ishiguro, *J. Mol. Liq.*, 2008, **143**, 64-69.

8. Y. Umebayashi, T. Fujimori, T. Sukizaki, M. Asada, K. Fujii, R. Kanzaki and S. Ishiguro, *J. Phys. Chem. A*, 2005, **109**, 8976-8982.

9. R. Holomb, A. Martinelli, I. Albinsson, J. C. Lassegues, P. Johansson and P. Jacobsson, *J. Raman Spectrosc.*, 2008, **39**, 793-805.

10. R. Wen, B. Rahn and O. M. Magnussen, *Angew. Chem. Int. Edit.*, 2015, **54**, 6062-6066.

11. E. C. Le Ru, S. A. Meyer, C. Artur, P. G. Etchegoin, J. Grand, P. Lang and F. Maurel, *Chem. Commun.*, 2011, **47**, 3903-3905.

12. V. O. Santos, M. B. Alves, M. S. Carvalho, P. A. Z. Suarez and J. C. Rubim, *J. Phys. Chem. B*, 2006, **110**, 20379-20385.

13. M. Herstedt, M. Smirnov, P. Johansson, M. Chami, J. Grondin, L. Servant and J. C. Lassegues, *J. Raman Spec.*, 2005, **36**, 762-770.

14. K. Fujii, T. Fujimori, T. Takamuku, R. Kanzaki, Y. Umebayashi and S. I. Ishiguro, *J. Phys. Chem. B*, 2006, **110**, 8179-8183.

15. A. Martinelli, A. Matic, P. Johansson, P. Jacobsson, L. Borjesson, A. Fernicola, S. Panero, B. Scrosati and H. Ohno, *J. Raman Spectrosc.*, 2011, **42**, 522-528.

16. F. M. Vitucci, F. Trequattrini, O. Palumbo, J. B. Brubach, P. Roy and A. Paolone, *Vib. Spectrosc.*, 2014, **74**, 81-87.

17. F. M. Vitucci, F. Trequattrini, O. Palumbo, J. B. Brubach, P. Roy, M. A. Navarra, S. Panero and A. Paolone, *J. Phys. Chem. A*, 2014, **118**, 8758-8764.

18. I. Rey, P. Johansson, J. Lindgren, J. C. Lassegues, J. Grondin and L. Servant, *J. Phys. Chem. A*, 1998, **102**, 3249-3258.

19. J. C. Lassegues, J. Grondin, R. Holomb and P. Johansson, *J. Raman Spectrosc.*, 2007, **38**, 551-558.

20. M. Castriota, T. Caruso, R. G. Agostino, E. Cazzanelli, W. A. Henderson and S. Passerini, *J. Phys. Chem. A*, 2005, **109**, 92-96.

21. O. Palumbo, F. Trequattrini, G. B. Appetecchi and A. Paolone, *Challenges*, 2017, **8**.

Chapter 4: The SSV SERS Response in Ionic Liquids

The substrate plays a vital role in electrochemical – surface enhanced Raman spectroscopy (EC-SERS) experiments with regards to both the electrochemistry and spectroscopy. To ensure the best quality and understanding of results for the forthcoming chapters, it is important to take into consideration the effect the substrate can have on Raman spectra.

Most publications using SERS, have focused on studying self-assembled monolayers (SAMs) or molecules adsorbed on the substrate in air or in weak Raman scattering media, such as weakly concentrated aqueous electrolytes.[1-5] The work in this thesis will deviate from previous publications, by studying the interface between Au and 1-butyl-1-methylpyrrolidinium bis(trifluoromethylsulfonyl)imide (BMP TFSI) and SAMs adsorbed on Au in the presence of ionic liquids (ILs). Unlike previously studied electrolytes, ILs are highly concentrated. The BMP TFSI and 1-butyl-3-methylimidazolium (BMI) TFSI ILs used here have effective concentrations of 3.3 M and 3.4 M, respectively. ILs are also very good Raman scatterers, which makes it very easy to obtain good quality Raman spectra. However, this can provide issues with high Raman signals from the bulk IL contributing to the spectra, making it difficult to identify if a spectrum is surface-specific or heavily influenced by the bulk. Publications on the study of ILs using SERS have thus far been very qualitative and have not touched on the effect of the bulk IL Raman signal on SERS spectra.[6-10]

This chapter attempts to examine the bulk effect of ILs by comparing the SERS spectra of a SAM, BMP TFSI, BMI TFSI and of varying concentrations of pyridine (Py), taken on Au sphere segment void (SSV) substrates and on flat Au. The EC responses of the spectra of BMP TFSI have also been compared and the importance of the spatial resolution of the spectrometer has been highlighted.

Lastly, the effects of applied EC potential on SERS enhancement and intensity have been discussed in previous publications.[11, 12] Potential dependent reflectance spectroscopy has been used in this chapter to examine such effects in the IL system.

4.1 Raman on Flat Gold and SERS on Sphere Segment Void Gold

4.1.1 Self-Assembled Monolayers

Raman spectra of a 4-mercaptobenzonitrile (4-MBN) SAM on the flat and nanostructured regions of a Au SSV substrate are presented in figure 4-1. While numerous very intense peaks appear for the SAM on the SSV region of the substrate, no peaks are visible on the flat region, due to the lack of Raman enhancement at the flat Au surface. This type of graph has been used in the literature

to successfully demonstrate the enhanced Raman signal which can be obtained by using SERS-active substrates.[3, 13-15]. However, graphs demonstrating the same effect for non-adsorbed molecules or for liquids with inherently high Raman signals, such as ILs, haven't been used in the same way. This is despite the numerous publications on the study of ILs using SERS.[6-10, 16, 17]

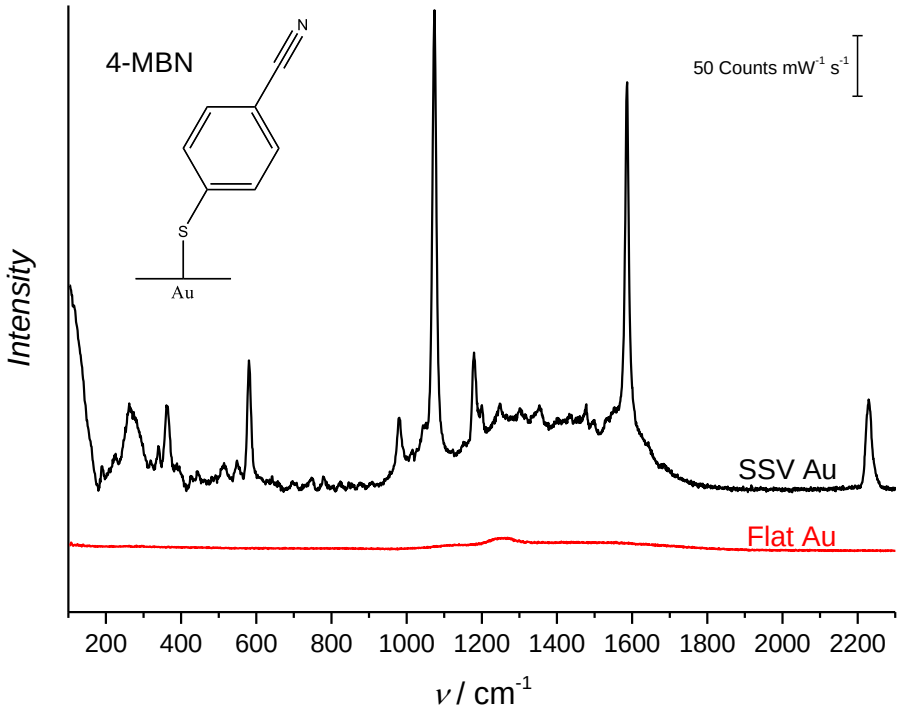

Figure 4-1 Raman spectra of a 4-MBN (structure displayed) SAM on the flat and nanostructured regions of a Au SSV substrate (made with 600 nm diameter spheres and a thickness of 468 nm). The spectra have been normalised by the laser power and exposure time used and have been offset for clarity by 50 Counts mW^{-1} s^{-1}.

4.1.2 Ionic Liquids

In figure 4-2, Raman spectra have been compared of two different ILs on the flat and nanostructured regions of a Au SSV substrate. Unlike with the SAM, the peaks of the IL on the SSV region of the substrate are lower in intensity than those obtained on the flat region of the substrate. This is somewhat counter-intuitive, as one would expect an enhanced signal of the liquids near the SSV substrate, as with the 4-MBN spectra in figure 4-1.

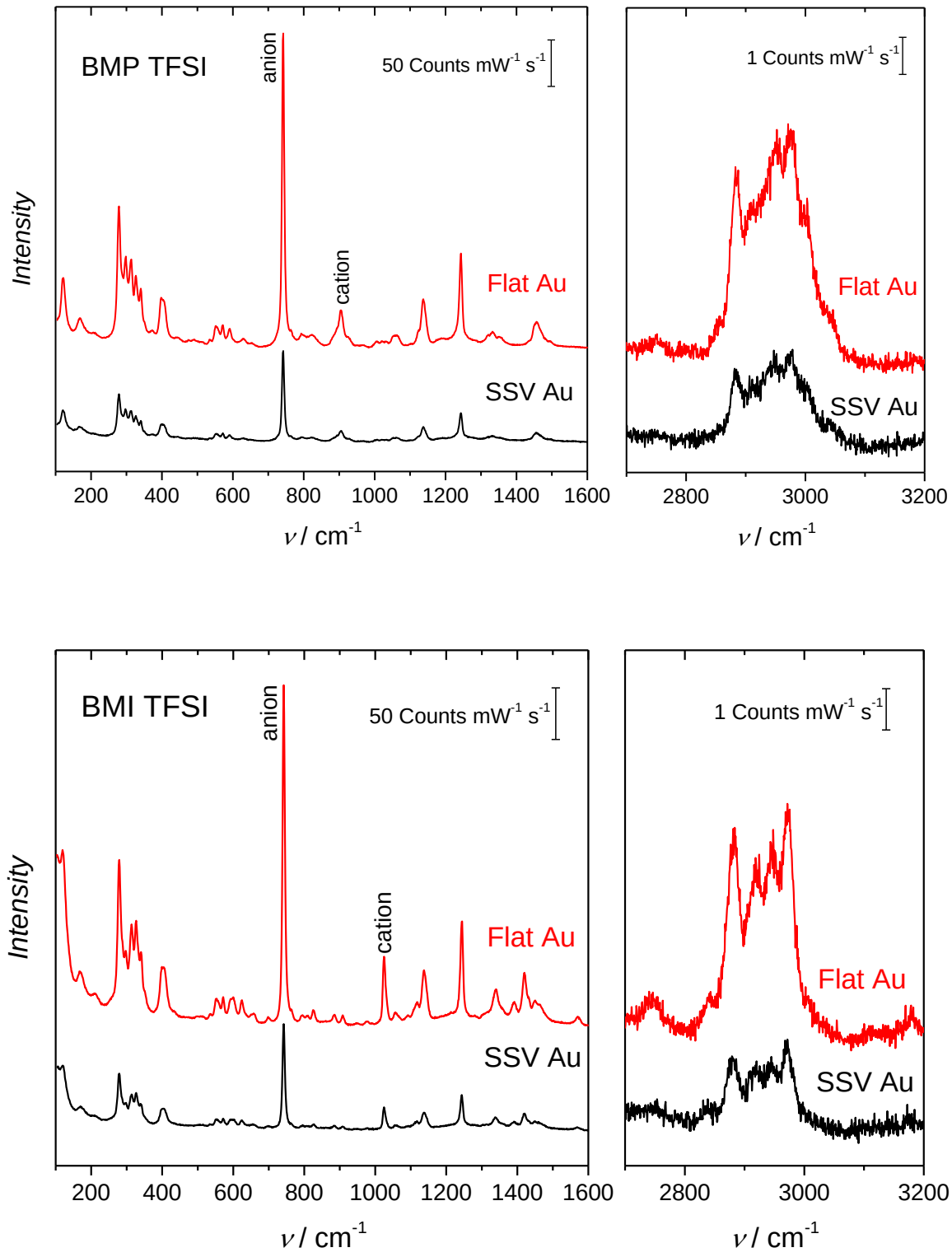

Figure 4-2 Raman spectra of BMP (top) and BMI (bottom) TFSI on the SSV (black) and flat (red) areas of a Au substrate (made with 600 nm diameter spheres and a thickness of 468 nm). The centres and intensities of the labelled peaks, which correspond to an anion and cation vibration, are presented in table 4-1. The spectra have been offset for clarity, by 100 Counts mW^{-1} s^{-1} for the low frequency region (left) and by 2 Counts mW^{-1} s^{-1} for the high frequency region of the spectra. All spectra have been normalised by the laser power and exposure time used.

Peak centres and intensities of characteristic peaks for the anion and cation of each IL, have been measured and are presented in table 4-1. Three key observations can be made from these values. Firstly, none of the peak centres for either of the ILs shift between the flat and nanostructured Au areas of the substrates. Secondly, both anion and cation peak intensities are ~ 3 x more intense on the flat Au compared to on the nanostructured Au, for both ILs. Lastly, the intensity ratio between the anion and cation peaks is different for each IL, but doesn't change from flat to nanostructured Au. These three results don't indicate any significant vibrational changes between flat Au and SSV Au.

Table 4-1 Centres and intensities of Raman peaks to the anion and cation of each IL, as seen in figure 4-2, for spectra obtained on the flat and nanostructured regions of Au SSV substrates (made with 600 nm diameter spheres and a thickness of 468 nm).

Analyte	**Substrate Region**	**Anion Peak**		**Cation Peak**	
		Centre / cm^{-1}	Intensity / Counts mW^{-1} s^{-1}	Centre / cm^{-1}	Intensity / Counts mW^{-1} s^{-1}
BMP TFSI	Flat	742	343	905	39
	SSV	742	108	905	12
BMI TFSI	Flat	742	325	1025	64
	SSV	742	114	1025	23

This effect can somewhat be seen in the literature, though it has never been clearly discussed. For example, when Rubim et al. published their work on SERS of BMI BF_4 on Ag surfaces, they scaled their pure IL Raman spectrum by 0.5 to make the peak intensities similar to the SERS spectrum of the Ag – BMI BF_4 colloidal solution.[9] They then subtracted the spectra to show which peaks were more enhanced in the SERS spectrum. While this subtraction seems like a reasonable method to establish which peaks are more enhanced, the authors did not give any information on why they chose a scaling factor of 0.5. Furthermore, they used arbitrary units for Raman intensity, with no information of laser power or exposure times. From the presented spectra, one can observe the IL peaks were at least similar, if not higher, in intensity in the Raman spectrum as opposed to the SERS spectrum. However, this is assuming the laser powers and exposure times used were the same in both circumstances.

Similarly, in a publication by Brandão et al. on SERS of the same IL on a roughened Cu electrode, the IL Raman peaks presented are of similar or higher intensity on the flat Cu compared to on the roughened Cu electrode.[6] Again, arbitrary intensity units were used and no information was provided regarding the laser power and exposure time used.

Weaker spectra of ILs on SERS-active substrates compared to Raman spectra can very clearly be seen in a publication by Harroun et al..[10] They presented a Raman spectrum of a neat isobutyl-based homemade IL and EC-SERS spectra of the same IL on carbon electrodes coated with Ag nanoparticles. The TFSI Raman peak at 742 cm^{-1} was ~ 10x more intense and the cation peak at 1036 cm^{-1} was ~ 8x more intense in the Raman spectrum than in the SERS spectrum at open circuit potential (OCP).

Lastly and most recently, Mahurin et al. published work on EC-SERS of EMI TFSI on a graphene-over-silver electrode.[17] They discussed the bulk spectrum of the IL being of higher intensity than the SERS spectrum and attributed this to the restricted thickness and volume of IL probed during SERS in the cell compared to the volume of bulk IL probed. They mentioned that a measurement of the same IL, in the same cell, on a non-SERS substrate produced no signal. However, they chose not to include this spectrum in the main body or the supporting information of their publication. This result contradicts the spectra presented in figure 4-2 of this study. It is also important to note that the authors estimated the IL thickness in the cell to be ~ 0.1 mm and that they used a confocal spectrometer, which one would expect to give good spatial resolution, though they have not included a specific value for this in their publication. If the spatial resolution of their system was lower than 100 µm, the thickness of the IL probed should, in theory, not have an effect on the Raman intensity. However, no assumptions can be made without this information.

4.1.3 Pyridine

To examine if this effect was specific to ILs on SSV substrates, spectra were obtained of pure Py on the nanostructured and flat Au regions of a SSV substrate, which are presented in figure 4-3. For comparison, Raman spectra were also obtained of pure Py and of an aqueous 0.05 M Py 0.1 M KCl solution in a Quartz crystal cuvette and these have been included in section B.1 of appendix B, as figures B-1 and B-2, respectively. Py was used as it has been extensively studied by both Raman and SERS and also because there are well established spectral differences between pure Py, aqueous Py solutions and Py adsorbed on Au.[11, 15]

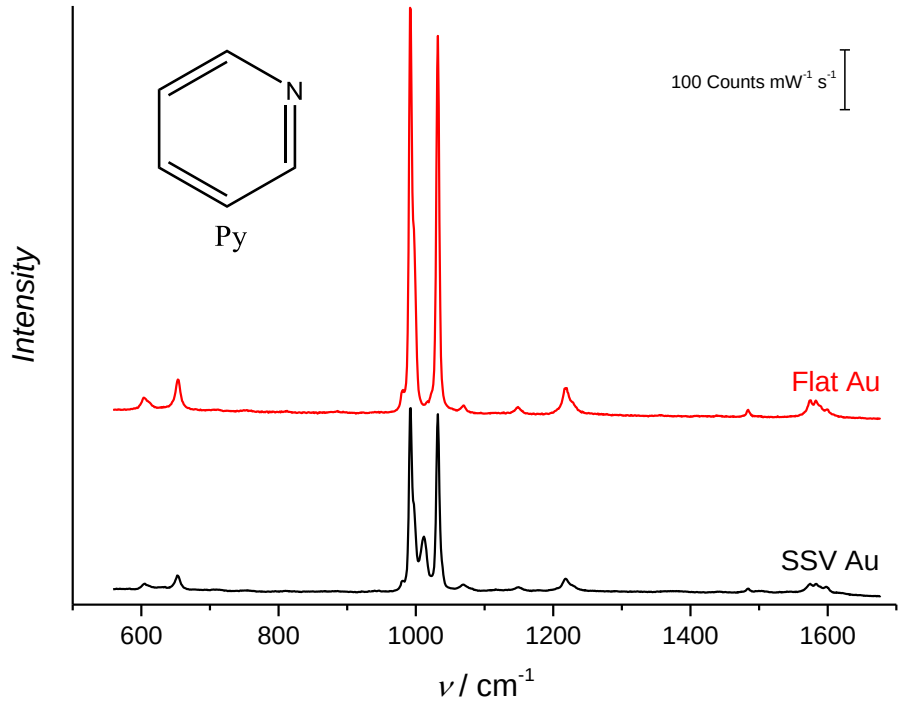

Figure 4-3 Raman spectra of pure liquid Py on the SSV and flat areas of a Au substrate (made with 600 nm diameter spheres and a thickness of 468 nm). The spectra have been offset by 300 Counts mW^{-1} s^{-1}, for clarity. Both spectra have been normalised by the laser power and exposure time used.

As with the ILs, the Raman peaks of Py were more intense on the flat Au region compared to the SSV Au region. This shows that for concentrated analytes, the Raman intensity obtained on flat Au is higher than on SSV Au. However, it is important to note that unlike with the ILs, there was a distinct new peak at 1012 cm^{-1} in the spectrum obtained on SSV Au, which had not appeared in the spectrum on flat Au. This matches the peak found by Tian et al., corresponding to the ring breathing mode (ν_1, Wilson notation) of Py adsorbed on a roughened Au electrode at OCP.[11] As this is a surface specific peak, its appearance in the SSV spectrum indicates the surface enhancement present. However, this peak was still weaker than the peaks at 992 cm^{-1} (ν_1) and 1032 cm^{-1} (ν_{12}) which correspond to the ring breathing mode and the symmetric triangular ring deformation of pure Py, respectively. Unlike the peak at 1012 cm^{-1}, these peaks are not surface specific, so they could either arise from Py near the surface or from the bulk liquid.

To further examine the relationship between Raman peaks from the bulk and from the surface, spectra were obtained of aqueous 0.1 M KCl solutions containing varying concentrations of Py and of pure Py, which has an effective concentration of 12.4 M, on the flat and nanostructured regions

of a Au SSV substrate. Once again, Py was used as it has good miscibility in water, making the preparation of the required solutions straightforward.

The most intense peaks obtained were between 930 and 1100 cm^{-1} which are shown in figures 4-4 (A) and (B) for the flat and SSV regions of the same Au substrate, respectively. These were fitted using three peaks; one between 991-1003 cm^{-1}, corresponding to the ν_1 vibration of pure or aqueous Py, one at 1012 cm^{-1}, corresponding to the ν_1 vibration of Py adsorbed on Au and one at 1032-1038 cm^{-1}, corresponding to the ν_{12} vibration of Py. The ν_1 vibration was fitted using the first two peaks, in order to easily distinguish between the peak from the bulk Py and the peak from the surface bound Py. Because the ν_{12} vibration peak doesn't shift as much as the ν_1 vibration peak upon changing the chemical environment, it was only fitted using one peak.

On flat Au, the peak at 1012 cm^{-1} was very weak and was not detectable for Py concentrations above 0.5 M. On the other hand, the same peak appeared for all concentrations on SSV Au and its position did not shift by more than 2 cm^{-1}, showing the surface enhancement present on the SSV Au. Furthermore, the intensity of this peak did not increase as much as of the other two peaks with increasing Py concentration, as it was only influenced by the amount of Py adsorbed at the surface. Actually, it is interesting to note that its intensity decreased in pure Py, but this may be explained by the lack of Cl^- ions, which have been found to increase the SERS intensity of peaks from adsorbates.[15, 18, 19]

The centre of the 1032-1038 cm^{-1} peak on SSV Au was always closer to 1038 cm^{-1} than it was on flat Au, which was the value expected for Py adsorbed on Au as described by Tian et al..[11] This was due to the peak centre being influenced by the surface bound Py on the SSV Au, again demonstrating the surface enhancement expected on the SSV structure.

If the volume of liquid probed was the same on flat and on SSV Au, the signal produced by the bulk liquid on the SSV Au would be equal to or higher than that produced on flat Au. However, this was not the case at high Py concentrations. Up to Py concentrations of 1 M, the bulk Py peak at 991-1003 cm^{-1} was more intense on the SSV substrate than on the flat Au, again demonstrating the surface enhancement present. As Py concentration increased above 5 M, the same peak from the bulk liquid became more intense on the flat Au than on the SSV Au. This possibly indicated a greater volume of liquid probed at the flat Au surface than at the SSV Au surface. This will be further discussed with regards to spatial resolution in section 4.1.4.

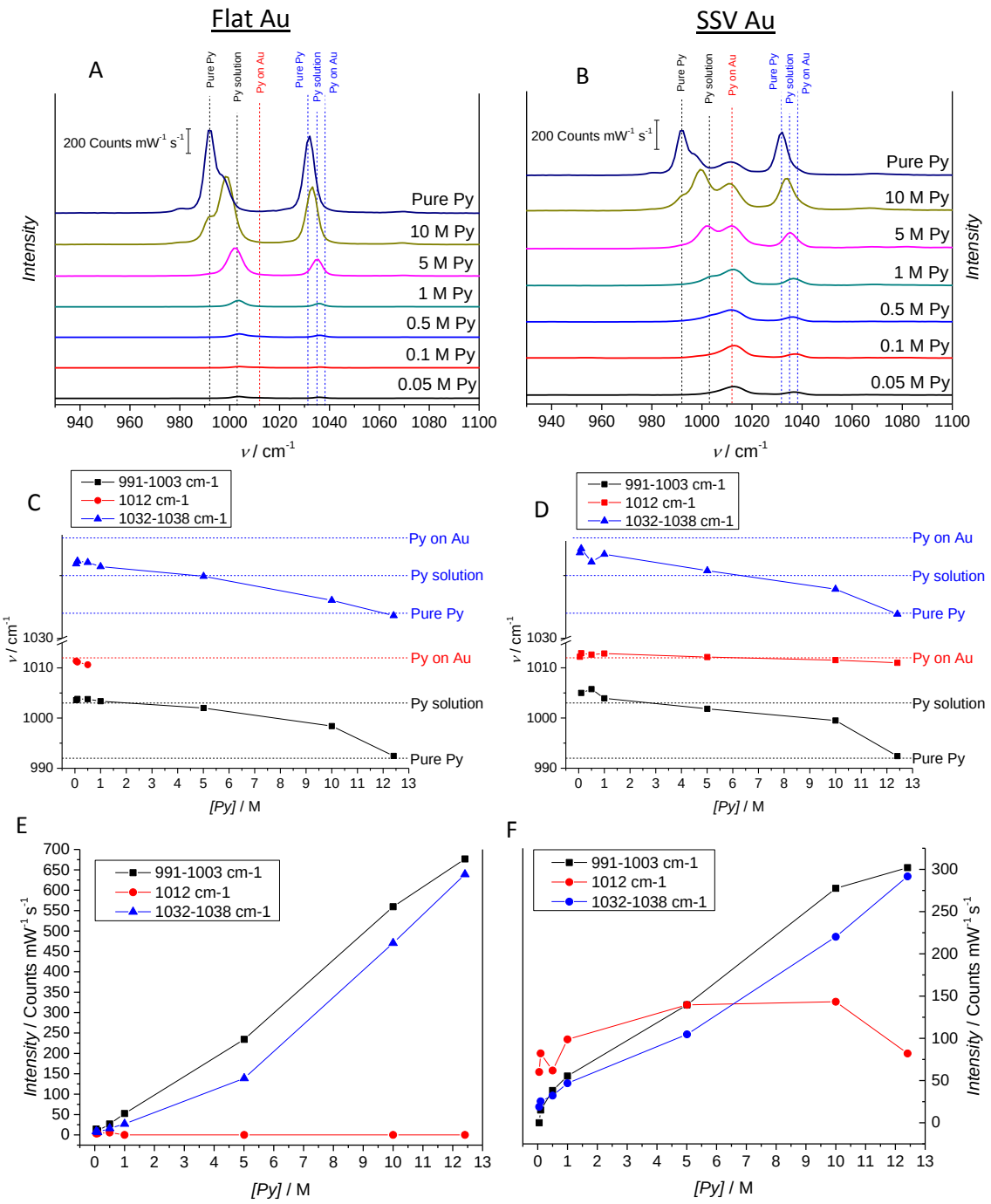

Figure 4-4 (A) & (B) Raman spectra, (C) & (D) peak centres and (E) & (F) intensities for various concentrations of Py in 0.1 M aqueous KCl and for pure Py, taken on the flat ((A), (C) & (E)) and SSV ((B), (D) & (E)) Au regions of the same substrate (made with 600 nm diameter spheres and a thickness of 468 nm). Spectra were offset by 250 Counts mW^{-1} s^{-1} and were normalised by the laser power and exposure time used. Peak centres and intensities presented in (C) - (F) were obtained by fitting three peaks at 991-1003 cm^{-1}, ~1012 cm^{-1} and 1032-1038 cm^{-1}. The dashed lines in (A) – (D) represent the peak centres in Raman spectra of pure Py and of an aqueous 0.05 M Py 0.1 M KCl solution in cuvettes (figures B-1 and B-2, respectively, shown in appendix B). The value used for the dashed line for Py on Au, was taken from a publication by Tian et al..[11]

Lastly, in the spectra obtained for Py concentrations of up to 5 M on SSV Au, the surface specific peak at 1012 cm^{-1} was more intense than the bulk Py peak at 991-1003 cm^{-1}. For the 10 M Py solution and for pure Py, the bulk peak was more intense than the surface peak. For very concentrated Py, the surface enhancement of the SSV substrate was not enough to enhance the surface-specific peak to higher intensities than the bulk Py peak.

To summarise, the varying Py concentration experiment demonstrated, firstly, that the volume probed on a flat Au surface may be larger than that probed on a SSV Au surface. Secondly, at Py concentrations greater than 5 M on SSV Au, the peaks from bulk Py were more intense than those from Py adsorbed on the surface, despite the surface enhancement present.

4.1.4 Depth Resolution

The depth resolution of the Raman microscope determines the sample volume of the analyte probed and depends on the confocality of the system. Confocality gives the user the ability to reject signal from regions away from the point of interest.[20] The Renishaw inVia spectrometer is built with an optical lay-out which makes the system confocal. 'High' confocality can be further achieved by introducing a 'pin hole' in the lay-out. According to the Renishaw technical support team, depth resolutions of the order of a few µm can be achieved. For example, a 785nm line laser with a pin hole fitted and a x100 objective should give a resolution of 2.8µm. However, the system used in this study is 'pin hole-free' and so only 'standard' confocality can be achieved.

The depth resolution for this system was measured using a Si wafer and a depth profile is shown in figure 4-5.[21] To obtain this, the microscope stage was moved in the vertical direction by 5 µm steps, so that the surface passed through the plane of focus of the laser beam, represented by 0 on the x axis of figure 4-5. At the same time, Raman spectra were obtained for every stage position or depth and the intensity of the characteristic 520 cm^{-1} peak for Si recorded. It is important to note that the stage was moved in the vertical direction manually, which would not be as accurate as using a motorised encoded stage. The depth profile was fitted as a peak using a Lorentzian function in Origin 9.1 software. The fitting had a full width at half maximum (FWHM) of 28.6 ± 0.3 µm, which corresponds to the depth resolution of the system.

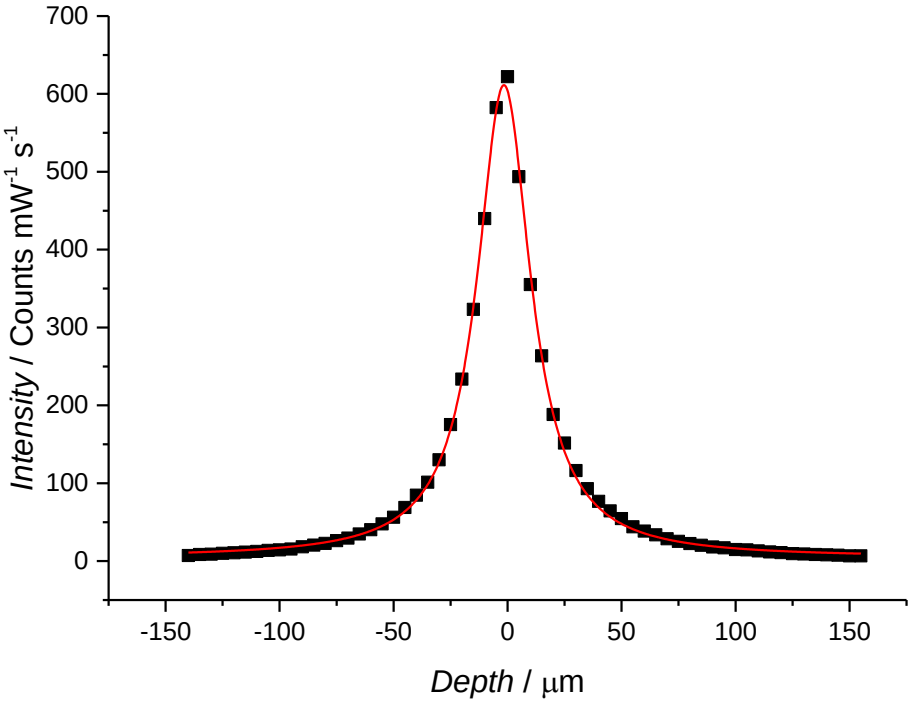

Figure 4-5 Depth profile of a Si wafer. The intensities correspond to the characteristic 520 cm^{-1} Si peak, obtained while manually changing the stage height by 5 μm steps. The line represents the Lorentzian function fitting carried out on the data using Origin 9.1 software, yielding a FWHM and depth resolution of 28.6 ± 0.3 μm.

The relationship between the SERS intensity and the distance of an analyte from the SSV substrate has not been examined. Theory predicts this relationship using the following equation, which has been used in publications in the past[22, 23]:

$$I_{SERS} = \left(1 + \frac{r}{a}\right)^{-10}$$

Equation 4-1

where *r* is the distance of the vibration from the surface and *a* is the radius of the curvature of the field enhancing feature of the substrate, equal to 300 nm for the SSV substrates in this study. A simulated curve for this equation is displayed in figure 4-6.

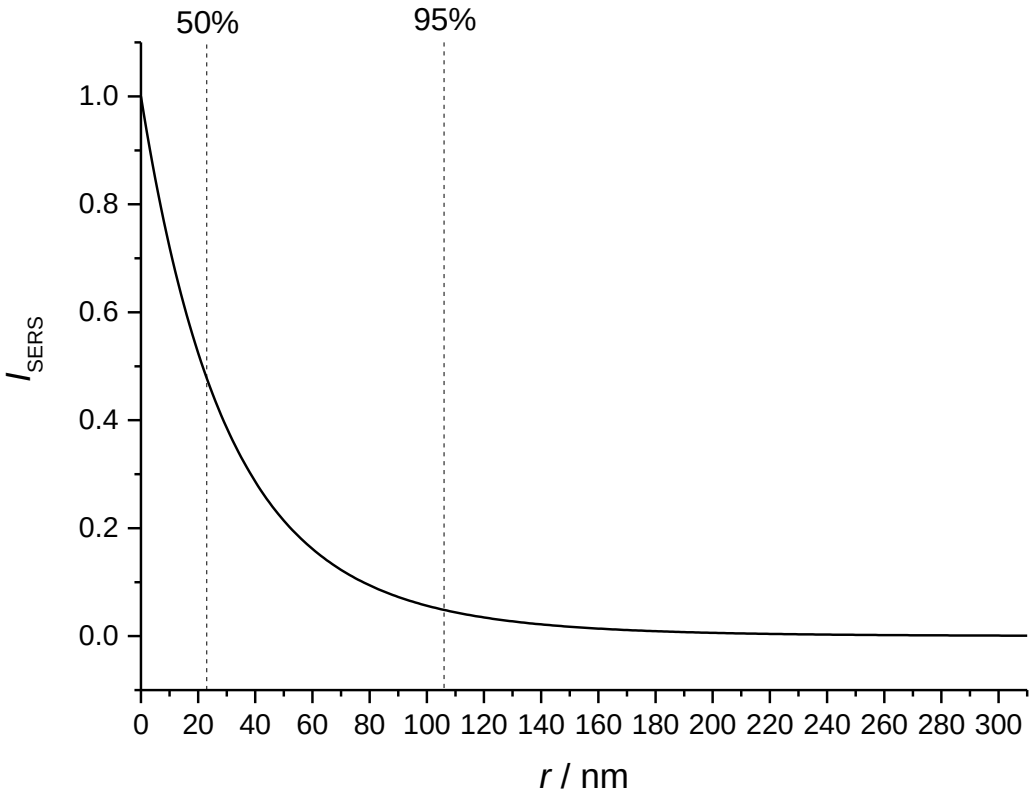

Figure 4-6 Simulated curve from equation 4-1, showing the decaying SERS intensity of a molecule located at *r* distance from the type of SSV substrate used in this study (made with 600 nm diameter spheres and a thickness of 468 nm, *a* = 300 nm). The dashed lines indicate the distance at which 50% and 95% of the SERS intensity has decayed.

From the simulated curve in figure 4-6, one can observe that 50% of the SERS intensity is predicted to be lost within 23 nm from the surface and 95% of the SERS intensity is predicted to be lost within 106 nm from the surface. Assuming that equation 4-1 offers an accurate prediction for the relationship between the SERS intensity of a molecule and its distance from a SSV substrate, then we can expect that the substrate yields a good surface enhancement to sub-µm depths. As a result, the SERS enhancement depth of a SSV substrate made with 600 nm spheres, as predicted using equation 4-1, is more than two orders of magnitudes smaller than the depth resolution of the spectrometer, as calculated using the depth profile presented in figure 4-5.

The surface plasmons of the SSV substrate responsible for the SERS enhancement, effectively restrict the optical field to a region near the surface. Because this is not present on flat Au, the Raman signal originates from the full volume probed, defined by the spectral resolution of the Raman microscope. However, it is important to also note that even though there are fewer

molecules in the volume of liquid probed on the SSV substrate, the signal/molecule ratio is higher as a result of the SERS enhancement. An enhancement factor of 2.6 x 10^7 for a Au SSV substrate has previously been reported in the literature.[24] However, this does not take into account the SERS signal decay with distance from the substrate described by equation 4-1. Therefore, the relationship between the number of molecules probed and the resulting signal in the Raman and SERS spectra is very complex.

Despite this complexity, the smaller depth and thus, volume, of liquid enhanced on a SSV substrate compared to the total volume probed on flat Au, is believed to be the main reason behind the lower signal obtained for concentrated liquids on SSV Au compared to on flat Au.

4.1.5 Potential-Dependent Raman

As this study focuses on the potential-dependent behaviour of ILs, Raman spectra intensities have also been compared for the same IL on flat and nanostructured Au regions of a SSV substrate at various potentials. In figure 4-7 the intensity-potential profiles of a cation and an anion peak of the BMP TFSI IL are compared for Raman spectra obtained on the flat and nanostructured regions of a Au SSV substrate. Spectra of BMP TFSI and full peak assignments were presented in chapter 3 of this thesis.

The peak at 742 cm^{-1} was the most intense peak of the spectrum and has been assigned to anion vibrations. In figure 4-7 (A), the intensity of this peak has been presented as a function of potential, for the spectra on flat Au and the spectra on SSV Au. As seen earlier, the peak intensity on flat Au was greater than the intensity on SSV Au. Additionally, the peak intensity on flat Au does not change as much with potential as it does on SSV Au. More specifically, the peak intensity changes by a maximum of 16.5 Counts $mW^{-1} s^{-1}$ between 0 V and -1.5 V vs. Pt Quasi-Reference Electrode (PQRE) on SSV Au and by a maximum of 6.2 Counts $mW^{-1} s^{-1}$ between 0 V and -0.8 V vs. PQRE on flat Au. This is what one would expect, as on the SSV Au, the peak intensity is representative of the changes occurring close to the Au surface, where the potential changes will have a larger effect on the ions and thus the spectra. The peak intensity changes on flat Au will be largely affected by the Raman signal of the IL further away from the Au surface, the bulk IL, where potential changes are less likely to have an effect.

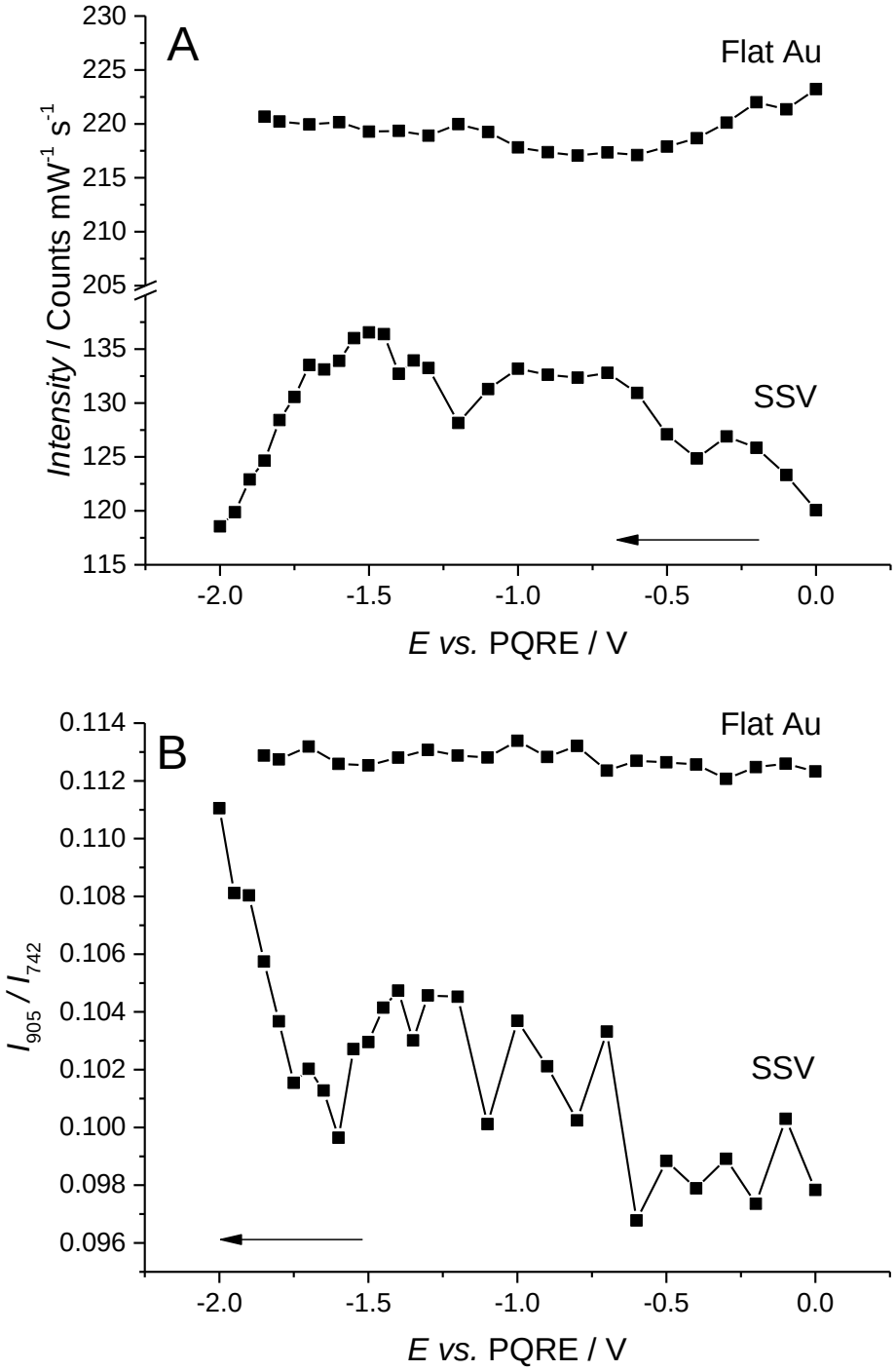

Figure 4-7 (A) Peak intensity of the 742 cm^{-1} peak of Raman spectra of the BMP TFSI IL, taken on the flat and SSV regions of a Au substrate. (B) Ratio of intensity of the 905 cm^{-1} peak to the intensity of the 742 cm^{-1} peak of Raman spectra of the BMP TFSI IL, taken on the flat and SSV regions of a Au substrate, at different potentials. The 742 cm^{-1} and 905 cm^{-1} peaks correspond to anion and cation vibrations of the BMP TFSI IL, respectively. For full assignments and spectra of the IL, see chapter 3. The SSV substrate had been prepared with 600 nm diameter spheres and a thickness of 468 nm. The spectra and derived intensities have been normalised by the laser power and exposure time used. The arrows indicate the direction in which the potential was changed.

However, even when spectra are obtained on the SSV substrate, it is likely that the strong Raman scattering bulk IL, may interfere with the surface-specific signal. Furthermore, it is likely that the refractive index of the IL will change with changing the potential due to packing and redistribution of the ions.[25] This can affect the surface plasmons of the SSV substrate and hence, the Raman surface enhancement.[26, 27] These systematic effects which may cause changes in spectral intensities need to be addressed.

Rubim et al. took the bulk signal into account by subtracting a scaled bulk IL spectrum from the SERS spectrum.[9] While this is acceptable for a qualitative study of the IL SERS peaks, it does not work in an EC study, as the bulk spectrum of the IL will change with potential and it would be difficult to obtain SERS and bulk Raman spectra of the IL simultaneously at each potential. Liu et al. mention that they used a confocal Raman system to exclude the bulk system.[16] however, they do not mention the spatial resolution the system produces. Other EC-SERS studies of ILs have not mentioned how they have addressed the bulk IL signal, changes in the refractive index of the IL, or any other systematic effects.

In this study, peak intensities will be examined by their ratio to the intensity of other peaks. For example, the ratio of the intensities of a cation and an anion peak will be studied as a function of potential, as has been presented in figure 4-7 (B). The changes in this ratio will give an indication of how the differently charged ion distributions at the surface change with respect to each other, while any interference from the bulk IL signal or changes in the plasmonic effects of the Au SSV substrate with potential, will be cancelled out.

In figure 4-7 (B), the ratio of intensity of the 905 cm^{-1} peak, the most intense cation peak of BMP TFSI, to the intensity of the 742 cm^{-1} anion peak, changes by a maximum of 0.009 between -0.6 V and -1.85 V vs. PQRE on the SSV Au region of the substrate. However, on the flat Au region of the substrate, the ratio only changes by a maximum of 0.001 between -0.3 V and -1 V vs. PQRE. Similarly to the 740 cm^{-1} peak intensity in figure 4-7 (A), this was expected due to greater changes in ion distributions close to the Au electrode surface with potential, which were enhanced on the SSV substrate region, compared to the mostly bulk IL signal probed on the flat Au surface.

4.2 Reflectance Spectroscopy

It is known that the EC potential has a complex effect on the SERS intensity. Potential-induced specific adsorption of ions on the metal surface can increase the refractive index of the electrolyte in the region, which can cause a red-shift in the surface plasmons.[11, 25, 26] Since Raman spectroscopy uses single wavelength light, a shift in surface plasmons would result in a change in intensity. Other than molecular changes close to or at the electrode surface, a changing EC

potential can cause the redistribution of conduction band electrons at the surface, thus changing the charge density and dielectric constant of the metal.[11, 28] This has an effect on the optical properties of the metal. According to Wu et al. applying a potential negative to the potential of zero charge (PZC) will result in an increase and red-shift in the plasmon resonance band.[11]

Reflectance spectroscopy has been used in the past to study the plasmonic effects of SERS substrates.[24] Absorbance features observed in reflectance spectra may be described by contributions by surface plasmons. As a result, the reflectance has been found to depend on the SSV film thickness, with decreased reflectance corresponding to increased SERS intensity. Similarly, by obtaining reflectance spectra while varying the potential of a Au SSV substrate in an IL, any potential-dependent plasmonic changes at the Au surface may be detected.

An example of a reflectance spectrum has been displayed in figure 4-8 (a). As the wavelength used for SERS in this study was 785 nm, the plasmon band at 781 nm was the one contributing to the surface enhancement and Raman intensity. The logarithm of reflectance of this band has been plotted vs. potential in figure 4-8 (c). There is an overall increase in the reflectance towards negative potentials, which should correspond to a decrease in the surface plasmon resonance and could thus lead to a decrease in Raman intensity. However, this increase in reflectance is very small and the shape of the reflectance spectrum did not change with potential, as can be seen in figure B-3 in section B.2 of appendix B.

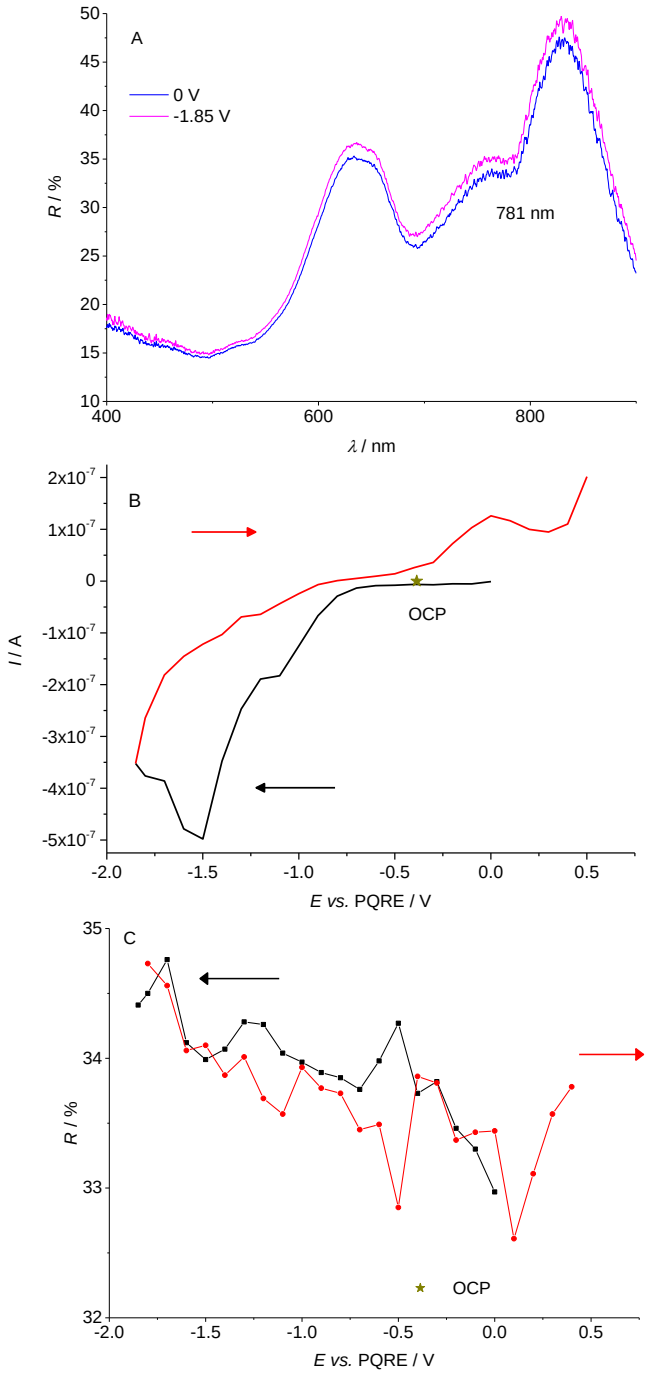

Figure 4-8 (A) Reflectance spectra of a Au SSV substrate (prepared with 600 nm diameter spheres and a thickness of 468 nm) in BMP TFSI at 0 V and at -1.85 V vs. PQRE. The spectrum was obtained using a white light laser source. (B) Resting currents at various potentials of the Au SSV substrate in BMP TFSI during the reflectance measurements. (C) Reflectance values at 781 nm obtained at various potentials of the Au SSV substrate. The arrows indicate the direction in which the potential was changed. The asterisks indicate the values of resting current, reflectance and potential at the OCP.

It was considered highly unlikely that these small changes would affect the SERS intensity more than the molecular changes and movements of the ions near the electrode surface, which are very sensitive to the EC potential. However, in order to ensure these changes could not influence the results and their interpretation presented in the following chapters, the peak intensities examined in this study have been presented as ratios.

4.3 Summary

In this chapter, the SERS response of the SSV substrate has been examined for the application to the study of the metal-IL interface. It was found that, as opposed to the behaviour commonly found with SAMs, the SERS spectra of BMP TFSI on Au SSV substrates were less intense than the Raman spectra on flat Au. This was also found for spectra of pure Py and it was further investigated using varying concentrations of Py. For Py concentrations higher than 5 M on SSV Au, the bulk Py peaks became more intense than the peaks corresponding to Py adsorbed on Au. This demonstrated that the signal of bulk Py molecules has a significant effect on the overall signal obtained on SSV Au substrates at high concentrations of molecules, such as those found in ILs.

Additionally, the depth resolution of the spectrometer was measured to be 28.6 ± 0.3 μm whilst 95% of the SERS enhancement on a Au SSV substrate was expected to be lost within 106 nm from the surface. This significant difference could lead to a larger volume of bulk liquid being probed on flat Au, corresponding to the depth resolution of the spectrometer, compared to the smaller volume of liquid enhanced on SSV Au. Larger differences in peak intensities of BMP TFSI at varying EC potentials on SSV Au compared to on flat Au, re-enforce the concept that on SSV Au the smaller volume of liquid close to the metal surface is being probed, as opposed to a larger volume of bulk liquid on flat Au.

Lastly, potential-dependent reflectance spectroscopy was used to examine if there were any plasmonic changes which could affect the collective intensity of the Raman spectrum, due to either refractive index changes of the electrolyte due to ion packing or conduction band electron re-distribution at the metal. There was an overall increase in reflectance at negative potentials, however, this increase was very small and as a result shouldn't affect the peak intensities obtained. In any case, peak intensities presented throughout this report will be studied as ratios. This should eliminate any effects which can affect the collective intensity of the SERS spectrum.

4.4 References

1. M. E. Abdelsalam, P. N. Bartlett, J. J. Baumberg, S. Cintra, T. A. Kelf and A. E. Russell, *Electrochem. Commun.*, 2005, **7**, 740-744.

2. N. G. Tognalli, A. Fainstein, E. J. Calvo, M. Abdelsalarn and P. N. Bartlett, *J. Phys. Chem. C*, 2012, **116**, 3414-3420.

3. A. Celiktas, M. A. Ghanem and P. N. Bartlett, *J. Electroanal. Chem.*, 2012, **670**, 42-49.

4. R. P. Johnson, N. Gale, J. A. Richardson, T. Brown and P. N. Bartlett, *Chem. Sci.*, 2013, **4**, 1625-1632.

5. M. J. Weaver, S. Z. Zou and H. Y. H. Chan, *Analytical Chemistry*, 2000, **72**, 38A-47A.

6. C. R. R. Brandao, L. A. F. Costa, H. S. Breyer and J. C. Rubim, *Electrochem. Commun.*, 2009, **11**, 1846-1848.

7. V. O. Santos, M. B. Alves, M. S. Carvalho, P. A. Z. Suarez and J. C. Rubim, *J. Phys. Chem. B*, 2006, **110**, 20379-20385.

8. H. S. Schrekker, M. A. Gelesky, M. P. Stracke, C. M. L. Schrekker, G. Machado, S. R. Teixeira, J. C. Rubim and J. Dupont, *J. Colloid Interface Sci.*, 2007, **316**, 189-195.

9. J. C. Rubim, F. A. Trindade, M. A. Gelesky, R. F. Aroca and J. Dupont, *J. Phys. Chem. C*, 2008, **112**, 19670-19675.

10. S. G. Harroun, T. J. Abraham, C. Prudhoe, Y. Zhang, P. J. Scammells, C. L. Brosseau, C. C. Pye and R. D. Singer, *Phy. Chem. Chem. Phys.*, 2013.

11. D. Y. Wu, J. F. Li, B. Ren and Z. Q. Tian, *Chem. Soc. Rev.*, 2008, **37**, 1025-1041.

12. S. Mahajan, R. M. Cole, J. D. Speed, S. H. Pelfrey, A. E. Russell, P. N. Bartlett, S. M. Barnett and J. J. Baumberg, *J. Phys. Chem. C*, 2010, **114**, 7242-7250.

13. K. Fukami, M. L. Chourou, R. Miyagawa, A. M. Noval, T. Sakka, M. Manso-Silvan, R. J. Martin-Palma and Y. H. Ogata, *Materials*, 2011, **4**, 791-800.

14. M. A. Bryant and J. E. Pemberton, *J. Am. Chem. Soc.*, 1991, **113**, 8284-8293.

15. Barnes, Tian, Aggaral, Goodacre, Donaldson, M. Muniz, Baumberg, Vlckova, Creighton, Natan, Kosower, Alexander, Khan, Russell, Murakoshi, Kneipp, Domke, R. Le, Green, Poponin, Stone, Ren, Pettinger, Milton, Jarvis, Tantra, Kall, Sugawara, Roy, Whitby and Richards, *Faraday Discuss.*, 2006, **132**, 227-247.

16. Y. Liu, Y. X. Yuan, X. R. Wang, N. Zhang, M. M. Xu, J. L. Yao and R. A. Gu, *J. Electroanal. Chem.*, 2014, **728**, 10-17.

17. S. M. Mahurin, S. P. Surwade, M. Crespo and S. Dai, *J. Raman Spectrosc.*, 2016, **47**, 585-590.

18. P. Etchegoin, L. F. Cohen, H. Hartigan, R. J. C. Brown, M. J. T. Milton and J. C. Gallop, *J. Chem. Phys.*, 2003, **119**, 5281-5289.

19. R. Pang, X. G. Zhang, J. Z. Zhou, D. Y. Wu and Z. Q. Tian, *J. Phys. Chem. C*, 2017, **121**, 10445-10454.

20. inVia: spatial resolution, http://www.renishaw.com/en/invia-spatial-resolution--25900, (accessed 27th of August, 2017).

21. F. Adar, *Spectroscopy*, 2010, **25**, 16-23.

22. B. J. Kennedy, S. Spaeth, M. Dickey and K. T. Carron, *J. Phys. Chem. B*, 1999, **103**, 3640-3646.

23. S. S. Masango, R. A. Hackler, N. Large, A. I. Henry, M. O. McAnally, G. C. Schatz, P. C. Stair and R. P. Van Duyne, *Nano Lett.*, 2016, **16**, 4251-4259.

24. S. Cintra, M. E. Abdelsalam, P. N. Bartlett, J. J. Baumberg, T. A. Kelf, Y. Sugawara and A. E. Russell, *Faraday Discuss.*, 2006, **132**, 191-199.

25. J. C. Abanulo, R. D. Harris, P. N. Bartlett and J. S. Wilkinson, *Appl. Optics*, 2001, **40**, 6242-6245.

26. J. C. Abanulo, R. D. Harris, A. K. Sheridan, J. S. Wilkinson and P. N. Bartlett, *Faraday Discuss.*, 2002, **121**, 139-152.

27. A. K. Sheridan, P. Ngamukot, P. N. Bartlett and J. S. Wilkinson, *Sensor. Actuat. B-Chem.*, 2006, **117**, 253-260.

28. C. G. Blatchford, O. Siiman and M. Kerker, *Journal of Physical Chemistry*, 1983, **87**, 2503-2508.

Chapter 5: Electrochemical-SERS of BMP TFSI on Gold

The aim of this chapter is to use electrochemical surface enhanced Raman spectroscopy (EC-SERS) to further understand the voltammetry of 1-butyl-1-methylpyrrolidinium bis(trifluoromethylsulfonyl)imide (BMP TFSI).

Low current features seen in cyclic voltammograms (CVs) of metal – ionic liquid (IL) interfaces have been discussed in the literature. Atkin et al. attributed three cathodic waves C_1-C_3 in their CV of a custom made BMP-based IL on Au, to different surface processes that occur upon IL adsorption.[1] In the same publication, scanning tunnelling microscopy (STM) and atomic force microscopy (AFM) revealed the formation of a Au herringbone superstructure due to strong adsorption of the cation in the potential region of C_1 and C_2 and the disappearance of the structure in the potential region of C_3. The oxidation waves A_2 and A_3 were found to be directly correlated to the waves C_2 and C_3.

Later on, Wen et al. performed CV and STM on the BMP TFSI - Au(111) interface.[2] While scanning the potential between -0.35 V and -1.7 V vs. Pt Quasi-Reference Electrode (PQRE), they found two large cathodic waves in their CV, which correspond to C_2 and C_3 in the CV presented by Atkin et al..[1] A much smaller wave can also be seen in their CV, which could correspond to C_1, but this was not discussed in their publication. They attributed the two larger waves, which will be referred to as C_2 and C_3 for simplicity, to changes in the molecular arrangement of adsorbed BMP cations on the Au electrode surface. The first wave, C_2, was found to coincide with the close packing and planar adsorption of the BMP cation heterocycles, with the butyl chains lying parallel to the electrode surface. Scanning the potential further negatively, the second wave, C_3, appeared, which was accompanied by a higher packing density of BMP cations in the STM images. They suggested that for this level of packing to be feasible, the BMP cations were adsorbed on the electrode with the heterocycle still parallel to the surface, while the alkyl chains were oriented upright, directed away from the electrode surface.

The presence of impurities, even in trace amounts, may also produce peaks or waves, such as those seen in the CVs presented by Atkin et al. and Wen et al..[1, 2] For example, the formation and oxidation of the superoxide ion, O_2^-, from oxygen was reported by Grande et al. as peaks in a CV of BMP TFSI on a glassy carbon electrode.[3] The formation of superoxide has also been reported using Raman spectroscopy. Peng et al. reported the formation of superoxide in the EC-SERS spectra of a roughened Au electrode in an oxygen saturated aqueous electrolyte, with the appearance of Au-O and O-O stretching peaks at 491 and 1109 cm^{-1}, respectively.[4] Frith et al. also reported the appearance of the superoxide peak at 1107 cm^{-1} in the Raman spectra of a Au

electrode in oxygen saturated BMP TFSI.[5] Most recently, the superoxide ion formation was reported using EC-SERS by Radjenovic et al..[6]

Firstly, this chapter contains a discussion of the electrochemical behaviour of BMP TFSI with the help of CV and staircase potential electrochemical impedance spectroscopy (SPEIS). This behaviour has then been used as a starting point for the analysis of potential-dependent SERS data of BMP TFSI on a Au sphere segment void (SSV) substrate. EC-SERS peaks corresponding to the cation and anion have been compared and the cation orientation and conformation have also been examined. The formation of superoxide and Au oxide at the negative and positive potential limits of the measurements has also been studied, which originated from the presence of trace oxygen and water in the system, respectively.

5.1 Cyclic Voltammetry and Electrochemical Impedance Spectroscopy

As one of the most broadly used methods in electrochemistry, CVs are also broadly used in the study of ILs. EIS is also commonly used to study the double layer between electrodes and ILs.[1, 7-14] Many of the existing publications have focused on measuring or calculating the capacitance from the EIS data, which can yield valuable information about the double layer, specifically about the potential of zero charge (PZC). This will also be examined later on in this section.

5.1.1 Cyclic Voltammetry

In figure 5-1, CVs of a Au SSV substrate in BMP TFSI in the spectroelectrochemical cell can be seen. The wide potential range CV of figure 5-1 (A) is used to establish the EC stability window of the system. The window is limited by the irreversible reduction of BMP at -3 V vs. PQRE and by the dissolution of the Au substrate at +2 V vs. PQRE.[15] This EC stability window of 5 V is somewhat narrower than those found in the literature for the same IL on Au(111), which may be a result of the nanostructuring of the Au or differences in the amount of impurities.[2, 15]

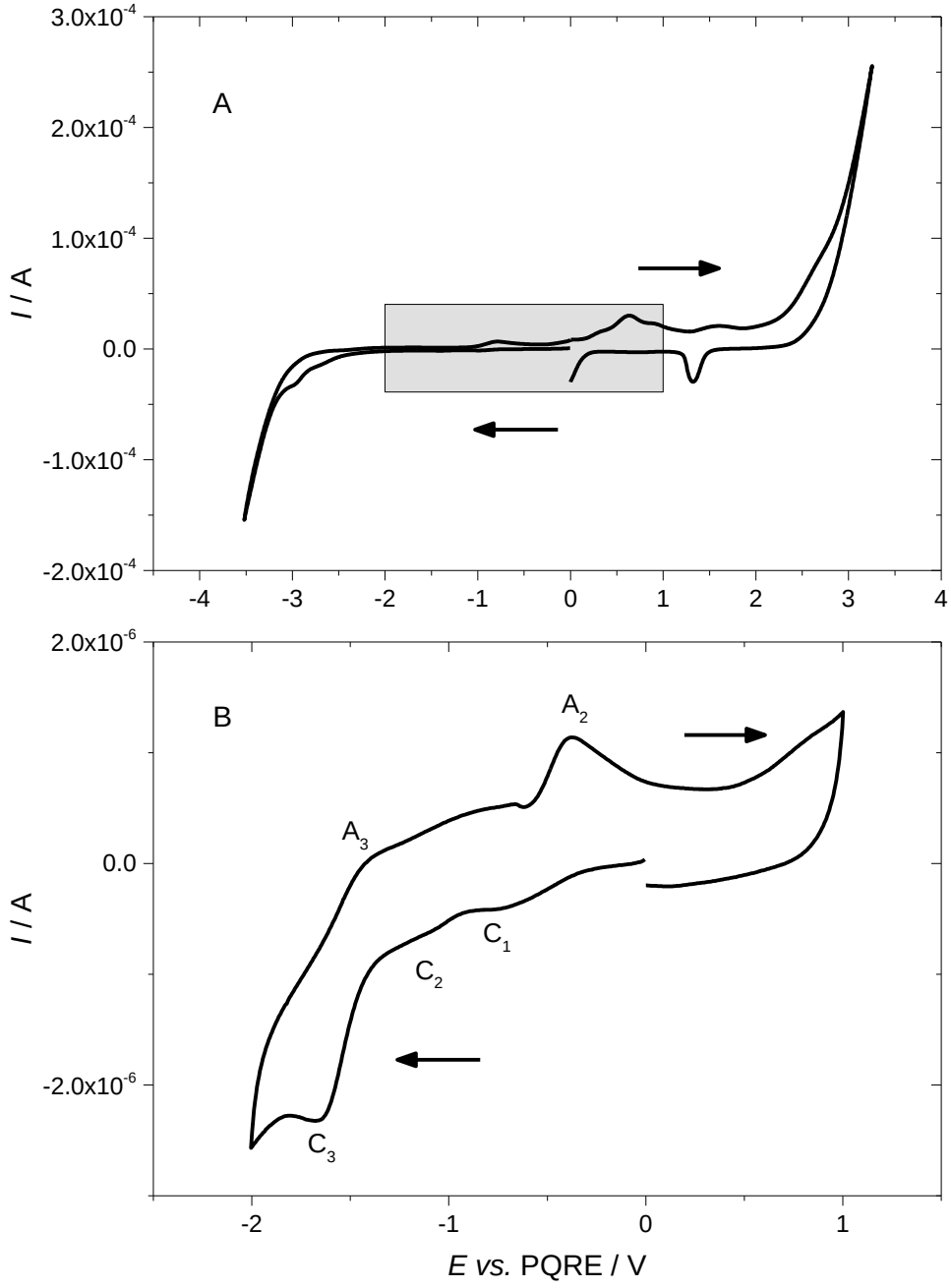

Figure 5-1 CVs of a Au SSV substrate in BMP TFSI, obtained at a scan rate of 10 mV s^{-1}. The highlighted area of the wide potential window CV (A) indicates the potential window used for the small potential window CV (B). The first cycle is shown for each CV, starting from 0 V vs. PQRE and the arrows indicate the direction the potential was scanned in. The counter electrode was a Pt wire, while a second Pt wire acted as the PQRE.

Despite drying of the electrodes, cell and the IL, an oxide stripping peak can be seen in the CV at +1.3 V vs. PQRE, denoting the presence of water. This was known from the Karl Fischer (KF) results described in chapter 2, which gave a water content of 109.3 ppm. Additional water may have entered the system through the equipment, before or during the experiment. The presence of water in ILs has been found to affect the conformation of cations, which in turn affects their Raman spectra.[16, 17] Niu et al. studied the effect of water concentration on the EC-SERS of an IL on a Ag electrode.[18] However, in the studies referenced here, the water content of ILs was at least two orders of magnitude higher than the water contents found in this study. Nevertheless, given the oxide formation and stripping peaks visible in figure 5-1, it is important to remain vigilant to any effects due to water which may arise in the spectra.

The potential range used for this chapter has been highlighted in figure 5-1 (A) and a CV obtained within this potential window is shown in figure 5-1 (B). The presence of Au oxide has been found to decrease the SERS enhancement.[19] To avoid any oxide formation on the substrates during the experiments, the EC potential window was limited to +1 V vs. PQRE, as can be seen in figure 5-1 (B). To avoid decomposition of the IL, the EC potential window was limited to -2 V vs. PQRE. Three cathodic waves appear in the CV of figure 5-1 (B) at similar potentials to cathodic waves C_1, C_2 and C_3 found in the CV by Atkin et al., as discussed in the introduction to this chapter. [1] Hence, all features in the CV of figure 5-1 (B) have been labelled in the same way.

5.1.2 Electrochemical Impedance Spectroscopy

The relationship between the phase of the impedance and the electrochemical potential will be discussed. This relationship has been studied in the literature by Singh and Kant, who developed a model to explain the impedance phase modulation as a result of 'multiple states' of cations in the compact layer on a Au electrode.[20]According to the authors, these states may result from the application of potential, differences in cation sizes, shape asymmetry or orientations. They modelled theoretical impedance, phase and complex capacitance curves for different levels of contribution of these molecular states and electrode heterogeneity. They then compared these curves to experimental EIS data of the same IL on two different Au single crystal electrodes. However, they did not study the effect of potential on these curves.

Singh and Kant reported that phase curves with a relatively simple sigmoidal curve correspond to a single molecular state compact layer at the electrode, which shows characteristic behaviour of a constant phase element (CPE). The existence of more than one molecular state leads to the appearance of a "camel hump" shape, i.e. a minimum flanked by two maxima. The magnitude of the camel hump depends on the amount of Au surface occupied by each state of cations. While

Singh and Kant only attribute these changes to cation orientation changes, it is safe to assume that these may also arise from conformation changes as well, as their states refer to any differences which alter the cation symmetry.

As the phase curves showed the largest differences in shape between different extents of molecular states in the publication by Singh and Kant, similar impedance phase curves of the BMP TFSI on a Au SSV substrate have been presented for various EC potentials in figure 5-2 (A). The current response to the EC potentials used during these EIS measurements has also been displayed in figure 5-2 (B).

The camel hump shape and its magnitude are potential-dependent in the curves presented in figure 5-2 (A). From 0 to -0.9 V there is a hump present but it is relatively unpronounced and flat. This corresponds to the region of figure 5-2 (B) where there are no features visible and the current remains close to 0 A. This would suggest that there is one main cation state in the double layer and no significant changes are occurring between these potentials. At -1.2 V and -1.3 V the hump becomes more pronounced and symmetrical in shape. This also corresponds to a shallow peak or plateau in the current, following a sharp increase in negative current. The presence of the camel hump in the phase curves shows a clear existence of two states. At -1.35 V and -1.4 V, the shape of the camel hump broadens and decreases in magnitude with the potential appearance of a second, smaller hump at lower frequencies. This may indicate the appearance of a third intermediate state. This was accompanied by a steep increase in the negative current.

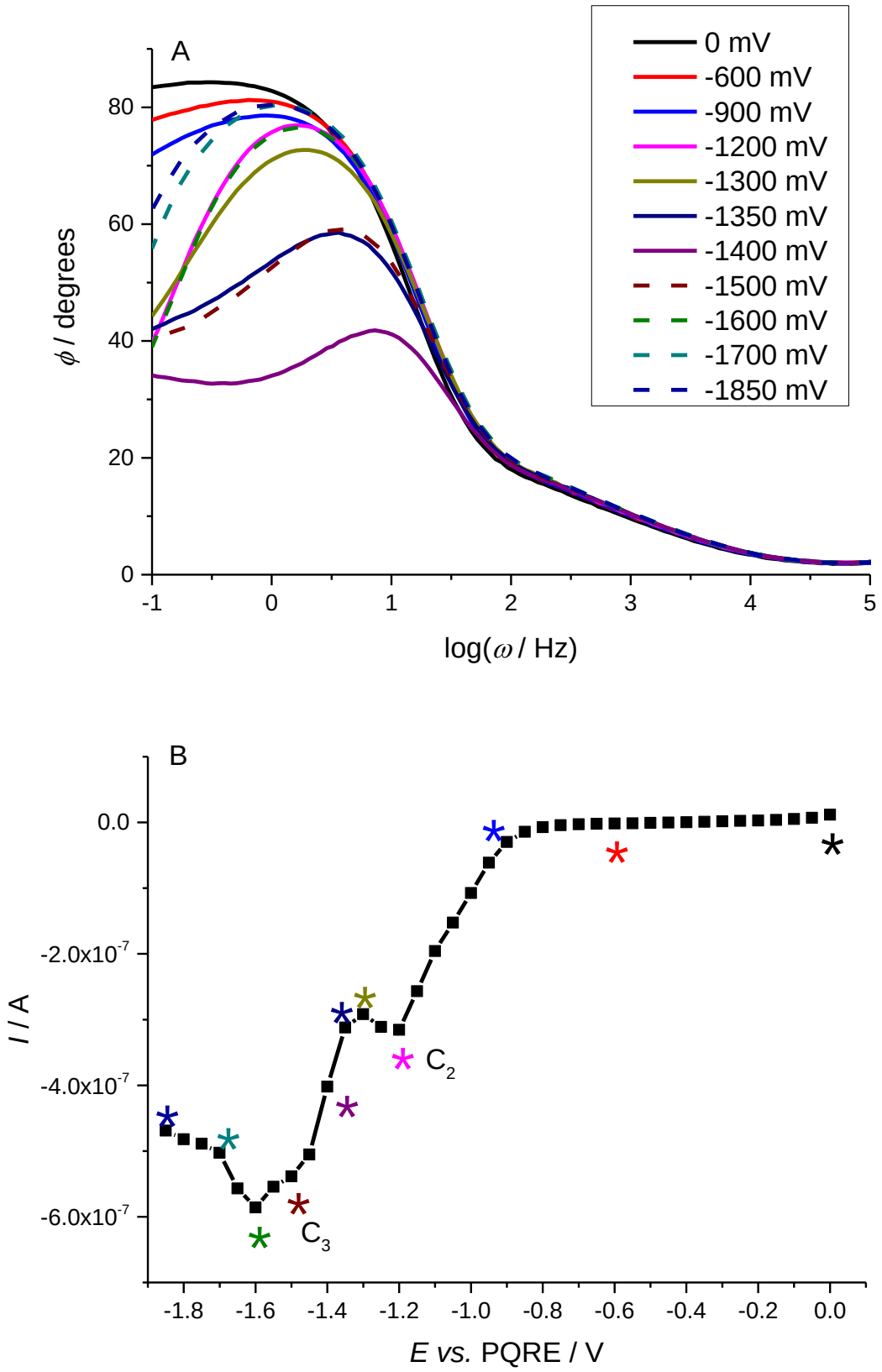

Figure 5-2 (A) Effect of EC potential on the impedance phase vs. the logarithm of frequency curve and (B) resting current at the potentials held during the EIS measurements. The asterisks highlight the potentials at which the impedance phases in (A) were obtained.

With the plateau of the current at -1.5 V, the camel hump in the phase curve begins to return to its original shape and magnitude, indicating the return towards fewer states, potentially signifying the end of the cation re-orientation process at the interface. Consequently, the two sharp increases in current between -0.9 V and -1.2 V and between -1.35 V and -1.45 V could correspond to the creation of multiple cation states as a result of packing of the compact double layer at the Au-BMP TFSI interface. Referring back to section 5.1.1, these two current waves match closely with waves C_2 and C_3 seen in the CV of figure 5-1 (B). They are also in agreement with the waves seen by Wen et al. in their CVs of Au(111) in BMP-based ILs, between -1 V and -1.4 V vs. PQRE and between -1.4 V and -1.6 V vs. PQRE.[2] As mentioned earlier, these authors have attributed the first wave to the transition to ordered cation orientations, with their rings and alkyl chains laid flat and parallel to the Au surface and the second wave to the change in cation conformation, so that the alkyl chains are facing away from the Au surface, in order to facilitate closer packing.

Finally, the largest negative current in figure 5-2 (B) appears at -1.6 V at which point the current begins to decrease. As the phase curves begin to return to their original shapes and magnitudes at earlier potentials after -1.4 V, this continued small increase in current could not be explained by the re-ordering of the cations. This small feature will be further explored in following sections of this chapter.

While the observations of the change in shape of the impedance phase curves with potential are qualitative, they provide further indication from the literature that there may be potential-dependent changes in cation orientation and/or conformation upon adsorption on the Au electrode surface. It is hoped that EC-SERS may assist in determining the nature of these changes.

As mentioned earlier, most existing studies use EIS to calculate or measure the differential capacitance in order to determine the PZC. Baldelli and Lockett et al. obtained camel-shaped capacitance-potential curves for their metal-IL interfaces.[8, 11] They attributed the PZC to the potential at the minimum in the differential capacitance, due to the expected relatively depleted concentration of ions at the electrode surface.[21] Forsman et al. have carried out density functional theory (DFT) calculations on ILs, taking into account adsorbing and non-adsorbing ion-electrode surface interactions.[22] For non-adsorbing cases, their calculations produced camel-shaped capacitance curves with a minimum at the PZC, similar to those seen in the publications by Baldelli and Lockett et al.. However, when IL adsorption was introduced to the model, this minimum in the capacitance curve was significantly reduced, to the point where it looked more like a wave than like a minimum. This type of capacitance-potential curve shape has also been found recently by Friedl et al., who carried out EIS measurements on BMP TFSI on a Au(111) electrode.[23]

An example of a Nyquist plot obtained at 0 V vs. PQRE is demonstrated in figure 5-3. Impedance data were obtained at various potentials and then fitted to an equivalent circuit. Lockett et al. have fitted their Nyquist impedance plots to an equivalent circuit consisting of a resistance in series with a CPE.[11] Figueiredo et al. fitted their Nyquist plots of deep eutectic solvents using the same circuit but with an added resistance in parallel to the CPE.[24] This was done in order to account for any slight curvature in their plots, which arose due to slow electron transfer reactions or adsorption steps. The same type of circuit was used to fit the Nyquist plots in this study and has been depicted in figure 5-3. It consists of a solution resistance, R_s and a CPE in parallel with an additional resistance, R. The fittings where only carried out over the frequency range 0.1-33 Hz, in order to obtain a good fit, with $\chi^2 \leq 10^{-3}$.

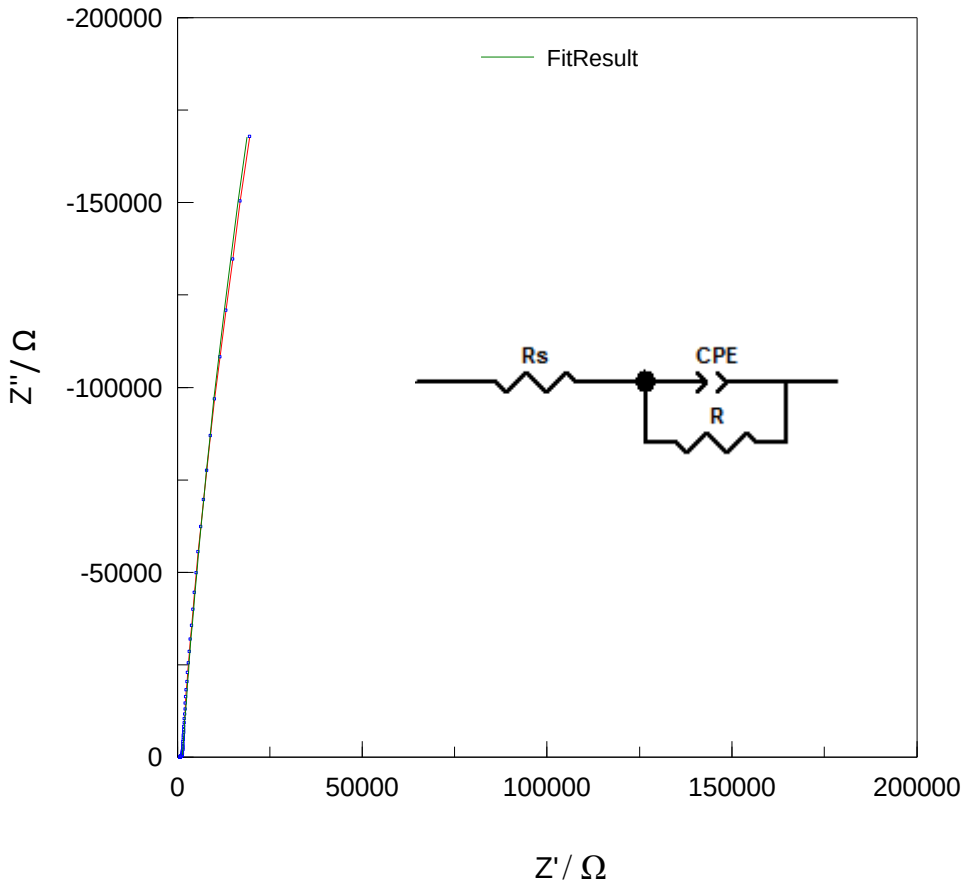

Figure 5-3 Nyquist plot for BMP TFSI on a Au SSV substrate at 0 V vs. PQRE with a 0.1 Hz – 200 kHz frequency range. The blue data points and red line correspond to the data obtained, while the green line corresponds to the impedance fitting with the depicted equivalent circuit.

The capacitance was calculated from the fitting results using the following equation[24, 25]:

$$C_d = \sigma^{\frac{1}{\alpha}} \left(\frac{1}{R_s} + \frac{1}{R} \right)^{\frac{\alpha-1}{\alpha}}$$

Equation 5-1

where α and σ are the applied components. The results from the calculations are presented in figure 5-4 (A) as a function of potential. Figure 5-4 (B) contains a CV of the same system before the EIS measurements took place, in order to establish an EC window for the measurements.

The shapes of the capacitance curves of figure 5-4 (A) vaguely resemble the camel shape obtained by Lockett et al., with a minimum around -0.85 V vs. PQRE and two humps at -0.95 V and between -0.2 V and -0.4 V vs. PQRE.[11] The capacitance decreases either side of the two humps. The minimum at -0.85 V vs. PQRE has tentatively been assigned to the PZC. As the potential is scanned away from the PZC the capacitance increases due to packing of counter-ions to oppose the charge at the Au surface. This is also in line with the increasing negative current at potentials negative of -0.9 V vs. PQRE seen earlier in figure 5-2 (B), which was attributed to the ordering of the cations in the flat configuration to counter the negative charge on the Au surface. Scanning the potential past the two camel humps causes the charge at the Au surface to increase. However, as the layer of counter-ions at the electrode surface cannot fully compensate for the excess charge, the double layer thickens with the addition of counter-ions, which causes the subsequent decrease in capacitance. This PZC assignment can only be tentative as the minimum in the capacitance curve was not as distinctive as in previous studies.

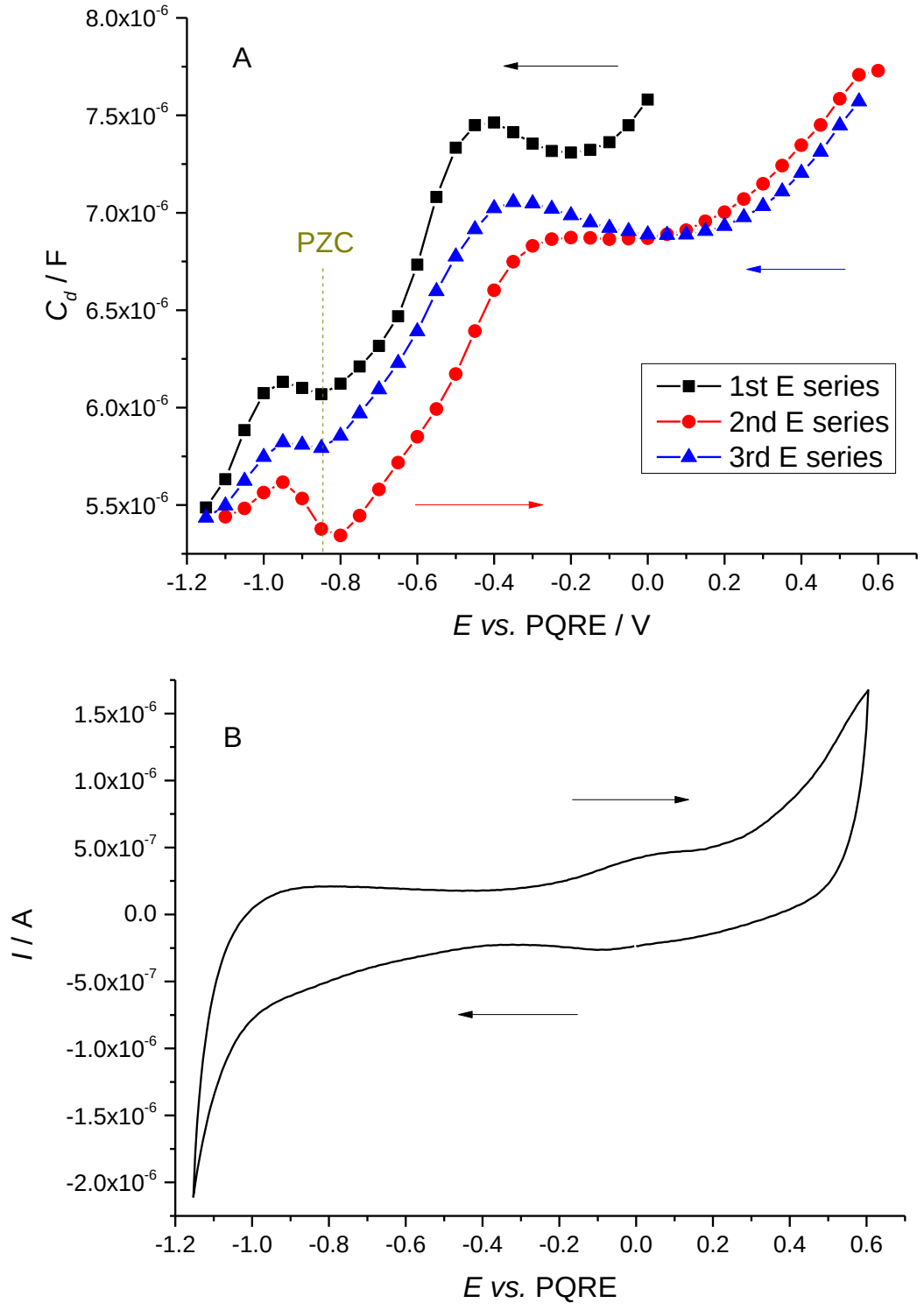

Figure 5-4 (A) Potential dependence of differential capacitance and (B) CV obtained before the EIS measurements at 10 mV s^{-1}, starting at 0 V vs. PQRE, for a Au SSV substrate in BMP TFSI. The arrows demonstrate the direction in which the potential was scanned.

Even though the camel shape is generally visible in the capacitance curves of figure 5-4 (A), there are features which complicate the shape of the curves and differentiate it from the curve found by Lockett et al. for BMP TFSI on Au.[11] The curves in figure 5-4 (A) are slanted which gives them a wave-like appearance and the capacitance minimum was not as pronounced as in the publication by Lockett et al.. Another unusual feature of the capacitance-potential curves was that the capacitance increased after the hump at positive potentials, in a way forming a second minimum between -0.2 V and -0.05 V vs. PQRE.

As mentioned earlier, Forsman et al. used calculations to predict the shape of the capacitance-potential curve with and without ion adsorption.[22] Their calculated capacitance curves are slanted in both cases, although they don't provide a direct explanation for this. Their capacitance curve with ion adsorption demonstrated a diminished capacitance minimum, giving it a wave-like appearance, similar to that seen in this study. Similarly shaped curves have also been found experimentally by Friedl et al..[23] This suggests ion adsorption may be taking place on the Au surface, which is very likely due to the tendency of ILs for specific adsorption. Lockett et al. have also discussed that potential-dependent ion re-arrangement may affect the capacitance-potential curve shape, especially when BMP and TFSI ions are used. This is in line with the potential-dependent BMP ion re-ordering discussed earlier on in this section, with respect to the potential-dependent shape of the impedance phase curves.

Observing the CV in figure 5-4 (B), the increasing negative current can be seen at potentials below -1 V vs. PQRE, similar to the current-potential plot of figure 5-2 (B), which as discussed earlier, corresponds to ordering of the cations at the Au surface. Furthermore, there are features at positive potentials which may indicate the formation of oxide, followed by what looks like a small oxide stripping peak at -0.1 V vs. PQRE.

As was seen in figure 5-1 (A) in the introduction of this chapter, the main Au oxide stripping peak appeared at approximately +1.3 V vs. PQRE. Hoogvliet and Bennekom have published CVs of Au thin-film electrodes containing a Cr adhesion layer in dilute aqueous $HClO_4$.[26] The Au oxide reduction peak in their publication appeared at +0.8 V vs. saturated calomel electrodes (SCE). Cr was also found to oxidise at potentials anodic of -0.1 V vs. SCE with the oxide being reduced at about -0.5 V vs. SCE. They gave the following mechanism for this process:

$$2Cr + 3H_2O \rightleftarrows Cr_2O_3 + 6H^+ + 6e^-$$

$$Cr_2O_3 + H_2O \rightleftarrows 2CrOOH$$

Comparing the Au oxide stripping peaks, Cr should oxidise at potentials higher than +0.4 V vs. PQRE and the oxide should be reduced at 0 V vs. PQRE in the CV of figure 5-4 (B). Indeed, at

potentials positive of +0.4 V vs. PQRE the current increases, indicating that the Cr adhesion layer of the SSV substrate may be being oxidised. Similarly, the broad oxide reduction peak appeared at about -0.1 V vs PQRE, which was within 100 mV of what was expected, indicating that the Cr oxide is being reduced. While the Cr is only a sub-layer of the Au SSV substrate, it is very likely that it may be oxidised, as the edges of the substrate will have Cr exposed to the electrolyte, as well as Cr which may have been exposed due to scratches or other imperfections in the Au layer.

Cation specific adsorption and Cr oxidation and reduction can contribute to the electrode charge. Specific adsorption induces partial charge transfer between the ions and the electrode due to the short range forces that dominate the interaction.[11] On the other hand, Cr oxide formation and reduction will have a direct effect on the electrode charge, as can be seen from the mechanism above. The basic thermodynamic definition of the capacitance is the dependence of the surface charge, q, on the electrode potential, φ:

$$C_d = \frac{\partial q}{\partial \varphi}$$

Equation 5-2

This means that any change in the electrode charge at a specific potential due to specific adsorption or rearrangement of the cations, or due to oxidation, will have a direct effect on the differential capacitance. Thus, the unexpected increased capacitance at positive potentials in figure 5-4 is attributed to the oxidation of the Cr in the Au SSV substrate. It is important to note that even though Cr oxidation has a direct effect on the EC results, this may not be picked up on through EC-SERS as these are surface-specific measurements which only focus on a very small area of the SSV substrate.

5.2 Surface Enhanced Raman Spectroscopy

Each EC-SERS spectrum was collected after holding each potential for 5 minutes and whilst continuing to hold the potential during the measurements. Spectra were obtained at potentials between 0 V and -2 V vs. PQRE, -2 V and +1 V vs. PQRE and +1 V and -2 V vs. PQRE, in what will from now on be referred to as first, second and third potential series. The current measured at the end of each EC-SERS spectrum acquisition has been plotted against the potential in figure 5-5 (A). CVs were also obtained of the same system after the EC-SERS experiments and these have been depicted in figure 5-5 (B).

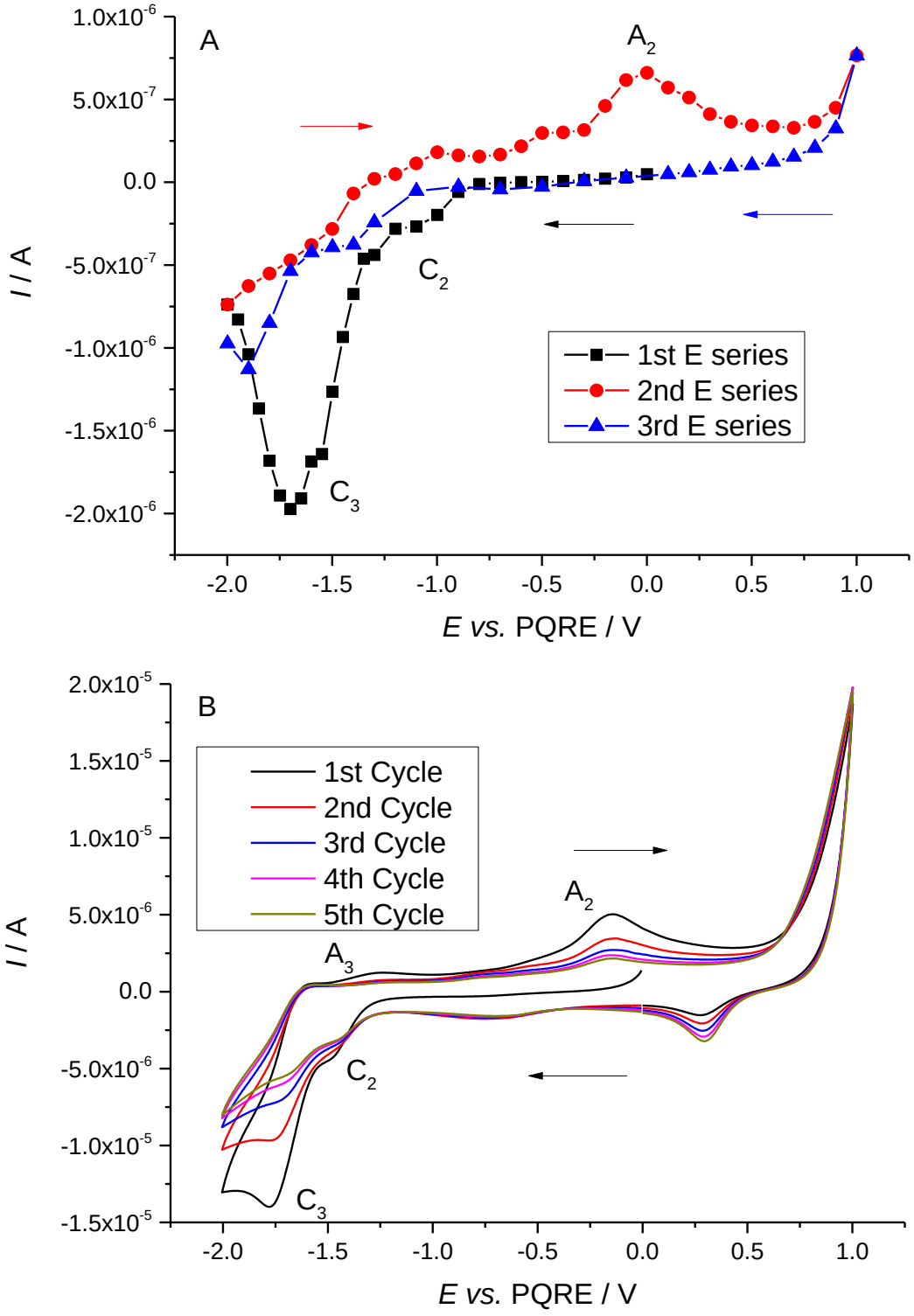

Figure 5-5 (A) Current vs. potential obtained during each EC-SERS spectrum acquisition of BMP TFSI on a Au SSV substrate. Each potential was held for 5 minutes before the spectrum acquisition and for approximately 140 s during the spectrum acquisition. The first potential series is in black (squares), the second in red (circles) and the third in blue (triangles). (B) CVs of the same system obtained after the EC-SERS experiment, obtained at 10 mV s^{-1}. The arrows indicate the direction in which the potential was scanned.

The shape of the current-potential plot for the first series in figure 5-5 (A) is generally the same as that obtained during the EIS measurements, depicted earlier on in figure 5-2 (B). The main broad peak C_3 appears here at -1.7 V vs. PQRE, whereas in figure 5-2 (B) it appeared at -1.6 V vs. PQRE. Any shift up to 0.1 V between the curves is attributed to the relative instability of the PQRE, which is sensitive to levels of oxide on the Pt or impurities, such as O_2 or H_2O, in the IL. The peak appears in the CVs of figure 5-5 (B) at about -1.8 V vs. PQRE, so at a slightly more negative potential.

The negative current begins to increase rapidly after about -0.9 V vs. PQRE, which is similar to what was seen for the EIS experiment data. This increase in current was earlier attributed to the ordering of the cations at the Au surface in a flat configuration at potentials negative to the PZC, earlier attributed to about -0.85 V vs. PQRE. Another difference between the two plots is that the small peak C_2 seen at -1.3 V vs. PQRE in the EIS data was not as pronounced in figure 5-5 (A). There are some small plateaus between -1 V and -1.4 V vs. PQRE in figure 5-5 (A) which probably correspond to the same peak. This peak separated the two increases in current in the EIS data and so was assumed to signify the change in cation ordering processes; from the cations ordering in a flat configuration on the Au surface, to their alkyl chains orienting away from the Au surface for closer packing. The reason for the lack of pronunciation is unknown at this point.

In the second potential series data, there is one distinct anodic peak, A_2, which as mentioned earlier has previously been paired with the C_2 cathodic peak.[1] It is interesting to note that this peak did not fully appear in the CV in figure 5-5 (B), potentially confirming the link between C_2 and A_2. In the third series data of figure 5-5 (A), the current is similar to the first E series data until -1 V vs. PQRE. Peaks C_2 and C_3 do not appear as pronounced and the negative current does not increase as much. This is also evident in the CVs, where the same peaks decrease in current with each cycle, especially C_3. In the CVs the onset of an oxidation process at positive potentials followed by two reductive peaks in the reverse scan, are much more pronounced than in the current-potential data. In the current-potential data, there are no evident oxide reduction processes. These redox peaks may be due to oxidation of Au or Cr, as discussed earlier.

In the following three sections, the EC-SERS spectra obtained alongside the current-potential data of figure 5-5 (A) have been studied and specific peaks have been analysed. The aim is to provide a better understanding of the processes discussed with respect to the EC data of the Au SSV substrate in BMP TFSI system.

5.2.1 Superoxide Ion and Gold Oxide Formation

General trends and broad features were difficult to detect when observing the raw SERS spectra obtained at different potentials. To overcome this issue, the first spectrum obtained at 0 V vs.

PQRE was subtracted from all subsequent spectra. The resulting subtracted spectra are displayed in figures 5-6, 5-9 and 5-12, for the first, second and third potential series, respectively.

Superoxide ions have been found to form through the reduction of oxygen at negative potentials through the following mechanism:[3, 4]

$O_2 + e^- \rightarrow O_2^-$

During the first potential series the formation of superoxide ions is evident from -1.6 V to -2 V vs. PQRE in figure 5-6, with the appearance of broad features assigned to *ν*(Au-O) at 476 cm^{-1} and 582 cm^{-1} and *ν*(O-O) at 1034 cm^{-1} and at 1075 cm^{-1}. The development of these features over the negative potential range is also visible in the raw spectra displayed in figure 5-7. Similar peaks were also reported by Peng et al., who found the *ν*(Au-O) peak at 491 cm^{-1} and the *ν*(O-O) peak at 1109 cm^{-1}.[4] Frith et al. found a peak at 1107 cm^{-1}, which they assigned to the superoxide ions, but they did not give a specific vibrational assignment.[5]

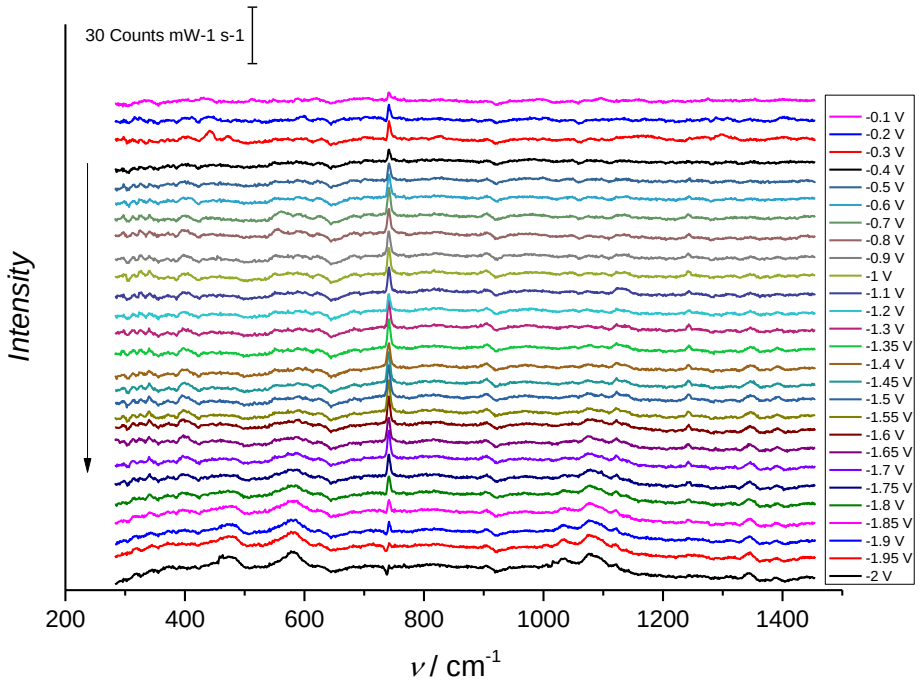

Figure 5-6 SERS spectra of BMP TFSI on a Au SSV substrate at various potentials in the 1st potential series, each subtracted by the first SERS spectrum obtained at 0 V vs. PQRE. Spectra were obtained using a 785 nm near-infrared (NIR) laser and a 50x objective. The spectra have been normalised by the laser power and exposure time and have been offset by 10 counts mW^{-1} s^{-1} from each other. The arrow indicates the direction in which the potential was scanned and the order in which the spectra were obtained.

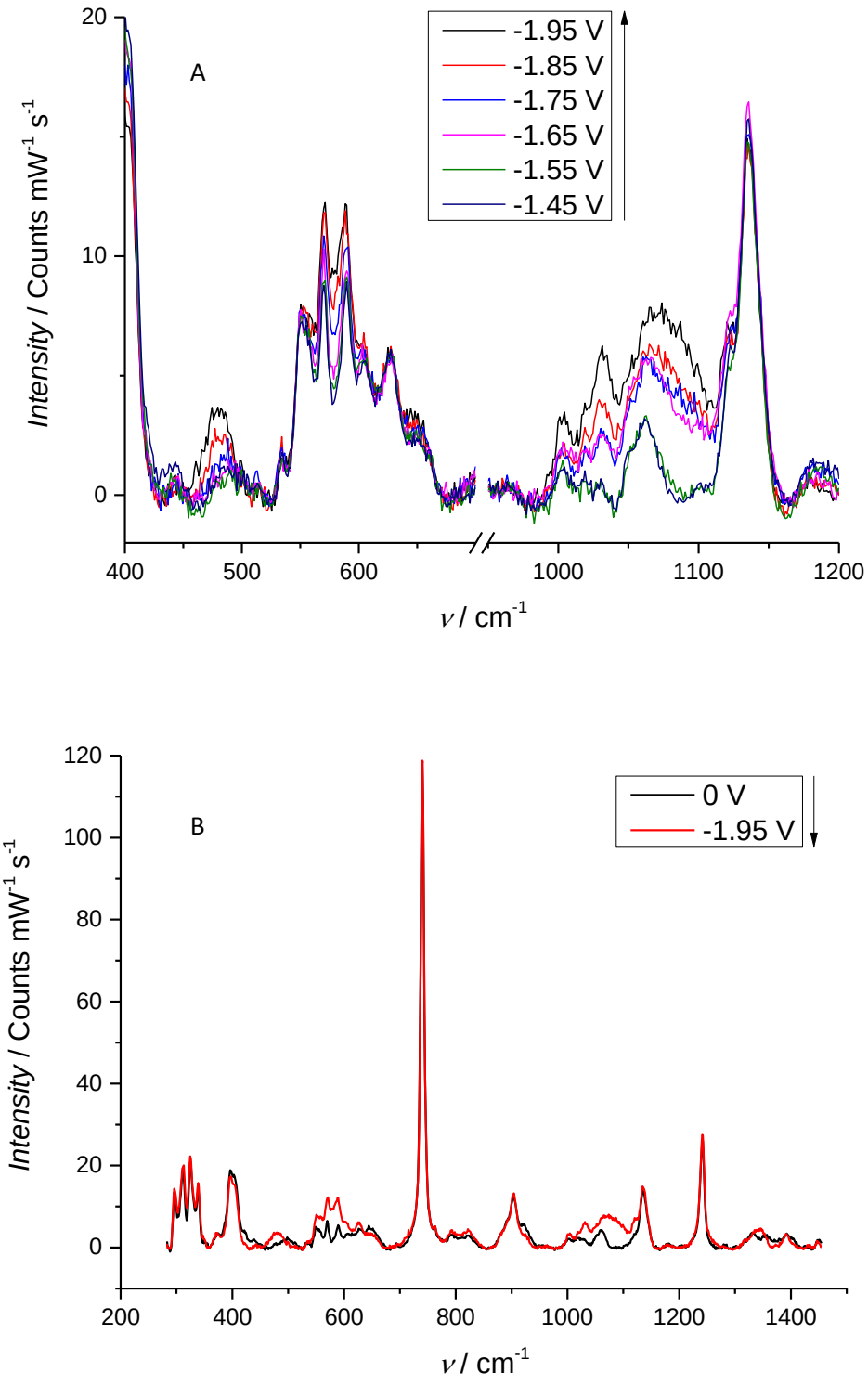

Figure 5-7 SERS spectra of BMP TFSI on a Au SSV substrate in the first potential series, (A) at negative potentials vs. PQRE, highlighting features resulting from superoxide ion formation and (B) at 0 V and at -1.95 V vs. PQRE. The arrows indicate the direction in which the potential was scanned and the order in which the spectra were obtained. The spectra were obtained using a 785 nm NIR laser and a 50x objective and have been normalised by the laser power and exposure time used. The backgrounds of all spectra have been removed for clarity.

Earlier on, in section 5.1 of this chapter, the re-ordering of the BMP cations on the electrode surface was estimated to occur between potentials -0.9 V and -1.45 V vs. PQRE, coinciding with an increase in the negative current in figure 5-2. After -1.45 V vs. PQRE the current increased further, reaching a maximum at -1.6 V vs. PQRE, signifying the presence of a different, unknown process. The BMP cation re-ordering process and this second unknown process both contributed to feature C_3 which consistently appeared in current-potential data. However, the two processes were separated by a slight plateau in the negative current, around -1.45 V vs. PQRE.

Observing the current-potential data of the first potential series in figure 5-8, the increase in the negative current due to BMP re-ordering appears between -0.9 V and -1.55 V vs. PQRE. This includes feature C_2, between -0.9 V and -1.3 V vs. PQRE. Between -1.35 V and -1.55 V vs. PQRE there is a steep negative current increase, labelled $C_{3,+}$, to indicate that this part of feature C_3 is attributed to BMP cation re-ordering. An additional negative current increase due to the unknown process mentioned above appears between -1.6 V and -1.7 V vs. PQRE. There is a small plateau in the current between -1.55 V and -1.6 V vs. PQRE. As observed in the spectra of figures 5-6 and 5-7, the formation of the superoxide ions begins to occur from -1.6 V vs. PQRE, coinciding with the second increase in the negative current after the plateau. Thus, this has been labelled $C_{3,S}$, to indicate that this part of feature C_3 is attributed to superoxide ion formation.

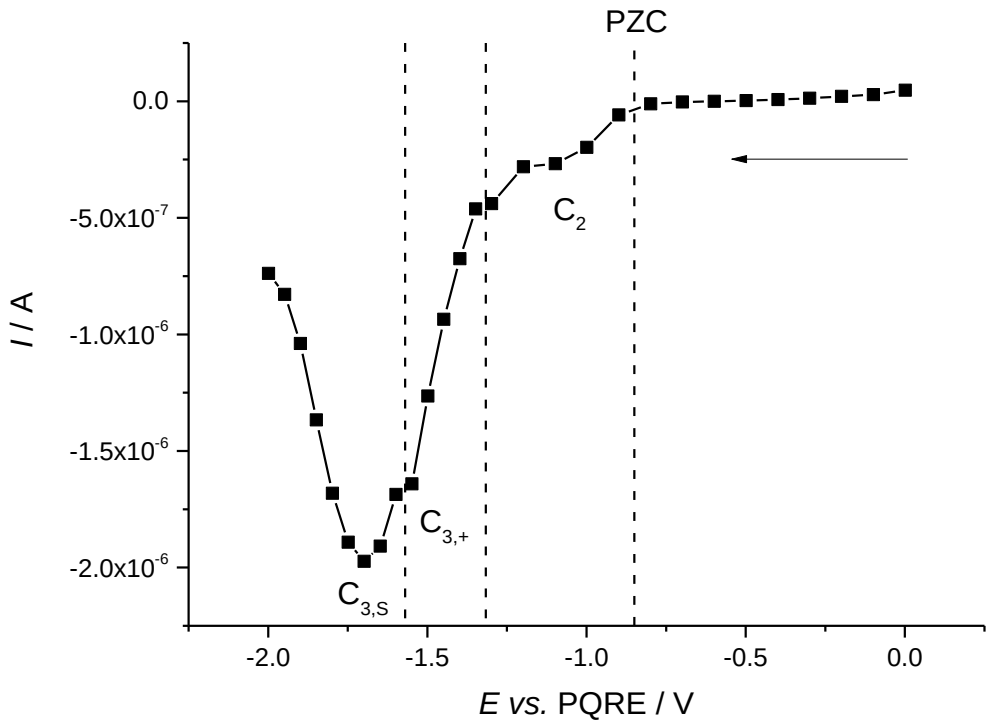

Figure 5-8 Current vs. potential obtained during each EC-SERS spectrum acquisition of the first potential series, of BMP TFSI on a Au SSV substrate. Each potential was held for 5 minutes before the spectrum acquisition and for approximately 140 s during the spectrum acquisition. The arrow indicates the direction in which the potential was scanned.

Peng et al. and Grande et al. attributed feature C_3 in their CVs to superoxide ion formation.[3, 4] This contradicts interpretations by Wen et al. and Atkin et al., who attributed similar features to ordering and dis-ordering of the BMP cations at the Au electrode surface.[1, 2] From the results discussed here and if oxygen is present, it is likely that feature C_3 is the result of the combination of both processes; $C_{3,+}$ corresponding to BMP cation ordering and $C_{3,S}$ to superoxide ion formation. Disagreement in the literature is likely due to the fact that distinguishing the two processes in CVs is difficult, due to the relatively fast scan rates used, usually 10 mV s^{-1}. This can be seen when comparing the CVs of figure 5-5 (B), where there was no visible plateau in the current, to the slow current-potential curves of figure 5-5 (A). The time-scales used when obtaining the EC-SERS data and current curves in figure 5-5 (A) are much longer than the CVs, with potentials every 0.05-0.1 V held for 5 minutes before the spectral acquisition and for a further ~2 minutes during the spectral acquisition. As a result, small changes in current between BMP cation re-arrangement processes and superoxide ion formation are resolved.

The spectra obtained during the second potential series were also subtracted by the first 0 V vs. PQRE spectrum and they are presented in figure 5-9. The superoxide ion features are initially visible but decrease in intensity until around -1.4 V vs. PQRE, after which point they are hardly visible. The disappearance of these features is also visible in figure 5-10 (B) by comparing the raw spectra obtained at -1.9 V and at 0 V vs. PQRE. The disappearance of the superoxide ion features coincides with a distinct increase in the current, forming a small feature A_3 in the current-potential data if figure 5-11.

At positive potentials, from +0.7 V upwards, a broad feature appears in figure 5-9 with a centre at 577 cm^{-1}. The development of this feature is also visible in the raw spectra of figure 5-10. Comparison the literature suggests that this peak may be assigned to the *ν*(Au-O) vibration of the Au surface oxide, which forms from water.[27] This also coincides with an increase in current from +0.7 V to +1 V vs. PQRE in figure 5-11, as expected when Au is oxidised. The water content of the BMP TFSI IL has been measured by KF titration to be 109.3 ppm. Au oxidation caused through these small amounts of water in the IL, along with any additional amount left after drying the cell and electrodes, is thus clearly detectable through SERS.

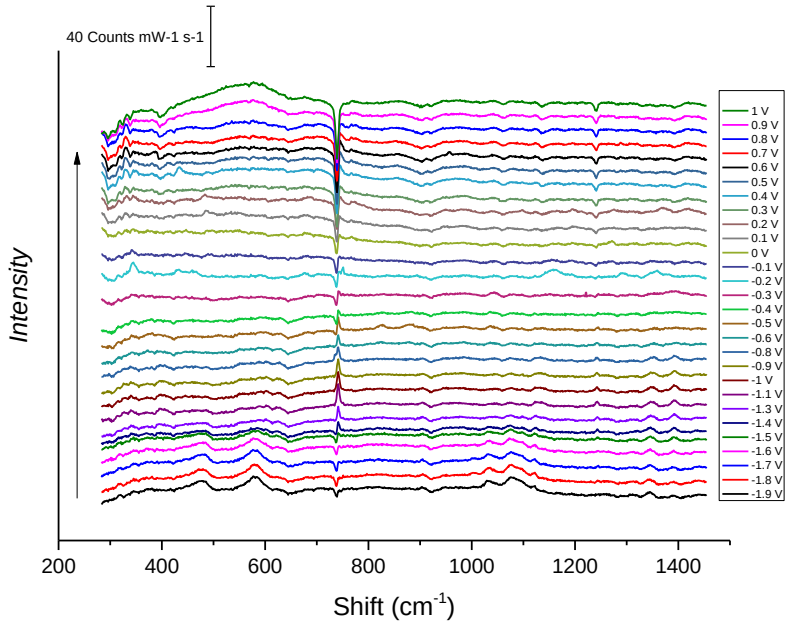

Figure 5-9 SERS spectra of BMP TFSI on a Au SSV substrate at various potentials in the second potential series, each subtracted by the first SERS spectrum obtained at 0 V vs. PQRE. The spectra were obtained using a 785 nm NIR laser and a 50x objective. The spectra have been normalised by the laser power and exposure time used and have been offset by 20 counts mW^{-1} s^{-1} from each other. The arrow indicates the direction in which the potential was scanned and the order in which the spectra were obtained.

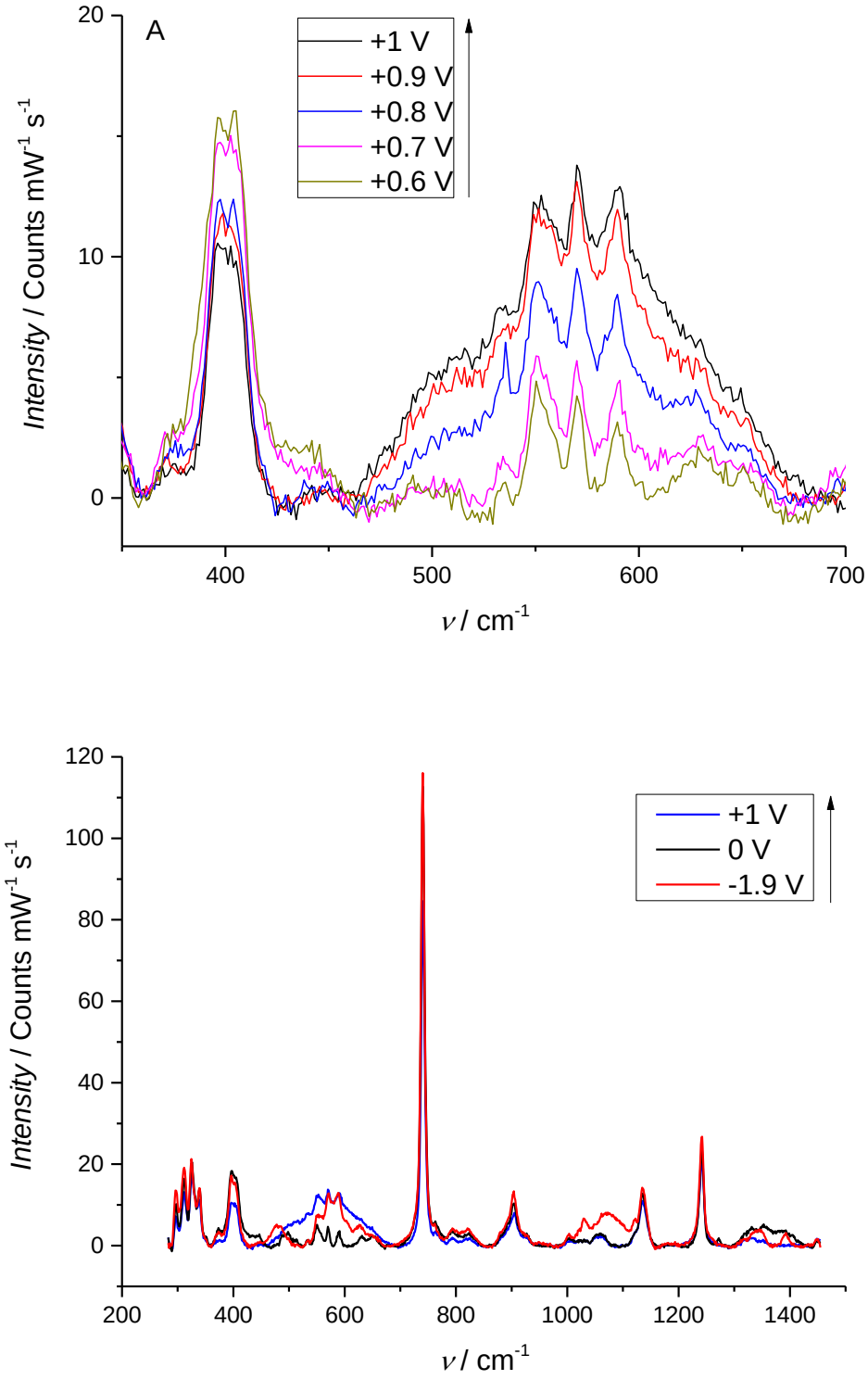

Figure 5-10 SERS spectra of BMP TFSI on a Au SSV substrate in the second potential series, (A) at positive potentials vs. PQRE, highlighting features resulting from Au oxide formation and (B) at -1.9 V, 0 V and +1 V vs. PQRE. The arrows indicate the direction in which the potential was scanned and the order in which the spectra were obtained. The spectra were obtained using a 785 nm NIR laser and a 50x objective and have been normalised by the laser power and exposure time used. The backgrounds of all spectra have been removed for clarity.

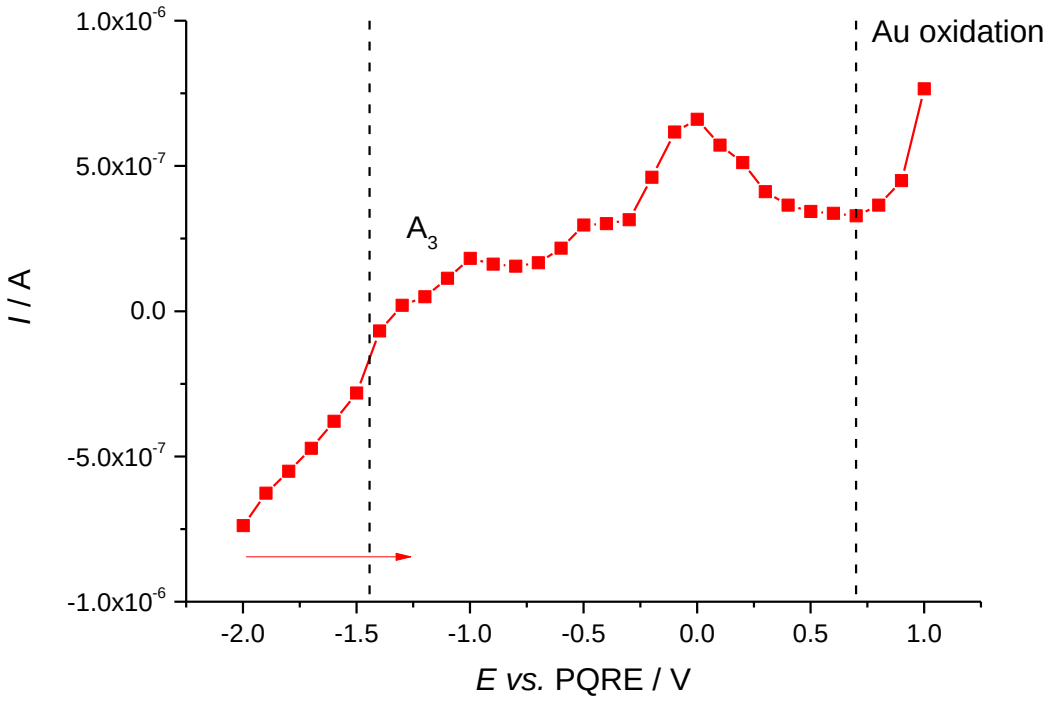

Figure 5-11 Current vs. potential obtained during each EC-SERS spectrum acquisition of the second potential series, of BMP TFSI on a Au SSV substrate. Each potential was held for 5 minutes before the spectrum acquisition and for approximately 140 s during the spectrum acquisition. The arrow indicates the direction in which the potential was scanned.

Finally, the spectra obtained during the third potential series, subtracted by the same 0 V vs. PQRE spectrum have been presented in figure 5-12. The broad Au oxide feature at 577 cm^{-1} gradually becomes smaller with decreasing the potential, which is accompanied by a decrease in the current, as can be seen in figure 5-13. However, due to the very small amount of Au oxide formed, a Au oxide reduction peak in the current is not visible.

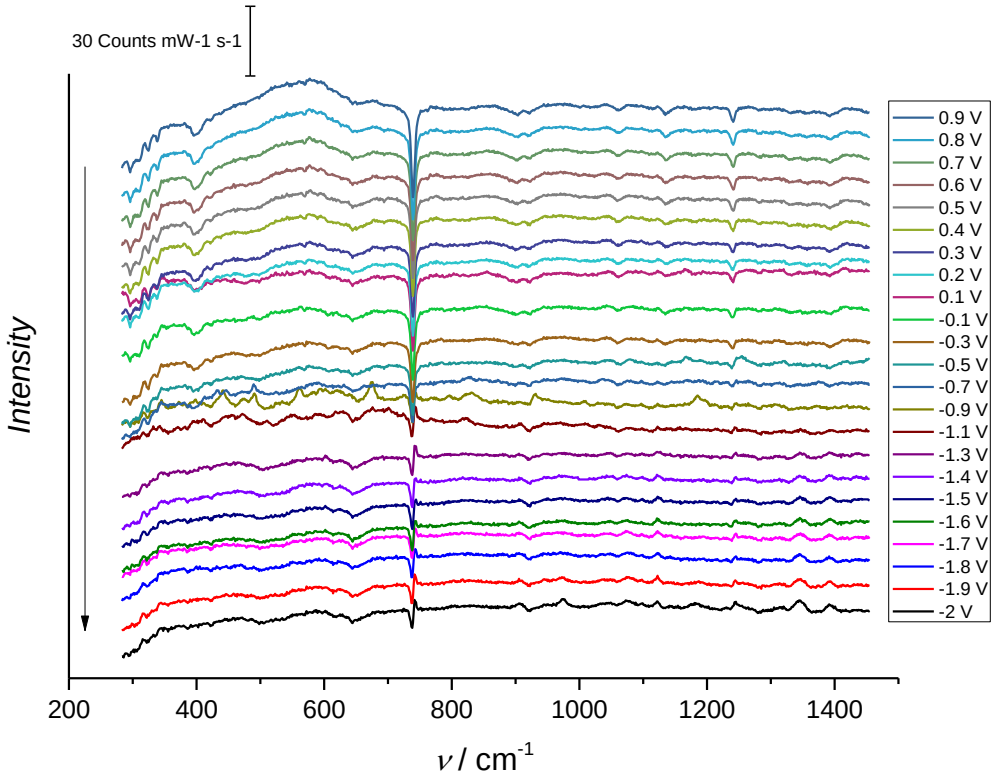

Figure 5-12 SERS spectra of BMP TFSI on a Au SSV substrate at various potentials in the third potential series, each subtracted by the first SERS spectrum obtained at 0 V vs. PQRE. The spectra were obtained using a 785 nm NIR laser and a 50x objective. The spectra have been normalised by the laser power and exposure time used and have been offset by 10 counts mW^{-1} s^{-1} from each other. The arrow indicates the direction in which the potential was scanned and the order in which the spectra were obtained.

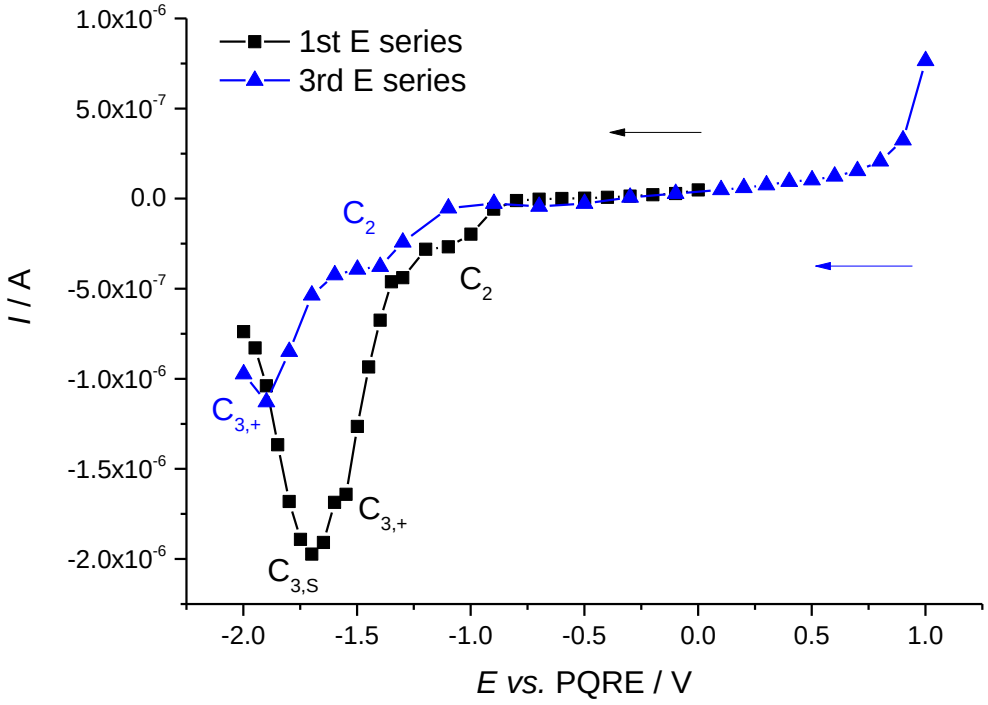

Figure 5-13 Current vs. potential obtained during each EC-SERS spectrum acquisition of the first (black) and third (blue)potential series, of BMP TFSI on a Au SSV substrate. Each potential was held for 5 minutes before the spectrum acquisition and for approximately 140 s during the spectrum acquisition. The arrows indicate the direction in which the potential was scanned.

As discussed earlier, when the potential is scanned negatively past -1.6 V vs. PQRE, superoxide ion formation is evident in the spectra with the appearance of broad features at 476 cm^{-1}, 582 cm^{-1}, 1034 cm^{-1} and 1075 cm^{-1}. However, these features do not appear in the spectra of figure 5-12, when the same potentials were reached. The lack of superoxide ion features in the spectra of the third potential series compared to the first series is highlighted in the comparison of the raw spectra at -1.9 V vs. PQRE in figure 5-14. This indicated that superoxide ion formation did not occur in the third potential series, at least not to the same extent as in the first potential series.

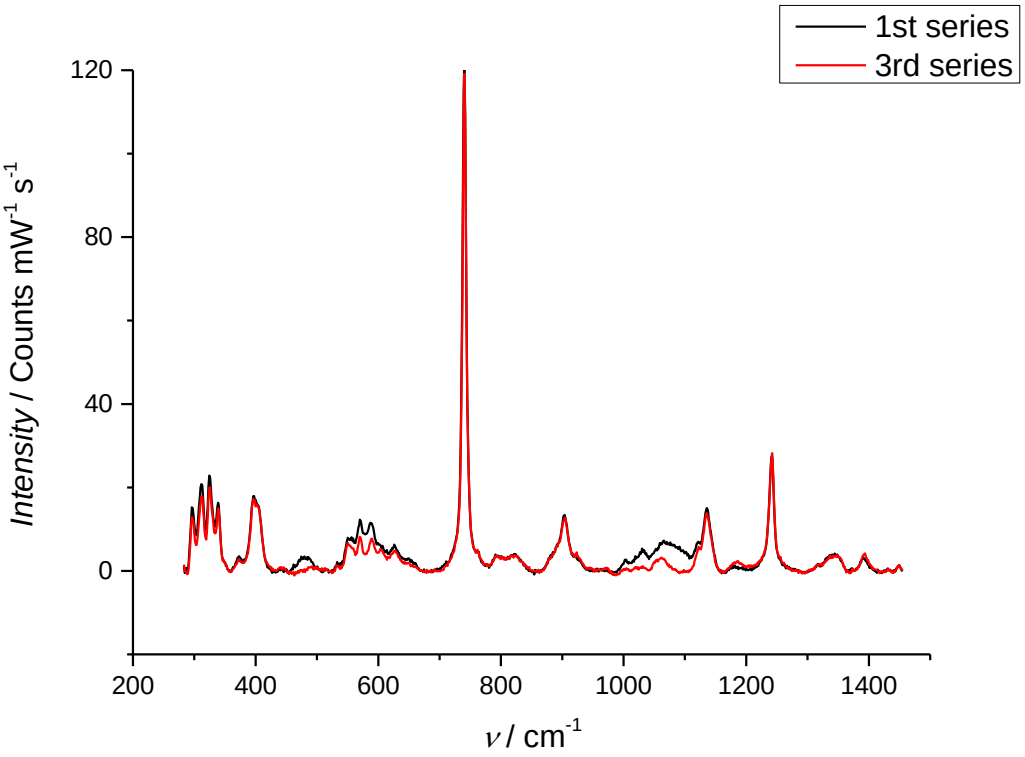

Figure 5-14 SERS spectra of BMP TFSI on a Au SSV substrate at -1.9 V vs. PQRE, highlighting the lack of features resulting from superoxide ion formation during the third (red) potential series, compared to the first (black). The spectra were obtained using a 785 nm NIR laser and a 50x objective and have been normalised by the laser power and exposure time used. The backgrounds of the spectra have been removed for clarity.

The lack of superoxide ion formation is also evident in the current-potential data of figure 5-13. The current in feature C_3 does not decrease as much in the third series when compared to the first. It is important to note that features C_2 and C_3 in the third potential series appear at more negative potentials by approximately 0.35 V compared to the first potential series. This may be due to the electrode oxidation and reduction leading to a delay in the system reaching its PZC, as discussed in section 5.1. When features C_2 of the first and third potential series are aligned, the peak in the current of the third series aligned with the small plateau in the current of the first series, separating features $C_{3,+}$ and $C_{3,S}$. As a result, the peak in the current of the third potential series at -1.9 V vs. PQRE is assigned to $C_{3,+}$ and the re-organisation of the BMP cations on the Au surface. $C_{3,S}$ corresponding to superoxide ion formation does not appear in the third potential series, which results from the consumption of trace oxygen in the system during the previous series.

From this discussion it is evident that SERS is a useful tool in probing the electrochemical formation of oxides and reduction of oxygen at Au surfaces, even when water and oxygen are only present in very small amounts. These processes have a significant effect on the charge and potential-dependent behaviour of the ions at the Au-IL interface, as will be discussed later in the remainder of this chapter.

5.2.2 Cation and Anion Peaks as a Function of Potential

In order to study the relationship between the cations and anions at the interface, the most intense cation peak at 905 cm^{-1} and the most intense anion peak at 740 cm^{-1} have been examined. The peak at 905 cm^{-1} corresponds to a mixture of $\nu_{ip}(NC_{(7)})$, ip ring breathing and $\delta(C_{(9)}C_{(10)}H_3)$ vibrational modes of both the eq-BMP and ax-BMP conformers. The 740 cm^{-1} peak corresponds to the whole anion breathing mode of both the cis-TFSI and trans-TFSI conformers. The intensities of these peaks were measured and their ratio was plotted against potential in figure 5-15. The potentials were changed from 0 V to -2 V vs. PQRE, then to +1 V vs. PQRE and finally back down to -2 V vs. PQRE, in the first, second and third potential series.

The general trend observed in figure 5-15 is that the ratio generally increases towards negative potentials and decreases towards positive potentials, in line with what one would expect, as more cations accumulate at negative charged surfaces and more anions at positively charged surfaces. The PZC had been estimated to be about -0.85 V vs. PQRE, based on the EIS and CV data. When the potential is positive to the PZC, one would expect an increase in anions, so the I_{905}/I_{740} ratio should decrease. At potentials negative to the PZC, one would expect an increase in cations, so the I_{905}/I_{740} ratio should increase.

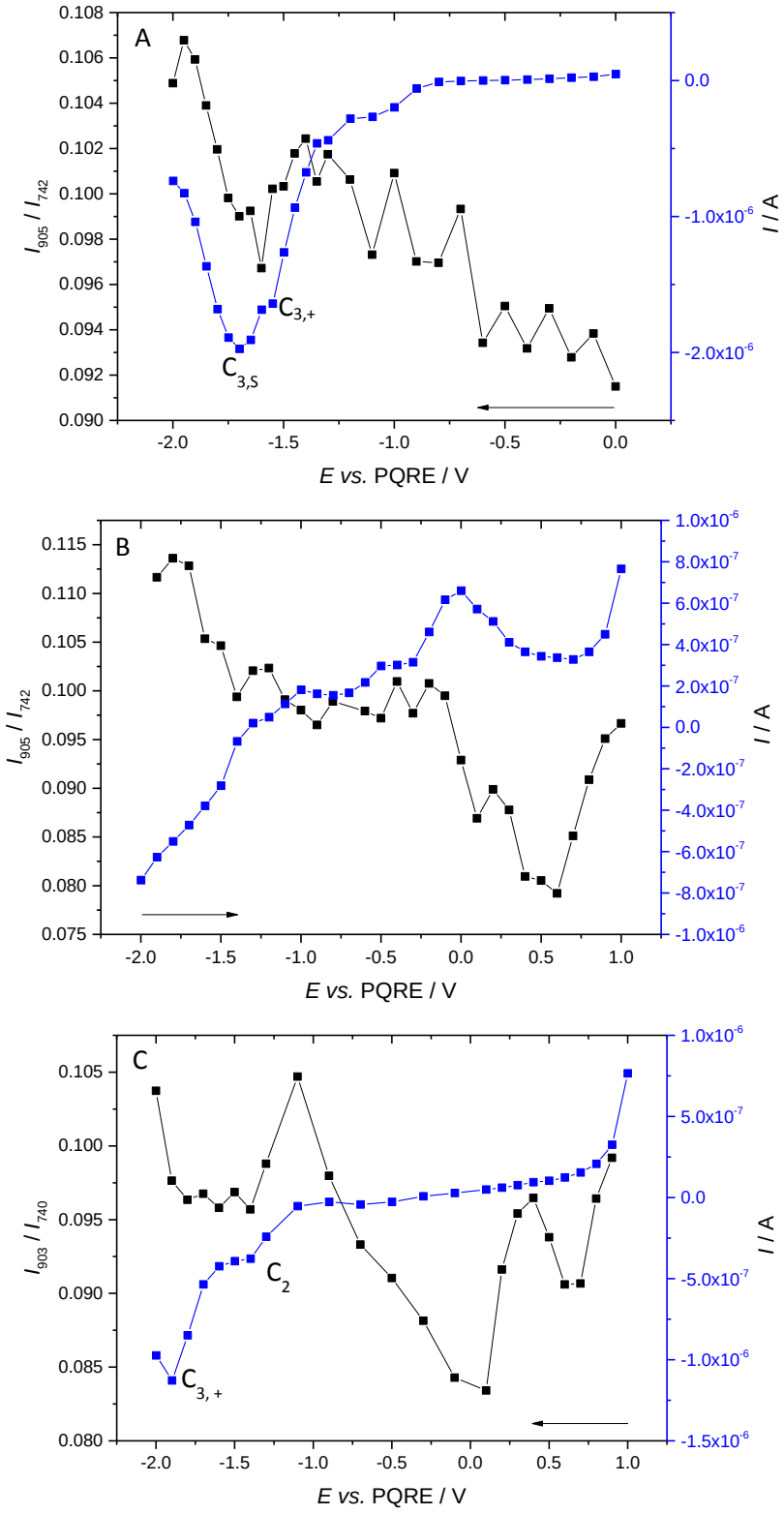

Figure 5-15 Intensity ratios of a BMP peak (905 cm^{-1}) over a TFSI peak (740 cm^{-1}) at different potentials (black). The current recorded at each potential during the EC-SERS measurements has also been plotted (blue). (A), (B) and (C) correspond to the first, second and third potential series of the experiment. The arrows indicate the direction in which the potential was changed.

In the first potential series, from 0 V vs. PQRE and scanning the potential negatively, the I_{905}/I_{740} ratio increases consistently, past the PZC at -0.85 V vs. PQRE, until -1.4 V vs. PQRE. Around the PZC, the ratio of the cation peak intensity over the anion peak intensity is approximately 0.097. At potentials negative to -1.4 V vs. PQRE the ratio decreases until -1.7 V vs. PQRE, towards the PZC value of 0.097. This indicates that between these potentials, the amount of cations is decreasing, or the amount of anions is increasing, or both. This potential range coincides with the rapid negative current increase of $C_{3,+}$, which was previously attributed to cation re-ordering when the alkyl chains oriented away from the Au surface, to facilitate tighter cation packing. If the BMP cations are specifically adsorbing on the Au electrode surface, there may be a decrease in the negative charge at the interface, leading towards a second PZC. This may have resulted in the decrease in the BMP cations required to counter the negative charge and thus the decrease in the I_{905}/I_{740} ratio occurring between -1.4 V and -1.7 V vs. PQRE.

The current decrease stops after -1.7 V vs. PQRE, as the I_{905}/I_{740} ratio rapidly increases again with scanning the potential negatively. This is likely due to further increase in the cation population at the interface with further negative charging and negatively charged superoxide ion formation.

In the second potential series, from -2 V vs. PQRE and scanning the potential positively, the I_{905}/I_{740} ratio decreases consistently, until -0.9 V vs. PQRE, close to the estimated PZC at -0.85 V vs. PQRE. At this point the ratio enters a plateau with values close to 0.097, corresponding to the PZC, until -0.2 V vs. PQRE, indicating there are no significant changes in the relative numbers of cations and anions at the interface in this potential region. From -0.1 V until +0.6 V vs. PQRE, the ratio decreases again, due to the increase in anions at the interface with the positive charging at the interface. From +0.7 V to + 1 V vs. PQRE, the ratio increases, which coincides with the increasing current and appearance of the broad feature in the spectra around 580 cm^{-1}, attributed to Au oxide formation in section 5.2.1. Au oxide begins to form from +0.7 V vs. PQRE upwards, resulting in a decrease in the positive charge on the Au surface. As a result, fewer TFSI anions are required to counter the positive charge and so the I_{905}/I_{740} ratio increased.

In the third potential series, from +1 V vs. PQRE and scanning the potential negatively, the I_{905}/I_{740} ratio decreases until +0.1 V vs. PQRE. This coincides with Au oxide reduction which causes an increase in the positive charge on the Au and thus an increase in the anions required to counter the charge, resulting in the decrease of the I_{905}/I_{740} ratio. However, there is an increase in the ratio at +0.5V and +0.4 V vs. PQRE before it decreases again, which may have been due to a temporary decrease in the positive charge on the electrode leading to the decrease in TFSI anions. Any remaining Au oxide is then reduced until +0.1 V vs. PQRE, with the positive charge on the Au being

reduced, past the PZC near -0.9 V vs. PQRE. Fewer anions and then more cations accumulate at the Au surface, hence the I_{905}/I_{740} ratio increases until -1.1 V vs. PQRE.

After -1.1 V vs. PQRE, the ordering of the cations begins, corresponding to the current decreasing in feature C_2. The I_{905}/I_{740} ratio then remains constant until -1.8 V vs. PQRE, at approximately 0.097, which was the value found at the PZC in the first potential series. This suggests that ordering of the BMP cations between -1.1 V and -1.4 V vs. PQRE leads to specific adsorption on the Au, increasing the charge to a value close to PZC. Lastly, with further negative charging of the electrode, the cations need to counter the charge increased, resulting in the increase of the I_{905}/I_{740} ratio until -2 V vs. PQRE.

To conclude, the relationship between cations and anions at the Au – BMP TFSI interface, during the first, second and third potential series has been discussed. The PZC, specific adsorption, superoxide ion and Au oxide ion formation have all been taken into account in the assessment of the SERS peak intensities, with the help of current and EIS results obtained previously. While EC-SERS cannot provide a picture for how the isolated cations and anions are behaving with changing the electrochemical potential, it can provide some idea of how the relative number of cations and anions is changing. However, at this point it is important to remember that bulk IL effects may still have an effect on the data, even though the ratio of peak intensities has been studied.

5.2.3 Cation Orientation and Conformation

SERS has been successfully used in the literature to probe the orientation of molecules close to a substrate surface, including IL cations.[28-33] This has been possible due to SERS surface selection rules which state that when a vibration occurs along the surface normal, its Raman signal is more enhanced than that of a vibration parallel to the substrate surface.

As discussed in the introduction of this chapter, Wen et al. have suggested that at negative potentials the BMP cations arrange themselves with the pyrrolidinium ring lying flat on the Au surface in order to counter the negative electrode charge.[2] By studying ip and oop vibrations of the pyrrolidinium ring, such a change in orientation should be evident, with the Raman signal of any oop vibrations being enhanced more than any ip vibrations when the ring is lying flat on the Au surface.

Diagrams of vibrations which are out of plane (oop) and in plane (ip) with the pyrroldinium ring of BMP, obtained from DFT calculations, are presented in figures 5-16 (A) and (B), respectively. The ratio of the peak intensities of the oop peak at 825 cm^{-1} and the ip peak at 1007 cm^{-1} has been plotted against potential in figure 5-17 for the first, second and third potential series. When the

ratio increases, it is an indication of more cations rings lying flat on the Au electrode surface, while when the ratio decreases it should be an indication of the cations being randomly oriented.

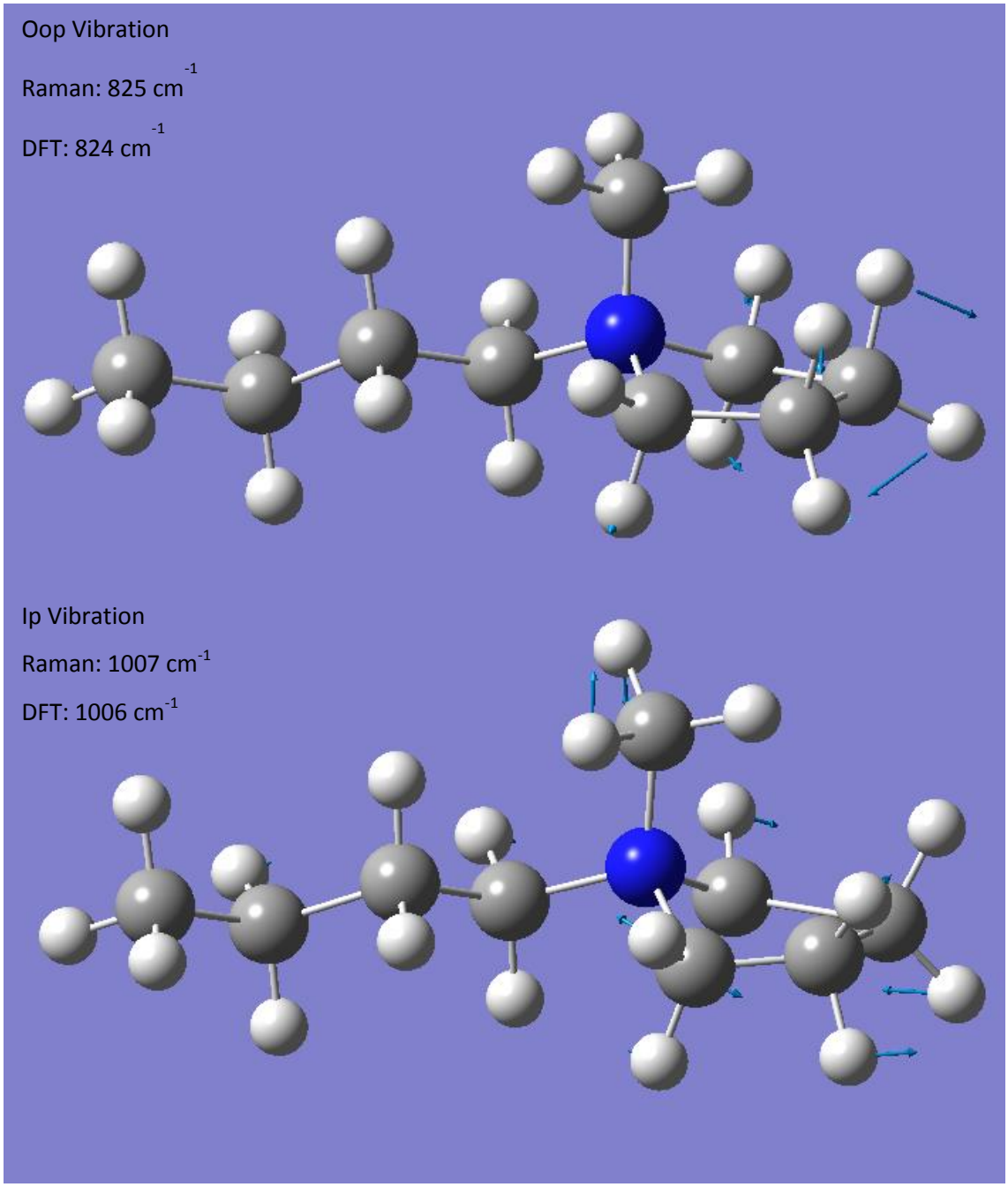

Figure 5-16 Diagram of (A) an oop and (B) an ip vibration of the eq-BMP cation, calculated using the B3LYP/6-311+G(d,p) levels of DFT. The arrows indicate the displacement of atoms during the vibration. The DFT-calculated and experimentally obtained Raman frequencies of each vibration have also been included.

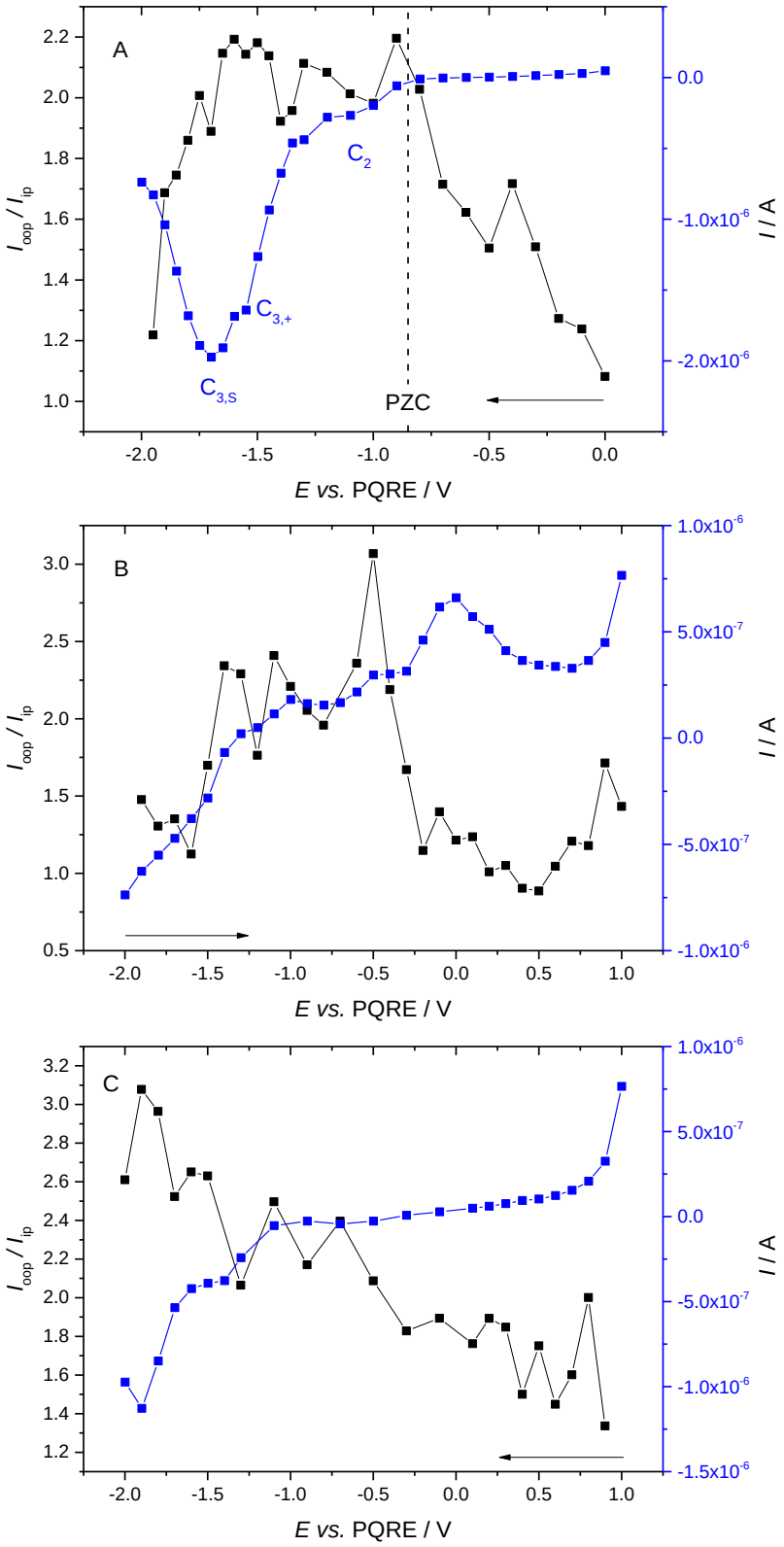

Figure 5-17 Ratio of the 825 cm^{-1} peak intensity corresponding to an oop vibration over the 1007 cm^{-1} peak intensity corresponding to an ip vibration (black) and current (blue) at various potentials during the (A) first, (B) second and (C) third potential series. The arrows indicate the direction in which the potential was changed.

In the first potential series, the I_{oop}/I_{ip} ratio increases with the potential change from 0 V to -1.3 V vs. PQRE, indicating that more cations are orienting flat on the electrode surface. This is in line with negative charging of the electrode surface and the previous interpretation of feature C_2 in the current-potential data. From -1.3 V until -1.65 V vs. PQRE the ratio remains almost constant, indicating that not much change was occurring in the ring orientation. -1.3 V vs. PQRE was the potential at which the $C_{3,+}$ feature begins to formulate in the current-potential data. This corresponds to re-ordering of the BMP cations on the Au surface with the alkyl chains orienting away from the electrode surface. However, in this orientation the pyrrolidinium rings of the BMP cations still remain flat on the Au surface, which indeed did not seem to affect the I_{oop}/I_{ip} ratio.

Below -1.65 V vs. PQRE, when feature $C_{3,S}$ assigned to the superoxide ion formation develops, the ratio decreased continuously until -2 V vs. PQRE, indicating that there were fewer cations lying flat on the electrode surface. This is to be expected as the cations would be displaced by the oxygen and superoxide ions formed, resulting in the BMP cation pyrrolidinium rings orienting randomly at the interface.

In the second potential series, after -1.6 V vs. PQRE the I_{oop}/I_{ip} ratio increases again towards -0.5 V vs. PQRE, after which it decreases until +0.5 V vs. PQRE. As the potential is scanned positively towards the PZC and upon removal of the superoxide ions, the cations are able to orient with their pyrrolidinium rings flat on the electrode surface. After the PZC is passed, more anions accumulate at the surface, so the BMP cations once again return to random orientations. From +0.6 V to +1 V vs. PQRE, the I_{oop}/I_{ip} ratio increases again, indicating there are more cations orienting with their rings flat on the Au surface. This is occurring in the potential region where Au oxidation is found and which, as discussed in section 5.2.2, is accompanied by an increase in the ratio of cations over anions. However, the increase in the orientation ratio cannot be explained by Au oxidation.

Finally, in the third potential series, the I_{oop}/I_{ip} ratio has a general increasing trend with decreasing the potential from +1 V to -2 V vs. PQRE, with no other discernible, potential-dependent features.

The discussion above highlights the difficulty of using this type of data for analysis of orientation changes of pyrrolidinium rings and more generally, of processes occurring at a single layer of ions at the Au surface. The main issue is that there aren't clear oop and ip vibrational modes in the pyrrolidinium ring, as can be seen in figure 5-16. Furthermore, as mentioned in chapter 4, there is partially enhanced Raman signal originating within 100 nm of the substrate surface. Even by using the ratio of intensities of oop and ip peaks, bulk effects may still be present in the data.

An attempt was also made to use the ratio of intensities of peaks specific to each of the eq-BMP and ax-BMP conformations, seen in figure 5-18, to detect any potential-dependent conformation changes which may be occurring. Feature $C_{3,+}$ in the current-potential data has been assigned by Wen et al. to the BMP cations ordering with the alkyl chains oriented away from the Au surface, to facilitate tighter cation packing.[2] This can only occur with either a change in conformation from eq-BMP to ax-BMP, or with more of the ax-BMP conformers already present in the liquid accumulating at the surface. Either way, the ratio of intensity of a peak corresponding to the ax-BMP conformer over the intensity of a peak corresponding to the eq-BMP conformer, should increase if the alkyl changes were oriented away from the electrode surface.

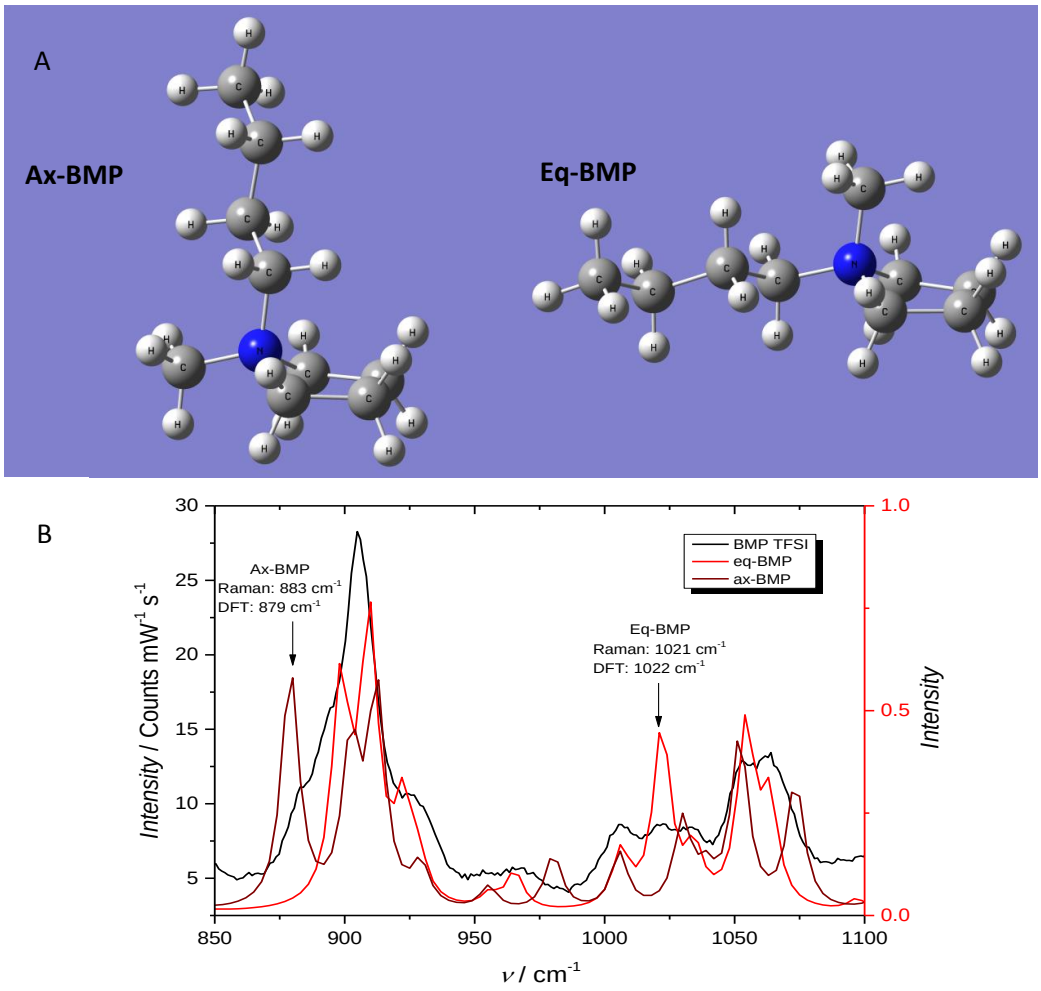

Figure 5-18 (A) DFT-optimised geometries of the ax-BMP and eq-BMP conformers. (B) DFT-calculated Raman spectra of the optimised eq-BMP and ax-BMP conformers (red) and an experimentally obtained Raman spectrum of BMP TFSI (black). DFT calculations were carried out on the basis of the B3LYP/6-311+G(d,p) levels of theory. The Raman spectrum was obtained using a 785 nm NIR laser and a 50x objective and has been normalised by the laser power and exposure time used. The peaks for which the intensities will be studied have been highlighted in (B).

In figure 5-18 (B), the experimentally obtained Raman spectrum of BMP TFSI has been compared to the DFT-calculated Raman spectra of the ax-BMP and eq-BMP conformers, shown in figure 5-18 (A). Two peaks which stand out for each of the conformers are the 883 cm^{-1} peak, corresponding to the $\nu(NC_{(7)})$ + ip ring breathing vibrations of the ax-BMP conformer and the 1021 cm^{-1} peak, corresponding to the $\nu_a(C_{(7)}NC_{(6)})$ of the eq-BMP conformer. The potential-dependence of the ratio of the intensity of the ax-BMP peak over the eq-BMP peak has been presented in figure 5-19, alongside the current-potential data obtained during the SERS spectrum acquisitions.

In the first potential series, the I_{ax}/I_{eq} ratio does not change much at potentials near the PZC, between -0.5 V and -1.35 V vs. Between potentials -1.35 V and -1.6 V vs. PQRE, coinciding with feature $C_{3,+}$ in the current-potential data, corresponding to the orientation of the BMP alkyl chains away from the Au surface, predicted by Wen et al.. From -1.65 V to -2 V vs. PQRE the ratio decreases, most likely due to superoxide ion formation predicted for feature $C_{3,S}$ in the current-potential data.

In the second potential series, the general trend in the I_{ax}/I_{eq} ratio data is it increasing with changing the potential negatively until -0.5 V vs. PQRE, possibly due to the removal of superoxide ions and then it decreasing again until +1 V vs. PQRE. The decrease in the ratio at positive charges is likely due to the anions displacing any ordered BMP cations at the Au surface.

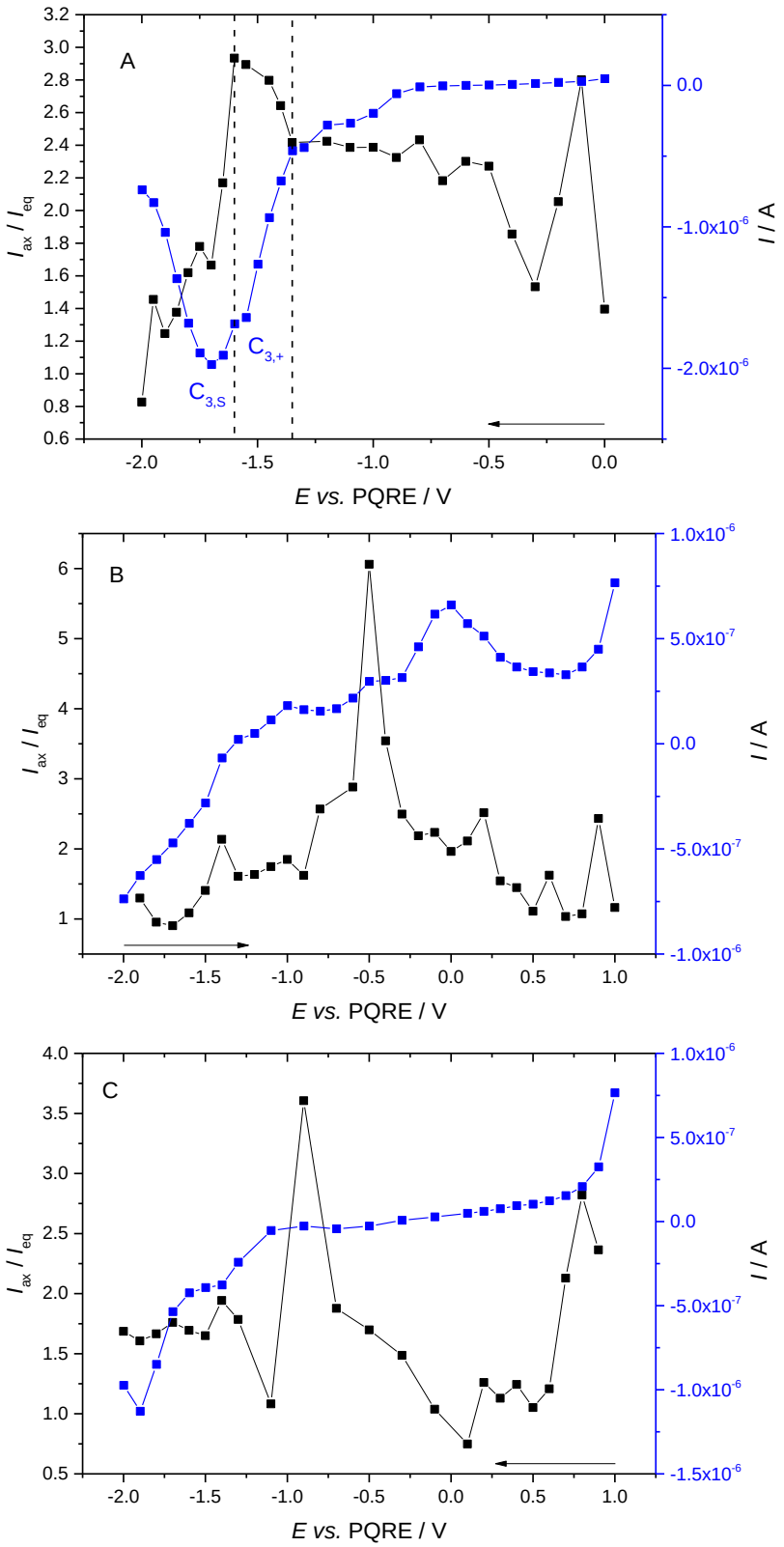

Figure 5-19 Ratio of the 883 cm^{-1} peak intensity corresponding to a vibration of the ax-BMP conformer over the 1021 cm^{-1} peak intensity corresponding to a vibration of the eq-BMP conformer (black) and currents (blue) at various potentials during the (A) first, (B) second and (C) third potential series. The arrows indicate the direction in which the potential was changed.

Finally, in the third potential series, there is a decrease in the I_{ax}/I_{eq} ratio until +0.1 V vs. PQRE due to the Au oxide reduction and increase in the number of TFSI anions required to counter the positive charge on the electrode. The ratio then increases until -0.7 V vs. PQRE, similarly to the first potential series. However, the next two data points at -0.9 V and -1.1 V vs. PQRE show significant variation and the trend cannot be explained in this potential region. Between -1.3 V and -2 V vs. PQRE the ratio remains relatively constant, indicating no significant changes in the proportion of ax-BMP and eq-BMP conformers are occurring.

In conclusion, while the increase in ax-BMP conformers relative to eq-BMP conformers may have been detected in the first potential series between -1.35 V and -1.6 V vs. PQRE, this has not been detected in the third potential as well. Hence, the data in the first potential series confirm that feature $C_{3,+}$ corresponds to an increase in BMP cations with their alkyl chains oriented away from the Au surface. However, the smaller feature in the third potential series which had earlier been attributed to the same process as $C_{3,+}$ has not been confirmed in this instance. It may be useful in future work to repeat these measurements, obtaining spectra at smaller potential intervals, especially in the third potential series.

5.3 Summary

Some useful conclusions were derived from the results and discussion in this chapter and these are summarised in the diagrams of figure 5-20. The PZC, when unaffected by specific adsorption, superoxide ion and metal oxide formation was tentatively assigned by using EIS to -0.85 V vs. PQRE. Features C_2, $C_{3,+}$ and $C_{3,S}$ in the current-potential data of the first potential series have been assigned to the orienting of the BMP cations, increase in ax-BMP conformers and superoxide ion formation, respectively, tying together varying interpretations from the literature.[1-3] The separation of C_3 into $C_{3,+}$ and $C_{3,S}$ was made possible in the current-potential data, due to the very slow nature of the experiment, compared to CV. In the second potential series, feature A_3 was confirmed to result from removal if the superoxide ion, A_2 was found to coincide with the decrease in cations at the surface and there was also a small increase in current at high potentials due to the formation of Au oxide. Lastly, the Au oxide reduction was evident in the third potential series, but unlike the first potential series, it was difficult to assign BMP orientation and conformation changes.

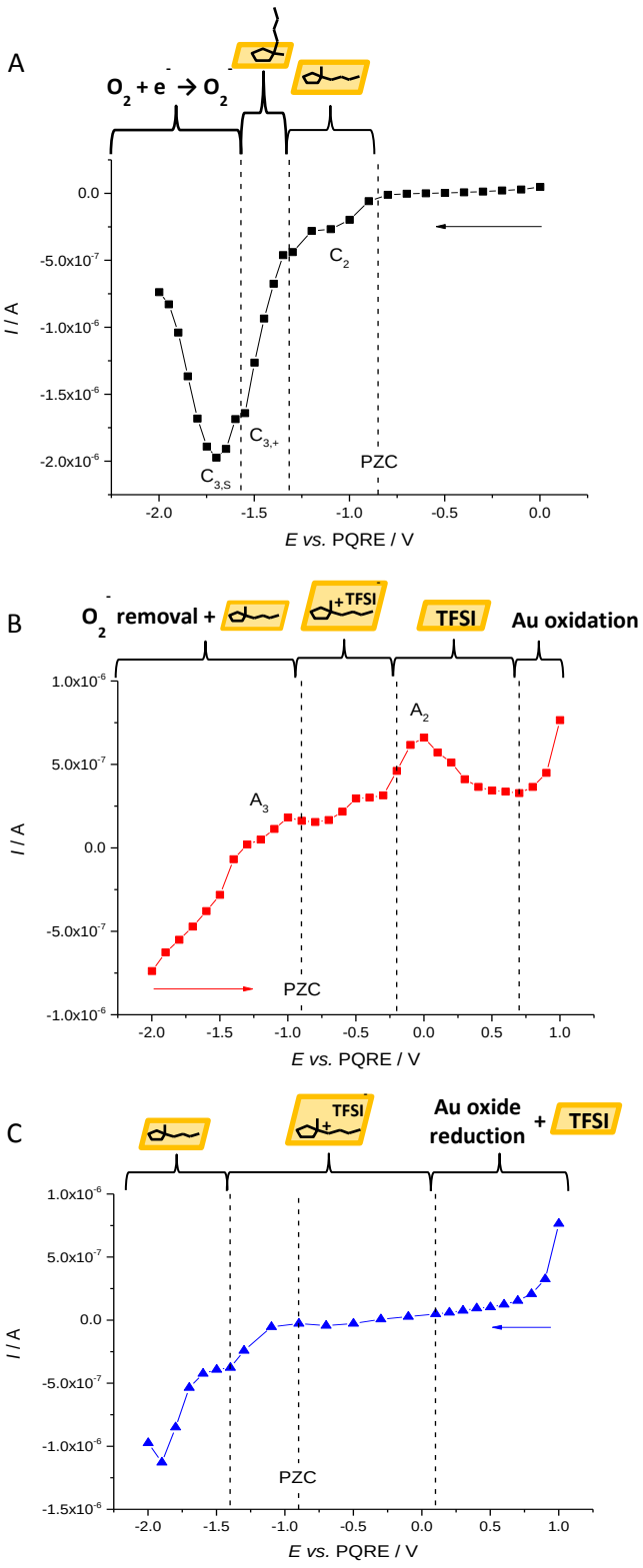

Figure 5-20 Conclusions about the EC behaviour at the Au – BMP TFSI interface, derived from the results and discussion of the CV, EIS and EC-SERS data of this chapter, presented alongside the current-potential data obtained during the SERS spectra acquisitions. (A), (B) and (C) represent the first, second and third potential series and the arrows indicate the direction in which the potential was changed.

However, this chapter has also confirmed the difficulties expected from chapter 4 and also highlighted some new difficulties with using EC-SERS data for analysis of IL processes occurring in the innermost ion layers at the interface. Full analysis of some of the data was not always reliable, likely due to bulk effects and due to the complex vibrational assignments of some of the peaks. For example, cation orientation was difficult to estimate, especially due to the lack of strictly ip and oop vibrations on the pyrrolidinium ring with peaks which were intense enough and didn't overlap with the TFSI anion peaks.

There was also an issue with reproducibility of current-potential data, specifically between the data obtained during the SPEIS and EC-SERS experiments. The features and peaks in the current-potential data were shifted by 0.1 V between the two experiments, due to the instability of the PQRE. More importantly, feature C_2 which was very well pronounced in the SPEIS current-potential data was not as pronounced in the EC-SERS data. The reason for this is unknown. Lastly, the current-potential data of the first and third potential series were different, with conclusions about the third series data becoming difficult to derive from the EC-SERS results. This may have been due to the fewer data points obtained over larger potential intervals during the third potential series. However, it is believed the data was also heavily influenced by the presence and subsequent removal of gold oxide at positive potentials.

5.4 References

1. R. Atkin, N. Borisenko, M. Druschler, S. Z. El Abedin, F. Endres, R. Hayes, B. Huber and B. Roling, *Phys. Chem. Chem. Phys.*, 2011, **13**, 6849-6857.

2. R. Wen, B. Rahn and O. M. Magnussen, *Angew. Chem. Int. Edit.*, 2015, **54**, 6062-6066.

3. L. Grande, E. Paillard, G. T. Kim, S. Monaco and S. Passerini, *Int. J. Mol. Sci.*, 2014, **15**, 8122-8137.

4. Z. Q. Peng, S. A. Freunberger, L. J. Hardwick, Y. H. Chen, V. Giordani, F. Barde, P. Novak, D. Graham, J. M. Tarascon and P. G. Bruce, *Angew. Chem. Int. Ed.*, 2011, **50**, 6351-6355.

5. J. T. Frith, A. E. Russell, N. Garcia-Araez and J. R. Owen, *Electrochem. Commun.*, 2014, **46**, 33-35.

6. P. M. Radjenovic and L. J. Hardwick, *Faraday Discuss.*, 2018, **206**, 379-392.

7. S. Baldelli, *J. Phys. Chem. B*, 2005, **109**, 13049-13051.

8. S. Baldelli, *Acc. Chem. Res.*, 2008, **41**, 421-431.

9. V. Lockett, R. Sedev, J. Ralston, M. Horne and T. Rodopoulos, *J. Phys. Chem. C*, 2008, **112**, 7486-7495.

10. M. Gnahm, T. Pajkossy and D. M. Kolb, *Electrochim. Acta*, 2010, **55**, 6212-6217.

11. V. Lockett, M. Horne, R. Sedev, T. Rodopoulos and J. Ralston, *Phys. Chem. Chem. Phys.*, 2010, **12**, 12499-12512.

12. Y. T. Tang, X. Pan, C. N. Zhang, L. H. Hu, F. T. Kong and S. Y. Dai, *Electrochim. Acta*, 2011, **56**, 3395-3400.

13. T. Pajkossy and D. M. Kolb, *Electrochem. Commun.*, 2011, **13**, 284-286.

14. T. F. Esterle, D. N. Sun, M. R. Roberts, P. N. Bartlett and J. R. Owen, *Phys. Chem. Chem. Phys.*, 2012, **14**, 3872-3881.

15. R. Atkin, S. Z. El Abedin, R. Hayes, L. H. S. Gasparotto, N. Borisenko and F. Endres, *J. Phys. Chem. C*, 2009, **113**, 13266-13272.

16. D. K. Singh, S. Cha, D. Nam, H. Cheong, S. W. Joo and D. Kim, *Chemphyschem*, 2016, **17**, 3040-3046.

17. V. H. Paschoal, L. F. O. Faria and C. C. Ribeiro, *Chem. Rev.*, 2017, **117**, 7053-7112.

18. T. C. Niu, Y. X. Yuan, J. L. Yao, F. Lu and R. A. Gu, *Sci. China Ser. B*, 2011, **54**, 200-204.

19. H. S. Schrekker, M. A. Gelesky, M. P. Stracke, C. M. L. Schrekker, G. Machado, S. R. Teixeira, J. C. Rubim and J. Dupont, *J. Colloid Interface Sci.*, 2007, **316**, 189-195.

20. M. B. Singh and R. Kant, *J. Phys. Chem. C*, 2014, **118**, 8766-8774.

21. J. R. Macdonald and W. R. Kenan, *Impedance Spectroscopy: Emphasizing Solid Materials and Systems*, Wiley, 1987.

22. J. Forsman, C. E. Woodward and M. Trulsson, *J. Phys. Chem. B*, 2011, **115**, 4606-4612.

23. J. Friedl, I. I. E. Markovits, M. Herpich, G. Feng, A. A. Kornyshev and U. Stimming, *Chemelectrochem*, 2017, **4**, 216-220.

24. M. Figueiredo, C. Gomes, R. Costa, A. Martins, C. M. Pereira and F. Silva, *Electrochim. Acta*, 2009, **54**, 2630-2634.

25. B. Hirschorn, M. E. Orazem, B. Tribollet, V. Vivier, I. Frateur and M. Musiani, *Electrochim. Acta*, 2010, **55**, 6218-6227.

26. J. C. Hoogvliet and W. P. van Bennekom, *Electrochim. Acta*, 2001, **47**, 599-611.

27. O. Diaz-Morales, F. Calle-Vallejo, C. de Munck and M. T. M. Koper, *Chem. Sci.*, 2013, **4**, 2334-2343.

28. A. G. Brolo, D. E. Irish and J. Lipkowski, *J. Phys. Chem. B*, 1997, **101**, 3906-3909.

29. A. J. Wilson and K. A. Willets, *Analyst*, 2016, **141**, 5144-5151.

30. S. G. Harroun, T. J. Abraham, C. Prudhoe, Y. Zhang, P. J. Scammells, C. L. Brosseau, C. C. Pye and R. D. Singer, *Phy. Chem. Chem. Phys.*, 2013.

31. Y. Liu, Y. X. Yuan, X. R. Wang, N. Zhang, M. M. Xu, J. L. Yao and R. A. Gu, *J. Electroanal. Chem.*, 2014, **728**, 10-17.

32. V. O. Santos, M. B. Alves, M. S. Carvalho, P. A. Z. Suarez and J. C. Rubim, *J. Phys. Chem. B*, 2006, **110**, 20379-20385.

33. E. C. Le Ru, S. A. Meyer, C. Artur, P. G. Etchegoin, J. Grand, P. Lang and F. Maurel, *Chem. Commun.*, 2011, **47**, 3903-3905.

Chapter 6: EC-SERS and the Stark Effect of SAMs on Au

Self-assembled monolayers (SAMs) are commonly studied by surface enhanced Raman spectroscopy (SERS) as the surface-specific enhancement is necessary for the detection of their Raman signal, which can provide information on redox reactions, changes in their orientation and the electric field near the electrode surface.[1] Thiol based SAMs are easy to create on Au surfaces through the formation of a Au-S bond when soaking the Au surface in a solvent-thiol solution, as described in chapter 2. In the study of ILs they are especially useful, as they inhibit the specific adsorption of ions on the electrode surface. SAMs don't produce bulk Raman signal and so any information obtained from the SAM peaks is from within a single layer of molecules. Lastly, by using molecules containing a group with a large dipole moment, such as a nitrile group, the Stark effect may be used to obtain information on the electric field close to the electrode surface. The electric field and thus, the Stark effect is dependent on the electrode charge and the double layer formed by the ions. However, the downside to introducing SAMs in the metal – ionic liquid (IL) system, is that the electrochemical stability window is reduced, due to the reductive desorption of thiols.[2]

In this chapter, the Stark tuning rates of ν(CN) of the 4-mercaptobenzonitrile (4-MBN) SAM on Au sphere segment void (SSV) substrates in ILs and in an aqueous medium will be measured from electrochemical (EC) – SERS spectra. Subtle differences with potential will be discussed and the orientation of the SAMs will be taken into account by studying the ratio of intensities of one out of plane (oop) and one in plane (ip) peak of the phenyl ring. Differences in Stark tuning rates and ν(CN) peak intensities between the 4-MBN and 4'-mercaptobiphenylcarbonitrile (4'-MBPCN) SAMs have also been discussed and the SERS signal decay with distance from the Au SSV substrate has been examined.

6.1 SERS of the 4-MBN SAM on a Gold SSV Substrate in Various Media

The structure and a SERS spectrum of a 4-MBN SAM on a Au SSV substrate are demonstrated in figure 6-1. 4-MBN contains a thiol group for binding to the Au surface and a nitrile group for probing the Stark effect at the interface with the IL. When adsorbed on Au, 4-MBN molecules are tilted away from the surface normal. Hamoudi et al. have measured the tilt angle θ for the 4-MBN molecules on a Au surface in air to be 33°±3°.[3] There are a number of peaks available in the SERS spectrum of 4-MBN and DFT calculations were once again used to assign the peaks and visualise the molecular vibrations. The density functional theory (DFT) – calculated spectrum may be found

in appendix C. Key peaks which will be discussed in this section and their vibrational assignments are tabulated below, in table 6-1.

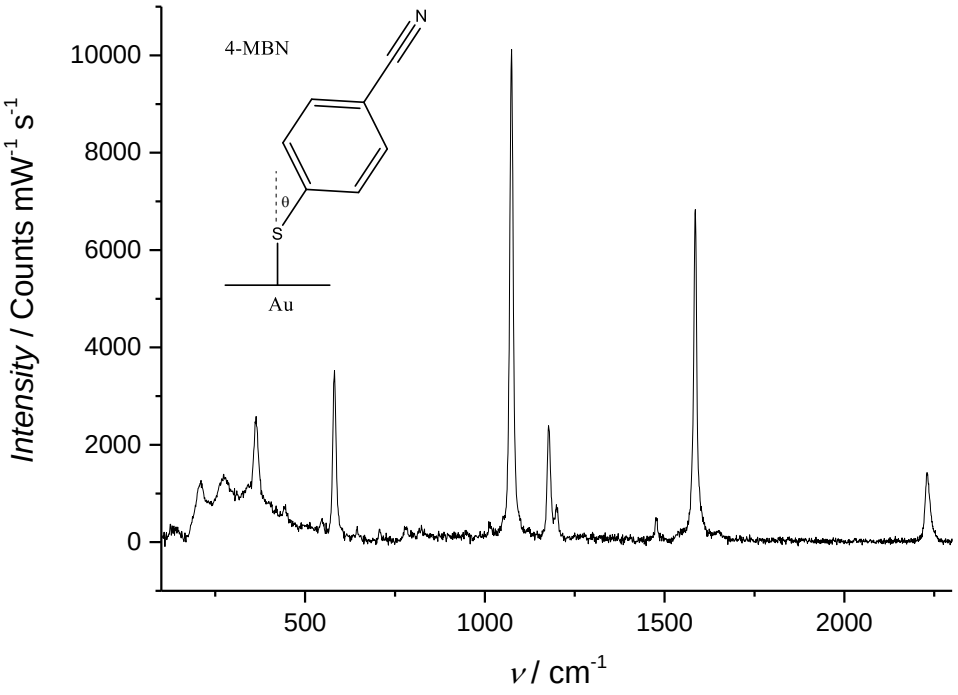

Figure 6-1 SERS spectrum of a 4-MBN (structure displayed) SAM on a Au SSV substrate (made with 600 nm diameter spheres and a thickness of 468 nm) in air. The spectrum was obtained using a 785 nm near-infrared (NIR) laser and a 50x objective and has been normalised by the laser power and exposure time used. The background of the spectrum has also been removed for clarity.

Table 6-1 Centres of peaks in the 4-MBN SERS spectra discussed in this chapter, along with vibrational assignments and corresponding Wilson numbers for the phenyl ring modes, mainly based on the DFT-calculated Raman spectrum of a 4-MBN thiol molecule, which can be found in appendix C.

Peak Centres / cm^{-1}		**Vibrational Assignments**	
Raman	**DFT**	**Mode(s)**	**Wilson number[4, 5]**
822	838	ω_{oop}(CH)	10a
1074	1104	δ_{ip}(CH) + ν(SC)	18b
1175	1203	δ_{ip}(CH)	9a
2228	2334	ν(CN)	-

The peak corresponding to the *ν*(CN) vibration will be used to examine the Stark effect in ILs and in an aqueous potassium phosphate buffer (PPB). The peak corresponding to vibration 18b will be used to normalise the *ν*(CN) peak intensity to account for any differences in coverage between the 4'-MBPCN and 4-MBN SAMs, for the distance dependence analysis of section 6.2.1, later on in this chapter. Lastly, the peaks corresponding to the oop and ip vibrations of the phenyl ring, 10a and 9a, respectively, will be used to examine the orientation of the phenyl ring of the 4-MBN SAM.

6.1.1 Stark Effect in BMP TFSI, BMI TFSI and Aqueous Potassium Phosphate Buffer

The vibrational Stark effect can be described as a perturbation of the energy of vibrational transitions of a probe molecule, in this case 4-MBN, by the presence of an electric field, in this case created by the application of electrochemical potential.[6] More specifically, the change in energy arises from the interaction of the ground and excited states of the 4-MBN dipoles and the local electric field. The change in energy is expressed by the shift in the *ν*(CN)peak position with potential, as the high dipole moment of the group induces the Stark effect. An example of this shift has been demonstrated in figure 6-2.

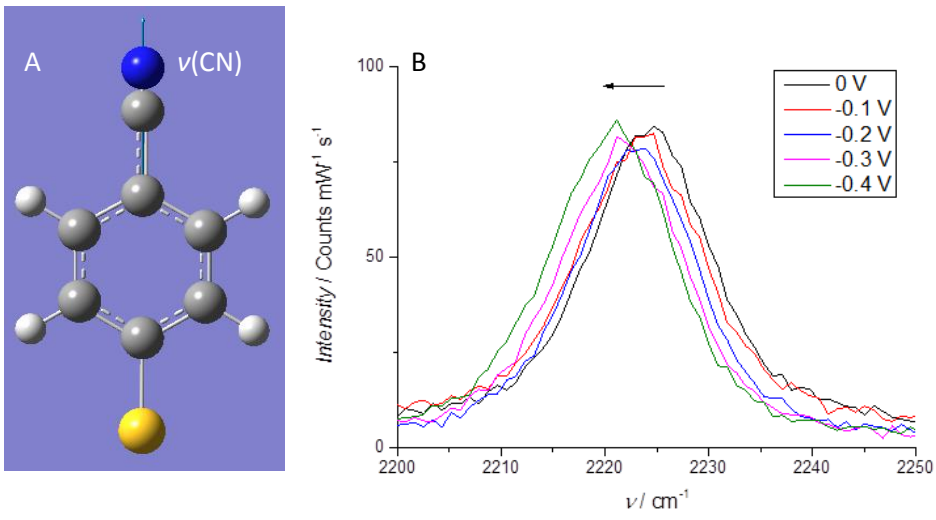

Figure 6-2 (A) DFT-calculated still of the *ν*(CN) vibration of the 4-MBN thiol on the basis of the B3LYP/6-311+G(d,p) levels of theory and (B) the *ν*(CN)peaks of SERS spectra of a 4-MBN SAM on a Au SSV substrate (made with 600 nm diameter spheres and a thickness of 468 nm) in BMP TFSI, obtained at various potentials vs. PQRE. The arrow indicates the direction the potential was scanned in. Each potential was held for 5 minutes before spectrum acquisitions. The spectra were obtained with a 785 nm NIR laser and 50x objective and have been normalised by the laser power and exposure time. The backgrounds of the spectra have also been removed for clarity.

According to Pope et al.[7] the relationship between the change in peak shift Δ*v* due to the Stark effect and the change in electric field Δ*E* can be provided by the following equation:

$$h\Delta\nu = -\Delta\mu\,\Delta E\cos\vartheta - \frac{1}{2}\Delta\alpha\,\Delta E^2\cos\vartheta$$

Equation 6-1

where *h* is the Planck constant; $\Delta\mu$ is the change in dipole moment between the ground and excited state of the probe; ϑ is the angle between the electric field vector and the change in dipole moment vector, i.e. the tilt angle of the probe molecule from the Au surface normal, as the electric field vector is presumed to be normal to the surface; and $\Delta\alpha$ is the change in polarizability between the ground and excited states of the probe. The second, quadratic term of this equation is usually negligible for electric field magnitudes below 10 MV cm^{-1}, as is the case for systems studied here.[7-9] Assuming that the angle ϑ is not changing with applied electrochemical potential, the change in the *v*(CN) peak shift with potential $\Delta\nu/\Delta E_{app}$, called the Stark tuning rate, is proportional to the change in the electric field with potential $\Delta E/\Delta E_{app}$.

The Stark tuning rates have been measured in figure 6-3 for 4-MBN SAMs on Au SSV substrates in 1-butyl-1-methylpyrrolidinium bis(trifluoromethylsulfonyl)imide (BMP TFSI) and 1-butyl-3-methylimidazolium (BMI) TFSI ILs and for a 10 mM, pH 7 PPB. The current-potential data obtained from the three systems during the EC-SERS measurements have demonstrated in figure 6-3 (A) and were used to establish the potential regions in where the current was small. This was to establish a potential range in which the electric field strength was the only likely contributor to the Stark effect, avoiding any effects due to SAM desorption or the IL ions penetrating the SAM. The Stark tuning rates were then calculated as the slopes of straight lines fitted through the *v*(CN)-potential data for each of the systems.

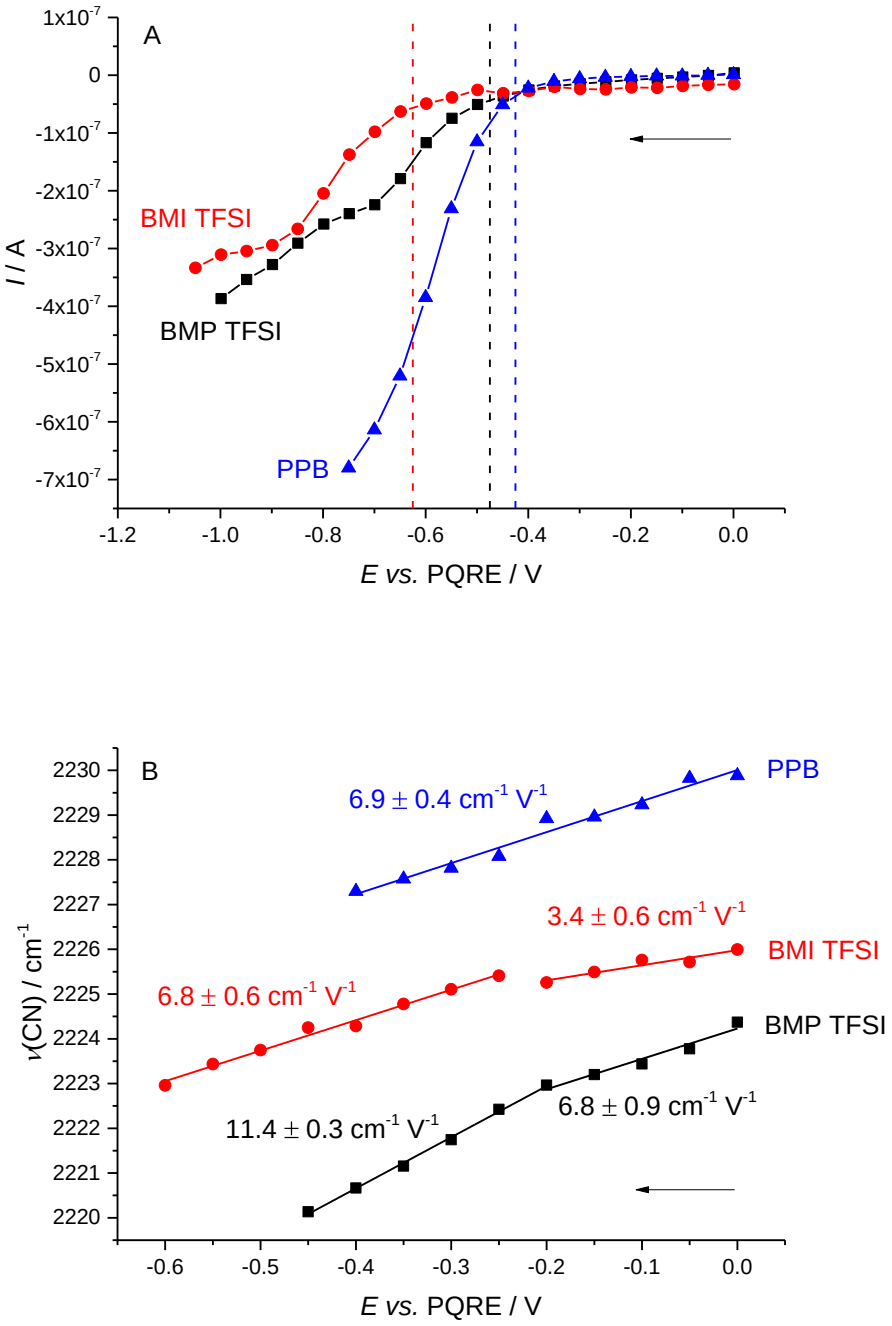

Figure 6-3 (A) Current-potential data obtained during EC-SERS spectral acquisitions and (B) the *ν*(CN) peak positions (data points), linear fittings and corresponding Stark tuning rates, for 4-MBN SAMs on Au SSV substrates (made with 600 nm diameter spheres and a thickness of 468 nm)in BMP TFSI (black squares), BMI TFSI (red circles) and 10 mM, pH 7 PPB (blue triangles). The arrows indicate the direction in which the potential was changed and the order in which the data were collected. Each potential was held for 5 minutes before spectrum acquisitions. The spectra were obtained using a 785 nm NIR laser and a 50x objective. The dashed lines in (A) correspond to the negative potential limits for the data studied in (B).

It is important to note that for the ILs, Two distinct slopes were visible and so the data has been fitted by two lines, resulting in two Stark tuning rates separated at approximately -0.2 V vs. Pt Quasi-Reference Electrode (PQRE). It is suggested that this is due to the presence of a potential of zero charge (PZC) near these potentials. The difference in the Stark tuning rates may correspond to the change from TFSI anions at the SAM interface to the BMP or BMI cations. A PZC is characterised by a change in the direction of the electric field at the interface and so the change in electric field with applied potential $\Delta E/\Delta E_{app}$ would be expected to be smaller at potentials near the PZC. As was seen earlier from equation 6-1, the Stark tuning rate is proportional to $\Delta E/\Delta E_{app}$ which would result in the Stark tuning rate and the slopes in figure 6-3 (B) becoming smaller. The PZC could thus be positioned between 0 V and -0.2 V vs. PQRE for both IL systems. This type of distinction was not visible for the PPB system and has not been seen for this system in the literature.[8] This could be due to faster solvation dynamics in aqueous electrolytes compared to ILs, making the electric field changes faster with the transition through the PZC.[9]

It would be interesting to extend the potential window of these type of measurements positively in future work, in order to see if the slope and Stark tuning rates change any more at more positive potentials. A plateau in the Stark tuning rate could further indicate a PZC, which could then be confirmed by staircase potential electrochemical impedance spectroscopy (SPEIS), similarly to the previous chapters.

The Stark tuning rate of 4-MBN on Au has been measured in PPB to be 8.0 $cm^{-1} V^{-1}$ by Schkolnik et al., which is slightly larger than the value of 6.9 ± 0.4 $cm^{-1} V^{-1}$ measured here. The Stark tuning rates in PPB and BMI TFSI at negative potentials are similar, with values of 6.9 ± 0.4 $cm^{-1} V^{-1}$ and 6.8 ± 0.6 $cm^{-1} V^{-1}$, respectively. On the other hand, the Stark tuning rate in BMP TFSI at negative potentials is 11.4 ± 0.3 $cm^{-1} V^{-1}$. The vibrational frequency of the *ν*(CN) mode and its sensitivity to the electric field may be affected by hydrogen bonding interactions.[10] There is a large amount of hydrogen bond formation between water and the nitrile probe, which also causes a blue shift in *ν*(CN), also seen here in figure 6-3.[9] This causes depolarisation of the nitrile group and a dampening of the Stark effect, leading to a smaller Stark tuning rate in the aqueous PPB compared to in BMP TFSI. The Stark tuning in BMI TFSI is unexpectedly low, as one would expect it would be more similar to BMP TFSI than to PPB. In order to examine any additional interactions between the BMI cations and the nitrile probe that may have affected the Stark tuning rate, the orientation of the 4-MBN molecules in the SAM has been analysed in the next section.

6.1.2 Out of Plane and In Plane Phenyl Ring Vibrations

In order to study the orientation of the 4-MBN molecules in the SAM, peaks corresponding to the 10a oop phenyl ring vibration and the 9a ip phenyl ring vibration, at 822 cm^{-1} and 1175 cm^{-1}, respectively, were analysed. Diagrams of these vibrations have been presented in figure 6-4 (A). The potential dependence of the ratio of the oop peak intensity over the ip peak intensity, I_{oop}/I_{ip}, has been presented for the 4-MBN SAM on Au SSV substrates in BMP TFSI, BMI TFSI and PPB in figure 6-4 (B).

As mentioned in the previous chapter, SERS surface selection rules state that when a vibration occurs along the surface normal, its Raman signal is more enhanced than that of a vibration occurring parallel to the substrate surface.[11] Hence, when a phenyl ring is oriented flat against a SERS-active substrate surface, its oop ring vibrations will be more enhanced, while its ip ring vibrations will be less so. The opposite happens if a phenyl ring is oriented upright against a SERS-active substrate surface. An increase in the I_{oop}/I_{ip} ratio indicates that the 4-MBN molecules may be tilting away from the Au surface normal towards a more flat orientation. On the other hand, a decrease in the I_{oop}/I_{ip} ratio indicates that the 4-MBN molecules may be orienting more upright and away from the Au surface.

The I_{oop}/I_{ip} ratios in BMP TFSI and PPB are fairly similar, close to the I_{oop}/I_{ip} ratio found in air and don't change much with potential. This is beneficial for studying the Stark effect, as the data should not be affected by changes in orientation and the distance of the probe from the Au substrate surface should not change. However, the ratio in BMI TFSI increases dramatically and more than doubles between potentials -0.15 V and -0.6 V vs. PQRE. This indicates that the 4-MBN SAM is changing in a way that allows the phenyl rings to orient in a more flat configuration against the Au surface. There also seems to be a relaxation in this effect when scanning the potential negatively, past -0.6 V vs. PQRE. No significant changes were seen in the current-potential data of figure 6-3 (A) earlier on in the chapter, so the change in orientation is unlikely to be due to desorption of the 4-MBN molecules. The more flat orientation of the phenyl ring, along with the relatively low Stark tuning rate observed in BMI TFSI, compared to in BMP TFSI, indicate a compression of the SAM and strong interactions between the BMI cations and the nitrile groups of the SAM.

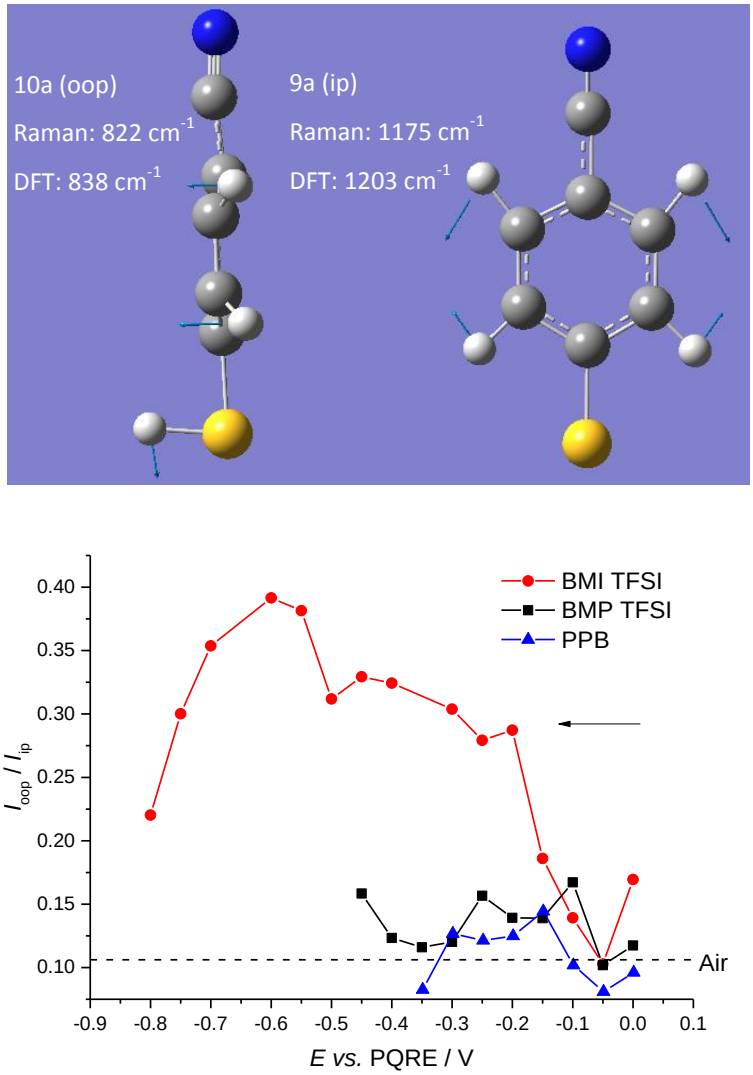

Figure 6-4 (A) DFT-calculated animation image stills of the 10a (oop) and 9a (ip) phenyl ring vibrations of an optimised 4-MBN thiol molecule on the basis of the B3LYP/6-311+G(d,p) levels of theory. The position of the peaks in the DFT-calculated Raman spectrum (as presented in figure C-1 of appendix C) and the corresponding peak positions in the SERS spectrum of the 4-MBN SAM on a Au SSV substrate in air (as presented in figure 6-1 earlier on in this chapter) have been included. The blue arrows indicate the displacement of the atoms during the vibrations. (B) Ratio of the oop (10a) peak intensity over the ip (9a) peak intensity plotted against potential, for the 4-MBN SAM on Au SSV substrates (made with 600 nm diameter spheres and a thickness of 468 nm) in BMP TFSI (black squares), BMI TFSI (red circles) and 10 mM, pH 7 PPB (blue triangles). The dashed line corresponds to the same peak intensity ratio obtained from the SERS spectrum of figure 6-1, of the 4-MBN SAM on a Au SSV substrate in air. The black arrow indicates the direction in which the potential was scanned and the order in which the data were obtained. Each potential was held for 5 minutes before spectrum acquisitions. The spectra were obtained using a 785 nm NIR laser and a 50x objective.

The BMI cation possesses a larger positive charge delocalisation than the BMP cation, due to its conjugated imidazolium ring.[9] However, the positively charged nitrogen on the BMP cation is less exposed than that of the BMI cation, with the methyl and butyl groups on the BMP providing steric hindrance. It is thus likely, that the BMP cation cannot interact as strongly with the nitrile groups in the SAM, as the BMI cation can. BMI cations have been found to be less stable in the past, with the cations in the BMI TFSI IL being much more susceptible to nucleophilic attack by the superoxide ion, than the BMP cations in the BMP TFSI IL.[12] While a similar degradation of the BMI cations is unlikely in this case, this is an example of how the positive charge on the BMI cations is more exposed than that on the BMP cations.

The exact circumstances of the peculiar behaviour of the 4-MBN SAM in the BMI TFSI IL compared to the BMP TFSI IL, remain unknown. There is a clear dampening of the Stark effect coinciding with a reorientation of the SAM towards a more flat configuration of the phenyl rings, which possibly arises from strong interactions between the BMI cations and the nitrile groups of the SAM. The more available positive charge on the BMI cations compared to the BMP cations may be the reason for this. However, more work would need to be carried out to establish the exact nature of these interactions.

6.2 SERS Comparison of 4-MBN and 4'-MBPCN SAMs on Gold in IL

The SERS spectra of a 4-MBN SAM and a 4'-MBPCN SAM on Au SSV substrates in air are demonstrated in figure 6-5. Just like 4-MBN, 4'MBPCN contains a thiol group for binding to the Au surface and a nitrile group for probing the Stark effect at the interface with the IL. The 4'-MBPCN molecules are tilted away from the surface normal, similarly to the 4-MBN molecules. However, the tilt angle θ for the 4'-MBPCN molecules on a Au surface in air has been measured to be slightly higher than that of 4-MBN molecules by Ballav et al., at 39.5°.[13] The presence of an additional phenyl ring in 4'-MBPCN results in distinct differences between its spectrum and that of 4-MBN. Once again, DFT calculations were used to assign the peaks and visualise the molecular vibrations of 4'-MBPCN and the DFT-calculated spectrum may be found in appendix C. Key peaks which will be discussed in this section and their vibrational assignments have been tabulated below, in table 6-2.

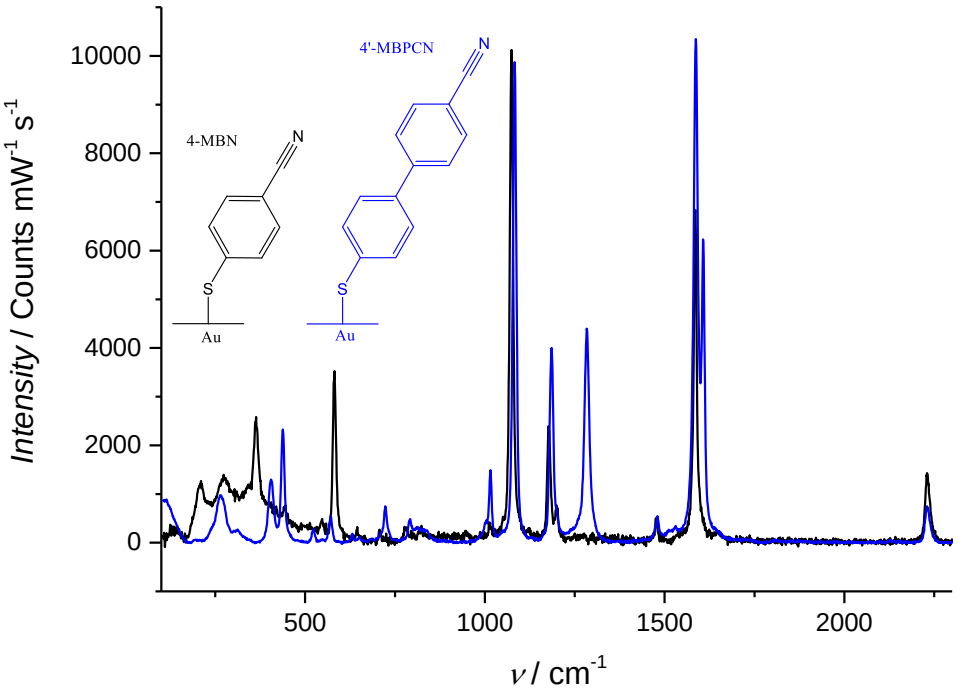

Figure 6-5 SERS spectra of a 4-MBN SAM (black) and a 4'-MBPCN SAM (blue) on Au SSV substrates (made with 600 nm diameter spheres and a thickness of 468 nm) in air. The structures of 4-MBN (black) and 4'-MBPCN (blue) molecules adsorbed on Au have also been included. The spectra were obtained using a 785 nm NIR laser and a 50x objective and have been normalised by the laser power and exposure time used. The backgrounds of the spectra have also been removed for clarity.

Table 6-2 Centres of peaks in the 4'-MBPCN and 4-MBN SERS spectra discussed in this chapter, along with vibrational assignments and corresponding Wilson numbers for the phenyl ring modes. Assignments were based on the DFT-calculated Raman spectra of the 4'-MBPCN and 4-MBN thiol molecules, which can be found in appendix C.

Peak Centres / cm^{-1}				**Vibrational Assignments**	
4-MBPCN		**4-MBN**		**Mode(s)**	**Wilson number[4, 5]**
Raman	**DFT**	**Raman**	**DFT**		
1083	1115	1074	1104	δ_{ip}(CH) + ν(SC)	18b
2231	2328	2228	2334	ν(CN)	-

The peak corresponding to the ν(CN) vibration will be used to examine the Stark effect and to examine the dependence of SERS enhancement on the distance from the substrate. The peak

corresponding to vibration 18b will be used to normalise the *ν*(CN) peak intensity to account for any differences in coverage between the 4'-MBPCN and 4-MBN SAMs, for the distance dependence analysis.

6.2.1 Stark Effect

The Stark tuning rates for 4-MBN and 4'-MBPCN SAMs on Au SSV substrates in BMP TFSI have been presented in figure 6-6 (B). The current-potential data obtained from the two systems during the EC-SERS measurements have also been demonstrated in figure 6-6 (B) and were used to establish the potential regions in where the current was small. This was to establish a potential range in which the electric field strength was the only likely contributor to the Stark effect, avoiding any effects due to SAM desorption or the IL ions penetrating the SAM. The Stark tuning rates were then calculated as the slopes of straight lines fitted through the *ν*(CN)-potential data for each of the systems.

Unlike the two different Stark tuning rates found in the 4-MBN SAM, in the data for the 4'-MBPCN SAM only one Stark tuning rate was visible. This may result from the low Stark tuning rate of the 4'-MBPCN SAM with a value of 2.8 ± 0.1 cm^{-1} V^{-1}, in comparison to the that of the 4-MBN SAM, with a value of 11.4 ± 0.3 cm^{-1} V^{-1}. The low Stark tuning rate for 4'-MBPCN likely arises from the larger distance between the Au substrate surface and the nitrile probe, compared to 4-MBN. As discussed in section 6.1.1, the Stark tuning rate is proportional to the change in electric field with applied potential, according to equation 6-1. As the potential is applied to the electrode surface, the electric field change with potential will be lower the further away the nitrile probe is from the Au surface.[6] The *ν*(CN) peak position for the 4'-MBPCN SAM is also generally higher than it is for the 4-MBN SAM. This was also seen for the SAMs in air and in the DFT calculated Raman peaks, presented earlier in table 6-2. This was likely due to the additional phenyl ring present affecting the electron distribution in the 4'-MBPCN molecule and its nitrile group in particular, causing the blue shift in the *ν*(CN) peak position.

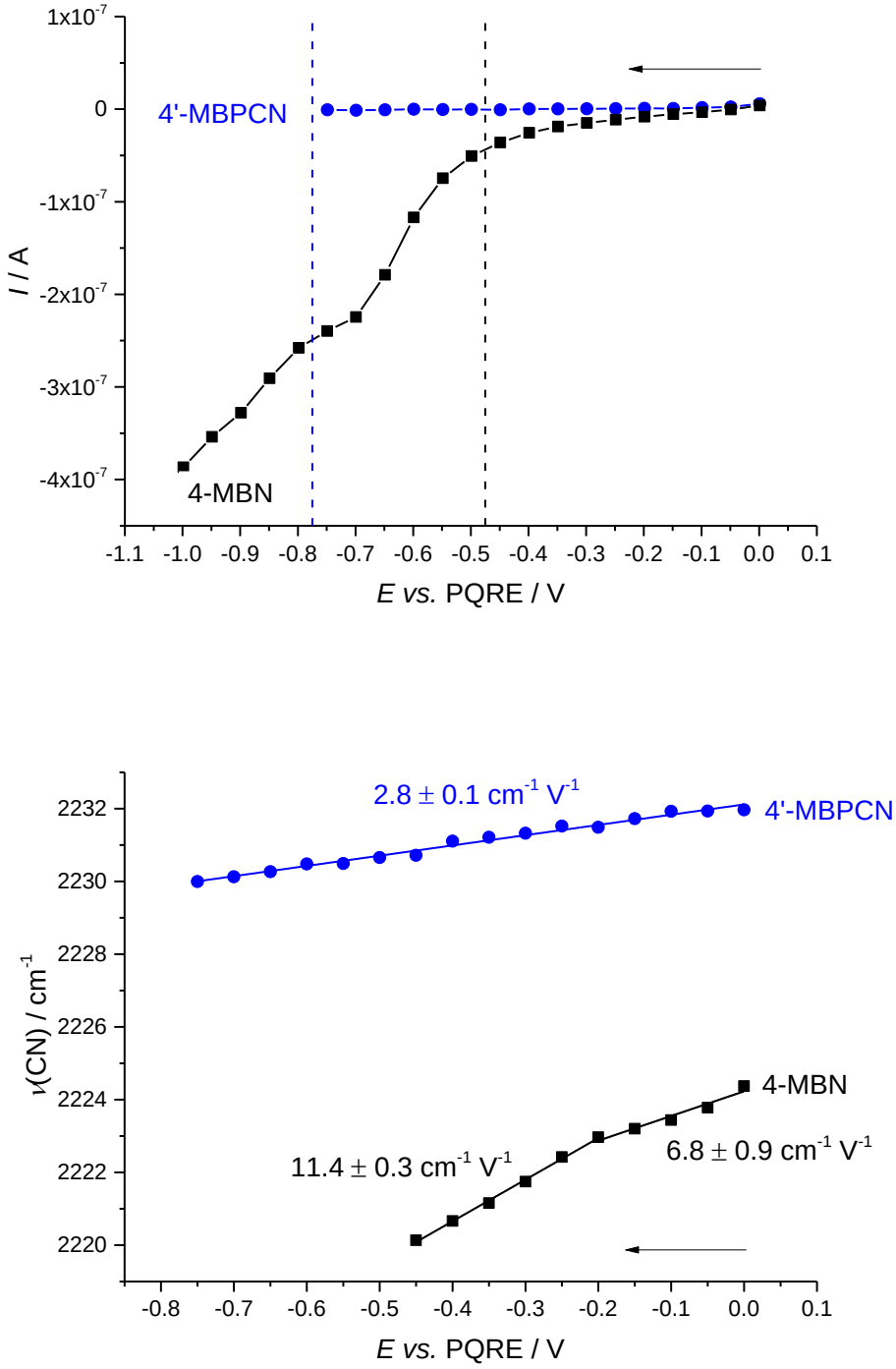

Figure 6-6(A) Current-potential data obtained during EC-SERS spectrum acquisitions and (B) *ν*(CN) peak positions (data points), linear fittings and corresponding Stark tuning rates, for 4'-MBPCN (blue circles) and 4-MBN (black squares) SAMs on Au SSV substrates (made with 600 nm diameter spheres and a thickness of 468 nm)in BMP TFSI. The arrows indicate the direction in which the potential was changed and the order in which the data were collected. Each potential was held for 5 minutes before spectrum acquisitions. The spectra were obtained using a 785 nm NIR laser and a 50x objective and have been normalised by the laser power and exposure time used. The dashed lines in (A) correspond to the negative potential limits for the data studied in (B).

6.2.2 Nitrile Stretching Peak Intensity and the Distance Dependence of SERS

Referring back to chapter 4 and equation 4-1, the decay of the SERS intensity of a vibration with distance from the substrate can be described by the following relationship:

$$I_{\mathrm{SERS}} = \left(1 + \frac{r}{a}\right)^{-10}$$

Equation 6-2

where *r* is the distance of the vibration from the surface and *a* is the radius of the curvature of the field enhancing feature of the substrate, equal to 300 nm for the SSV substrates in this study.[14, 15]

Equation 6-2 was used in chapter 4 to explain the relatively low intensities of IL spectra on Au SSV substrates, compared to on flat Au substrates, as a result of the smaller volume of liquid probed, due to the SERS enhancement on the SSV substrate. The dependence of SERS intensity to the distance from the SERS-active substrate will be examined again here, by comparing the *ν*(CN) peak intensities of the 4-MBN and 4'-MBPCN SAMs on the SSV Au substrate, in the BMP TFSI IL. However, in order account for any differences in coverage which may exist between the two SAMs, the *ν*(CN) peak intensities have been normalised by the intensity of the 18b benzene ring vibration occurring at 1074 cm^{-1} and 1083 cm^{-1} for 4-MBN and 4'-MBPCN, respectively. This peak was chosen as it is very intense for both SAMs and it arises from the same vibrations occurring at the same distance from the substrate for both SAMs. As a result, its intensity should not be influenced by the difference in SAM.

By fitting the *ν*(CN) and 18b peaks of both the 4-MBN and 4'-MBPCN SAMs and measuring their intensities, the experimentally obtained ratio of the normalised *ν*(CN) peak intensities for the 4-MBN SAM over the 4'-MBPCN SAM was:

$$Ratio_{\mathrm{exp}} = \frac{\frac{I_{\mathrm{CN,MBN}}}{I_{\mathrm{18b,MBN}}}}{\frac{I_{\mathrm{CN,MBPCN}}}{I_{\mathrm{18b,MBPCN}}}} = \frac{0.08}{0.07} = 1.10$$

Considering equation 6-2, the ratio of the normalised *ν*(CN) peak intensities for the 4-MBN SAM over the 4'-MBPCN SAM should theoretically be:

$$Ratio_{\mathrm{th}} = \frac{\frac{I_{\mathrm{CN,MBN}}}{I_{\mathrm{18b,MBN}}}}{\frac{I_{\mathrm{CN,MBPCN}}}{I_{\mathrm{18b,MBPCN}}}} = \left[\frac{\left(1+\frac{r_{(\mathrm{Au-CN}),\mathrm{MBN}}}{a}\right)\left(1+\frac{r_{(\mathrm{Au-18b}),\mathrm{MBPCN}}}{a}\right)}{\left(1+\frac{r_{(\mathrm{Au-18b}),\mathrm{MBN}}}{a}\right)\left(1+\frac{r_{(\mathrm{Au-CN}),\mathrm{MBPCN}}}{a}\right)}\right]^{-10}$$

Equation 6-3

where $r_{(Au\text{-}CN),MBN}$ and $r_{(Au\text{-}CN),MBPCN}$ are the distances between the *ν*(CN) vibrations and the Au surface in the 4-MBN and 4'-MBPCN SAMs, respectively and $r_{(Au\text{-}18b)}$ is the distance between the 18b vibration from the surface.

The distances $r_{(Au\text{-}CN),MBN}$, $r_{(Au\text{-}CN),MBPCN}$, $r_{(Au\text{-}18b),MBN}$ and $r_{(Au\text{-}18b),MBPCN}$ can be calculated using basic trigonometry rules, demonstrated in a diagram in figure 6-7 for 4-MBN, resulting in the following equation:

$$r_{(\mathrm{Au-X})} = r_{(\mathrm{Au-S})} + r_{(\mathrm{S-X})} \times \sin(90° - \theta)$$

Equation 6-4

where $r_{(Au\text{-}X)}$ is the distance to be calculated between the Au surface and vibration X, which in this case is either *ν*(CN) or 18b; $r_{(Au\text{-}S)}$ is the distance between the Au surface and S in the SAM molecules; $r_{(S\text{-}X)}$ is the distance between S and vibration X, i.e. either the *ν*(CN) or the 18b vibration; and ϑ is the tilt angle of the SAM molecule from the Au surface normal. The calculation results, along with the values for all terms in equation 6-4 have been tabulated in table 6-3.

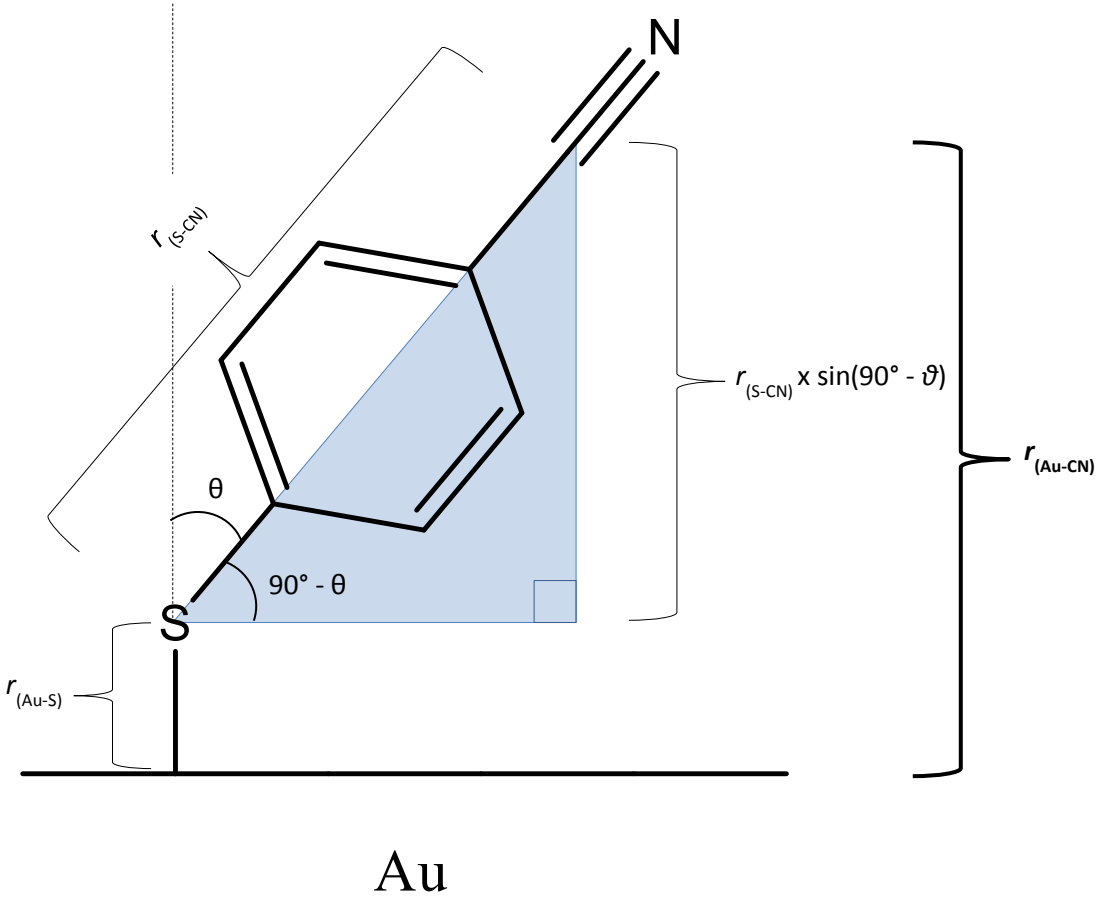

Figure 6-7 Diagram of a 4-MBN molecule adsorbed on a Au surface, demonstrating the terms of equation 6-4 and the trigonometry rules used to derive equation 6-4.

Table 6-3 Values for all the terms of equation 6-4 for each of the 4-MBN and 4'-MBPCN SAMs on a Au SSV substrate. Intra-molecular distances were measured from DFT-optimised structures of the 4-MBN and 4'-MBPCN thiol molecules and a Au - 4-MBN thiolate molecule. DFT calculations were carried out using the B3LYP/6-311+G(d,p) levels of theory. Values for the tilt angle ϑ were obtained from the literature, which has been referenced within the table.

	$r_{(Au-S)}$/Å	$r_{(S-X)}$/Å		ϑ/°	$r_{(Au-X)}$/Å	
		$r_{(S-CN)}$/Å	$r_{(S-18b)}$/Å		$r_{(Au-CN)}$/Å	$r_{(Au-18b)}$/Å
4-MBN	2.4	6.0	1.8	33.0[3]	7.4	3.9
4'-MBPCN	2.4	10.3	1.8	39.5[13]	10.3	3.7

By substituting the values of table 6-3 into equation 6-3, the theoretically predicted value for the ratio of normalised *ν*(CN) SERS intensities for 4-MBN over 4'-MBPCN can be calculated:

$$Ratio_{\mathrm{th}} = \left[\frac{\left(1+\frac{r_{(\mathrm{Au-CN}),\mathrm{MBN}}}{a}\right)\left(1+\frac{r_{(\mathrm{Au-18b}),\mathrm{MBPCN}}}{a}\right)}{\left(1+\frac{r_{(\mathrm{Au-18b}),\mathrm{MBN}}}{a}\right)\left(1+\frac{r_{(\mathrm{Au-CN}),\mathrm{MBPCN}}}{a}\right)}\right]^{-10} = 1.01$$

This theoretically predicted value of 1.01 is very similar to the experimentally obtained value of 1.10. This once again confirms that the SERS signal decays with distance from the substrate surface and that equation 6-2 can provide a fairly accurate prediction of this decay.

6.3 Summary

EC-SERS has been carried out for the 4-MBN SAM on a Au SSV substrate in BMP TFSI. The Stark tuning rate of the *ν*(CN) peak of the 4-MBN SAM in BMP TFSI has been compared to the Stark tuning rates in BMI TFSI and in 10 mM, pH 7 PPB. Two different Stark tuning rates were observed in the two ILs, likely to originate from the PZC and the different changes in electric field with potential expected when the cations or the anions are aligned at the SAM-IL interface. This was not observed when PPB was the electrolyte, due to faster solvation dynamics in aqueous electrolytes compared to ILs, making the electric field changes smoother with the transition through the PZC. In future work, it would be interesting to extend the potential window of these measurements positively in order to establish if the PZC is denoted by a plateau. If so, the alignment of more anions at the SAM-IL interface may cause the increase in the Stark tuning rates at positive potentials.

The Stark tuning rate of the *ν*(CN) peak of the 4-MBN SAM in BMP TFSI was 11.4 ± 0.3 $cm^{-1} V^{-1}$, larger than the Stark tuning rate of 6.9 ± 0.4 $cm^{-1} V^{-1}$ in PPB. This was as expected due to the dampening of the Stark effect caused by hydrogen bonding interactions between water and the nitrile probe. However, the Stark tuning rate in BMI TFSI was very low, 6.8 ± 0.6 $cm^{-1} V^{-1}$, similar to that in PPB. It was suggested that this was due to the more available positive charge on the BMI cation compared to the BMP cation, allowing it to interact with the nitrile probe, dampening its Stark effect. However, orientation analysis of the 4-MBN phenyl ring also showed that the phenyl ring in BMI TFSI becomes more flat with negative potential, compared to in BMP TFSI and PPB. Hence, the interaction between BMI cations and the 4-MBN molecules in the SAM may also be causing the SAM to compress. However, more work would need to be carried out in order to establish the exact interactions taking place.

Finally, the Stark tuning rate of 4-MBN in BMP TFSI was compared to that of the 4'-MBPCN in BMP TFSI. The Stark tuning rate for 4'-MBPCN was found to be very low, 2.8 ± 0.1 $cm^{-1} V^{-1}$ compared to

11.4 ± 0.3 $cm^{-1} V^{-1}$ for 4-MBN. This was expected due to the larger distance of the nitrile probe from the electrode surface in the 4'-MBPCN SAM, compared to the 4-MBN SAM, calculated to be 10.3 Å and 7.4 Å, respectively. The electric field change with potential is proportional to the Stark tuning rate and is expected to be much smaller the further away from the electrode surface the nitrile probe is positioned. The *v*(CN) peak intensity was also used to compare the experimentally obtained ratio of the normalised *v*(CN) peak intensities for 4-MBN over 4'-MBPCN, to a theoretically predicted ratio, using equation 6-2, describing the SERS signal decay with distance from the substrate surface, used in chapter 4. The experimentally obtained value of 1.10 was very close to the theoretically predicted value of 1.01, showing that equation 6-2 is appropriate for use with the SSV substrates.

6.4 References

1. A. J. Wilson and K. A. Willets, *Analyst*, 2016, **141**, 5144-5151.

2. D. Oyamatsu, T. Fujita, S. Arimoto, H. Munakata, H. Matsumoto and S. Kuwabata, *J. Electroanal. Chem.*, 2008, **615**, 110-116.

3. H. Hamoudi, P. Kao, A. Nefedov, D. L. Allara and M. Zharnikov, *Beilstein J. Nanotechnol.*, 2012, **3**, 12-24.

4. R. Holze, *Phys. Chem. Chem. Phys.*, 2015, **17**, 21364-21372.

5. E. B. Wilson, *Phys. Rev.*, 1934, **45**, 706-714.

6. V. Oklejas, C. Sjostrom and J. M. Harris, *J. Phys. Chem. B*, 2003, **107**, 7788-7794.

7. J. M. Pope and D. A. Buttry, *J. Electroanal. Chem.*, 2001, **498**, 75-86.

8. G. Schkolnik, J. Salewski, D. Millo, I. Zebger, S. Franzen and P. Hildebrandt, *Int. J. Mol. Sci.*, 2012, **13**, 7466-7482.

9. S. G. Zhang, Y. Zhang and Y. Q. Deng, *RSC Adv.*, 2013, **3**, 11480-11484.

10. A. T. Fafarman, P. A. Sigala, D. Herschlag and S. G. Boxer, *J. Am. Chem. Soc.*, 2010, **132**, 12811-12813.

11. M. Moskovits, D. P. Dilella and K. J. Maynard, *Langmuir*, 1988, **4**, 67-76.

12. J. T. Frith, A. E. Russell, N. Garcia-Araez and J. R. Owen, *Electrochem. Commun.*, 2014, **46**, 33-35.

13. N. Ballav, B. Schupbach, S. Neppl, P. Feulner, A. Terfort and M. Zharnikov, *J. Phys. Chem. C*, 2010, **114**, 12719-12727.

14. B. J. Kennedy, S. Spaeth, M. Dickey and K. T. Carron, *J. Phys. Chem. B*, 1999, **103**, 3640-3646.

15. S. S. Masango, R. A. Hackler, N. Large, A. I. Henry, M. O. McAnally, G. C. Schatz, P. C. Stair and R. P. Van Duyne, *Nano Lett.*, 2016, **16**, 4251-4259.

16. A. Ulman, *Accounts Chem. Res.*, 2001, **34**, 855-863.

Chapter 7: Conclusions and Future Work

7.1 Overview

When a charge is applied to an electrode in the metal – Ionic Liquid (IL) interface, an electrochemical double layer (EDL) is expected to form due to the arrangement of ions at surface to counter the charge on the electrode surface. However, this arrangement of ions in ILs can be complicated by effects such as specific adsorption, ion re-orientation and superoxide ion and Au oxide formation. Traditional techniques used in the study of metal-IL interfaces, have provided a good indication of underlying processes. However, additional proof from new methods is required, as interpretations of the results sometimes vary.

With the use of a bespoke spectroelectrochemical cell, the acquisition of surface enhanced Raman (SERS) spectra from the electrochemically (EC) controlled Au-IL interface can be achieved. By analysing the intensity and positions of peaks in the spectra which correspond to specific vibrations in the different ions of the IL, useful information may be obtained about the processes occurring at the interface at a molecular level.

In chapter 3, a comprehensive vibrational assignment of Raman peaks of the BMP TFSI IL has been made. Density functional theory (DFT) calculations were carried out on the two most common conformers of the BMP and TFSI ions that exist within the BMP TFSI IL. Distinct peak differences between the calculated Raman spectra of the different conformers were discussed, which were used in chapter 5 for the analysis of EC-SERS spectra of the Au – BMP TFSI interface. The comparison of the DFT-calculated Raman spectra to the experimentally obtained Raman spectra of the BMP TFSI IL, along with the visualisation of vibrations aided by the Gaussian software package, facilitated the comprehensive vibrational assignment of the BMP TFSI IL spectrum.

In chapter 4, the SERS response of sphere segment void (SSV) substrates in concentrated liquids, such as ILs, has been characterised with respect to the bulk signal interference and the volume of liquid probed. Using pyridine (Py) to probe the effect of bulk Raman signal on SERS spectra as a function of concentration, it was found that the signal of bulk Py molecules at high concentrations has a significant effect on the overall signal. Additionally, the calculated depth resolution of the spectrometer was two orders of magnitude larger than the distance from the substrate at which most of the SERS signal is lost. This accounts for the larger signal seen in Raman spectra of 1-butyl-1-methylpyrrolidinium bis(trifluoromethylsulfonyl)imide (BMP TFSI) on flat Au, compared to the SERS spectra of BMP TFSI on Au SSV substrates.

In chapter 5, the potential-dependent Au-BMP TFSI interface has been studied with a combination of cyclic voltammetry (CV), electrochemical impedance spectroscopy (EIS) and EC-SERS. The PZC was tentatively assigned to -0.85 V vs. Pt Quasi-Reference Electrode (PQRE). Three separate features seen in the current-potential data at negative potentials were assigned to the orienting of the BMP cations, increase in ax-BMP conformers and superoxide ion formation, respectively. Au oxide formation from trace H_2O was also found to occur at positive potentials, which as expected affected the detection of the processes mentioned above at negative potentials. However, the results in this chapter have also confirmed the challenges expected from chapter 4 and have highlighted the difficulty of detecting processes occurring in the innermost ion layers at the interface, due to bulk effects and the complexity of vibrational assignments of IL peaks.

Chapter 6 contains a brief EC-SERS study of 4-mercaptobenzonitrile (4-MBN) self-assembled monolayer (SAM) on a Au SSV substrate in two ILs and in an aqueous potassium phosphate buffer (PPB). The Stark tuning rates of the 4-MBN SAM in BMP TFSI was larger than that in PPB, due to the dampening of the Stark effect in the aqueous solution from hydrogen bonding between the nitrile group of 4-MBN and H_2O. The Stark tuning rate in BMI TFSI was unexpectedly low and analysis of the orientation of the benzene ring of 4-MBN indicated the presence of additional interactions between the ions and the 4-MBN molecules, causing them to reorient and become more flat on the Au surface. The effect of distance on both the Stark tuning rate and the intensity of the nitrile stretching peak were also examined by using a 4'-mercaptobiphenylcarbonitrile (4'-MBPCN) SAM. The distance dependence on the SERS intensity was in accordance with that predicted by a theoretical model obtained from the literature.

In this chapter, the insights gained into the behaviour of the Au – BMP TFSI interface and the challenges faced when using EC-SERS in the study of this interface are discussed and summarised in detail. Finally, some experiments are suggested for the future applications of the EC-SERS technique in the study of the metal-IL interface.

7.2 Conclusions

7.2.1 The Gold – BMP TFSI Interface

CVs of BMP-based ILs on Au electrodes in the literature have consistently contained a set of features at negative potentials which have somewhat been discussed. Atkin et al. attributed three cathodic waves C_1-C_3 in their CV of a custom made BMP-based IL on Au, to different surface processes that occur upon IL adsorption.[1] Wen et al. attributed the two larger waves in their CV of the Au(111) - BMP TFSI interface, which will be referred to as C_2 and C_3 for simplicity, to changes

in the molecular arrangement of adsorbed BMP cations on the Au electrode surface.[2] However, the two publications disagree on the exact processes responsible for the CV features. Furthermore, similar CV features have been attributed to superoxide ion formation, O_2^-, from oxygen in the BMP TFSI IL on a glassy carbon electrode by Grande et al..[3]

Figure 7-1 contains the current-potential data obtained during the EC-SERS acquisitions and the diagrams help summarise the information obtained about the EC Au – BMP TFSI interface, from the EIS, CV and EC-SERS results and analysis presented in chapter 5. The current-potential data are split into three potential series. In the first series, the potential was scanned from 0 V to -2 V vs. PQRE; in the second series, the potential was scanned from -2 V to +1 V vs. PQRE and in the third series, the potential was scanned from +1 V to -2 V vs. PQRE.

The PZC, when unaffected by specific adsorption, superoxide ion and metal oxide formation was tentatively assigned by EIS to -0.85 V vs. PQRE. Features C_2, $C_{3,+}$ and $C_{3,S}$ in the current-potential data of the first potential series have been assigned to the orienting of the BMP cations, increase in ax-BMP conformers and superoxide ion formation, respectively, tying together varying interpretations from the literature.[1-3] The deconvolution of feature C_3 into $C_{3,+}$ and $C_{3,S}$ was made possible in the current-potential data of the SERS experiment, due to the very slow nature of the experiment, compared to the CV. In the second potential series, feature A_3 was confirmed to result from removal if the superoxide ion, A_2 was found to coincide with the decrease in coverage of cations at the surface. There was also a small increase in current at high potentials due to the formation of Au oxide. Lastly, the Au oxide reduction was evident in the third potential series and unlike for the first potential series, it was difficult to assign BMP orientation and conformation changes.

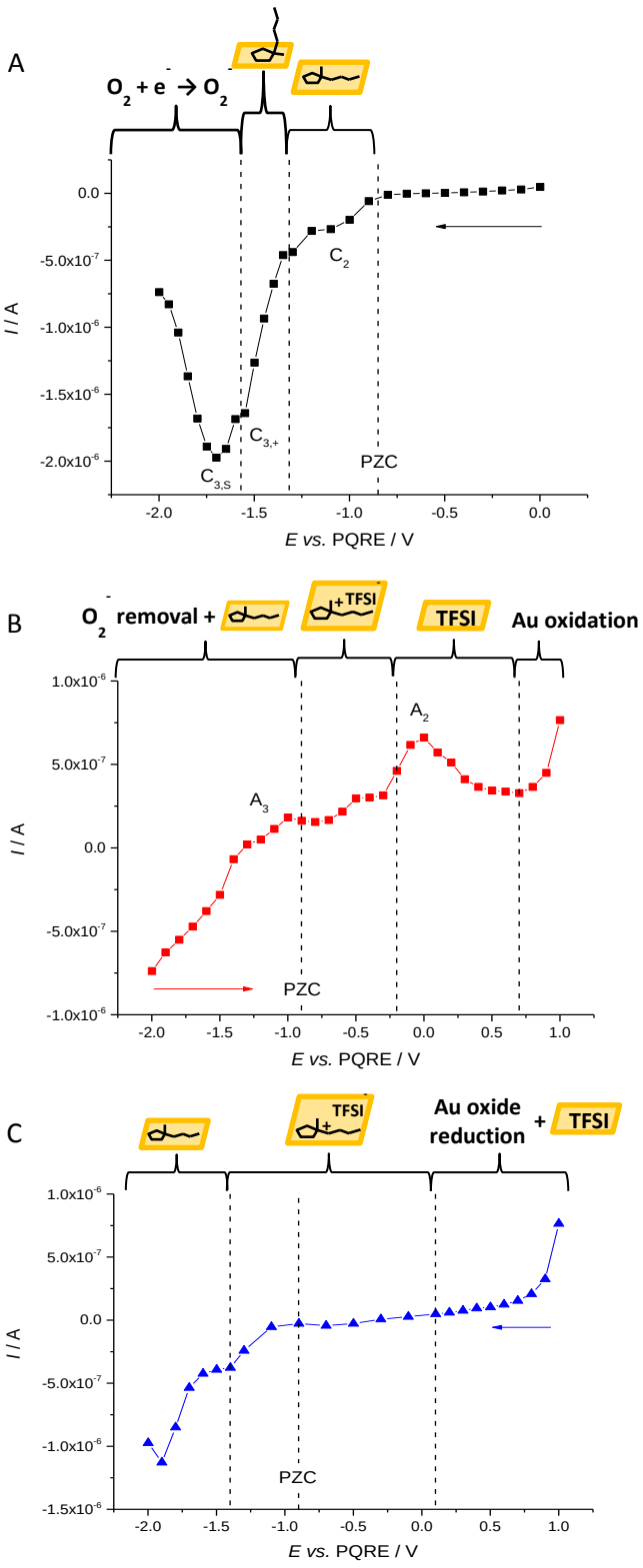

Figure 7-1 Conclusions about the EC behaviour at the Au – BMP TFSI interface, derived from the results and discussion of the CV, EIS and EC-SERS data of chapter 5, presented alongside the current-potential data obtained during the SERS spectra acquisitions. (A), (B) and (C) represent the first, second and third potential series and the arrows indicate the direction in which the potential was changed.

7.2.2 Challenges in Surface Enhanced Raman Spectroscopy of ILs on Gold SSV Substrates

During the course of this work, it has become evident that the study of metal-IL interfaces with EC-SERS is not as straightforward as the study of SAMs or molecules in weakly concentrated electrolytes. Efforts have been made to examine the challenges faced and the reasons behind them, in order to find ways of overcoming them to make EC-SERS a successful and powerful technique in the study of these interfaces.

A simple comparison of the Raman spectrum of BMP TFSI on flat Au to a SERS spectrum on SSV Au, initially led to confusion, as it was expected that the SERS enhancement on the SSV substrate would yield higher intensity peaks. However, this was not the case with the spectra being more intense on flat Au, in both the BMP TFSI and 1-butyl-3-methylimidazolium (BMI) TFSI ILs and in pure Py, which was initially used to ensure this effect was not specific to ILs. This unexpectedly low peak intensity in the spectra from SSV substrates was explained by the smaller volume of liquid probed on SSV substrates compared to on flat Au.

The depth resolution of the spectrometer, which determines the sample volume of the analyte probed, was estimated to be 28.6 ± 0.3 μm, by measuring a depth profile on a Si wafer. The distance from the substrate at which 95% of the SERS enhancement is lost was estimated to be 106 nm. This was estimated by applying an equation found in the literature to the SSV substrates used in this study.[4, 5] The validity of this equation to describe the SERS signal decay with distance from SSV substrates was also successfully verified in this study, by comparing the intensities of the *ν*(CN) peaks of a 4-MBN SAM and a 4'-MBPCN SAM in BMP TFSI. The volume of liquid probed on a flat Au surface is likely defined by the depth resolution of the spectrometer which is at least two orders of magnitude higher than the volume of liquid probed on a Au SSV substrate, which is defined by the exponential SERS signal decay with distance from the substrate.

The dependence of the bulk signal interfering with the spectra on SSV substrates on the concentration of the studied molecules in solution was examined using Py. Py was used because its Raman spectrum has separate peaks for Py in solution and Py adsorbed on Au, so the bulk signal of Py can be easily distinguished from the surface-specific signal. For Py concentrations below 5 M, the bulk Py peak intensity was smaller than the surface specific peak intensity. However, when the Py concentration reached 5 M, the bulk Py peaks became more intense than the surface bound Py peaks, indicating that when the concentration rises above a certain value, the SERS spectra are likely dominated by the bulk liquid signal.

Interestingly, the effect of the bulk signal from concentrated liquids has never been discussed in the literature, mainly due to the fact that most SERS studies involve SAMs, where there is no bulk

signal, or molecules existing at small concentrations in liquids.[6-10] Only a few of publications on SERS of the metal-IL interface present bulk spectra of the ILs and even though the larger signal for bulk Raman spectra of ILs is sometimes evident, it has never been noted upon or discussed.[11, 12] Examining the effect that the signal from the bulk electrolyte has on the SERS spectra is important for any system, where the target is to study the interfacial region very close to the substrates. If processes occurring within the first few ion layers at the metal-IL interface, such as specific adsorption, are to be successfully studied, improving the depth resolution and SERS enhancement ability of the substrate is crucial.

Another challenge faced whilst studying the Au – BMP TFSI interface, especially with regards to the potential-dependent behaviour of the BMP cations, was the complexity of the vibrational assignment of the Raman peaks. Most intense peaks present in IL Raman spectra are associated with the anions because of large polarizability fluctuation from their vibrations, which results in many cation peaks being overshadowed.[13] In the authors' opinion, DFT calculations are necessary in the study of ILs by SERS, as they have added extremely valuable insight into the identity of the vibrations occurring in each ion and vibrational assignments purely based on the literature have proven inadequate. However, even with the use of DFT calculations, the presence of 70 peaks in the BMP TFSI spectrum, many of which overlapped, complicated their deconvolution and fittings. Therefore, the ions of the IL used and their spectra have to be carefully considered, in order to establish if the peaks to be analysed are clearly distinguishable from the rest of the spectrum.

7.3 Further Work

7.3.1 Improving the Quality of Results from EC-SERS Experiments

As discussed earlier, most of the bulk liquid signal interfering with the SERS spectra of concentrated liquids is due to the SERS signal decay with distance from the SERS substrate. As SSV substrates are already optimised to give the best level of enhancement possible, the next best way of restricting the bulk signal is to improve the depth resolution of the spectrometer.

The Renishaw inVia spectrometer is built with an optical lay-out which makes the system confocal. 'High' confocality can be further achieved by introducing a 'pin hole' in the lay-out. According to the Renishaw technical support team, depth resolutions of the order of a few µm can be achieved. For example, a 785nm line laser with a pin hole and a x100 objective should give a resolution of 2.8µm. However, the system used in this study is 'pin hole-free' and so only 'standard' confocality can be achieved.

There is a fully confocal microscope available in the Department of Chemistry at the University of Southampton, which should have a better depth resolution. It is combined with a 633 nm He-Ne laser and can only reach laser powers of up to 2-3 mW. Given the availability of the microscope, it would be interesting to repeat the EC-SERS experiment of BMP TFSI on a Au SSV substrate with the 633 nm spectrometer, in an attempt to remove bulk IL signal. However, one can expect higher backgrounds from fluorescence effects due to the wavelength of the laser and potentially weaker peaks due to the relatively low laser power. Overall, the best results can be expected by using a fully confocal spectrometer with a fitted pinhole, so that the best depth resolution is achieved.

The only region in the BMP TFSI spectrum, where BMP peaks could be analysed without the interference of high intensity TFSI peaks, was between 800 cm^{-1} and 1100 cm^{-1}. In order to solve the issue of the high number of peaks in the BMP TFSI IL, which complicated the analysis of weak BMP peaks, a BMP-based IL could be used with a smaller and simpler anion, such as BF_4 or PF_6. For example, the BF_4 anion spectrum only really has one intense peak at 765 cm^{-1}.[11] Unless specifically required, halide anions should be avoided as their co-adsorption onto substrates has been found to affect the SERS enhancement.[14-16]

Once a potential region of interest has been identified, the collection of more data points in this potential range may make the separation of processes more clear. For example, in EC-SERS measurements for the BMP TFSI IL on a Au SSV substrate discussed in chapter 5, a SERS spectrum was obtained at 50 mV intervals. The potential region between the tentatively assigned PZC at -0.85 V and -1.75 V vs. PQRE was identified as a region of high interest, as the cation arrangement and superoxide production processes were occurring at these potentials. Obtaining SERS spectra at smaller potential steps, for example every 10 mV, may improve the clarity of the data corresponding to separate processes.

7.3.2 SAMs and the Stark Effect

The Stark effect of a 4-MBN SAM on a Au SSV substrate was compared in ILs and in an aqueous PPB. There were two separate regions in the Stark tuning rates in the ILs, as can be seen in figure 7-2, which were suggested to be the result of the presence of the PZC. However, it would be beneficial to expand the data obtained towards more positive potentials, in order to determine if the lower Stark tuning rates continued into the positive potential region. This would determine if the low Stark tuning rates are the result of the arrangement of the anions at the interface or the result of the PZC itself. This should then be re-enforced by the estimation of the PZC using EIS, as carried out in chapter 5, for the pure metal-IL interface.

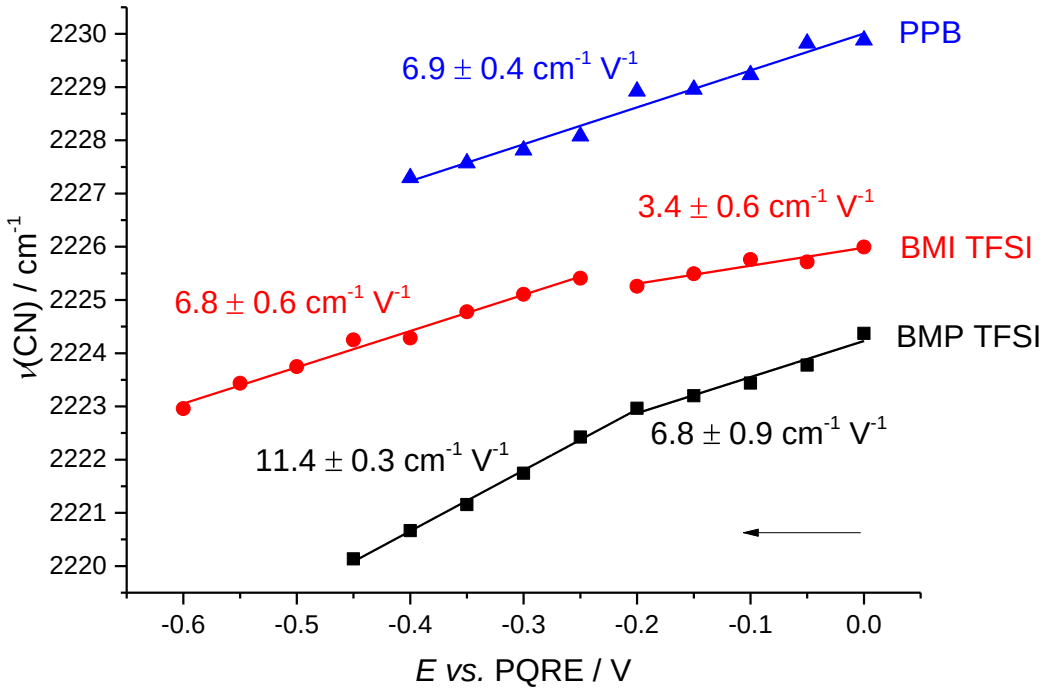

Figure 7-2 *ν*(CN) peak positions, linear fittings and corresponding Stark tuning rates, for 4-MBN SAMs on Au SSV substrates (made with 600 nm diameter spheres and a thickness of 468 nm)in BMP TFSI (black squares), BMI TFSI (red circles) and 10 mM, pH 7 PPB (blue triangles). The arrow indicates the direction in which the potential was changed and the order in which the data were collected. The spectra were obtained using a 785 nm near-infrared (NIR) laser and a 50x objective and have been normalised by the laser power and exposure time used.

Zhang et al. have probed the Au – BMI BF_4 interface by using SERS and the Stark effect of nitrile probes on adsorbed molecules of different lengths.[17] They carried out their study on a roughened Au surface so it would be interesting to carry out a similar study on SSV substrates. The molecules they used as the Stark effect probes have been displayed in figure 7-3 (A) and did not form dense SAMs like thiol molecules do. They were purposely selected so that the IL ions could fill the volume down to the electrode surface and not just be in contact with a SAM surface. This allowed the authors to study the electrostatic effects within different thicknesses of the EDL.

Oklejas et al. carried out a similar study of the Stark effect at various lengths into the diffuse EDL in aqueous $NaClO_4$ solutions.[18] They used a series of SAMs composed of alkanethiols and mercaptododecanenitrile, as demonstrated in figure 7-3 (B). The densely packed alkanethiols keep the IL ions at a certain distance away from the electrode surface, so that the nitrile probe is detecting the electric field from the ions in different depths of the electrolyte. These are two

examples of how the vibrational Stark effect may be used as a spatial probe of interfacial electric fields in the EDL of ILs. It would be interesting to examine if the results from the two types of probe are different and use them at the Au-IL interface.

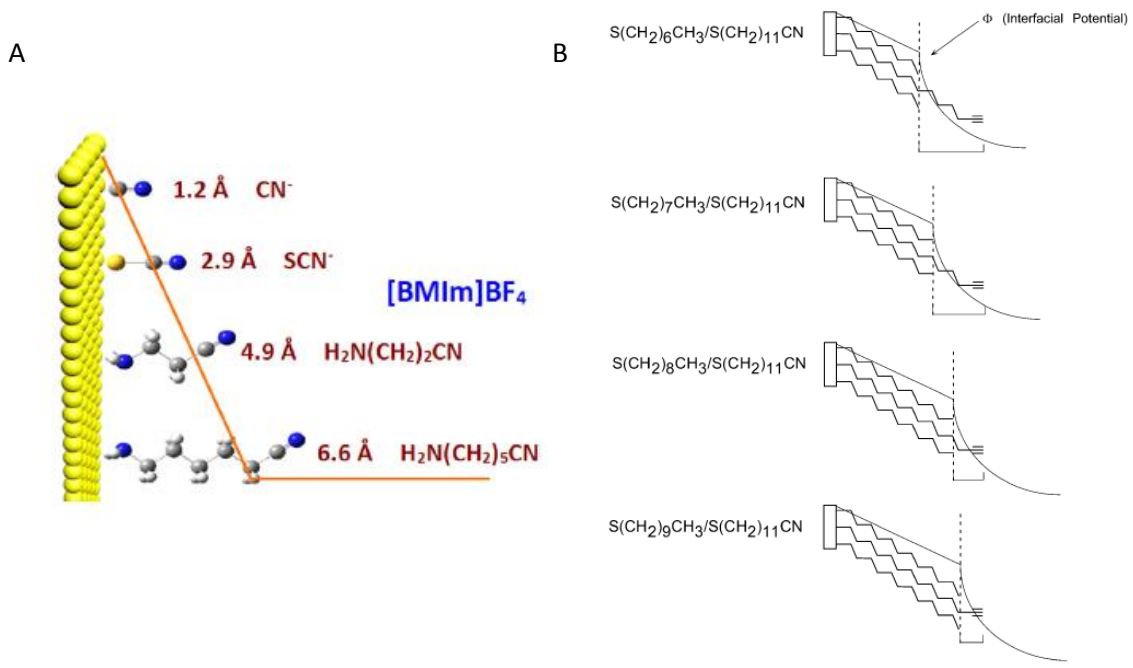

Figure 7-3 (A) Schematic diagram of different probes adsorbed at the Au – BMI BF_4 interface, taken from the publication by Zhang et al..[17] (B) Graphical depiction of the interfacial boundary region for each mixed-monolayer system Investigated in the study by Oklejas et al..[18]

There is clearly much work that can still be done in order to optimise EC-SERS for the study of the metal-IL interface and to fully understand some of the challenges facing researchers who use the technique. Nevertheless, certain capabilities of the method in the study of these interfaces have been demonstrated in this report. The work in this thesis has laid down the foundations upon which future research projects can progress, with a deeper understanding of the requirements for the successful application of EC-SERS in the study of Au-IL interfaces and of the types of information that can be extracted.

7.4 References

1. R. Atkin, N. Borisenko, M. Druschler, S. Z. El Abedin, F. Endres, R. Hayes, B. Huber and B. Roling, *Phys. Chem. Chem. Phys.*, 2011, **13**, 6849-6857.

2. R. Wen, B. Rahn and O. M. Magnussen, *Angew. Chem. Int. Edit.*, 2015, **54**, 6062-6066.

3. L. Grande, E. Paillard, G. T. Kim, S. Monaco and S. Passerini, *Int. J. Mol. Sci.*, 2014, **15**, 8122-8137.

4. B. J. Kennedy, S. Spaeth, M. Dickey and K. T. Carron, *J. Phys. Chem. B*, 1999, **103**, 3640-3646.

5. S. S. Masango, R. A. Hackler, N. Large, A. I. Henry, M. O. McAnally, G. C. Schatz, P. C. Stair and R. P. Van Duyne, *Nano Lett.*, 2016, **16**, 4251-4259.

6. M. E. Abdelsalam, P. N. Bartlett, J. J. Baumberg, S. Cintra, T. A. Kelf and A. E. Russell, *Electrochem. Commun.*, 2005, **7**, 740-744.

7. N. G. Tognalli, A. Fainstein, E. J. Calvo, M. Abdelsalarn and P. N. Bartlett, *J. Phys. Chem. C*, 2012, **116**, 3414-3420.

8. A. Celiktas, M. A. Ghanem and P. N. Bartlett, *J. Electroanal. Chem.*, 2012, **670**, 42-49.

9. R. P. Johnson, N. Gale, J. A. Richardson, T. Brown and P. N. Bartlett, *Chem. Sci.*, 2013, **4**, 1625-1632.

10. M. J. Weaver, S. Z. Zou and H. Y. H. Chan, *Analytical Chemistry*, 2000, **72**, 38A-47A.

11. J. C. Rubim, F. A. Trindade, M. A. Gelesky, R. F. Aroca and J. Dupont, *J. Phys. Chem. C*, 2008, **112**, 19670-19675.

12. C. R. R. Brandao, L. A. F. Costa, H. S. Breyer and J. C. Rubim, *Electrochem. Commun.*, 2009, **11**, 1846-1848.

13. V. H. Paschoal, L. F. O. Faria and C. C. Ribeiro, *Chem. Rev.*, 2017, **117**, 7053-7112.

14. Barnes, Tian, Aggaral, Goodacre, Donaldson, M. Muniz, Baumberg, Vlckova, Creighton, Natan, Kosower, Alexander, Khan, Russell, Murakoshi, Kneipp, Domke, R. Le, Green, Poponin, Stone, Ren, Pettinger, Milton, Jarvis, Tantra, Kall, Sugawara, Roy, Whitby and Richards, *Faraday Discuss.*, 2006, **132**, 227-247.

15. P. Etchegoin, L. F. Cohen, H. Hartigan, R. J. C. Brown, M. J. T. Milton and J. C. Gallop, *J. Chem. Phys.*, 2003, **119**, 5281-5289.

16. R. Pang, X. G. Zhang, J. Z. Zhou, D. Y. Wu and Z. Q. Tian, *J. Phys. Chem. C*, 2017, **121**, 10445-10454.

17. N. Zhang, X. R. Wang, Y. X. Yuan, H. F. Wang, M. M. Xu, Z. G. Ren, J. L. Yao and R. A. Gu, *J. Electroanal. Chem.*, 2015, **751**, 137-143.

18. V. Oklejas, C. Sjostrom and J. M. Harris, *J. Phys. Chem. B*, 2003, **107**, 7788-7794.

19. N. Borisenko, A. Lahiri, G. Pulletikurthi, T. Cui, T. Carstens, J. Zahlbach, R. Atkin and F. Endres, *Faraday Discuss.*, 2018, **206**, 459-473.

Appendix A Vibrational Assignment of Ionic Liquids

This appendix contains tables accompanying section 3.2 of chapter 3.

Table A-1 Vibrational assignment of peaks in density functional theory DFT-calculated Raman spectra of optimised eq-BMP and ax-BMP structures. DFT calculations were carried out on the basis of the B3LYP/6-311+G(d,p) levels of theory.

Calculated peak centre / cm^{-1}	**Conformer**	**Assignment**
102	Ax-BMP	$\rho(C_{(3)}H_2)$ + $\rho(C_{(4)}H_2)$ + oop ring deformation
108	Eq-BMP	$\omega(C_{(10)}H_3)$ + $\rho(CH_2)_{ring}$
148	Ax-BMP	$\rho(C_{(3)}H_2)$ + $\rho(C_{(2)}H_2)$ + oop ring deformation + $\rho(C_{(10)}H_3)$
190	Eq-BMP	$\rho(CH_2)_{ring}$ + $\rho(C_{(7)}H_2)$ + $\rho(C_{(6)}H_3)$ + $\rho(C_{(10)}H_3)$
197	Ax-BMP	$\rho(C_{(5)}H_2)$ + $\rho(C_{(4)}H_2)$ + oop ring deformation + $\tau(C_{(6)}H_3)$
237	Ax-BMP	$t(C_{(6)}H_3)$ + $t(C_{(10)}H_3)$
244	Eq-BMP	
279	Eq-BMP	$t(C_{(6)}H_3)$ + $\rho(C_{(5)}H_2)$ + $\rho(C_{(10)}H_3)$
285	Ax-BMP	$t(C_{(6)}H_3)$ + $\rho(C_{(5)}H_2)$ + $\rho(C_{(2)}H_2)$ + oop ring deformation + $\rho(C_{(10)}H_3)$
291	Eq-BMP	$t(C_{(6)}H_3)$ + $\delta(C_{(7)}C_{(8)}C_{(9)})$
300	Ax-BMP	$\rho(C_{(5)}H_2)$ + $\rho(C_{(2)}H_2)$ + $\rho(C_{(6)}H_3)$ + $\delta(C_{(7)}C_{(8)}C_{(9)})$
342	Ax-BMP	$\delta(C_{(6)}NC_{(7)})$
361	Eq-BMP	
385	Ax-BMP	$\delta(C_{(6)}NC_{(7)})$
391	Eq-BMP	$\delta(C_{(6)}NC_{(2)})$
435	Eq-BMP	$\delta(C_{(6)}NC_{(5)})$
467	Ax-BMP	$\delta(C_{(2)}NC_{(7)})$ + $\delta(C_{(8)}C_{(9)}C_{(10)})$
468	Eq-BMP	$\delta(C_{(8)}C_{(9)}C_{(10)})$ + $\delta(C_{(2)}NC_{(6)})$
486	Ax-BMP	$\delta(NC_{(2)}C_{(5)}C_{(6)})$
586	Ax-BMP	Ip ring deformation
631	Eq-BMP	
655	Eq-BMP	Ip ring deformation
	Ax-BMP	
726	Eq-BMP	$\rho(C_{(3)}H_2)$ + $\rho(C_{(4)}H_2)$
730	Ax-BMP	
747	Eq-BMP	$\rho(C_{(8)}H_2)$ + $\rho(C_{(9)}H_2)$

Appendix A

Calculated peak centre / cm^{-1}	Conformer	Assignment
800	Ax-BMP	$\rho(CH_2)_{chain} + \rho(C_{(10)}H_3)$
803	Eq-BMP	
807	Ax-BMP	$\rho(C_{(3)}H_2) + \rho(C_{(2)}H_2) + \rho(C_{(7)}H_2) + \rho(C_{(9)}H_2)$
816	Eq-BMP	$\rho(C_{(4)}H_2) + \rho(C_{(3)}H_2) + \rho(C_{(5)}H_2)$
824	Ax-BMP	
879	Ax-BMP	$\nu(NC_{(7)})$ + ip ring breathing
899	Eq-BMP	$\nu_{ip}(NC_{(7)})$ + ip ring breathing
902	Ax-BMP	
909	Eq-BMP	$\delta(C_{(9)}C_{(10)}H_3)$
912	Ax-BMP	
923	Eq-BMP	$\omega(C_{(6)}H_3)$
929	Ax-BMP	Whole molecule vibration
955	Ax-BMP	$\tau(C_{(10)}H_3) + \rho(C_{(7)}H_2) + \tau(C_{(8)}H_2) + \tau(C_{(9)}H_2)$
956	Eq-BMP	$\rho(C_{(2)}H_2) + \rho(C_{(5)}H_2)$
965	Eq-BMP	$\rho(C_{(6)}H_3)$
980	Ax-BMP	$\tau(CH_2)_{ring}$
1006	Eq-BMP	Ip ring deformation + $\rho(C_{(6)}H_3)$
	Ax-BMP	
1022	Eq-BMP	$\nu_a(C_{(7)}NC_{(6)})$
1030	Ax-BMP	$\nu_a(C_{(7)}C_{(8)}C_{(9)}C_{(10)})$
1034	Eq-BMP	
1039	Ax-BMP	$\nu(C_{(3)}C_{(4)})$
1052	Ax-BMP	$\nu_a(C_{(7)}C_{(8)}C_{(9)}C_{(10)})$
1054	Eq-BMP	
1063	Eq-BMP	Ip ring deformation
1073	Ax-BMP	
1097	Eq-BMP	oop ring deformation + $\tau(C_{(6)}H_3) + \rho(CH_2)_{ring}$
1112	Ax-BMP	oop ring deformation+ $\omega(C_{(10)}H_3)+ \rho(CH_2)_{ring}$
1134	Eq-BMP	$\delta(HC_{(10)}C_{(9)}) + \omega(C_{(10)}H_3) + \delta(C_{(10)}C_{(9)}C_{(8)})$
	Ax-BMP	$\delta(HC_{(6)}N) + \omega(C_{(10)}H_3)$
1147	Ax-BMP	$\tau(C_{(6)}H_3) + \tau(C_{(2)}H_2)$
1158	Eq-BMP	$\tau(C_{(6)}H_3) + \tau(C_{(7)}H_2)$
1184	Ax-BMP	$\delta(HC_{(6)}N)$
1192	Eq-BMP	$\delta(HC_{(6)}N) + \omega(C_{(6)}H_3) + \tau(C_{(2)}H_2) + \tau(C_{(5)}H_2)$
1208	Ax-BMP	$\tau(C_{(6)}H_3) + \tau(CH_2)_{chain} + \tau(C_{(10)}H_3)$
1216	Eq-BMP	$\delta(HC_{(6)}N) + \omega(C_{(6)}H_3)$
1239	Ax-BMP	$\tau(C_{(2)}H_2)$

Calculated peak centre / cm^{-1}	Conformer	Assignment
1249	Eq-BMP	$\tau(C_{(5)}H_2) + \tau(C_{(7)}H_2)$
1250	Ax-BMP	$\tau(CH_2)_{ring}$
1262	Eq-BMP	$\tau(CH_2)_{ring} + \tau(C_{(6)}H_3)$
1272	Ax-BMP	$\tau(C_{(3)}H_2) + \tau(C_{(4)}H_2)$
1277	Eq-BMP	$\tau(C_{(2)}H_2) + \tau(C_{(4)}H_2)$
1285	Ax-BMP	$\tau(C_{(3)}H_2) + \tau(C_{(8)}H_2) + \tau(C_{(9)}H_2)$
1296	Ax-BMP	$\tau(C_{(5)}H_2)$
1297	Eq-BMP	
1307	Eq-BMP	$\omega(C_{(8)}H_2) + \omega(C_{(9)}H_2)$
1308	Ax-BMP	
1335	Eq-BMP	$\tau(CH_2)_{chain} + \omega(C_{(3)}H_2) + \omega(C_{(2)}H_2) + \omega(C_{(4)}H_2)$
1339	Ax-BMP	$\tau(C_{(8)}H_2) + \tau(C_{(9)}H_2) + \omega(C_{(4)}H_2)$
1342	Eq-BMP	$\tau(C_{(9)}H_2) + \tau(C_{(8)}H_2) + \tau(C_{(3)}H_2)$
1348	Ax-BMP	$\omega(C_{(4)}H_2) + \omega(C_{(3)}H_2) + \tau(C_{(5)}H_2) + \tau(C_{(2)}H_2)$
1362	Eq-BMP	$\tau(C_{(2)}H_2) + \omega(C_{(4)}H_2)$
	Ax-BMP	$\tau(C_{(8)}H_2) + \tau(C_{(7)}H_2)$
1371	Eq-BMP	$\omega(C_{(5)}H_2) + \omega(C_{(3)}H_2)$
1382	Ax-BMP	$\omega(C_{(5)}H_2) + \omega(C_{(2)}H_2) + \omega(C_{(8)}H_2) + \omega(C_{(9)}H_2)$
1387	Eq-BMP	$\omega(C_{(9)}H_2) + \omega(C_{(8)}H_2)$
1393	Eq-BMP	$\omega(C_{(2)}H_2)$
1397	Ax-BMP	$\omega(C_{(5)}H_2) + \omega(C_{(2)}H_2)$
1414	Ax-BMP	$\omega(C_{(7)}H_2)$
1425	Ax-BMP	$\delta(C_{(10)}H_3)$
1427	Eq-BMP	$\omega(C_{(7)}H_2) + \delta(C_{(10)}H_3)$
1461	Ax-BMP	$\delta\ (C_{(6)}H_3)$
1462	Eq-BMP	
1490	Ax-BMP	$\delta(C_{(10)}H_3) + \delta(C_{(6)}H_3) + \delta(C_{(7)}H_2) + \delta(C_{(8)}H_2)$
1493	Eq-BMP	$\delta(C_{(9)}H_2) + \delta(C_{(8)}H_2) + \delta(C_{(10)}H_3) + \delta(CH_2)_{ring} + \delta(C_{(6)}H_3)$
1500	Ax-BMP	$\delta(C_{(10)}H_3) + \delta(C_{(6)}H_3) + \delta(C_{(5)}H_2)$
1503	Eq-BMP	$\delta(C_{(10)}H_3)$
1512	Ax-BMP	$\delta(CH_2)_{ring} + \delta(C_{(7)}H_2)$
1513	Eq-BMP	$\delta(C_{(9)}H_2) + \delta(C_{(8)}H_2) + \delta(C_{(10)}H_3) + \delta(C_{(5)}H_2) + \delta(C_{(3)}H_2) + \delta(C_{(4)}H_2) + \delta(C_{(6)}H_3)$
1521	Eq-BMP	$\delta(C_{(3)}H_2) + \delta(C_{(4)}H_2) + \delta(C_{(2)}H_2) + \delta(C_{(6)}H_3) + \delta(C_{(7)}H_2) + \delta(C_{(8)}H_2)$
1523	Ax-BMP	$\delta(C_{(4)}H_2) + \delta(C_{(2)}H_2) + \delta(C_{(5)}H_2) + \delta(CH_2)_{chain} + \delta(C_{(6)}H_3)$
1535	Eq-BMP	$\delta(CH_2)_{ring}$
	Ax-BMP	

Appendix A

Calculated peak centre / cm^{-1}	**Conformer**	**Assignment**
3018	Eq-BMP	$\nu_s(C_{(9)}H_2)$
	Ax-BMP	
3034	Ax-BMP	$\nu_s(C_{(8)}H_2) + \nu_s(C_{(10)}H_3)$
3035	Eq-BMP	
3046	Eq-BMP	$\nu_a(C_{(9)}H_2)$
	Ax-BMP	
3060	Eq-BMP	$\nu_s(C_{(7)}H_2)$
3074	Ax-BMP	$\nu_s(C_{(4)}H_2) + \nu_s(C_{(3)}H_2) + \nu_a(C_{(8)}H_2) + \nu_s(C_{(7)}H_2)$
3080	Eq-BMP	$\nu_s(C_{(3)}H_2) + \nu_s(C_{(4)}H_2) + \nu_s(C_{(6)}H_3)$
3088	Eq-BMP	$\nu_s(CH_2)_{ring}$
	Ax-BMP	
3110	Eq-BMP	$\nu_a(C_{(10)}H_3) + \nu_a(C_{(3)}H_2) + \nu_a(C_{(4)}H_2)$
	Ax-BMP	
3128	Eq-BMP	$\nu_a(CH_2)_{ring}$
3129	Ax-BMP	$\nu_a(C_{(3)}H_2) + \nu_a(C_{(4)}H_2) + \nu_a(C_{(7)}H_2) + \nu_a(C_{(2)}H_2)$
3145	Eq-BMP	$\nu_a(C_{(5)}H_2) + \nu_a(C_{(4)}H_2)$
3146	Ax-BMP	$\nu_a(C_{(2)}H_2) + \nu_a(C_{(3)}H_2)$
3152	Eq-BMP	$\nu_a(C_{(2)}H_2)$
3159	Ax-BMP	$\nu_a(C_{(5)}H_2) + \nu_a(C_{(6)}H_3)$
3170	Eq-BMP	$\nu_a(C_{(6)}H_3)$
3172	Ax-BMP	
3181	Eq-BMP	$\nu_a(C_{(6)}H_3)$

Table A-1 Vibrational assignment of peaks in DFT-calculated Raman spectra of optimised cis-TFSI and trans-TFSI structures. DFT calculations were carried out on the basis of the B3LYP/6-311+G(3df) levels of theory.

Calculated peak centre / cm^{-1}	**Conformer**	**Assignment**
108	Trans-TFSI	δ(NSC)
114	Cis-TFSI	$\omega(CF_3)$ + δ(NSC)
114	Cis-TFSI	δ(SNS) + $\omega(CF_3)$
151	Trans-TFSI	δ_{ip}(SNS)
153	Cis-TFSI	δ_{ip}(SNS) + $\rho_{ip}(SO_2)$
185	Cis-TFSI	ρ_{oop}(NSO)
195	Trans-TFSI	$\tau_{oop}(SO_2)$ + $\tau_{oop}(CF_3)$
197	Cis-TFSI	
263	Trans-TFSI	δ_{oop}(FCS) + δ(OSC)
267	Cis-TFSI	
290	Trans-TFSI	$\tau_{ip}(SO_2)$
301	Cis-TFSI	δ_{oop}(FCSO)
303	Trans-TFSI	ν_{oop}(CS) + δ(NSO)
313	Cis-TFSI	δ_{oop}(FCSO)
321		
331	Trans-TFSI	δ_{oop}(FCS) + $\tau_{oop}(SO_2)$
341	Cis-TFSI	ω_{oop}(NSO) + $\tau_{oop}(SO_2)$ + $\tau_{oop}(CF_3)$
347	Trans-TFSI	ω_{oop}(SNS)
387	Trans-TFSI	δ(NSO)
396	Cis-TFSI	δ(NSO) + $\rho(SO_2)$ + $\omega(SO_2)$ + $\omega(CF_3)$
402	Trans-TFSI	$\rho_{ip}(SO_2)$
431	Cis-TFSI	δ_{oop}(NSO) + $\rho(SO_2)$ + $\omega(CF_3)$
506	Cis-TFSI	$\delta_{ip}(SO_2)$ + $\delta_{ip}(CF_3)$
510	Trans-TFSI	$\delta_{ip}(SO_2)$
524	Cis-TFSI	$\delta(CF_3)$ + δ(NSO)
527	Trans-TFSI	$\delta(CF_3)$
541	Cis-TFSI	
542	Trans-TFSI	$\delta_{ip}(CF_3)$
551	Trans-TFSI & Cis-TFSI	$\delta(CF_3)$
565	Trans-TFSI	$\delta(CF_3)$ + $\delta(SO_2)$
567	Cis-TFSI	
585	Trans-TFSI	τ_{oop}(SNS) + $\delta_{oop}(SO_2)$
595	Cis-TFSI	$\delta_{oop}(NSO_2)$
616	Trans-TFSI	δ_{ip}(SNS) + ω_{oop}(SNS)

Appendix A

Calculated peak centre / cm^{-1}	**Conformer**	**Assignment**
646	Cis-TFSI	$\delta(NSO_2)$
730	Trans-TFSI & Cis-TFSI	Whole anion breathing
750	Cis-TFSI	$\delta(CF_3)$
772	Cis-TFSI	$\nu_{s,ip}(SNS) + \nu_s(CF_3)$
775	Trans-TFSI	$\nu_{ip,s}(SNS)$
1065	Cis-TFSI	$\nu_s(NSC) + \nu_s(SO_2)$
1126	Trans-TFSI	$\nu_a(FCS)$
1127	Cis-TFSI	
1151	Trans-TFSI	$\nu_a(CF_3)$
1155	Cis-TFSI	
1159	Trans-TFSI	$\nu_{ip,a}(CF_3)$
1166	Cis-TFSI	$\nu_a(CF_3)$
1185	Cis-TFSI	$\nu_a(FCS) + \nu_{ip,a}(SNS) + \nu_s(SO_2)$
1189	Trans-TFSI	
1217	Cis-TFSI	$\nu_a(SNC)$
1230	Trans-TFSI	$\nu_{oop,a}(CSO) + \nu_s(SO_2)$
1231	Cis-TFSI	
1343	Cis-TFSI	$\nu_a(SO_2)$
1344	Trans-TFSI	
1360	Cis-TFSI	$\nu_a(SO_2) + \delta_{ip}(SNS)$
1365	Trans-TFSI	

Appendix B The SSV SERS Response in Ionic Liquids

This appendix contains figures accompanying chapter 4.

B.1 Pyridine

This section contains figures accompanying section 4.1.3.

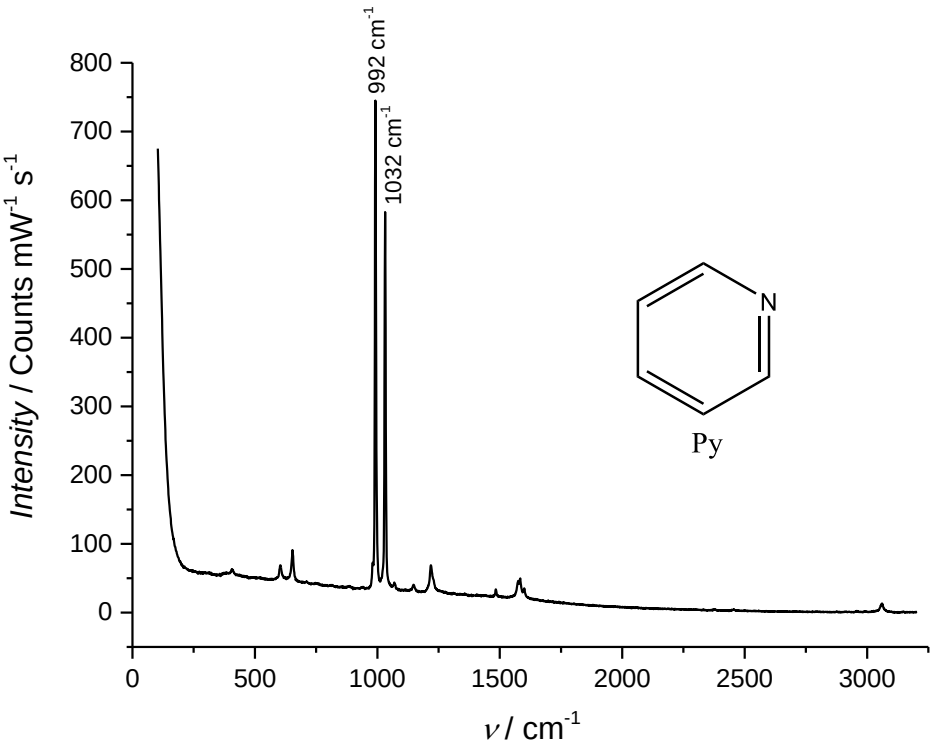

Figure B-1 Raman spectrum of pure Py taken in a Quartz crystal cuvette. The spectrum has been normalised by the laser power and exposure time used.

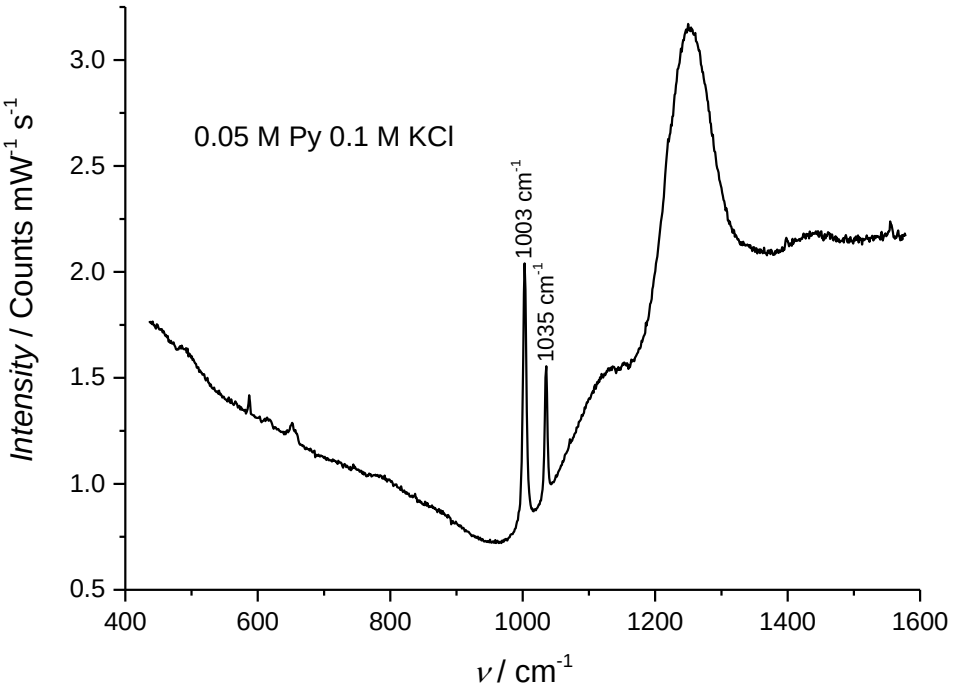

Figure B-2 Raman spectrum of an aqueous 0.05 M Py 0.1 M KCl solution taken in a Quartz crystal cuvette. The spectrum has been normalised by the laser power and exposure time used.

B.2 Reflectance Spectroscopy

This section contains a figure accompanying section 4.2.

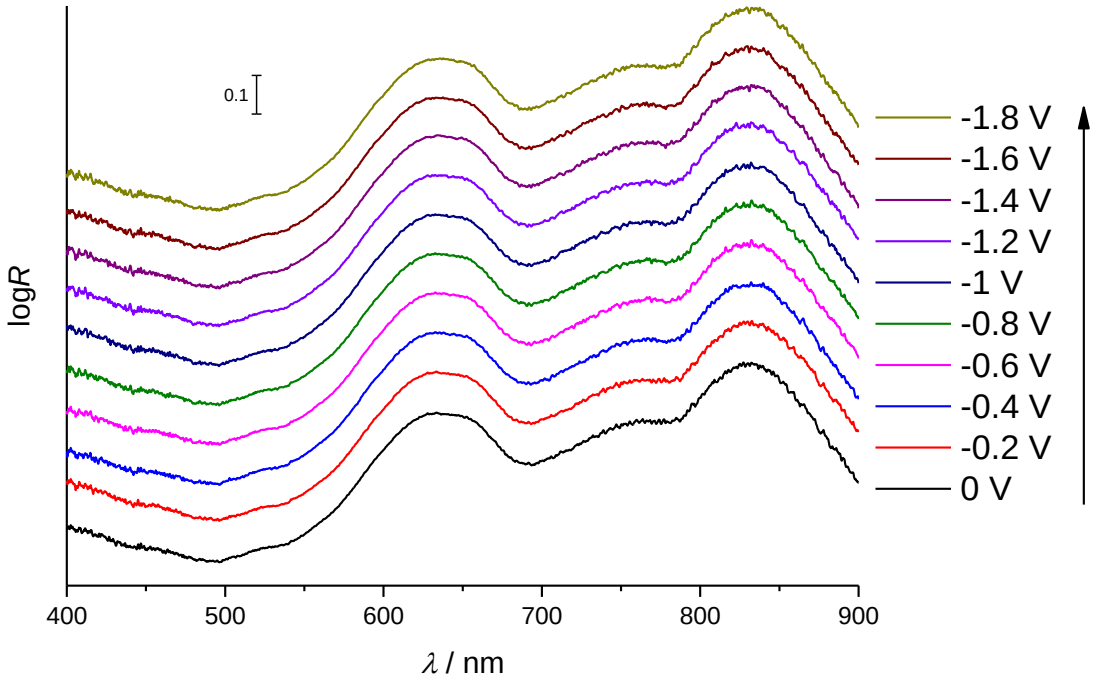

Figure B-3 Reflectance spectra presented as log*R* of a Au sphere segment void (SSV) substrate (prepared with 600 nm diameter spheres and a thickness of 468 nm) in BMP TFSI at various potentials vs. PQRE. The spectra were obtained using a white light laser source and have been offset by 0.1 for clarity. The arrow indicates the direction in which the potential was changed.

Appendix C EC-SERS and the Stark Effect of SAMs on Au

This chapter contains figures accompanying chapter 6.

C.1 SERS of the 4-MBN SAM on a Gold SSV Substrate

This section contains a figure accompanying section 6.1 of chapter 6.

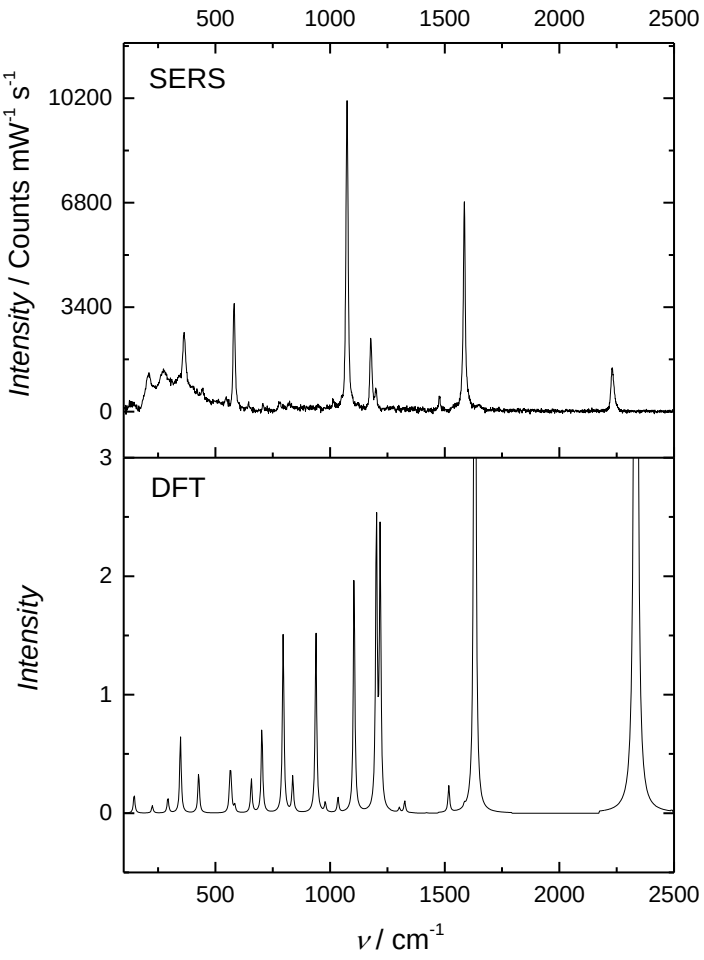

Figure C-4 Experimentally obtained SERS spectrum of a 4-MBN SAM on a Au SSV substrate in air (top) and a DFT-calculated Raman spectrum of the optimised 4-MBN thiol molecule (bottom). The SERS spectrum was obtained using a 785 nm NIR laser and a 50x objective. It has been normalised by the laser power and exposure time used and its background has been removed. DFT calculations were carried out on the basis of the B3LYP/6-311+G(d,p) levels of theory. The intensity of the DFT-calculated spectrum has been limited so that the lower frequency peaks could be observed in more detail.

C.2 SERS of the 4’-MBPCN SAM on a Gold SSV Substrate

This section contains a figure accompanying section 6.2 of chapter 6.

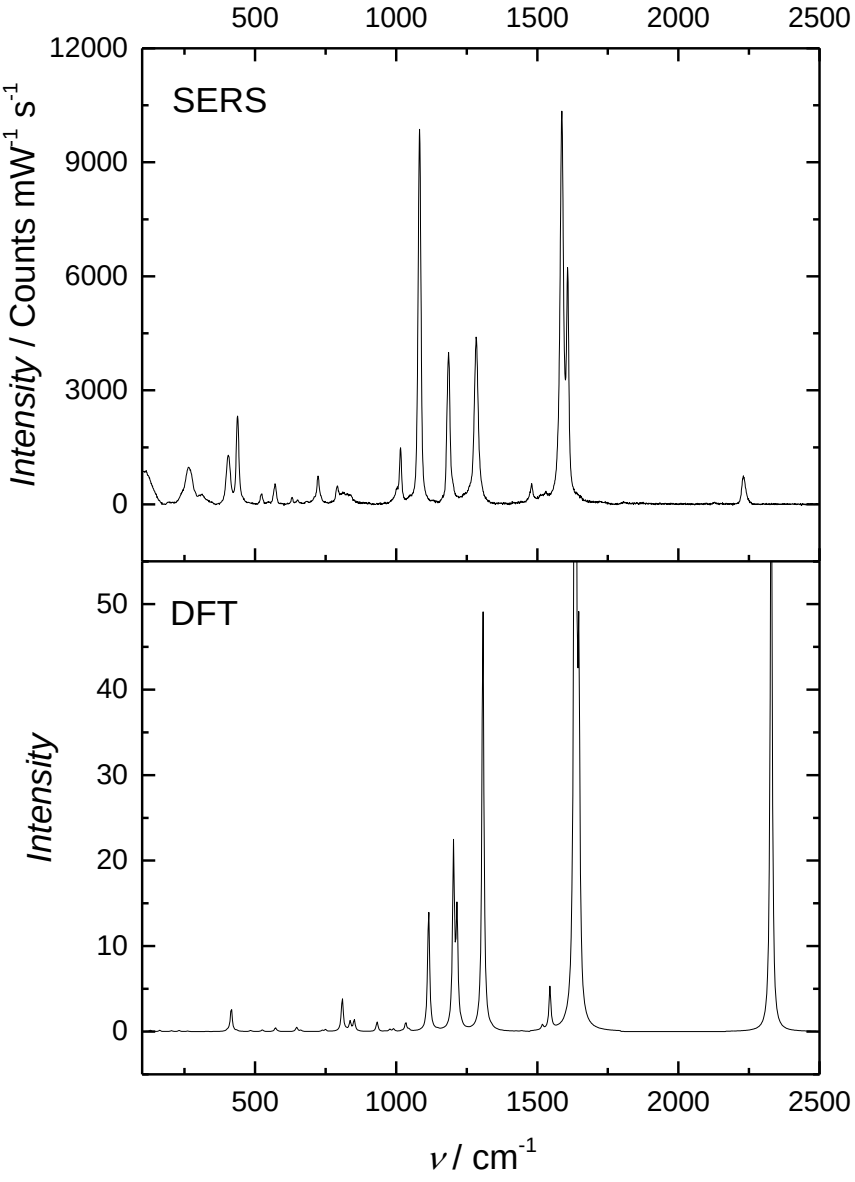

Figure C-5 Experimentally obtained SERS spectrum of a 4,4’-MBPCN SAM on a Au SSV substrate in air (top) and a DFT-calculated Raman spectrum of the optimised 4,4’-MBPCN thiol molecule (bottom). The SERS spectrum was obtained using a 785 nm NIR laser and a 50x objective. It has been normalised by the laser power and exposure time used and its background has been removed. DFT calculations were carried out on the basis of the B3LYP/6-311+G(d,p) levels of theory. The intensity of the DFT-calculated spectrum has been limited so that the lower frequency peaks could be observed in more detail.